



HAL
open science

Understanding and prediction of flow physics on a boundary layer ingestion air intake for a commercial aircraft

Hector Solorzano Flores

► **To cite this version:**

Hector Solorzano Flores. Understanding and prediction of flow physics on a boundary layer ingestion air intake for a commercial aircraft. Fluids mechanics [physics.class-ph]. Institut Polytechnique de Paris, 2023. English. NNT : 2023IPPAX093 . tel-04566494

HAL Id: tel-04566494

<https://theses.hal.science/tel-04566494>

Submitted on 2 May 2024

HAL is a multi-disciplinary open access archive for the deposit and dissemination of scientific research documents, whether they are published or not. The documents may come from teaching and research institutions in France or abroad, or from public or private research centers.

L'archive ouverte pluridisciplinaire **HAL**, est destinée au dépôt et à la diffusion de documents scientifiques de niveau recherche, publiés ou non, émanant des établissements d'enseignement et de recherche français ou étrangers, des laboratoires publics ou privés.



INSTITUT
POLYTECHNIQUE
DE PARIS

NNT : 2023IPPAX093

Thèse de doctorat



Understanding and prediction of flow physics on a boundary layer ingestion air intake for a commercial aircraft

Thèse de doctorat de l'Institut Polytechnique de Paris
préparée à l'École polytechnique

École doctorale n°626 École doctorale de l'Institut Polytechnique de Paris (EDIPP)
Spécialité de doctorat : Mécanique des fluides et des solides, acoustique

Thèse présentée et soutenue à Meudon, le 20 décembre 2023, par

HECTOR ADOLFO SOLORZANO FLORES

Composition du Jury :

Eric Goncalves Professeur, Ecole Nationale Supérieure de Mécanique et d'Aérotechnique	Président
David MacManus Professor, Cranfield University	Rapporteur
Nicolas Gourdain Professeur, ISAE-SUPAERO, University of Toulouse	Rapporteur
Arne Seitz Docteur, Bauhaus Luftfahrt e. V.	Examineur
Julien Dandois Directeur de recherche 2, ONERA (DAAA/MASH)	Directeur de thèse
Olivier Atinault Ingénieur de recherche, ONERA (DAAA/ACI)	Encadrant
Cyril Bonnaud Ingénieur, Airbus Opérations SAS	Invité

Dedicado a mi madre, Leticia Flores.

*En memoria de mi padre, Hector Solorzano,
y mi nana, Amalia Ramos.*

Abstract

The primary goal of new aircraft design is to increase energy efficiency, which is connected to a commitment to lessen aviation's impact on the environment and operating costs. The boundary layer ingestion (BLI) concept is a promising option to reduce fuel consumption by improving engine integration to the fuselage to create more efficient aircraft designs. For an aircraft with a classical tube-and-wing configuration the boundary layer created along any surface generates an increase in the aircraft base drag, having a negative impact on the overall performance. The BLI concept proposes to ingest and take advantage of the low momentum in the boundary-layer to generate thrust in a more efficient way [1]. This potential improvement has several drawbacks that make it difficult to fulfill some engine requirements. One of these requirements particularly concerns the flow distortion at the engine intake affected by a loss of total pressure and tangential velocities at the Aerodynamic Interface Plane (AIP). Notwithstanding all this, several studies [2][3][4] have demonstrated that it is still feasible to obtain benefits by using the BLI concept.

One of the physical phenomenon that might be expected in our study case is the loss of total pressure due to the thickness of the boundary layer. The heterogeneity of flow behavior leads to a reduction of the total pressure, which adversely affects the overall engine performance. Moreover, it may cause structural problems due to material fatigue of the engine components. This is not the only physical phenomenon triggering distortion at the AIP, secondary flows are also expected due to the double bending. The S-shaped duct is a typical geometry for such secondary phenomena [5]. The development of streamwise vorticity, as described above, is only one phenomenon among others. Another phenomenon is the creation of two horseshoe vortices upstream of the inlet lip on both sides of the nacelle. The predicted flow characteristics are a combination of all the physical phenomena outlined above, which result in an increase in distortion in general. Large total pressure losses within the intake reduce overall propulsion system efficiency and are frequently indicative of total pressure distortion and swirl issues.

The heterogeneity of the flow may lead to the appearance of aerodynamic instabilities of the fan blades. If the distortion is large enough, the fan might stall or the engine may surge. The distortion in this type of BLI intake is characterized by a loss of total pressure and large gradients in the intake velocity field. Those velocities gradients are both in axial and tangential

directions. This distortion, and the complexity of the flow behavior, can increase when operating in off-design conditions, such as take-off, emergency descent or crosswind, due to possible flow separations. To characterize the flow heterogeneity, distortion indices, like for example the Circumferential Distortion Index (IDC) and the Distortion index based on the lowest stagnation pressure θ degree sector ($DC(\theta)$), have been used. Nevertheless, some studies [6] have highlighted the limited description that these indices may offer. Most of them have been designed to analyze the distortion in a standard engine configuration and are based only on stagnation pressure losses. In the same study, the authors conclude that the velocity-based distortion criteria seem to be more appropriate than the pressure-based ones to characterize the distortion in a BLI configuration and more effort must be made to provide more appropriate distortion descriptions for BLI intakes. Most of distortion evaluations for this type of intake have so far been carried out using numerical simulations. Furthermore, various distortion research in S-ducts have been assessed using experimental data [7].

The simulation and prediction of complex flows like the one occurring in a BLI intake is one of the present issues facing the industry. The flow characteristics at the intake resemble those seen in a S-duct. This kind of geometry has been the subject of several Computational Fluid Dynamics (CFD) analyses, both to assess design modifications [8] and to compare with experimental results [5]. In comparison with the experimental data, these previous assessments show a large dispersion that is dependent on the numerical methodology used and, more importantly, on the turbulence model chosen. These inaccuracies might be a significant hurdle to the development of a concept when investigating highly optimized or creative designs. Some authors [9] have even recommended abandoning RANS model research in favor of focusing on scale-resolving simulations, such as Large Eddy Simulation (LES) or Direct Numerical Simulation (DNS), and standardizing its use in industrial applications.

Considering all the challenges and complexities explained above, this thesis evaluates the predictive capacity of turbulence models that are frequently used in an industrial context. The numerical solutions are compared with experimental results, and the effect of the turbulence modeling on the flow distortion at the AIP is assessed. The strengths and weaknesses of each model are highlighted, and finally some analyses are presented to explain possible deviations between numerical and experimental data.

Résumé en français

L'objectif principal de la conception de nouveaux avions est d'augmenter l'efficacité énergétique, ce qui est lié à un engagement à réduire l'impact de l'aviation sur l'environnement et les coûts d'exploitation. Le concept d'ingestion de couche limite (BLI) est une option prometteuse pour réduire la consommation de carburant en améliorant l'intégration du moteur au fuselage pour créer des conceptions d'avions plus efficaces. Pour un avion à configuration classique tube-aile, la couche limite créée le long de toute surface génère une augmentation de la traînée de base de l'avion, ayant un impact négatif sur les performances globales. Le concept BLI propose d'ingérer et de profiter du faible quantité de mouvement dans la couche limite pour générer une poussée de manière plus efficace [1]. Cette amélioration potentielle présente plusieurs inconvénients qui rendent difficile le respect de certaines exigences du moteur. L'une de ces exigences concerne particulièrement la distorsion d'écoulement à l'admission du moteur affectée par une perte de pression totale et des vitesses tangentielles au plan d'interface aérodynamique (AIP). Néanmoins, plusieurs études [2][3][4] ont démontré qu'il est toujours possible d'obtenir des avantages en utilisant le concept BLI.

L'un des phénomènes physiques qui pourrait être attendu dans notre cas d'étude est la perte de pression totale due à l'épaisseur de la couche limite. L'hétérogénéité du comportement de l'écoulement conduit à une réduction de la pression totale, ce qui affecte négativement les performances globales du moteur. De plus, cela peut causer des problèmes structurels en raison de la fatigue des matériaux des composants du moteur. Ce n'est pas le seul phénomène physique déclenchant une distorsion au niveau de l'AIP, des écoulements secondaires sont également attendus en raison de la double courbure de l'entrée. Le conduit en forme de S est une géométrie typique pour de tels phénomènes secondaires. Le développement de la vorticit  dans le sens du courant, tel que décrit ci-dessus, n'est qu'un phénomène parmi d'autres. Un autre phénomène est la création de deux tourbillons en forme de fer à cheval en amont de la lèvre d'entrée des deux côtés de la nacelle. Les caractéristiques d'écoulement prédites sont une combinaison de tous les phénomènes physiques décrits ci-dessus, qui se traduisent par une augmentation de la distorsion en général. Les pertes totales de pression importantes dans l'admission réduisent l'efficacité globale du système de propulsion et sont souvent indicatives d'une distorsion et de problèmes de tourbillonnement de la pression totale.

L'hétérogénéité de l'écoulement peut conduire à l'apparition d'instabilités aérodynamiques des aubes du compresseur. Si la distorsion est suffisamment importante, l'étage de compression pourrait caler ou le moteur pourrait surchauffer. La distorsion dans ce type d'admission BLI est caractérisée par une perte de pression totale et de grands gradients dans le champ de vitesse d'admission. Ces gradients de vitesse sont à la fois dans les directions axiale et tangentielle. Cette distorsion, ainsi que la complexité du comportement de l'écoulement, peut augmenter lorsqu'elle fonctionne dans des conditions hors conception, telles que le décollement, la descente d'urgence ou le vent de travers, en raison de possibles séparations d'écoulement. Pour caractériser l'hétérogénéité de l'écoulement, des indices de distorsion, tels que l'indice de distorsion circonférentielle (IDC) et l'indice de distorsion basé sur le secteur θ de plus basse pression stagnante ($DC(\theta)$), ont été utilisés. Néanmoins, certaines études ont souligné la description limitée que ces indices peuvent offrir [6]. La plupart d'entre eux ont été conçus pour analyser la distorsion dans une configuration de moteur standard et sont basés uniquement sur les pertes de pression totale. Dans la même étude, les auteurs concluent que les critères de distorsion basés sur la vitesse semblent être plus appropriés que ceux basés sur la pression pour caractériser la distorsion dans une configuration BLI et qu'il faut faire plus d'efforts pour fournir des descriptions de distorsion plus appropriées pour les admissions BLI. La plupart des évaluations de distorsion pour ce type d'admission ont jusqu'à présent été effectuées à l'aide de simulations numériques. En outre, diverses recherches sur la distorsion dans les conduits en forme de S ont été évaluées à l'aide de données expérimentales [7].

La simulation et la prédiction des écoulements complexes tels que celui qui se produit dans une configuration BLI est l'un des problèmes actuels auxquels l'industrie est confrontée. Les caractéristiques d'écoulement à l'admission ressemblent à celles observées dans un conduit en forme de S. Ce type de géométrie a fait l'objet de plusieurs analyses de dynamique des fluides numériques (CFD), à la fois pour évaluer les modifications de conception [8] et pour les comparer aux résultats expérimentaux [5]. En comparaison avec les données expérimentales, ces évaluations précédentes montrent une grande dispersion qui dépend de la méthodologie numérique utilisée et, plus important encore, du modèle de turbulence choisi. Ces inexactitudes pourraient constituer un obstacle important au développement d'un concept lors de l'étude de conceptions hautement optimisées ou créatives. Certains auteurs [9] ont même recommandé d'abandonner la recherche sur les modèles RANS au profit de la focalisation sur les simulations résolvant l'échelle, telles que la simulation des grandes échelles (LES) ou la simulation numérique directe (DNS), et de normaliser leur utilisation dans les applications industrielles.

Compte tenu de tous les défis et complexités expliqués ci-dessus, cette thèse évalue la capacité prédictive des modèles de turbulence fréquemment utilisés dans un contexte industriel. Les solutions numériques sont comparées aux résultats expérimentaux, et l'effet de la modélisation de la turbulence sur la distorsion d'écoulement au niveau de l'AIP est évalué. Les forces et les faiblesses de chaque modèle sont mises en évidence, et enfin, certaines analyses sont présentées

pour expliquer les écarts possibles entre les données numériques et expérimentales.

Acknowledgements

The end of my thesis allows me to make a journey through the last years, remembering everything that has happened since the moment I decided what professional path to take. I take the opportunity to show my gratitude to all those who at some point helped me to be where I am today.

I would like to first acknowledge the members of the thesis defense jury for dedicating their time and interest to my work. I would also like to express my gratitude to Onera for guiding me in the scientific aspect during the development of my thesis. I acknowledge my supervisor, Olivier Atinault, for his patience and exceptional guidance. He has been immensely helpful throughout this journey, providing invaluable advice. I would also like to acknowledge my thesis director, Julien Dandois, whom I deeply respect and admire for his scientific expertise. I extend my thanks to Michaël Méheut for his support in various administrative matters during my time at Onera. To all my colleagues in the ACI unit, especially Camille and Vincent, thank you for your unwavering support and the good times we've shared. I also thank Nicolas Rembaut for his assistance in analyzing experimental data. I also thank the comité de suivi, Eric Garnier and Denis Sipp.

I also want to acknowledge Airbus, which gave me the opportunity to fulfill a dream, to learn a lot and be part of an extraordinary group of people who have contributed a lot to my life. I would like express gratitude to Ludovic Gerard, who trusted me to do this task, who accompanied me and provided me with all his support throughout the thesis. I will always be grateful for the opportunity that he gave me. I would also like to acknowledge Cyril Bonnaud, who guided me throughout this thesis, who besides being an excellent professional and sharing his wisdom with me, also managed to forge a good friendship and provide me with the best personal advice. I also appreciate Alain Dega, who also helped me integrate into the team and guided me during my first year of thesis. I also want to thank all the colleagues of team 1GACT, who contributed a lot of technical knowledge, as well as pleasant moments shared inside and outside the company. I want to thank especially Christophe, Thomas and Benoit for sharing their experience on different topics, both in the aerodynamics area as well as in the use of different programs. To Benjamin for helping me with Tecplot so many times. To Lauren for her help with using the HPC and several other applications. To Valeria and María for sharing with me their previous experiences

with the unsteady analysis of different physical phenomena. To Diego and Atef for their pleasant conversations and fun moments during breaks. To Nicholas for helping me with different topics during the last part of the thesis. I would also like to acknowledge William Thollet for his help in solving different problems with mesh generation and simulations with elsA, Simon Trapier for helping me convert CGNS meshes to base damas and allow me to complete my work, and Luis López de Vega for helping me solve different problems in Python.

I would specially acknowledge my family, because they have always supported and contributed to achieve my professional goals. First, to my parents, Hector Solorzano Fonseca, and Leticia Flores, who with a lot of effort and love guided my dreams, helped and financially supported my personal and professional projects. 10 years have been passed since I left my country, and in a decision full of love and courage, they let me fly. I also express gratitude to my brothers, Elmer, Leticia, and Sinthia, whom I admire a lot and have served to me as an example of overcoming. To each one of them I keep a very special love. I thank my girlfriend, Brenda Valencia, with whom we have shared triumphs and good moments in the last years and provided me with all the support and love to be able to cope with difficult moments. I thank my aunts, Vilma, Marta, Mary, Velinda, Iris, Rosy, and Lineth, who have helped me in different moments to achieve my professional dreams. I also thank my godfather, Gerardo and uncle René for their time and help in different procedures. I thank all my family. Also, I acknowledge my friends in Honduras, Argentina, and France, which have become a second family and have provided me with all their support to achieve my goals.

Lastly, I want to express my gratitude to France, the country that has welcomed me and made me feel at home. It has provided me with opportunities to learn, grow, and succeed.

El final de esta etapa me permite hacer un recorrido a lo largo de los últimos años, recordando todo lo que ha pasado desde el momento que decidí que camino profesional toma. Aprovecho la oportunidad para mostrar mi gratitud hacia todos aquellos que en algún momento me ayudaron a llegar al punto en el que me encuentro hoy día.

Me gustaría primeramente agradecer a mi familia, ya que siempre me han apoyado y aportado para cumplir mis metas profesionales. Primeramente, a mis padres, Hector Solorzano Fonseca y Leticia Flores, quienes con mucho esfuerzo y amor guiaron mis sueños, me ayudaron y sostuvieron económicamente mis proyectos personales y profesionales. Hace 10 años deje mi país y en una decisión llena de amor y valentía ellos me dejaron volar. También agradezco a mis hermanos, Elmer, Leticia y Sinthia, a los cuales admiro mucho y me han servido como ejemplo de superación. A cada uno de ellos les guardo un amor muy especial. Agradezco a mi novia, Brenda Valencia, con la cual hemos compartido triunfos y buenos momentos en los últimos años y además me ha brindado todo el apoyo y amor para poder sobrellevar momentos difíciles. Agradezco a mis tías, Vilma, Marta, Mary, Velinda, Iris, Rosy y Lineth, las cuales me han ayudado en diferentes momentos para poder cumplir mis sueños profesionales. También agradezco a mi padrino Gerardo y tío René por su tiempo y ayuda en diferentes tramites. Agradezco a toda mi familia y estoy orgulloso de formar parte de esta. También aprovecho para agradecer a mis amigos en Honduras, Argentina y Francia, los cuales se han convertido en una segunda familia y me han brindado todo su apoyo para cumplir mis metas.

También quiero agradecer a Airbus, el cual me ha dado la oportunidad de cumplir un sueño, de aprender mucho y ser parte de un grupo extraordinario de personas que han aportado mucho en mi vida. Me gustaría agradecer especialmente a Ludovic Gerard, quien confió en mi para realizar esta tarea, el cual me acompañó y brindo todo su apoyo a lo largo de toda la tesis. Estaré siempre agradecido por la oportunidad que me brindo. También me gustaría agradecer a Cyril Bonnaud, quien me guio a lo largo de esta tesis, quien aparte de ser un excelente profesional y compartirme su sabiduría, también supo forjar una buena amistad y brindarme los mejores consejos personales. También agradezco a Alain Dega, quien también me ayudo a integrarme en el equipo y me guio durante mi primer año de tesis. También quiero agradecer a todos los colegas del equipo IGACT, los cuales aportaron mucho conocimiento técnico, además de agradables momentos compartidos dentro y fuera de la empresa. Quiero agradecer especialmente a Cristophe, Thomas y Benoit por compartir su experiencia en distintos temas, tanto en el área de aerodinámica como en la utilización de distintos programas. A Benjamin por las tantas veces que me ayudo con Tecplot. A Lauren por su ayuda con la utilización del HPC y varias otras aplicaciones. A Valeria y María por compartir conmigo sus experiencias previas con análisis no estacionarios de diferentes fenómenos físicos. A Diego y Atef por sus conversaciones amenas y momentos divertidos durante las pausas. A Nicholas con su ayuda en distintos temas durante la última parte de la tesis. También me gustaría agradecer a colegas de otros equipos. A William Thollet por su ayuda para resolver diferentes problemas con la generación de malla y simula-

ciones con elsA. A Simon Trapier por ayudarme a convertir mallas de CGNS a base damas y permitirme completar mis trabajos. A Luis López de Vega por ayudarme a resolver distintos problemas en Python.

También me gustaría agradecer al Onera por guiarme en el aspecto científico en el desarrollo de la tesis. Me gustaría agradecer especialmente a mi tutor Olivier Atinault, por su paciencia, quien me ha sabido guiar de la mejor manera, me ha ayudado enormemente a lo largo de este camino y me ha brindado los mejores consejos. También quiero agradecer a mi director de tesis Julien Dandois a quien le tengo un gran respeto y admiración por sus destrezas científicas. Quiero agradecer también a Michaël Méheut por su apoyo en diferentes aspectos administrativos durante mi estancia en el Onera. También agradezco a todos los colegas de la unidad ACI, especialmente a Camille y Vincent por su apoyo y buenos momentos. Agradezco a Nicolas Rembaut por su ayuda en el análisis de datos experimentales. También agradezco al comité de suivi, Eric Garier y Denis Sipp.

Me gustaría también agradecer a los miembros del jurado de la defensa de tesis por el tiempo y el interés que le han brindado a mi trabajo.

Finalmente me gustaría agradecer a Francia, país que me acoge y me hace sentir como en casa, que me ha dado la oportunidad de aprender, crecer y triunfar.

Table of Contents

- Abstract** VI
- Acknowledgements** IX
- List of Figures** XIV
- List of Tables** XXIV
- Nomenclature** XXVI
- 1 Introduction** 1
 - 1.1 Context and Motivations 1
 - 1.2 Research questions and goals 3
 - 1.3 Current challenges 3
- 2 State-of-the-art** 5
 - 2.1 Boundary Layer Ingestion concept 5
 - 2.2 Benefits of the Boundary Layer Ingestion 7
 - 2.3 Embedded engines vs. podded engines 8
 - 2.4 Boundary layer ingestion constraints 9
 - 2.5 BLI intake characteristics 10
 - 2.5.1 Boundary Layer 10
 - 2.5.2 S-ducts 11
 - 2.6 Physical phenomena linked with main adverse effects 12
 - 2.6.1 Secondary flow 13
 - 2.6.2 Horseshoe vortices 14
 - 2.6.3 Ground vortices 15
 - 2.6.4 Interaction with various aircraft components 16
 - 2.7 Measurement of engine intake distortion 16
 - 2.7.1 Pressure-based distortion criteria 17
 - 2.7.2 Velocity-based distortion criteria 18

2.8	Aerodynamic analysis and predictive challenges of BLI engine intake	21
3	Experimental Analysis of a semi-buried BLI intake	23
3.1	Wind tunnel facility	23
3.1.1	Model	23
3.2	Test conditions	29
3.3	Analysis and procedures for experimental signals	29
3.3.1	Statistics in the amplitude domain	29
3.3.2	Statistics in frequency domain.	31
3.4	Experimental boundary layer	31
3.5	Intake ramp analysis	33
3.5.1	Mean values analysis	33
3.5.2	Unsteady values analysis	35
3.6	Top-nacelle analysis	47
3.7	Side-nacelle analysis	47
3.8	Rake analysis	51
3.8.1	Mean values analysis	51
3.8.2	Unsteady analysis	54
3.9	Chapter summary and conclusions	62
4	Analysis of Reynolds-averaged numerical simulations	64
4.1	Reynolds-Averaged Navier-Stokes turbulence models	65
4.1.1	Eddy Viscosity Models	65
4.1.2	Reynolds Stress Model	70
4.2	Numerical simulations	72
4.2.1	Geometry and mesh generation	72
4.2.2	Simulation conditions and numerical setup	73
4.2.3	Mesh convergence study	74
4.2.4	Boundary layer thickness analysis	75
4.2.5	Simulation results analysis	77
4.3	Effects of flow parameters	86
4.3.1	Boundary layer thickness	86
4.3.2	Mach number	88
4.4	Chapter summary and conclusions	89
5	Analysis of the ZDES simulations	91
5.1	Scale-resolving simulations	92
5.1.1	Direct Numerical Simulation (DNS)	93
5.1.2	Large Eddy Simulation (LES)	94
5.1.3	Hybrid RANS/LES models	94

5.2	Zonal Detached Eddy Simulations	95
5.3	BLI intake simulation using ZDES mode 2	99
5.3.1	Spectral analysis discussion	119
5.4	Chapter summary and conclusions	125
6	Comparison of numerical results with experimental data	127
6.1	Intake Ramp analysis	128
6.2	Top-nacelle analysis	137
6.3	Side-nacelle analysis	142
6.3.1	Flow condition parameters effects over Cp distribution	148
6.4	Rake Analysis	149
6.4.1	Comparison of total pressures at the AIP	149
6.5	Unsteady analysis over the AIP	165
6.5.1	Intake ramp comparison	165
6.5.2	Rake comparison	169
6.6	Proper orthogonal decomposition at the AIP	174
6.7	Chapter summary and conclusions	180
7	Distortion characterisation for a BLI intake	182
7.1	Industrial distortion indices	183
7.1.1	Pressure based distortion criteria	183
7.1.2	Velocity based distortion criteria	189
7.2	Effects of flow conditions on distortion indices.	194
7.2.1	Boundary layer thickness effect	195
7.2.2	Mach number effect	196
7.3	Unsteady distortion analysis	198
7.3.1	Pressure-based distortion criteria	198
7.3.2	Velocity-Based distortion criteria	201
7.4	Chapter summary and conclusions	202
8	Work synthesis, conclusions and future work	204
8.1	Physical phenomena investigations	204
8.2	Numerical prediction capabilities	205
8.3	Distortion description	207
8.4	Recommendations for future work	208
A	Study of the effect of the boundary layer thickness and freestream Mach number	219
A.1	Boundary layer thickness effect	219
A.2	Mach number effect	221
B	Distortion indices propositions for a boundary layer intake	223

B.1 Velocity and Pressure Distortion Index (VPDI)	223
B.2 β-IDC	224

List of Figures

1.1 Comparison of A300 and A350	1
2.1 Onera NOVA BLI concept (credit: ONERA).	5
2.2 Boundary Layer Ingestion (BLI) principle	6
2.3 BLI intake (credit:ONERA).	10
2.4 S-duct on a commercial aircraft.	11
2.5 Secondary flow	13
2.6 Secondary flow	14
2.7 Horseshoe vortices	14
2.8 Ground vortex	15
2.9 Typical one-per-rev symmetric paired swirl pattern for single immersion.	19
2.10 Swirl Directivity (SD) for counter-clockwise compressor rotation.	20
2.11 Swirl Pairs(SP) for counter-clockwise compressor rotation.	20
3.1 S3Ch scheme (ONERA)	23
3.2 Geometry model	24
3.3 Model placed in S3Ch wind tunnel.	25
3.4 Pressure taps (in red, green and blue) and unsteady pressure sensors (in black)	
on the model.	25
3.5 Pressure taps (in red, green and blue) and unsteady pressure sensors (in black)	
on the model.	26
3.6 Rake at the AIP	28
3.7 Rake at the AIP	28
3.8 Experimental boundary layer measurement	31
3.9 Experimental boundary layer profile in wall units	32
3.10 Experimental repeatability at MFR $4.0 \text{ kg}\cdot\text{s}^{-1}$.	33
3.11 Experimental C_p distribution at intake ramp each $0.1 \text{ kg}\cdot\text{s}^{-1}$ from 3 to $4 \text{ kg}\cdot\text{s}^{-1}$	34
3.12 Comparison between the experimental data and an isentropic approach.	35
3.13 (a) k101 sensor statistics	36
3.14 (b) k102 sensor statistics	36
3.15 Kulite sensors at intake ramp statistics.	36

3.15 (c) k103 sensor statistics	37
3.16 (d) k104 sensor statistics	37
3.17 (e) k105 sensor statistics	38
3.18 (f) k106 sensor statistics	38
3.19 (g) k107 sensor statistics	39
3.20 (h) k108 sensor statistics	39
3.21 (i) k109 sensor statistics	40
3.23 Turbulent energy cascade	41
3.24 Inverse turbulent energy cascade	41
3.25 Kulite locations	42
3.26 (a) k101	43
3.27 PSD of Kulite sensors on the intake ramp.	43
3.27 (b) k102	44
3.28 (c) k103	44
3.29 (d) k104	45
3.30 (e) k105	45
3.31 (f) k106	46
3.32 (g) k107	46
3.34 Cp distribution over the top-nacelle	47
3.35 Cp distribution over the right-side of the nacelle.	48
3.36 Cp distribution over the left-side of the nacelle	48
3.37 Sideslip comparison. $\beta = 0.25^\circ$	49
3.38 Sideslip comparison. $\beta = 0.5^\circ$	50
3.39 Sideslip comparison. $\beta = 1^\circ$	50
3.40 Total pressure loss at fan face for various mass flow rate values	52
3.41 Distribution of the total pressure at the lower half of the fan face was investi- gated for different values of the mass flow rate.	53
3.42 (a) Rake Sensor. Arm 3, point 1	54
3.43 Statistical analysis of rake sensors as function of mass flow rate.	54
3.43 (b) Rake Sensor. Arm 3, point 2	55
3.44 (c) Rake Sensor. Arm 3, point 3	55
3.45 (d) Rake Sensor. Arm 3, point 4	56
3.46 (e) Rake Sensor. Arm 3, point 5	56
3.48 (a) Rake Sensor. Arm 7, point 5	57
3.49 Statistical analysis of rake sensors as function of mass flow rate.	57
3.49 (b) Rake Sensor. Arm 7, point 4	58
3.50 (c) Rake Sensor. Arm 7, point 3	58
3.51 (d) Rake Sensor. Arm 7, point 2	59
3.52 (e) Rake Sensor. Arm 7, point 1	59

3.54	Power Spectral Density of arm 3 calculated for various mas flow rate values.	60
3.55	Power Spectral Density of arm 7 calculated for various mas flow rate values.	61
4.1	Computational domain	73
4.2	Different meshes analyzed (left: coarse, mid: normal, right: fine).	74
4.3	Relative error of distortion indices compared to grid size.	75
4.4	Boundary conditions on the flat plate for the different boundary layer thicknesses. Up: $\delta = 21.3$ mm. Center: $\delta = 16.1$ mm. Down: $\delta = 14.3$ mm.	76
4.5	Comparison between numerical and experimental boundary layer profiles in log coordinates.	77
4.6	Comparison between numerical and experimental boundary layer profiles.	77
4.7	Flow separation and vortices for MFR = $3.0 \text{ kg}\cdot\text{s}^{-1}$.	78
4.8	Skin friction coefficient on the intake ramp, $y = 0$ mm.	80
4.9	Skin friction coefficient on the intake ramp, $y = 30$ mm.	81
4.10	Vorticity field at fan face for each turbulence model. Left: $3.0 \text{ kg}\cdot\text{s}^{-1}$, center: $3.4 \text{ kg}\cdot\text{s}^{-1}$, right: $4.0 \text{ kg}\cdot\text{s}^{-1}$	84
4.11	Evolution of the maximum vorticity value with the MFR value at the AIP for each turbulence model along MFR	85
4.12	Evolution of the mean vorticity value with the MFR value at the AIP for each turbulence model along MFR	85
4.13	Skin friction coefficient on the intake ramp for different boundary layer thicknesses, $y = 0$ mm.	86
4.14	Vorticity field at fan face for each boundary layer thickness. Left: $3.0 \text{ kg}\cdot\text{s}^{-1}$, center: $3.4 \text{ kg}\cdot\text{s}^{-1}$, right: $4.0 \text{ kg}\cdot\text{s}^{-1}$	87
4.15	Skin friction coefficient on the intake ramp for different boundary layer thicknesses, $y = 0$ mm at $3.4 \text{ kg}\cdot\text{s}^{-1}$.	88
4.16	Effect of Mach number on vorticity field at fan face for each Mach condition at $3.4 \text{ kg}\cdot\text{s}^{-1}$.	89
5.1	Total pressure loss along the BLI intake. Top: Spalart-Allmaras model. Bottom: ZDES mode 2 model.	91
5.2	Hierarchy of different levels of turbulence modeling.	92
5.3	Energy distribution and scales in turbulence modeling.	93
5.4	Illustration of the zonal solving with ZDES by the visualisation of flow velocity at the intake.	95
5.5	Classification of typical flow problems and associated ZDES modes ((credit:ONERA)).	96

5.6	The axial velocity was obtained using the Spalart-Allmaras model (SA) for a mass flow rate of $3.0 \text{ kg}\cdot\text{s}^{-1}$. The dark blue region indicates the recirculation zones. The left image shows the axial velocity distribution in the Aerodynamic Interface Plane (AIP), while the right image shows the axial velocity distribution in the symmetry plane.	100
5.7	The region to refine in preparation for the Zonal Detached Eddy Simulation (ZDES) method is shown in red. The left image shows the region to refine in the Aerodynamic Interface Plane (AIP), while the right image shows the region to refine in the symmetry plane.	100
5.8	The flow over a curved intake ramp is characterized by the presence of unsteady physical phenomena that result from the separation of the boundary layer from the surface of the ramp. These unsteady phenomena include vortex shedding, flow separation, and reattachment.	101
5.9	The Zonal Detached Eddy Simulation (ZDES) method employs a refined mesh with elements of maximum size 0.5 mm in each direction within a specific region. Left: AIP plane. Right: symmetry plane.	102
5.10	Instantaneous flow behavior predicted by the ZDES model. Left: $3.0 \text{ kg}\cdot\text{s}^{-1}$. Right : $3.4 \text{ kg}\cdot\text{s}^{-1}$. Up: Axial velocity in different planes. Center: Total pressure in different planes. Down: Axial velocity in the symmetry plane.	103
5.11	Turbulent structures visualized using an isovalue of Q Criterion for a mass flow rate of $3.0 \text{ kg}\cdot\text{s}^{-1}$. The color scale represents the vorticity magnitude.	104
5.12	Turbulent structures cut by the symmetry plane showing the turbulence behaviour near the wall. The turbulence structures are visualized using an isovalue of Q Criterion for a mass flow rate of $3.0 \text{ kg}\cdot\text{s}^{-1}$	105
5.13	Power Spectral Densities (PSD) calculated for the probes placed over the intake ramp. The dotted line represents the $-5/3$ characteristic turbulent slope. Up: $3.0 \text{ kg}\cdot\text{s}^{-1}$. Down: $3.4 \text{ kg}\cdot\text{s}^{-1}$	106
5.14	Cross Spectral density value between pressure and velocities signals from probe k101 at $3.0 \text{ kg}\cdot\text{s}^{-1}$. The right axis shows the CSD, represented by solid lines. The left axis shows the coherency, represented by dotted lines.	107
5.15	Power Spectral Densities for the sensors located on the vertical arms of the rake placed at the AIP. Left: lower arm 7 affected by the flow recirculation. Right: upper arm 3 located outside the recirculation zone.	108
5.16	Cross Spectral density value between pressure and velocities for probes placed on arm 7. Left: $3.0 \text{ kg}\cdot\text{s}^{-1}$. Right: $3.4 \text{ kg}\cdot\text{s}^{-1}$. The right axis shows the CSD, represented by solid lines. The left axis shows the coherency, represented by dotted lines.	110

5.17	Cross Spectral density value between pressure and velocities for probes placed on arm 3. Left: $3.0 \text{ kg}\cdot\text{s}^{-1}$. Right: $3.4 \text{ kg}\cdot\text{s}^{-1}$. The right axis shows the CSD, represented by solid lines. The left axis shows the coherency, represented by dotted lines.	111
5.18	Power Spectral Densities for probes located on the diagonal arms of the rake placed at the AIP. Left: lower-diagonal arm affected by the flow recirculation. Right: upper-diagonal arm located outside the recirculation zone.	112
5.19	Cross Spectral density value between pressure and velocities for probes placed on arm 6. Left: $3.0 \text{ kg}\cdot\text{s}^{-1}$. Right: $3.4 \text{ kg}\cdot\text{s}^{-1}$. The right axis shows the CSD, represented by solid lines. The left axis shows the coherency, represented by dotted lines.	114
5.20	Cross Spectral density value between pressure and velocities for probes placed on arm 2. Left: $3.0 \text{ kg}\cdot\text{s}^{-1}$. Right: $3.4 \text{ kg}\cdot\text{s}^{-1}$. The right axis shows the CSD, represented by solid lines. The left axis shows the coherency, represented by dotted lines.	115
5.21	Power Spectral Densities for the probes on the horizontal arms of the rake placed at the AIP. Left: left side arm. Right: right side arm.	116
5.22	Cross Spectral density value between pressure and velocities for probes placed on arm 5. Left: $3.0 \text{ kg}\cdot\text{s}^{-1}$. Right: $3.4 \text{ kg}\cdot\text{s}^{-1}$. The right axis shows the CSD, represented by solid lines. The left axis shows the coherency, represented by dotted lines.	117
5.23	Cross Spectral density value between pressure and velocities for probes placed on arm 1. Left: $3.0 \text{ kg}\cdot\text{s}^{-1}$. Right: $3.4 \text{ kg}\cdot\text{s}^{-1}$. The right axis shows the CSD, represented by solid lines. The left axis shows the coherency, represented by dotted lines.	118
5.24	Instantaneous flow field predicted by the ZDES model. The images show the lateral velocity with a sampling frequency of 450 Hz. Left: $3.0 \text{ kg}\cdot\text{s}^{-1}$. Right : $3.4 \text{ kg}\cdot\text{s}^{-1}$.	120
5.25	Instantaneous flow field predicted by the ZDES model at the symmetry plane . The images show the axial velocity with a sampling frequency of 2500 Hz. Left: $3.0 \text{ kg}\cdot\text{s}^{-1}$. Right : $3.4 \text{ kg}\cdot\text{s}^{-1}$.	121
5.26	Instantaneous flow field predicted by the ZDES model at the symmetry plane. The images show the vertical velocity with a sampling frequency of 2500 Hz. Left: $3.0 \text{ kg}\cdot\text{s}^{-1}$. Right : $3.4 \text{ kg}\cdot\text{s}^{-1}$.	122
5.27	PSD and Strouhal number for probes located on the AIP. Left: $3.0 \text{ kg}\cdot\text{s}^{-1}$. Right: $3.4 \text{ kg}\cdot\text{s}^{-1}$.	123
5.28	PSD and Strouhal number for probes located on the entrance ramp. Left: $3.0 \text{ kg}\cdot\text{s}^{-1}$. Right: $3.4 \text{ kg}\cdot\text{s}^{-1}$.	124

6.1	Comparison of wall pressure coefficient (C_p) along the intake ramp for various mass flow rate (MFR) values between experimental and numerical data obtained from the Standard Spalart-Allmaras model (SA).	128
6.2	Comparison of wall pressure coefficient (C_p) along the intake ramp for various mass flow rate (MFR) values between experimental and numerical data obtained from Spalart-Allmaras model with quadratic constitutive relation (SA-QCR2000).	129
6.3	Comparison of wall pressure coefficient (C_p) along the intake ramp for various mass flow rate (MFR) values between experimental and numerical data obtained from Spalart-Allmaras model with rotation and curvature correction (SA-RC).	129
6.4	Comparison of wall pressure coefficient (C_p) along the intake ramp for various mass flow rate (MFR) values between experimental and numerical data obtained from $k-\omega$ SST model.	130
6.5	Comparison of wall pressure coefficient (C_p) along the intake ramp for various mass flow rate (MFR) values between experimental and numerical data obtained from Speziale-Sarkar-Gatski/Launder-Reece-Rodi differential Reynolds-stress model (RSM).	130
6.6	Comparison of wall pressure coefficient (C_p) along the intake ramp for various turbulence models at a mass flow rate (MFR) of $4.0 \text{ kg}\cdot\text{s}^{-1}$. In this case there is no flow separation.	131
6.7	Comparison of wall pressure coefficient (C_p) along the intake ramp for various turbulence models at a mass flow rate (MFR) of $3.7 \text{ kg}\cdot\text{s}^{-1}$. In this case there is no flow separation.	132
6.8	Comparison of wall pressure coefficient (C_p) along the intake ramp for various turbulence models at a mass flow rate (MFR) of $3.6 \text{ kg}\cdot\text{s}^{-1}$. In this case there is no flow separation.	132
6.9	Comparison of wall pressure coefficient (C_p) along the intake ramp for various turbulence models at a mass flow rate (MFR) of $3.5 \text{ kg}\cdot\text{s}^{-1}$. In this case there is a slight flow separation.	133
6.10	Comparison of wall pressure coefficient (C_p) along the intake ramp for various turbulence models at a mass flow rate (MFR) of $3.4 \text{ kg}\cdot\text{s}^{-1}$. In this case there is a flow separation.	133
6.11	Comparison of wall pressure coefficient (C_p) along the intake ramp for various turbulence models at a mass flow rate (MFR) of $3.2 \text{ kg}\cdot\text{s}^{-1}$. In this case there is a flow separation.	134
6.12	Comparison of wall pressure coefficient (C_p) along the intake ramp for various turbulence models at a mass flow rate (MFR) of $3.0 \text{ kg}\cdot\text{s}^{-1}$. In this case there is a flow separation.	134

6.13 Comparison of boundary layer profile for ZDES and SA simulations at 3.0 kg·s ⁻¹	135
6.14 Comparison of wall pressure coefficient (Cp) along the intake ramp for ZDES and SA simulations at 3.0 kg·s ⁻¹	136
6.15 Comparison of wall pressure coefficients (Cp) along top upper side nacelle for various turbulence models at 4.0 kg·s ⁻¹	138
6.16 Comparison of wall pressure coefficients (Cp) along top upper side nacelle for various turbulence models at 3.7 kg·s ⁻¹	138
6.17 Comparison of wall pressure coefficients (Cp) along top upper side nacelle for various turbulence models at 3.6 kg·s ⁻¹	139
6.18 Comparison of wall pressure coefficients (Cp) along top upper side nacelle for various turbulence models at 3.5 kg·s ⁻¹	139
6.19 Comparison of wall pressure coefficients (Cp) along top upper side nacelle for various turbulence models at 3.4 kg·s ⁻¹	140
6.20 Comparison of wall pressure coefficients (Cp) along top upper side nacelle for various turbulence models at 3.2 kg·s ⁻¹	140
6.21 Comparison of wall pressure coefficients (Cp) along top upper side nacelle for various turbulence models at 3.0 kg·s ⁻¹	141
6.22 Wall pressure coefficient over the upper nacelle surface for different numerical turbulence models at 4.0 kg·s ⁻¹	141
6.23 Wall pressure coefficient over the upper nacelle surface for different numerical turbulence models at 3.0 kg·s ⁻¹	142
6.24 Comparison of wall pressure coefficients (Cp) over side-nacelle surfaces between experimental and numerical data obtained from Standard Spalart-Allmaras (SA) model. Up: right-side. Down: left-side.	143
6.25 Comparison of wall pressure coefficients (Cp) over side-nacelle surfaces between experimental and numerical data obtained from Spalart-Allmaras model with rotation and curvature correction (SA-RC). Up: right-side. Down: left-side.	144
6.26 Comparison of wall pressure coefficients (Cp) over side-nacelle surfaces between experimental and numerical data obtained from Spalart-Allmaras model with quadratic constitutive relation (SA-QCR2000). Up: right-side. Down: left-side.	145
6.27 Comparison of wall pressure coefficients (Cp) over side-nacelle surfaces between experimental and numerical data obtained from k- ω SST model. Up: right-side. Down: left-side.	146
6.28 Comparison of wall pressure coefficients (Cp) over side-nacelle surfaces between experimental and numerical data obtained from Speziale-Sarkar-Gatski/Lauder-Reece-Rodi differential Reynolds-stress model (RSM). Up: right-side. Down: left-side.	147

6.29 Comparison of wall pressure coefficients (C_p) over the intake ramp for different boundary layer thicknesses and Mach numbers. Left: Effect of the Boundary layer thickness. Right: Effect of the Mach number.	148
6.30 Comparison of pressure loss at the AIP between different turbulence models and experimental data for $3.0 \text{ kg}\cdot\text{s}^{-1}$.Up: Numerical simulations. Down: Experimental data.	150
6.31 Comparison of pressure loss at the AIP between different RANS models and experimental data for $3.2 \text{ kg}\cdot\text{s}^{-1}$.Up: Numerical simulations. Down: Experimental data.	151
6.32 Comparison of pressure loss at the AIP between different turbulence models and experimental data for $3.4 \text{ kg}\cdot\text{s}^{-1}$.Up: Numerical simulations. Down: Experimental data.	152
6.33 Comparison of pressure loss at the AIP between different RANS models and experimental data for $3.5 \text{ kg}\cdot\text{s}^{-1}$.Up: Numerical simulations. Down: Experimental data.	153
6.34 Comparison of pressure loss at the AIP between different RANS models and experimental data for $3.6 \text{ kg}\cdot\text{s}^{-1}$.Up: Numerical simulations. Down: Experimental data.	154
6.35 Comparison of pressure loss at the AIP between different RANS models and experimental data for $3.7 \text{ kg}\cdot\text{s}^{-1}$.Up: Numerical simulations. Down: Experimental data.	155
6.36 Comparison of pressure loss at the AIP between different RANS models and experimental data for $4.0 \text{ kg}\cdot\text{s}^{-1}$.Up: Numerical simulations. Down: Experimental data.	156
6.37 Comparison of the distribution of total pressure at the lower half of the fan face for various turbulence models at $3.0 \text{ kg}\cdot\text{s}^{-1}$	158
6.38 Comparison of the distribution of total pressure at the lower half of the fan face for various turbulence models at $3.2 \text{ kg}\cdot\text{s}^{-1}$	159
6.39 Comparison of the distribution of total pressure at the lower half of the fan face for various turbulence models at $3.4 \text{ kg}\cdot\text{s}^{-1}$	160
6.40 Comparison of the distribution of total pressure at the lower half of the fan face for various turbulence models at $3.5 \text{ kg}\cdot\text{s}^{-1}$	161
6.41 Comparison of the distribution of total pressure at the lower half of the fan face for various turbulence models at $3.6 \text{ kg}\cdot\text{s}^{-1}$	162
6.42 Comparison of the distribution of total pressure at the lower half of the fan face for various turbulence models at $3.7 \text{ kg}\cdot\text{s}^{-1}$	163
6.43 Comparison of the distribution of total pressure at the lower half of the fan face for various turbulence models at $4.0 \text{ kg}\cdot\text{s}^{-1}$	164

6.44	Power Spectral Density (PSD) comparison between experimental and numerical data, over the intake ramp probes, at $3.0 \text{ kg}\cdot\text{s}^{-1}$.	166
6.45	Power Spectral Density (PSD) comparison between experimental and numerical data, over the intake ramp probes, at $3.4 \text{ kg}\cdot\text{s}^{-1}$.	167
6.46	Comparison of experimental Power Spectral Density (PSD) results at different corrected mass flow rates.	168
6.47	Power Spectral Density (PSD) comparison between experimental and numerical data, over the rake 7 at the AIP for $3.0 \text{ kg}\cdot\text{s}^{-1}$ case.	170
6.48	Power Spectral Density (PSD) comparison between experimental and numerical data, over the rake 3 at the AIP for $3.0 \text{ kg}\cdot\text{s}^{-1}$ case.	171
6.49	Power Spectral Density (PSD) comparison between experimental and numerical data, over the rake 7 at the AIP for $3.4 \text{ kg}\cdot\text{s}^{-1}$ case.	172
6.50	Power Spectral Density (PSD) comparison between experimental and numerical data, over the rake 3 at the AIP for $3.4 \text{ kg}\cdot\text{s}^{-1}$ case.	173
6.51	Distribution of the modal shape and PSD at the AIP for the ZDES simulation at $\text{MFR} = 3.0 \text{ kg}\cdot\text{s}^{-1}$.	175
6.52	Distribution of the modal shape and PSD at the AIP for the experimental data at $\text{MFR} = 3.0 \text{ kg}\cdot\text{s}^{-1}$.	176
6.53	Distribution of the modal shape and PSD at the AIP for ZDES simulation at $\text{MFR} = 3.4 \text{ kg}\cdot\text{s}^{-1}$.	177
6.54	Distribution of the modal shape and PSD at the AIP for experimental results at $\text{MFR} = 3.4 \text{ kg}\cdot\text{s}^{-1}$.	178
7.1	Comparison of numerical and experimental averaged total pressure loss for various corrected mass flow rate values.	184
7.2	Comparison of numerical and experimental circumferential distortion index for various corrected mass flow rate values.	185
7.3	Comparison of numerical and experimental DC(60) index for various corrected mass flow rate values.	186
7.4	Comparison of numerical and experimental IDC index for various corrected mass flow rate values.	187
7.5	Comparison of numerical and experimental IDC index for various corrected mass flow rate values.	188
7.6	Swirl angle profile in function of azimuthal position according to different turbulence models for mass flow of $3.0 \text{ kg}\cdot\text{s}^{-1}$.	190
7.7	Swirl angle profile in function of azimuthal position according to different turbulence models for mass flow of $3.4 \text{ kg}\cdot\text{s}^{-1}$.	191
7.8	Swirl angle profile in function of azimuthal position according to different turbulence models for mass flow of $4.0 \text{ kg}\cdot\text{s}^{-1}$.	192

7.9 Comparison of numerical and experimental maximum swirl intensity for various corrected mass flow rate values.	193
7.10 Comparison of numerical and experimental maximum swirl intensity for various corrected mass flow rate values.	193
7.11 Effect of the boundary layer thickness on various distortion indices.	195
7.12 Effect of Mach number on various distortion indices.	197
7.13 PSD of the spatially averaged total pressure at the AIP for the ZDES and the experiments. Left: $3.0 \text{ kg}\cdot\text{s}^{-1}$. Right: $3.4 \text{ kg}\cdot\text{s}^{-1}$	198
7.14 PSD of the circumferential distortion $((\Delta PC/P)_{ave})$ for the ZDES and the experiments. Left: $3.0 \text{ kg}\cdot\text{s}^{-1}$. Right: $3.4 \text{ kg}\cdot\text{s}^{-1}$	199
7.15 PSD of radial distortion for the ZDES and the experiments. Left: $3.0 \text{ kg}\cdot\text{s}^{-1}$. Right: $3.4 \text{ kg}\cdot\text{s}^{-1}$	200
7.16 PSD of IDC value for the ZDES and the experiments. Left: $3.0 \text{ kg}\cdot\text{s}^{-1}$. Right: $3.4 \text{ kg}\cdot\text{s}^{-1}$	200
7.17 PSD of the DC(60) for the ZDES and the experiments. Left: $3.0 \text{ kg}\cdot\text{s}^{-1}$. Right: $3.4 \text{ kg}\cdot\text{s}^{-1}$	201
7.18 PSD of the mean swirl intensity value for the ZDES simulation. Left: $3.0 \text{ kg}\cdot\text{s}^{-1}$. Right: $3.4 \text{ kg}\cdot\text{s}^{-1}$	201
7.19 PSD of the maximum swirl intensity value for the ZDES simulation. Left: $3.0 \text{ kg}\cdot\text{s}^{-1}$. Right: $3.4 \text{ kg}\cdot\text{s}^{-1}$	202
A.1 Boundary layer thickness effects at AIP for $3.0 \text{ kg}\cdot\text{s}^{-1}$. Up: Total pressure field. Down: Axial velocity and streamlines.	220
A.2 Boundary layer thickness effects at AIP for $3.4 \text{ kg}\cdot\text{s}^{-1}$. Up: Total pressure field. Down: Axial velocity and streamlines.	220
A.3 Boundary layer thickness effects at AIP for $4.0 \text{ kg}\cdot\text{s}^{-1}$. Up: Total pressure field. Down: Axial velocity and streamlines.	221
A.4 Effect of the freestream Mach number. Left: recirculation region over the intake ramp shown in blue. Center: Momentum in the axial direction over the symmetry plane. Right: Momentum in the axial direction over the AIP.	222
B.1 Velocity and Pressure Distortion Index for different turbulence models at various mass flow rates.	224
B.2 Left: β -IDC Index for different turbulence models at various mass flow rates. Right: Velocity triangle	225

List of Tables

2.1 Advantages and drawbacks of podded engine configuration	9
2.2 Advantages and drawbacks of BLI engine configuration	9
3.1 Geometry parameters of the BLI intake	24
3.2 Kulites locations on the intake ramp.	27
3.3 Pressure tap locations on nacelle top.	27
3.4 Pressure tap locations on nacelle left side.	27
3.5 Pressure tap locations on nacelle right side.	27
3.6 Pressure tap locations on the intake ramp.	27
4.1 Spalart-Allmaras model coefficients	67
4.2 Model coefficients for Spalart-Allmaras with rotation and curvature correction model	68
4.3 Model coefficients for k- ω SST two-equations model	69
4.4 Bounding Values of ω -Equation Coefficients	72
4.5 Bounding Values of the SSG/LRR- ω Model Term Coefficients	72
4.6 Flow and boundary conditions	74
4.7 Turbulence models studied.	79
4.8 MFR values studied.	79
4.9 Location of the separation point on the intake ramp according to the skin friction coefficient, $y = 0$ mm.	82
4.10 Location of the reattachment point on the intake ramp according to the skin friction coefficient, $y = 0$ mm.	82
4.11 Location of the separation point on the intake ramp according to the skin friction coefficient, $y = 30$ mm.	83
4.12 Location of the reattachment point on the intake ramp according to the skin friction coefficient, $y = 30$ mm.	83
5.1 Zonal-Detached Eddy Simulation (ZDES) mode 2 numerical parameters	98
6.1 Location of the separation point for different MFR values and turbulence mod- els (the origin is located at the AIP)	136

7.1	Comparison of the distortion indices between numerical simulations and experimental data for $MFR = 4.0 \text{ kg}\cdot\text{s}^{-1}$.	188
7.2	Comparison of the distortion indices between numerical simulations and experimental data for $MFR = 3.4 \text{ kg}\cdot\text{s}^{-1}$.	189
7.3	Comparison of the distortion indices between numerical simulations and experimental data for $MFR = 3.0 \text{ kg}\cdot\text{s}^{-1}$.	189

Nomenclature

Roman symbols

A	Cross-sectional area
C_f	Friction coefficient
C_p	Pressure coefficient
D_A	Aircraft drag
$DC(\theta)$	Circumferential Distortion for a θ sector
F	Thrust given by the engine to the external flow
k	Turbulence kinetic energy
Ku_x	Statistical Kurtosis
M	Mach number
\dot{m}	Mass flow rate
P_i/P_{i0}	Total pressure loss ratio
P_{0i}	Average pressure of each i^{th} ring
$P_{0i,low}$	Average of the lower total pressure region
$P_{non-BLI}$	Propulsive power for a non-BLI aircraft configuration

P_{BLI}	Propulsive power for a BLI aircraft configuration
P_{∞}	Static pressure on the freestream
p_f	Mean total pressure at the AIP
$p_{f,low}$	Mean total pressure in the lowest stagnation pressure sector of the AIP
$\overline{P_{i,r}}$	Average total pressure on the r^{th} radius
$P_{i,r}^{min}$	Minimum stagnation pressure on the r^{th} radius
q_f	Dynamic pressure at the AIP
R	Ideal gas constant
Re	Reynolds number
Sk_x	Statistical skewness
St	Strouhal number
T_t	Stagnation temperature
u_e	Engine exhaust velocity
u_0	External flow velocity
U_{θ}	Tangential velocity
U_x	Axial velocity

Greek symbols

α	Swirl angle
β	Sideslip angle
γ	Heat capacity ratio
δ	Boundary-Layer thickness
δ_w	Shear layer momentum thickness
$(\Delta PC/P)_{ave}$	Circumferential distortion
$(\Delta PR/P)_{max}$	Radial distortion
η_{prop}	Propulsive efficiency of a single stream turbojet
θ	Azimuth angle
μ_t	Turbulent viscosity
ν_t	Dynamic turbulent viscosity
ρ	Density
$\tau_{i,j}$	Turbulent stress tensor
τ_w	Local wall shear stress

Abbreviations

AIP	Aerodynamics Interface Plane
BLI	Boundary Layer Ingestion
BPR	Bypass Ratio
CFD	Computational Fluid Dynamics
CSD	Cross Spectral Density
DNS	Direct Numerical Simulation
FPR	Fan Pressure Ratio
IDC	Circumferential Distortion Index
$k-\omega$ SST	Menter's Two-equation Eddy-viscosity model
LES	Large Eddy Simulation
MFR	Mass Flow Rate
PIV	Particle Image Velocimetry
POD	Proper orthogonal decomposition
PSC	Power Saving Coefficient
PSD	Power Spectral Density
RANS	Reynolds-Averaged Navier-Stokes
RMS	Root Mean Square
RSM	Reynolds Stress Model

SA	Spalart-Allmaras
SA-QCR2000	Spalart-Allmaras with Quadratic Constitutive Relation
SD	Swirl Directivity
SI	Swirl Intensity
SP	Swirl Pairs
SS	Swirl Sector
SSG/LRR- ω	Speziale-Sarkar-Gatski/Launder-Reece-Rodi Full Reynolds Stress Model
UHBR	Ultra High Bypass Ratio
URANS	Unsteady Reynolds-Averaged Navier-Stokes
ZDES	Zonal Detached Eddy Simulation

Chapter 1

Introduction

1.1 Context and Motivations

The commercial aircraft industry is widely recognized for its significant efforts to reduce aircraft fuel burn and pollutant emissions. Research in this regard is of particular importance to respect environmental constraints and to continue producing competitive airplanes. The industry has adopted several pathways to reduce emissions such as improvements in aircraft technology, operations, and infrastructure.



Figure 1.1: Comparison of A300 and A350

From an industrial perspective, it could be argued that no major improvements have been made in the design of civil aircraft since the first civil aircraft that used turbofan engines were created more than six decades ago. The aircraft configurations (two wings, one fuselage, engine podded under the wings) remain unchanged. However, this does not imply that no efforts have been made to improve commercial airplanes but rather that this configuration represents a local

optimum for the entire aircraft system. Between 1960 and 2010, the average fuel efficiency of commercial aircraft has approximately doubled [10]. This improvement can be attributed to several factors such as improved aerodynamics at transonic Mach numbers, better materials, and engines. Although further progress can be made in terms of external aerodynamics or systems and structure, significant improvements can be achieved by focusing on the engine and its integration with the aircraft. The propulsive efficiency has an important effect over the overall aircraft efficiency. The propulsive efficiency of a single stream turbojet is shown in equation [11]:

$$\eta_{prop} = \frac{2}{1 + \frac{u_e}{u_0}} \quad (1.1)$$

where u_e is the engine exhaust velocity and u_0 is the external flow velocity. The propulsive efficiency is maximum when the exhaust velocity is as close as possible to the external flow velocity. Moreover, the thrust given by the engine to the external flow is described as:

$$F = \dot{m}(u_e - u_0) \quad (1.2)$$

For a given thrust requirement, it is more efficient to give a small acceleration $u_e - u_0$ to a large amount of fluid \dot{m} . In practice, the exhaust velocity decreases with the Fan Pressure Ratio (FPR), and higher Mass Flow Rates (MFR) can be obtained with larger fan diameters. This explains why civil aircraft engines are designed with higher bypass ratios (BPR) to increase mass flow rates and improve efficiency, hence the Ultra High Bypass Ratio (UHBR) denomination for the near future turbofan engines [11]. However, this improvement in propulsive efficiency will not be as evident in the overall efficiency of the aircraft due to the increase in weight and drag caused by a larger surface area of the nacelle, and the aerodynamic interaction between the nacelle and the wing.

Alongside these advancements, efforts are being made to reduce some of the effects that would come with using UHBR turbofans. One possibility is to consider a shorter and thinner inlet nacelle. However, this approach leads to increased aerodynamic interactions between the air intake and the fan, which is no longer shielded from external flow. To ensure proper operation of both fan and air intake throughout the aircraft's entire flight envelope, these interactions must be mastered early in the design process of both components.

In the long term, new propulsion paradigms must be considered to further reduce fuel burn. One such paradigm is the Boundary Layer Ingestion (BLI) concept, which involves embedding the engines and airframe together so that the engines ingest a portion of the airframe boundary layer, reducing wake drag penalties. In this configuration, the aircraft and engines are fully coupled, as fans operate under distorted inflow and pressure distributions on the airframe are

affected by fans. Designing such an aircraft requires characterization of these interactions and affordable, robust numerical capabilities that capture each component's effect on others.

1.2 Research questions and goals

The first objective of this research is to **improve the knowledge on the physical phenomena involved in a BLI intake**. The synergy between different components of an aircraft plays a fundamental role in understanding and realizing possible advantages offered by a Boundary Layer Ingestion (BLI) configuration. Although this technology is already being used in other industries, such as naval applications, its application in the civil aviation industry brings with it several complexities that need to be understood and resolved before implementation. One of the difficulties and basic topics for this research is the comprehension of aerodynamic interaction in the fan intake. This work aims to evaluate different physical phenomena, such as loss of total pressure, flow recirculation zones, vortices, etc., which are highly dependent on the geometry of the inlet of the nacelle as well as flight conditions.

The second objective of this research is to **evaluate the CFD prediction capability**. The capacity offered by current computational fluid dynamics turbulence models commonly used in industry may generate uncertainty when studying aircraft configurations such as boundary layer ingestion (BLI). These turbulence models have been designed to solve non-complex situations that are very different from the possible scenarios that BLI entry could present. This work aims to compare these turbulence models with experimental results in order to evaluate their ability to predict such complex flows.

The third objective of this research is to **evaluate and propose distortion criteria for a BLI intake**. The physical phenomena inherent to boundary layer ingestion have a negative impact on the quality of flow ingested by the engine. During the design stage, the industry determines the engine's ability to tolerate some flow distortion. Taking into account flow behavior, this research will analyze and evaluate the ability of current distortion indices to describe flow quality in a boundary layer ingestion configuration.

1.3 Current challenges

The concept of boundary layer ingestion has been known for decades and has great potential in improving the overall efficiency of aircraft. However, until today it is not used in the civil aeronautical industry. The lack of implementation of this technology has several reasons, among them the limitation in different available technologies or even ignorance of the details of the physical phenomena.

From the design point of view, the first steps to be carried out are the understanding of the

physical phenomena, as well as its possible impact on engine performance throughout the flight profile. During the last decades several BLI configurations have been studied for commercial aircraft. In general, the main physical phenomena that govern the flow behavior are similar; however, there are certain physical differences that can make varying impact on overall engine performance.

The ability to study these physical phenomena is one of the challenges of the current industry. During the design stages, aerodynamic analyses are carried out through engineering analysis based on theoretical, numerical and experimental models. Numerical models, commonly known as CFD, have gained ground in recent decades due to their versatility in studying and identifying potential improvements, becoming a crucial tool in the various stages of aircraft conception. In general, the CFD models used in the industry meet the general needs of the current aeronautical industry; however, there are certain cases where their predictive capacity may be questioned due to the complexities of physical phenomena. The study of BLI inputs requires greater predictive capacity in second-order aerodynamic phenomena, in which current RANS models tend not to predict adequately. Different variants within this family of models have been proposed with the intention of improving this predictive capacity. Within the industry, other families of CFD models (LES or DNS) are also beginning to be used with the aim of improving this predictive capacity for complex physical phenomena.

The implementation of a boundary layer ingestion intake has a significant impact on the quality of flow ingested by the engine. The flow heterogeneity, known as distortion, can lead to aerodynamic instabilities of the fan blades. If the distortion is large enough, it can cause the fan to stall or the engine to surge. During the design phase, an index that measures distortion is necessary to define fan tolerance to perturbations in ingested flow. Several indices are used in industry to characterize distortion at engine intake. Most of these indices were designed to analyze distortion in standard engine configurations and are based on stagnation pressure losses. Several authors have analyzed distortion and performance prediction for a BLI engine using these typical distortion indices or using pressure-based distortion criteria. However, these distortion indices may not be suitable for use in a BLI engine configuration, especially given that physical phenomena of a BLI engine differ from those of an engine in standard configuration.

Chapter 2

State-of-the-art

2.1 Boundary Layer Ingestion concept

One of the primary goals in modern aircraft design centers around improving energy efficiency. This objective is closely tied to a commitment to minimize the environmental impact of aviation while also optimizing operating costs. To achieve the targeted goals in energy efficiency, new propulsion integration concepts must be developed. Boundary-Layer Ingestion (BLI) aircraft concepts, such as Aurora D8 [12] [3], NASA STARC-ABL [13] or ONERA NOVA-BLI [14] appear to be promising solutions. These concepts are based on increasing the interaction between the fuselage and the propulsion systems in such a way that the latter ingests the viscous boundary layer or fuselage wake.



Figure 2.1: Onera NOVA BLI concept (credit: ONERA).

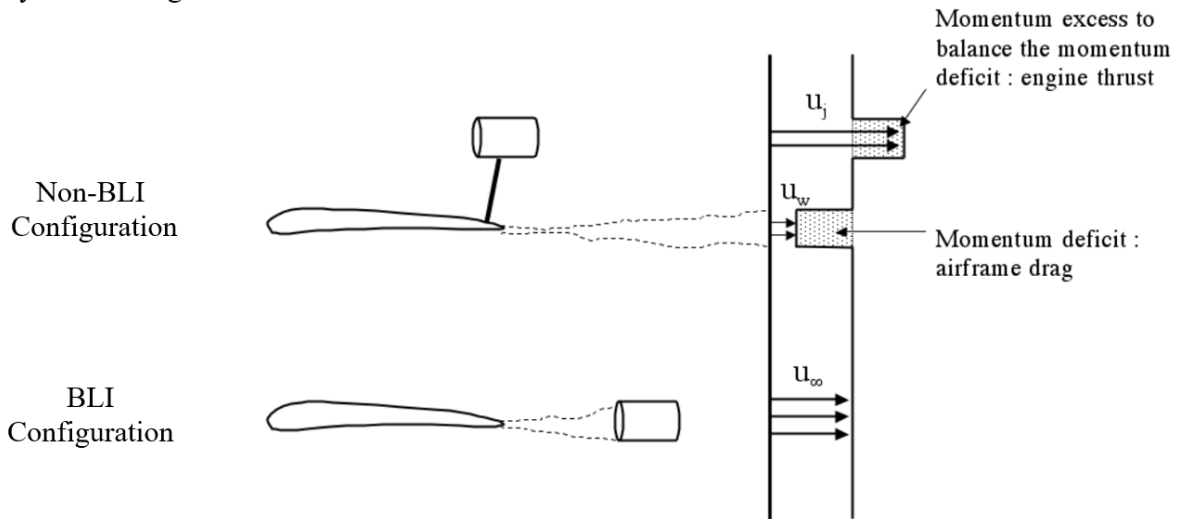


Figure 2.2: Boundary Layer Ingestion (BLI) principle

In a classic aircraft configuration with no BLI, as shown in Figure 2.2, the airframe produces a deficit of streamwise momentum (the wake) generating drag D_A . On the other hand, to compensate this drag, the engines produce an excess of momentum (the jet). In the thrust Equation 2.1, this excess of velocity is represented by $u_j - u_\infty$, the freestream velocity is u_∞ , and the mass flow rate is \dot{m} .

$$F = \dot{m}(u_j - u_\infty) = D_A \quad (2.1)$$

The propulsive power required for the aircraft flight at equilibrium is therefore:

$$P = D_A u_\infty = \dot{m}(u_j - u_\infty) u_\infty \quad (2.2)$$

Furthermore, the rate of addition of propulsive power given to the flow by using a classical engine configuration (non-BLI) is defined by Equation 2.3. This propulsive power is proportional to the difference in kinetic energy per unit mass between engine exit and upstream conditions.

$$P_{non-BLI} = \frac{\dot{m}}{2}(u_j^2 - u_\infty^2) = \frac{D_A}{2}(u_j + u_\infty) \quad (2.3)$$

Emphasizing that $u_j > u_\infty$ for a non-BLI aircraft configuration, the propulsive power required by the airplane is less than the power added by the engine to the flow. Now, by supposing that all the boundary layer is ingested and the engine increases the wake velocity, defined as u_w , to the freestream velocity, the force given by the engine to the flow is:

$$F_{engine} = \dot{m}(u_{\infty} - u_w) = D_A \quad (2.4)$$

The power required to produce this force by ingesting the boundary layer is:

$$P_{BLI} = \frac{\dot{m}}{2}(u_{\infty}^2 - u_w^2) = \frac{D_A}{2}(u_{\infty} + u_w) \quad (2.5)$$

By comparing the Equation 2.3 and Equation 2.5, and taking into account that $u_j > u_w$, it is clear that the power given to the flow by the non-BLI configuration is larger than the one used by the BLI configuration $P_{non-BLI} > P_{BLI}$. The difference of power transferred to the flow between both configurations occurs because, for a given thrust net force, less power needs to be added to a flow that enters to the engine with a lower velocity

It is possible to use the classical decomposition (drag and thrust) of the forces acting on the airframe and the engine only for the non-BLI configuration. A power balance [15] or exergy [2] analysis would, however, point out which portion of the kinetic energy from the wake could be recovered. The commonly used parameter to quantify those gains is the power-saving coefficient (PSC) which can be expressed as:

$$PSC = \frac{P_{non-BLI} - P_{BLI}}{P_{non-BLI}} \quad (2.6)$$

with $P_{non-BLI}$ being the fan power, calculated for the non-BLI configuration, and P_{BLI} being the fan power of the BLI configuration, calculated for the same streamwise net force.

In an ideal scenario, the engine is placed downstream of the airframe and reenergizes its wake by just the right amount to compensate the streamwise momentum deficit without any velocity excess (jet). According to this, the energy saving increases with the percentage of viscous boundary layer ingested and it has been shown that the ideal BLI engine position is precisely behind, near and centered to the fuselage, as shown in Figure 2. Experimental results show that a PSC value up to 0.23 can be obtained with a thrust equal to drag on academic cases [2].

2.2 Benefits of the Boundary Layer Ingestion

As shown in previous demonstration, the Boundary Layer Ingestion (BLI) is a promising aircraft technology that has the potential to significantly reduce fuel burn by ingesting the airframe boundary layer with aft-fuselage engine. The wake ingestion, which is a precursor of BLI, was identified as early as the 19th century by Froude [16] and has been applied to marine propulsion, e.g., torpedoes. In 1996 Betz [17] noted that the incoming low momentum wake can be ingested by the propulsor, and consequently, the propulsive power required can be reduced. Smith [1]

concluded in 1993 that as the aircraft wake is more dispersed due to the wing, it is less beneficial to apply wake ingestion to an aircraft design; instead, a BLI concept seems to be more promising for future aircraft.

The integration between the airframe and propulsors necessitates a significant alteration in the airframe design or modifications to the conventional tube-and-wing fuselage. Depending on the configurations and assumptions, literature reports a variation between 3% and 19% of fuel burn reduction due to the BLI application [18] [19] [20] [21] [22]. However, some authors [23] have reported an increase in fuel consumption using BLI technology due to the increase in weight from the BLI propulsor and turboelectric system outweighing the aerodynamic benefit. Similar results have been highlighted for the optimized STARC-ABL [24]. The variation in results highlights the uncertainty and risks associated with BLI arising from technological challenges. Furthermore, the ingested boundary layer represents an inlet distortion onto the BLI fan within the propulsor, resulting in reductions in fan efficiency and pressure rise. The performance penalty is sensitive to the inlet distortion, which has an important effect on the overall BLI benefit.

2.3 Embedded engines vs. podded engines

Boundary Layer Ingestion (BLI) cannot be achieved with podded engines that are out of the fuselage boundary layer. It requires embedded engines that are partly buried in the airframe, usually in the aft part of the fuselage to ingest a substantial part of the boundary layer created on the fuselage. This configuration offers a reduction in wetted surface and structural weight due to the disappearance of pylons. However, embedding the engines introduces several possible drawbacks. First, airframe and engine designs become much more coupled. Second, ingesting boundary layer results in a non-uniform flow at the inlet and fan face, which may result in operability issues and decreased engine performance. This non-uniformity is exacerbated by the curvature of the duct, which produces pressure gradients that result in secondary flows and may lead to boundary layer separation. Flow separation becomes a real possibility from the moment the inlet has to diffuse an already developed boundary layer. The flow distortion at the fan face may produce additional vibration and noise and also cause structural and operational difficulties with the engine as well as deteriorate performance [25]. On the one hand, traditional podded engines are a proven technology, whereas embedded engines are a new configuration that involves risk. Tables 2.1 and 2.2 shows a synthesis of advantages and disadvantages expressed in the bibliography cited above.

Podded engines	
Advantages	Drawbacks
Proven technology. Captures uniform flow.	Larger structural weight. Pylon-airframe interference. Larger wetted area.

Table 2.1: Advantages and drawbacks of podded engine configuration

BLI engines	
Advantages	Drawbacks
Fuel burn benefits. Less wetted area on nacelle. Weight savings.	Unproven technology. Non uniform flow. Distortion issues. Operability issues.

Table 2.2: Advantages and drawbacks of BLI engine configuration

2.4 Boundary layer ingestion constraints

In the preceding section, several studies have been cited that were conducted on the boundary layer ingestion (BLI), particularly on the development of aircraft using this technology and its potential improvement. However, these studies do not account for certain limitations associated with the use of this technology.

The limitations mentioned play significant roles throughout the design, certification and production process of an aircraft. At the design level, the integration of the engine into the fuselage leads to several complications. From a structural perspective, the fuselage structure would be more coupled to the engine, altering the stresses, vibrations and acoustics of the aircraft. If the engines are located at the rear, possible modifications must be taken into account to avoid a possible tailstrike or damage during takeoff or landing. In terms of certification, aircraft equipped with Boundary Layer Ingestion (BLI) technology have several areas that require improvement. Firstly, the acoustic emissions towards both the interior and exterior of the aircraft must be reduced. Secondly, the aircraft must demonstrate its ability to withstand an engine failure without affecting the fuselage or empennage and potentially critical aircraft systems. Finally, when sizing the aircraft, various parameters such as the free distance from the engine to the ground and adaptability to current infrastructure should be taken into account [26].

From an aerodynamic perspective, the use of a Boundary Layer Ingesting (BLI) engine involves the intake of non-uniform flow, which results in the creation of distortion to the engine input. This distortion has a direct impact on the engine's performance, including compressor stall, and generates additional fatigue in several components.

2.5 BLI intake characteristics

The physical phenomena that occur in a boundary layer intake are dependent on the geometry and configuration of the aircraft. In this study, we focus on an engine located at the rear of the aircraft. The engine is semi-buried on the fuselage as depicted in Figure 2.3. The following subsections present the most significant parameters that need to be considered to explain the physical phenomena in this type of intake.

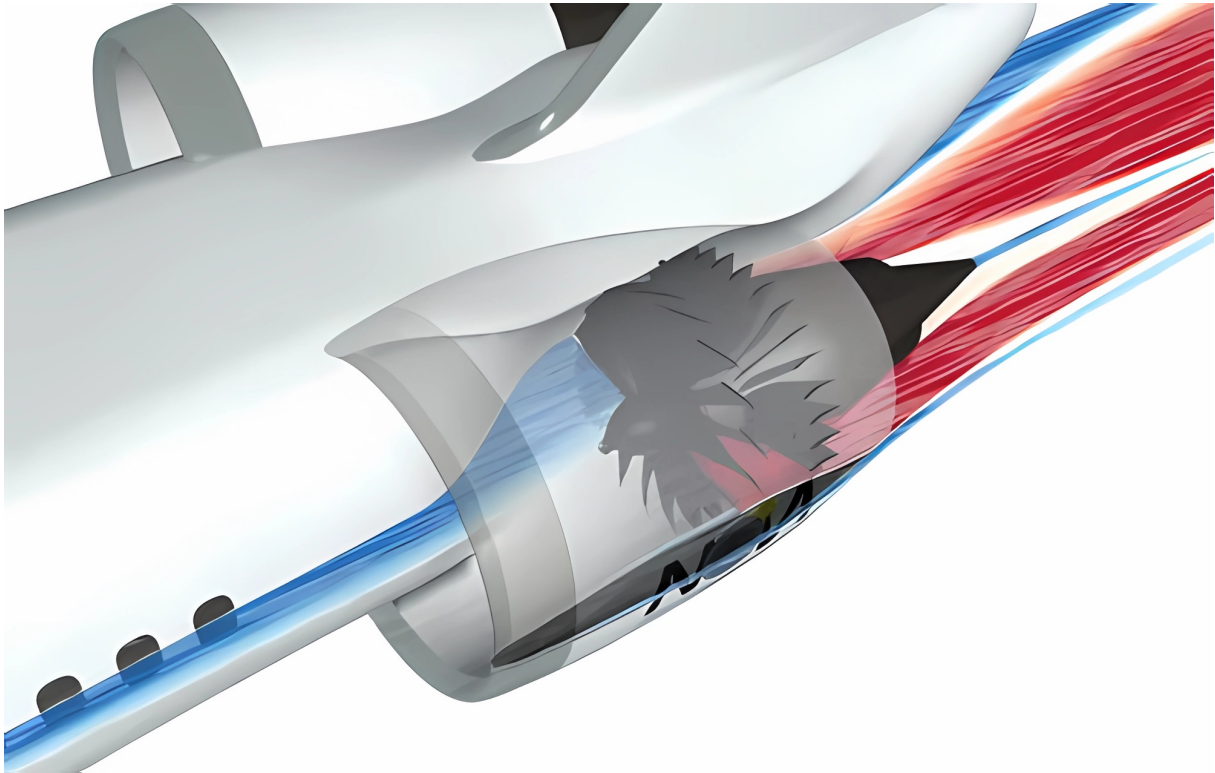


Figure 2.3: BLI intake (credit:ONERA).

2.5.1 Boundary Layer

The boundary layer is defined as the region where the velocity of the fluid relative to the moving solid varies from zero to 99% of the velocity of the undisturbed flow stream. In the context of rear fuselage BLI engines, there exists a strong interaction between the flow around the fuselage of the aircraft and the flow that the engine ingests. An important aspect of this interaction is the boundary layer that develops on the fuselage. The behavior of the boundary layer is usually characterized by different parameters, like its thickness δ and its displacement and momentum thicknesses.

2.5.2 S-ducts

Boundary layer intake engines are typically integrated into the fuselage and have an intake ramp, as depicted in Figure 2.3. The BLI intake ramps share certain similarities, both geometrically and in flow behavior with S-ducts. This type of curved duct is commonly used for military aircraft and its implementation has the potential to reduce drag, size, and weight by eliminating the boundary layer diverter and shortening the intake duct. Additionally, it can reduce ram drag by decreasing the momentum of an inlet flow and lower observability which is particularly interesting for military applications. Figure 2.4 shows a scheme of the implementation of a s-duct in a commercial aircraft.

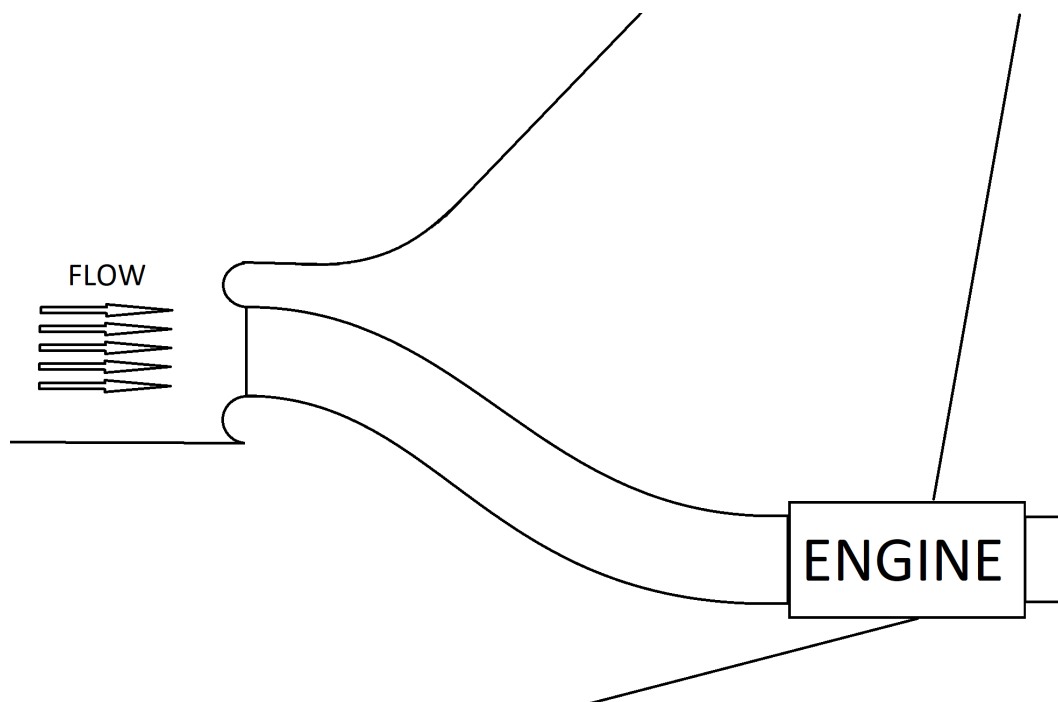


Figure 2.4: S-duct on a commercial aircraft.

However, problems with this kind of intakes become more complicated when combined with the effect of high ingestion of boundary layer and when the intake is located in the rear portion of the aircraft. This leads to more complex problems generating adverse effects in the ingestion of boundary layer as the complexity of the aerodynamic phenomena or the non-homogeneous distribution of pressure at the engine intake [27].

The use of certain geometries in aircraft engines can lead to the generation of unwanted side effects such as pressure distortion and a reduction in pressure recovery. These effects can significantly impact the operability of the engine and may even negate any potential benefits that could be gained from using such configurations. The primary physical phenomena that generate these unwanted effects are horseshoe vortices or secondary flow, which are inherent in this type of geometry [28][29].

Several design parameters have been investigated in various boundary-layer ingestion (BLI) studies using S-ducts [30]. Additionally, the effects of high Mach and Reynolds numbers have been analyzed [31]. Some of the conclusions that have been drawn from these simulations and experiments are:

- The ingestion of a large amount of boundary layer at the inlet of an S-duct results in a significant decrease in pressure recovery at the end of the S-duct. This decrease is in addition to losses associated with duct friction, separation at the lip inlet, and the effect of the curvature of the duct.
- Increasing the freestream Mach number generally has a detrimental effect on inlet performance in boundary layer ingestion, which increases distortion and decreases pressure recovery. These losses are linked to duct curvature and boundary layer ingestion effects.
- Increasing the mass flow rate increases inlet pressure recovery at high Mach numbers; however, it also increases inlet distortion. The increase in pressure recovery is linked to a reduction in the relative amount of boundary layer ingestion as the inlet mass flow rate is increased.
- Increasing the Reynolds number has a negligible effect on inlet distortion, and a slight effect on pressure recovery.

For this project, the S-duct is utilized with a less pronounced curvature, which could significantly reduce the effects described. Furthermore, when ingesting a larger portion of the boundary layer, less power is required to match the total drag generated by the aircraft. Therefore, the penalty in total thrust due to the use of S-duct is not as detrimental as initially expected.

2.6 Physical phenomena linked with main adverse effects

The previous sections have presented generalities of the BLI intake, as well as design characteristics and adverse effects. This section aims to highlight and improve the knowledge on the physical phenomena associated with the BLI intake.

The design guidelines for S-duct diffusers without a significant amount of boundary layer ingestion (BLI) seem to be well understood in the literature. However, when using this type of inlet, it is important to take into account their effects on flow behavior and understand the phenomena linked to them, especially their coupling with the BLI principle. An inherent effect of BLI ingestion is the reduction of Total Pressure Recovery and the high distortion generated, in which the inlet duct might play an essential role.

Some of the main physical phenomena that affect boundary layer ingestion and generate complexity in its simulation and predictability are vortices. Green [32] provides definitions of vor-

tices that affect boundary layer ingestion, some of which are shown and explained below.

2.6.1 Secondary flow

The creation of secondary flow can be explained qualitatively by considering the convection of vortex filaments in this layer as they pass through the bend. The velocity on the inside of the bend is higher than on the outside, and besides, the distance through the bend is smaller on the inside. Because of this boundary layer vortex filaments which are initially normal to the flow at the bend inlet, are tipped into the streamwise direction as they convect through the bend.

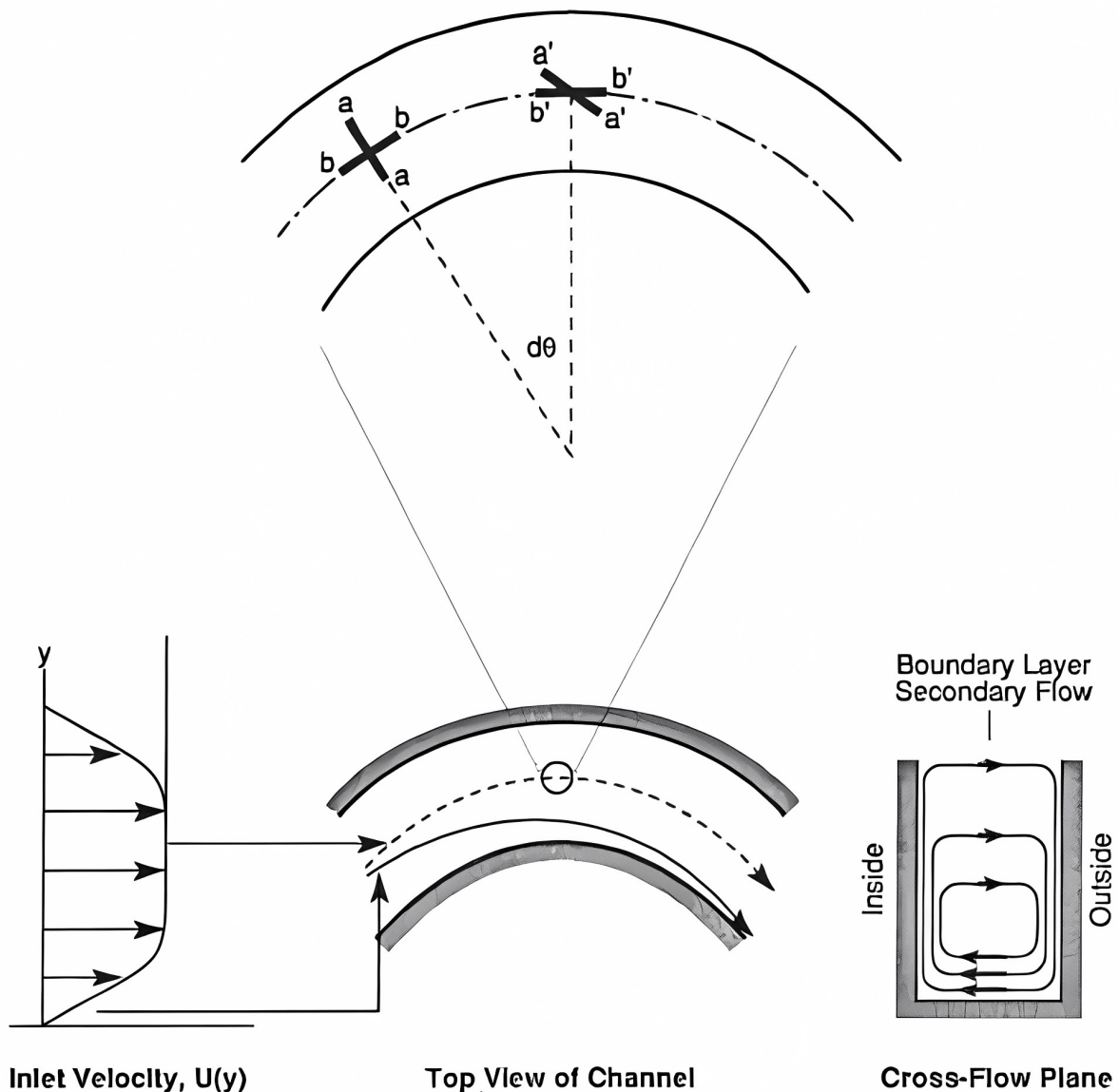


Figure 2.5: Secondary flow

A scheme of this type is shown in figure [2.6](#). Due to the curvature of the inlet, a pressure gradient is set up by the primary flow, of one sign over the first part of the duct (1 to 3), and then of the other sign over the latter part (3 to 5). It implies that in the first part of the duct there is

a generation of streamwise vorticity pointing in the upstream direction, and hence a secondary flow in the boundary layer towards the 180° location. Streamwise vorticity of an opposite sense is generated in the latter part of the duct.

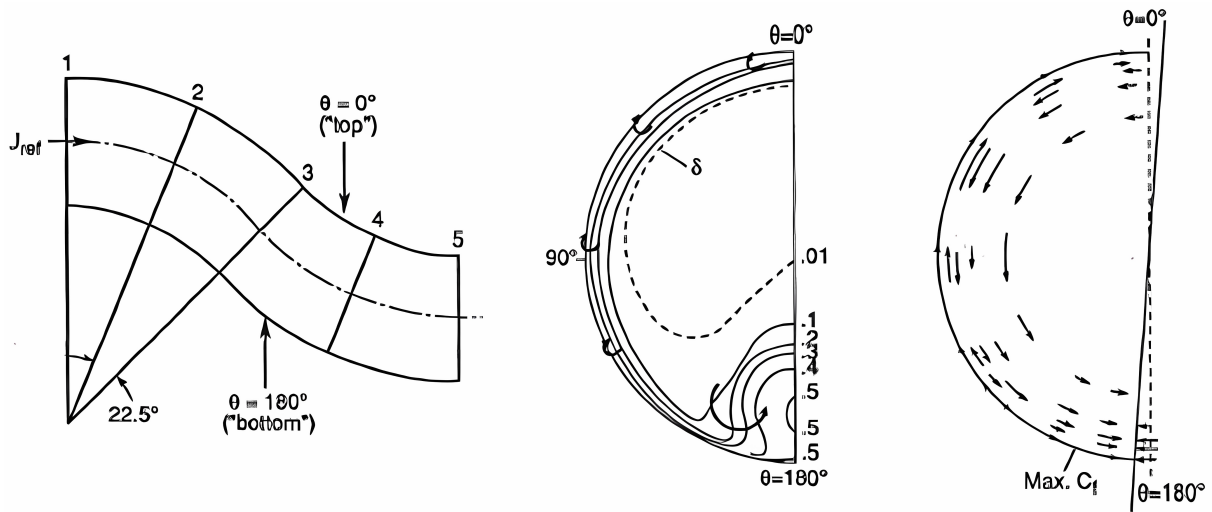


Figure 2.6: Secondary flow

2.6.2 Horseshoe vortices

The creation of concentrated vortices with high swirling velocities by vorticity amplification due to vortex stretching is another feature of flows in propulsion systems, in addition to the development of streamwise vorticity. A common example of this phenomenon is the flow of a boundary layer around a strut or other obstacles that protrude through it.

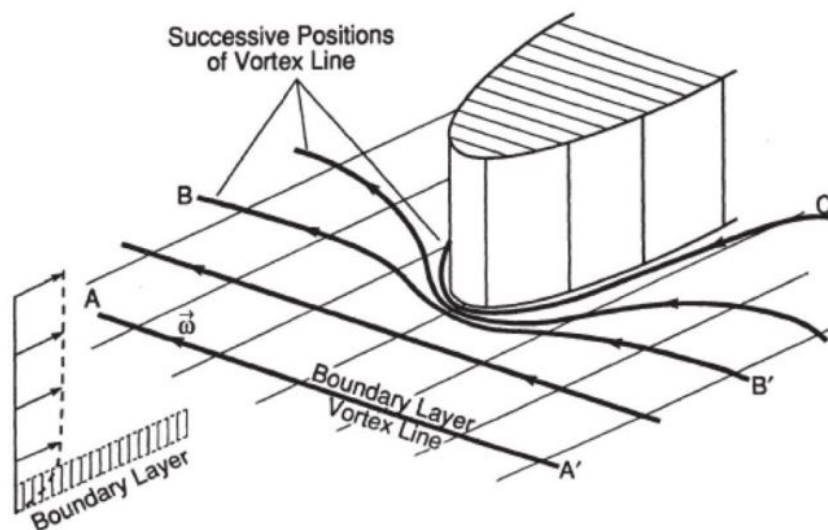


Figure 2.7: Horseshoe vortices

In Figure [2.7](#), the vortex lines far upstream in the boundary layer (lines AA') are straight and

normal to the velocity vectors. As the lines are convected towards the obstacle, fluid particles on the plane of symmetry are decelerated, whereas those away from this plane accelerate. As a result, the vortex lines bend around the obstacle (line BB'). Particles on the plane of symmetry remain at the front of the obstacle, while particles off this plane convect downstream. Material lines (and hence vortex lines) are thus stretched, increasing vorticity. The greatest stretching occurs on the plane of symmetry, where vorticity and swirl velocity associated with it will be largest. The maximum magnitude of vorticity is determined by a balance between intensification of vorticity due to stretching and viscous diffusion of vorticity. Both stretching and reorientation of vortex lines are important in overall dynamics of flow field

2.6.3 Ground vortices

The formation of inlet vortices is a well-known phenomenon in the aeronautical industry. It occurs when an aircraft engine is operating near a ground plane and under nearly static conditions. Figure 2.8 provides an example of this phenomenon. While studying conventional aircraft, the effects of inlet vortex formation are usually neglected. However, it is important to note that this phenomenon could also occur due to the interaction between the engine inlet and fuselage.

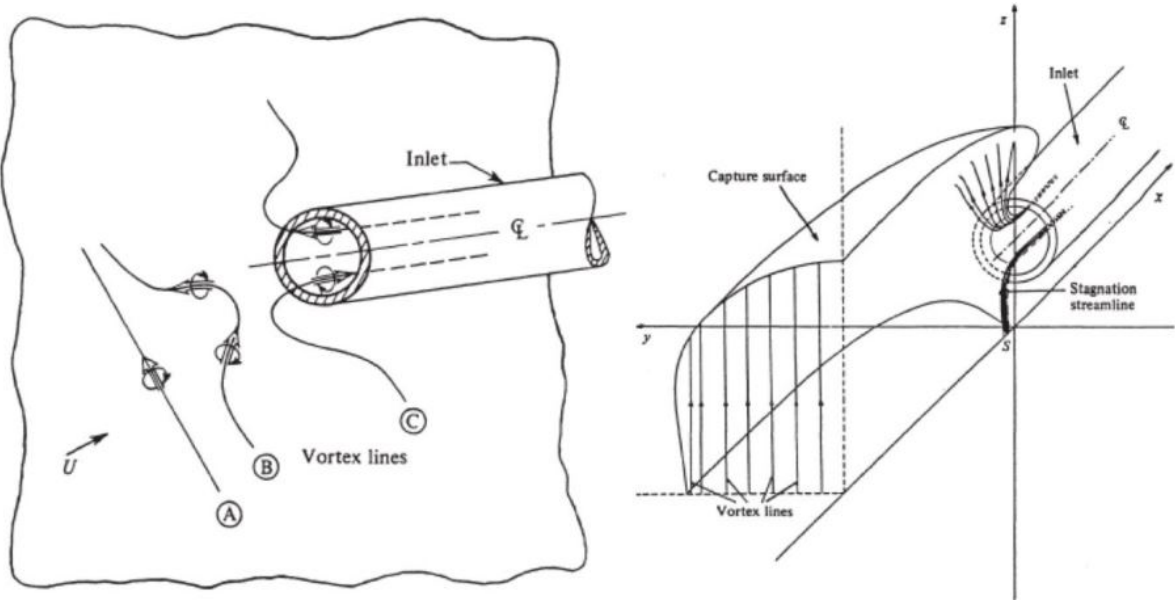


Figure 2.8: Ground vortex

Figure 2.8 (left) shows that the presence of essentially unidirectional and parallel flow will create two legs entering the inlet. Since the vortex line cannot end in a fluid, these two legs must possess an equal and opposite circulation. However, when there are vertical vortex lines, the situation is quite different. As the vortex lines are convected towards the inlet face by the primary flow, they evolve into a configuration in which the upper legs of the vortex lines are fanned out over the upper part of the inlet, while the lower legs are concentrated around the

stagnation streamline associated with the stagnation point on the ground plane. The structure of these vortices is shown in Figure 2.8 (right)

2.6.4 Interaction with various aircraft components

The interaction between the fuselage and the BLI engine can generate phenomena that affect the flow entering the engine. The wake generated by various components of the aircraft, such as the wing, can also affect the flow. This wake creates a stagnation pressure loss and increases the distortion in the engine intake. This effect can be particularly important in certain BLI engine configurations, such as when the engines are found directly in the wake of the wing or when a BLI engine is placed directly behind the fuselage and its sensitivity to changes of curvatures on it. This interaction could also occur in a low-wing aircraft flying at high angle of attack or in out-of-design conditions. In addition, vortices generated at the intersection between the wing and fuselage, wing tip or other devices that generate an aerodynamic force should also be considered. Most BLI input studies have been done modeling the fuselage as a flat plate or fuselage-like profile [33][34][35][36]. The reference [29] shows the sensitivity of boundary layer ingestion to various design parameters in different aircraft component designs.

2.7 Measurement of engine intake distortion

Distortion at the engine fan face is a significant contributor to engine efficiency loss. The efficiency of a turbofan engine is highly dependent on clean and uniform airflow conditions. Of primary interest are blockages and distortions of the flow, which are defined as any type of non-uniformity introduced to a free-stream flow parameter.

The most common distortion effect encountered in a turbofan engine is the drop in total pressure. This can be caused by many external factors that reduce performance in various ways. The most common causes of pressure distortion are blockage, flow separation or boundary layer ingestion that mimic a rigid blockage. When there is an obstruction in the flow, the mass flow rate of air transferred to the engine is reduced, which affects overall thrust, specific fuel consumption and compressor efficiency. These reductions are important to study when designing an engine to meet mission requirements.

Distortion also affects surge margin, which is the factor of safety between the operation point and the surge line. Surge is defined as the operational line of instability that is associated with violent oscillations in mass flow and can possibly lead to complete flow reversal. Engines have a steady-state operating surge margin stated as a function of engine geometry that can be greatly reduced when distortion is introduced. The surge line can shift to a lower value because of many different factors, including distortion (which is shown as the shaded region in the figure). Operating a distorted engine in the same manner as the undistorted situation, the engine could

approach or even meet the degraded surge line, causing a dangerous situation to occur that could lead to compressor problems including rotating stall and melted blades [37].

The aerodynamic effects of distortion are often considered in a section of design referred to as inlet/engine integration. Performance effects are based on the aerodynamics of the engine and are currently considered in the design process of engines during inlet design. Aside from these performance degradations, structural problems can also arise from the introduction of distortion to an engine and need to be studied as well.

During the design stages of an engine, it is crucial to measure the possible distortion that may occur. To accurately evaluate this distortion in the engine intake, several indices are typically employed to measure distortion for engines in standard configurations. These same indices are commonly used for Boundary Layer Ingestion (BLI) configurations as well. The amount of distortion at the fan face is in general characterized by a criterion that depends on the engine manufacturer. Presented below are the most widely used indices that could best capture distortion in our configuration according to the analyzed bibliography; however, they may not be sufficient.

2.7.1 Pressure-based distortion criteria

The distortion indices described in this section are widely used in the industry. They are all defined in the literature [38] [39].

DC(θ)

This distortion index quantify the total pressure in a sectional distortion coefficient. The DC(θ) value is given by equation 2.7, where P_f is the mean stagnation pressure at the engine inlet plane, q_f the dynamic pressure, and P_θ the mean stagnation pressure in the lowest stagnation pressure sector of the plane, of width angle θ . A sector of 60° is commonly used.

$$DC(\theta) = \frac{P_f - P_\theta}{q_f} \quad (2.7)$$

IDC

The IDC takes into account the pressure distribution across the circumference. It is based on experimental pressure rakes. Its value is given by Equation 2.8, where \bar{P}_i is the average stagnation pressure in the measurement plane, $P_{i,r}$ the average stagnation pressure on the r^{th} radius, and $P_{i,r}^{min}$ the minimum stagnation pressure on the r^{th} radius

$$IDC = \max_{1 \leq r \leq 5} 0.5 \left(\frac{\bar{P}_i - P_{i,r}^{min} + \bar{P}_{i,r+1} - P_{i,r+1}^{min}}{\bar{P}_i} \right) \quad (2.8)$$

Circumferential Distortion

Equation 2.9 presents an alternative version of a circumferential distortion index. This index calculates the average pressure of each ring P_{0i} and the section of the ring where the total pressure is lower than the average pressure at the AIP $P_{0i,low}$.

$$(\Delta PC/P)_{ave} = \frac{1}{5} \sum_{i=1}^5 \left(\frac{P_{0i} - P_{0i,low}}{P_{0i}} \right) \quad (2.9)$$

Radial Distortion

Radial distortion is described in terms of the radial distortion intensity, defined by equation 2.10. This index indicates the difference between the ring average total pressure (P_{0i}) and the face average total pressure ($\overline{P_f}$) normalised with the face average value

$$(\Delta PR/P)_{max} = \max_{i \in [1,5]} \left(\frac{\overline{P_f} - P_{0i}}{\overline{P_f}} \right) \quad (2.10)$$

2.7.2 Velocity-based distortion criteria

Typically, the impact of potential swirls on engine intakes during design stages is not taken into account. However, the study of S-ducts or BLI inputs can lead to very high swirl velocities, in which vortex intensity could affect engine operability. Several methodologies have been proposed for these cases; in this work, the methodology proposed by the Society of Automotive Engineers (SAE) is used as a reference [38]. All swirl descriptors are based on the swirl angle (α) distribution on each ring. Swirl angle is defined by equation 2.11

$$\alpha = \tan^{-1} \left(\frac{U_\theta}{U_x} \right) \quad (2.11)$$

Sector Swirl (SS)

The Swirl Sector is defined by equations 2.12 and 2.13. A positive swirl angle corresponds to a tangential speed that rotates in the same direction as the compressor while a negative swirl angle corresponds to a tangential speed that rotates in the opposite direction of the compressor for a given radial ring. Therefore, swirl sector elements are defined by SS_i^+ for positive swirl and SS_i^- for negative swirl. Figure 2.9 shows an example of a symmetric swirl pattern, θ_i^+ correspond to a positive swirl region and θ_i^- for a negative swirl region.

$$SS_i^+ = \frac{1}{\theta_i^+} \int_{\theta_i^+} \alpha(\theta)_i d\theta \quad (2.12)$$

$$SS_i^- = \frac{1}{\theta_i^-} \int_{\theta_i^-} \alpha(\theta)_i d\theta \quad (2.13)$$

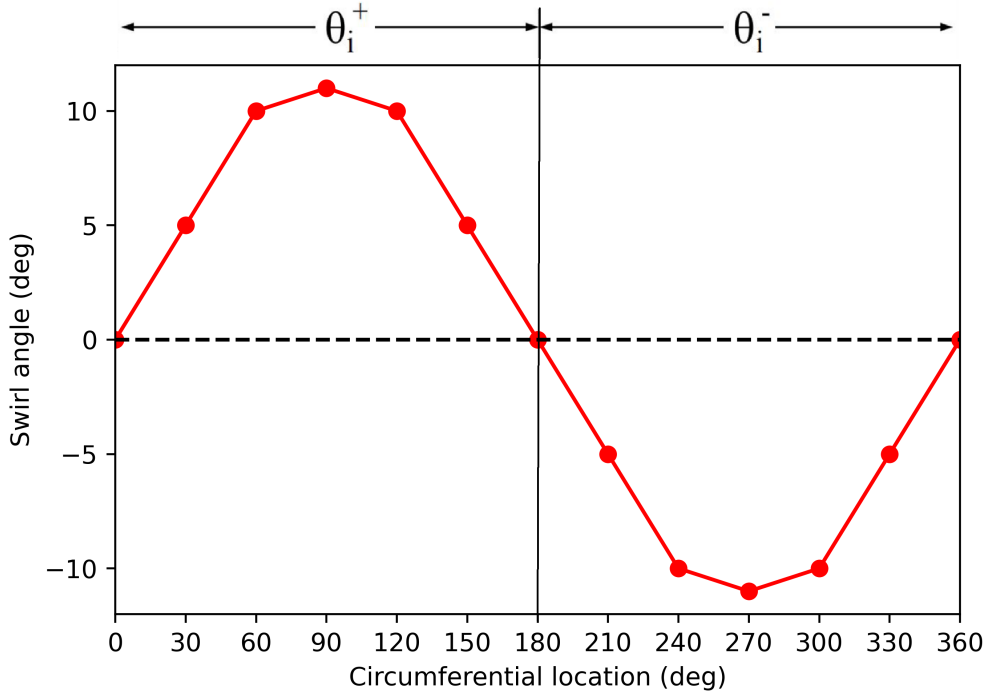


Figure 2.9: Typical one-per-rev symmetric paired swirl pattern for single immersion.

Swirl Intensity (SI)

The Swirl Intensity represents an average of the absolute, circumferential swirl angle in degrees for each ring at the AIP. This criteria is defined by equation [2.14](#).

$$SI_i = \frac{SS_i^+ \times \theta_i^+ + |SS_i^-| \times \theta_i^-}{360} \quad (2.14)$$

Swirl Directivity (SD)

The Swirl Directivity identifies the generalized rotational direction of the swirl distortion with respect to the compressor rotation at each ring. Swirl directivity has a value that ranges from -1 to +1. Its value is given by equation [2.15](#)

$$SD_i = \frac{SS_i^+ \times \theta_i^+ + SS_i^- \times \theta_i^-}{SS_i^+ \times \theta_i^+ + |SS_i^-| \times \theta_i^-} \quad (2.15)$$

For a sinusoidal swirl distribution resulting from a one-per-rev swirl pattern, as shown in figure [2.9](#), SD_i will be zero indicating there is equal and opposite swirl in one revolution around the

ring. For a pure co-rotating bulk swirl $-SS_i$ is zero while $+SS_i$ has some finite value; thus the swirl directivity SD_i will be equal to +1. Conversely, for a pure counter-rotating swirl SD_i will be equal to -1 because $-SS_i$ will be zero. Values of the Swirl Directivity, as related to different swirl patterns, are shown on a spectrum of patterns in Figure 2.10.

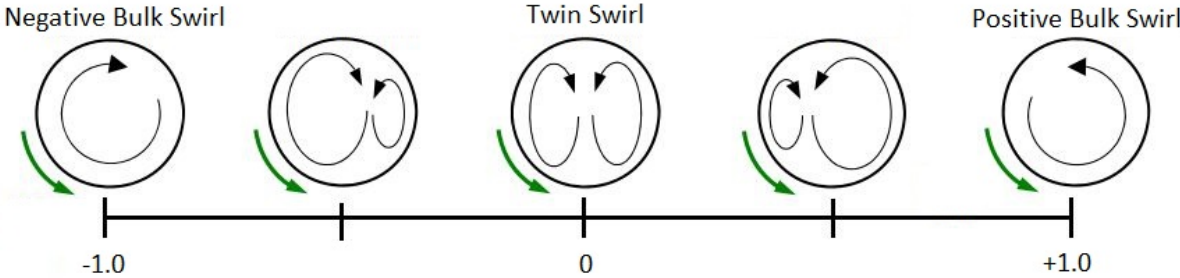


Figure 2.10: Swirl Directivity (SD) for counter-clockwise compressor rotation.

Swirl Pairs (SP)

The Swirl Pairs is a numerical indicator that represents the effective number of pairs of positive and negative swirl direction changes in the swirl measured at each ring. The Swirl Pairs is computed by Equation 2.16

$$SP_i = \frac{SS_i^+ \times \theta_i^+ + |SS_i^-| \times \theta_i^-}{2 \times \max[SS_i^+ \times \theta_i^+ \text{ or } SS_i^- \times \theta_i^-]} \tag{2.16}$$

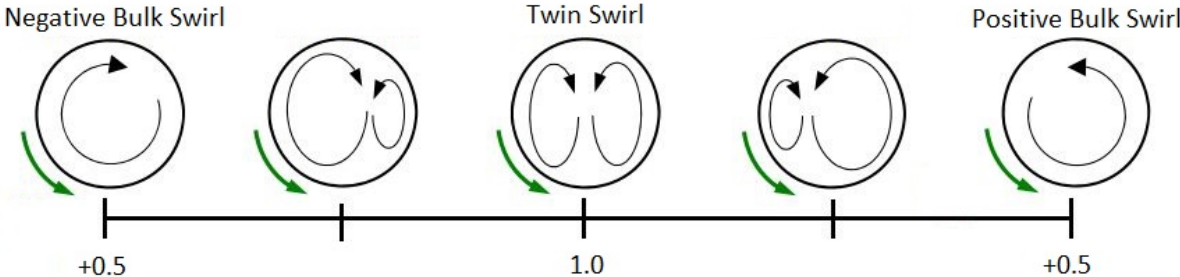


Figure 2.11: Swirl Pairs(SP) for counter-clockwise compressor rotation.

This swirl descriptor element also represents the range between 1/rev and bulk-swirl pattern. In a pure bulk swirl, the swirl angle $\alpha(\theta)_i$ is a constant value along the given ring. In an offset bulk

swirl, the swirl angles $\alpha(\theta)_i$ may vary circumferentially, but would remain either positive or negative for the full revolution. This will cause either $-SS_i$ or $+SS_i$ to go to zero, thus making intensity SI_i the average bulk swirl angle (on a given ring) and directivity SD_i to be a +1 for a co-rotating bulk swirl or -1 for a counter-rotating bulk swirl. The value of multiples of swirl pairs SP_i will be less than 1, with a finite value of 0.5 indicating bulk swirl. A pure bulk swirl is just one half of a pair with the other half being zero.

2.8 Aerodynamic analysis and predictive challenges of BLI engine intake

The primary research focus of this work is the comprehension of aerodynamic phenomena, as well as the simulation, prediction and quantification of distortion generated at the intake of the BLI engine.

CFD prediction limitations

To date, the research on the predictive accuracy of current numerical simulation models for Boundary Layer Ingesting intakes remains scant. Predominantly, investigations into BLI have adopted a broader analytical approach, often overlooking the intricate aerodynamic phenomena associated with this type of intake and its potential ramifications. While some comparative studies between numerical simulations and experimental outcomes have been conducted, they have not extensively explored the predictive proficiency of CFD models [40] [41].

Conversely, analogous physical phenomena have been documented in S-duct configurations, which have undergone more comprehensive scrutiny. The third [42] and fourth [43] aerodynamic workshops organized by the American Institute of Aeronautics and Astronautics (AIAA) concentrated on the comparative analysis of simulation results for an S-duct. The findings from both workshops demonstrated significant variability, heavily contingent upon the chosen turbulence models and mesh configurations. This disparity in outcomes further accentuates the limited precision of RANS models in simulating intricate flow fields. In contrast, more sophisticated models, such as the ZDES, have been employed for geometrically akin challenges, yielding marginally more accurate results [44].

In contrast to antecedent studies, this work primarily concentrates on elucidating the physical phenomena manifesting at the inlet of a Boundary Layer Ingestion engine, employing both numerical simulations and experimental methodologies. Furthermore, it delves into the comparative analysis of various turbulence models to ascertain their predictive capacity regarding the behavior of the flow field. The objective of this research is to investigate the accuracy of current turbulence models thereby facilitating the investigation and implementation of these innovative propulsion technologies.

Distortion impact

Flow distortion represents a dynamic and complex phenomenon with the potential to significantly impact the stability and functionality of propulsion engines. The implementation of boundary-layer-ingesting (BLI) systems within embedded propulsion architectures often leads to the manifestation of inlet flow distortions. These distortions arise from the intricate interplay between the boundary-layer vorticity and the engine's intake mechanism. Consequently, the introduction of low-momentum fluids into the system compels the fan to operate under persistent and heterogeneous inflow distortion conditions, which can degrade the aerodynamic performance of the fan. Should the magnitude of the distortion reach a critical threshold, it possesses the capacity to induce stalling within the fan or provoke surging within the engine.

The phenomenon of interference and the propagation of distortion through the compression stages in the context of BLI-type distortion have been subjects of investigation by numerous researchers [45][46][47]. The primary focus of these studies has been to elucidate the progression of distortion across the compression stages, often neglecting the interrelation between the physical processes responsible for the generation of distortion and the distortion itself. Commonly, these analyses utilize predefined profiles of velocity and pressure. In contrast, the present study endeavors to establish a connection between the distortion observed and the underlying physical phenomena that generate it. Moreover, these indices of distortion concurrently function as metrics for measuring the accuracy of various turbulence models in predicting physical phenomena associated with flow distortion in a BLI intake.

Chapter 3

Experimental Analysis of a semi-buried BLI intake

3.1 Wind tunnel facility

The experimental analysis of our intake was conducted in the S3Ch wind tunnel in Meudon. This wind tunnel is a continuous closed-circuit transonic facility running at atmospheric pressure. The air temperature is close to the ambient, being maintained close to a constant value during the tests by using a heat exchanger. The air flow is ensured thanks to a two-stage motor-ventilator group of 3.5 MW with a compression ratio of 1.25.

The test section is a guided one with sidewalls equipped with high-quality windows and lower/upper rigid or deformable adaptive walls (to follow the flow streamlines curvature around the model). Moreover, the facility is equipped with a sonic throat downstream of the test section in order to avoid pressure perturbations around the model in transonic regime.

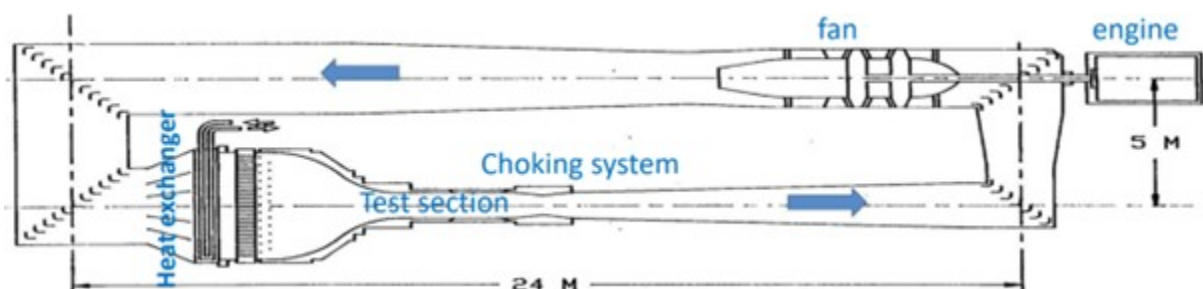


Figure 3.1: S3Ch scheme (ONERA)

3.1.1 Model

The experimental models used in the SUBLIME project aim to characterize the distortion at intake of a BLI engine and validate studies conducted with CFD simulations. Two semi-buried

intake geometries have been designed, in this work only the first geometry is studied.

The geometry has a moderate burial rate and also small L_{in} and L_{out} lengths. L_{out} and L_{in} are directly linked to the H value to avoid unwanted detachments at the entrance ramp in nominal conditions. The desired shape for the nacelle leading edge is pseudo-circular and defined by its height and length values. The chosen values for the main geometry, called BLI Intake EA1, are shown in Table 3.1. The fan diameter is 164mm.

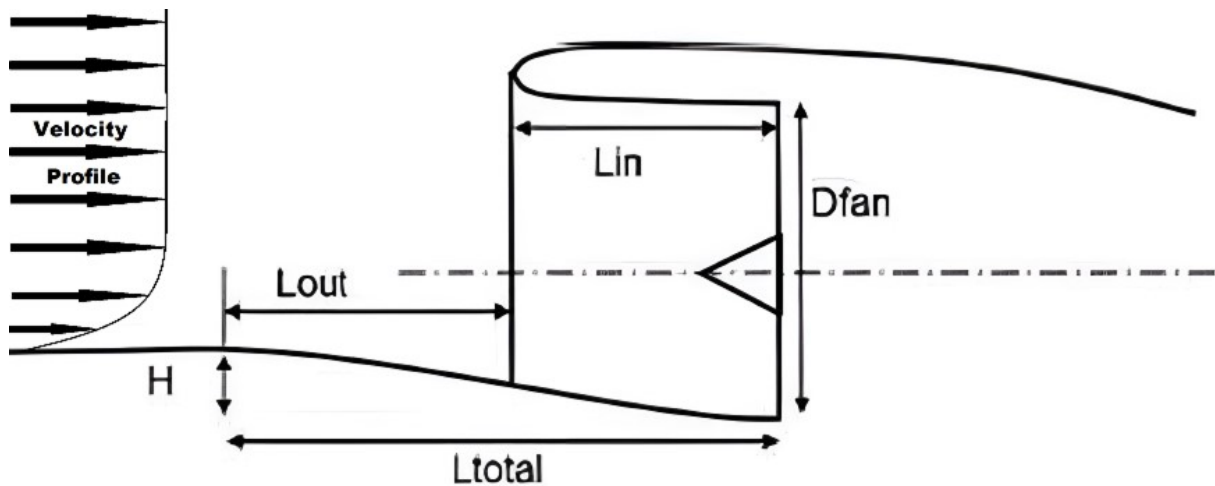


Figure 3.2: Geometry model

	Burial Rate / D_{fan}	L_{in}/D_{fan}	L_{out}/D_{fan}	Height/ D_{fan}	Length/ D_{fan}
BLI Intake EA1	0.20	0.75	0.75	0.88	1.17

Table 3.1: Geometry parameters of the BLI intake

The model is located on the left wall of the test area. The boundary layer of the wall is ingested by the air intake of the model. The flow through the intake is ensured by a blower suction device. The maximum mass flow rate is $4 \text{ kg}\cdot\text{s}^{-1}$. The right wall of the blower is equipped with a window to carry out optical measurements in the flow by PIV. Mounting allows a sideslip angle up to 12° .

Several measurements were carried out during the test in order to characterize and compare the flow field with numerical simulations. Static pressures and instantaneous pressures were measured on the surface of the models, particularly in the intake ramp. In addition, some sensors to measure the boundary layer characteristics were added upstream ramp intake. At the AIP a rake of total pressure measurements was used, in addition to velocity measurements by PIV. To summarize, the intake was equipped with 30 static pressure sensors and 9 Kulite sensors. The data acquisition frequency of the Kulite and rake sensors was 20kHz. All these sensors can be outlined in 4 groups: intake ramp, left-side nacelle, right-side nacelle and top nacelle. Figures 3.5 and 3.4 show the position and nomenclature of the sensors in the model.

Tables 3.2, 3.3, 3.4, 3.5 and 3.6 summarize the position of each sensor. The origin is located at the AIP, x is in the streamwise direction, y spanwise, z vertical. The total pressure rake is equipped with 40 sensors placed on 8 arms each 45° in azimuth. This rake can be rotated in order to obtain a higher density of sensors at the AIP. Figure 3.7



Figure 3.3: Model placed in S3Ch wind tunnel.

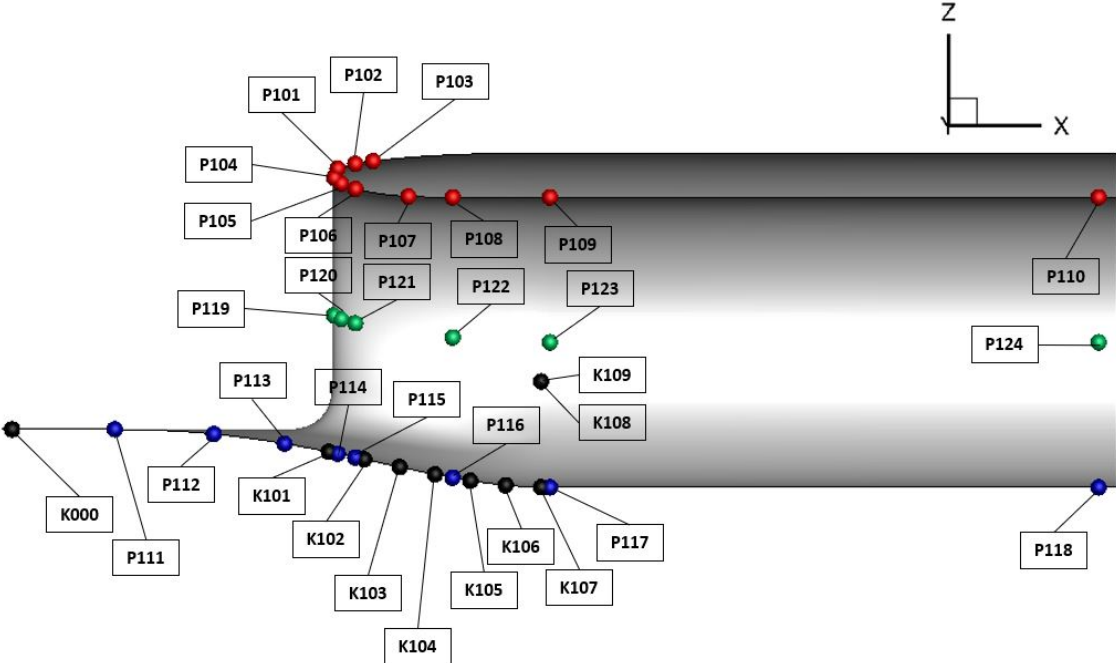


Figure 3.4: Pressure taps (in red, green and blue) and unsteady pressure sensors (in black) on the model.

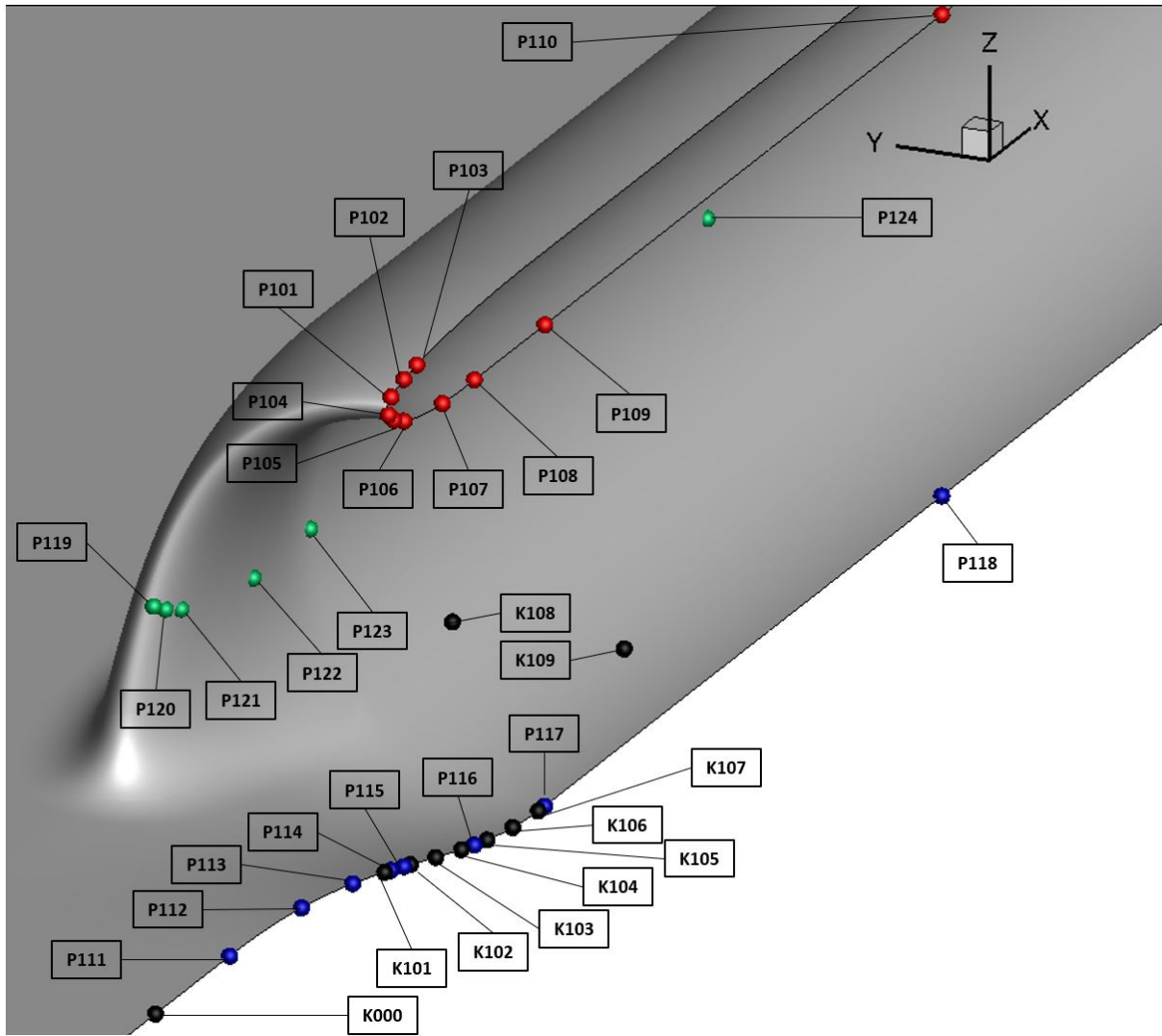


Figure 3.5: Pressure taps (in red, green and blue) and unsteady pressure sensors (in black) on the model.

	x [mm]	y [mm]	z [mm]
K000	-304	0	-32,8
K101	-125	0	-12,73
K102	-105	0	-16,94
K103	-85	0	-21,29
K104	-65	0	-25,45
K105	-45	0	-29,01
K106	-25	0	-31,56
K107	-5	0	-32,75
K108	-5	30	-27,08
K109	-5	-30	-27,08

Table 3.2: Kulites locations on the intake ramp.

	x [mm]	y [mm]	z [mm]
PS101	-120	0	147,52
PS102	-110	0	150,11
PS103	-100	0	151,63
PS104	-122	0	142,17
PS105	-118	0	138,98
PS106	-110	0	135,9
PS107	-80	0	131,66
PS108	-55	0	131,2
PS109	0	30	131,2
PS110	310	-30	131,2

Table 3.3: Pressure tap locations on nacelle top.

	x [mm]	y [mm]	z [mm]
PS119	-122	82,014	64,414
PS120	-118	79,713	62,407
PS121	-110	77,81	60,022
PS122	-55	77,231	51,937
PS123	0	82	49,2
PS124	310	82	49,2

Table 3.4: Pressure tap locations on nacelle left side.

	x [mm]	y [mm]	z [mm]
PS125	-122	-82,01	64,414
PS126	-118	-79,71	62,407
PS127	-110	-77,81	60,022
PS128	-55	-77,23	51,937
PS129	0	-82	49,2
PS130	310	-82	49,2

Table 3.5: Pressure tap locations on nacelle right side.

	x [mm]	y [mm]	z [mm]
PS111	-246	0	0
PS112	-190	0	-2,682
PS113	-150	0	-8,066
PS114	-120	0	-13,75
PS115	-110	0	-15,86
PS116	-55	0	-27,33
PS117	0	0	-32,8
PS118	310	0	-32,8

Table 3.6: Pressure tap locations on the intake ramp.



Figure 3.6: Rake at the AIP

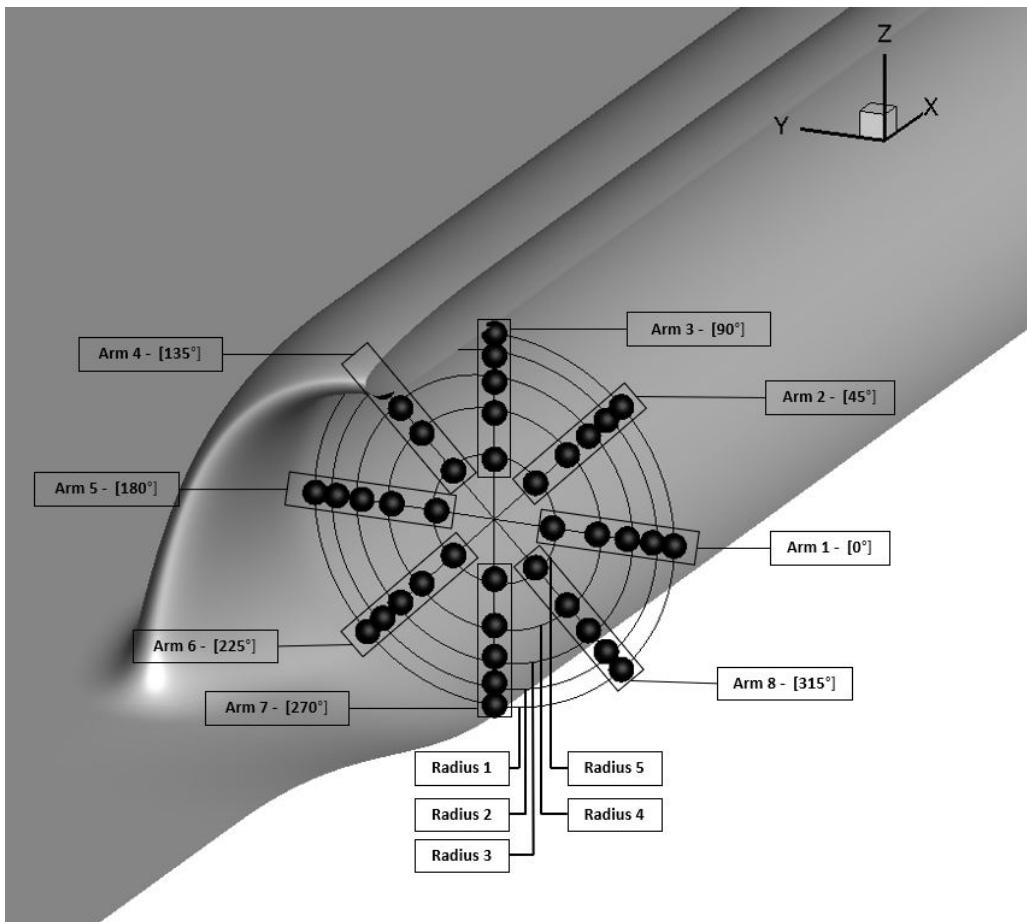


Figure 3.7: Rake at the AIP

3.2 Test conditions

The main objective of the tests was to characterize the physical phenomena and the distortion in the AIP, as well as to validate the studies carried out with CFD turbulence models. The conditions chosen are out-of-design conditions, which tend to produce complex physical phenomena at the engine intake. The Mach number in the test section is 0.82 for all cases. The pressure and temperature are the atmospheric conditions.

The only varied parameter was the corrected mass flow ingested by the engine, which has increased from 2.6 to 4.0 kg·s⁻¹. The corrected mass flow for a given temperature and pressure condition is calculated using Equation 3.1. The reference area is defined as the fan face, while R and γ are those for standard atmospheric conditions. In instances where there are low mass flow values, it is expected that there will be a flow separation at the intake ramp. In all cases, there will be a loss of total pressure due to boundary layer thickening.

$$\dot{m} = \frac{A P_t}{\sqrt{T_t}} \sqrt{\frac{\gamma}{R}} M \left(1 + \frac{\gamma-1}{2} M^2 \right)^{-\frac{\gamma+1}{2(\gamma-1)}} \quad (3.1)$$

3.3 Analysis and procedures for experimental signals

As a turbulent flow is chaotic, it is not possible to predict which instantaneous values will be obtained at a given point. A statistical description of the interesting variables is necessary to understand the turbulence behavior [48].

An aleatory signal experimentally obtained is described in equation 3.2. The value x represents any variable measured over time. This signal is formed by its mean value (\bar{x}) and the fluctuating component ($x'(t)$).

$$x(t) = \bar{x} + x'(t) \quad (3.2)$$

The statistics of a signal can be grouped according to the type of information they provide.

3.3.1 Statistics in the amplitude domain

These statistics provide information related to the distribution of signal amplitudes, however do not give information about their temporal evolution.

Mean Value

For discrete sampling with N extractions at equal time intervals the mean value is calculated using equation 3.3. This value is an unbiased estimator. The turbulence signals are ergodic processes; therefore, the initial value of t does not modify the mean value obtained.

$$\bar{x} = \frac{1}{N} \sum_{i=1}^N x_i \quad (3.3)$$

Variance and standard deviation

Variance is a measure of dispersion that represents the variability of a data set with respect to its mean value. The square root of the variance is the standard deviation. Equation 3.4 describes an unbiased estimator of the variance for a discretized signal.

$$\sigma^2 = \frac{1}{N-1} \sum_{i=1}^N (x_i - \bar{x})^2 = \frac{1}{N-1} \sum_{i=1}^N x_i'^2 \quad (3.4)$$

Higher order moments

The m -order moment for a discretized sample of $x(t)$ is defined in equation 3.5

$$\overline{x'^m} = \frac{1}{N} \sum_{i=1}^N x_i'^m \quad (3.5)$$

The 3rd order moment is usually presented in dimensionless form, as shown in equation 3.6. This parameter is called skewness and is an indicator of the statistical asymmetry of the signal. The 4th moment, also presented in dimensionless form, is called kurtosis. This parameter is an indicator of the importance of extreme values in the probability distribution of the sample. Kurtosis is calculated using equation 3.7, according to Fisher's kurtosis.

$$Sk_x = \frac{\overline{x'^3}}{\sigma^3} \quad (3.6)$$

$$Ku_x = \frac{\overline{x'^4}}{\sigma^4} - 3 \quad (3.7)$$

3.3.2 Statistics in frequency domain.

The Fourier transform is the tool that allows changing between the time and frequency domain. The approximation for discrete data is shown in equation 3.8 and 3.9.

$$\hat{x}(n) = \sum_{k=0}^{N-1} x_k e^{-i2\pi k\Delta t} \quad (3.8)$$

$$x(n) = \frac{1}{2\pi} \sum_{k=0}^{N-1} \hat{x}_k e^{i2\pi k\Delta t} \quad (3.9)$$

The power spectral density (PSD) represents the contribution of a frequency n to the total variance of the spectrum. The PSD gives us an idea of how much of the variance of a temporal sign is associated with a certain frequency.

$$PSD = \frac{|\hat{x}_n|^2}{T} \quad (3.10)$$

3.4 Experimental boundary layer

The first variable to take into account when analyzing a BLI intake is the boundary layer behavior. In the wind tunnel tests, the boundary layer characteristics upstream of the intake were measured just before the intake ramp at $x = -275$ mm. To make a direct comparison with numerical data, the chosen conditions to extract the boundary layer characteristics were a mass flow rate of $4.0 \text{ kg}\cdot\text{s}^{-1}$ and a Mach number of 0.80. When the mass flow rate is higher, we expect a decrease in the complexity of physical phenomena. Therefore, it is more likely to measure a more stable boundary layer that is less coupled to downstream behavior.

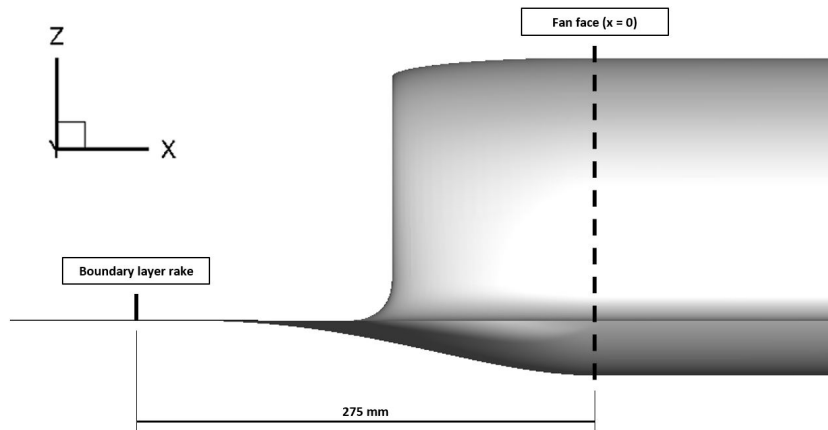


Figure 3.8: Experimental boundary layer measurement

Figure 3.8 shows the measurement position of the boundary layer. The measurement gives a thickness (δ) of 16.05 mm. The displacement thickness and momentum thickness are 2.36 mm and 1.82 mm respectively. The shape factor is equal to 1.3, close to typical values of turbulent flows [49]. Figure 3.9 shows boundary layer velocity profiles in wall units between theoretical and experimental behavior. The blue line represents the measured data, while the red line represents the expected values according to the logarithmic law. The obtained profile matches the numerical calculations between $Y+ = 20$ and $Y+ = 1000$.

By knowing the experimental boundary layer thickness, it is possible calculate the apparent length of the flat plate that would produce the same boundary layer thickness under our case condition by using the Equation 3.11. The first estimate provides an approximate length of 1300 mm. However, this distance can depend on the impact of phenomena occurring downstream.

$$\frac{\delta}{x} = 0.376Re_x^{-\frac{1}{5}} \tag{3.11}$$

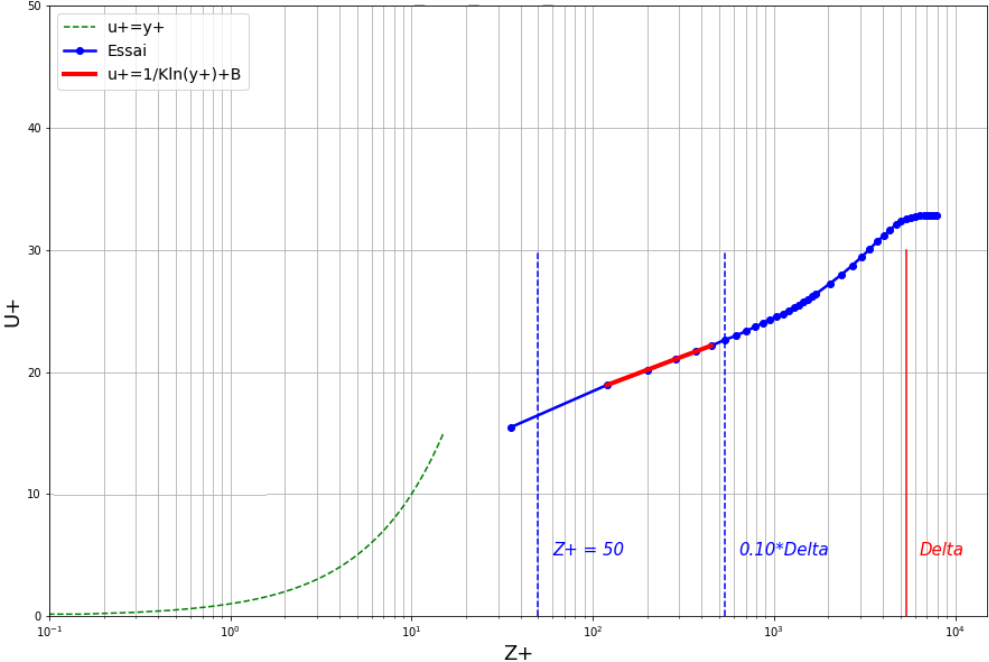


Figure 3.9: Experimental boundary layer profile in wall units

3.5 Intake ramp analysis

3.5.1 Mean values analysis

This section analyzes the wall pressures distributions obtained at the ramp intake. The pressure taps, defined from PS111 to PS117 and shown as blue dots in Figures 3.4 and 3.5, are used. To compare with numerical data, values are displayed in terms of pressure coefficient computed using Equation 3.12. In this case, P is the mean static pressure measured by each sensor, and P_∞ is the static pressure on the free stream.

$$C_p = \frac{2}{\gamma M_\infty^2} \left(\frac{P}{P_\infty} - 1 \right) \quad (3.12)$$

First, the repeatability of the experimental data is evaluated. For this, experimental data obtained at different times are used and plotted for a corrected mass flow rate of $4.0 \text{ kg}\cdot\text{s}^{-1}$. Figure 3.10 shows the C_p distribution obtained. By analyzing the pressure distribution it can be concluded that data dispersion is acceptable, and the repeatability is verified.

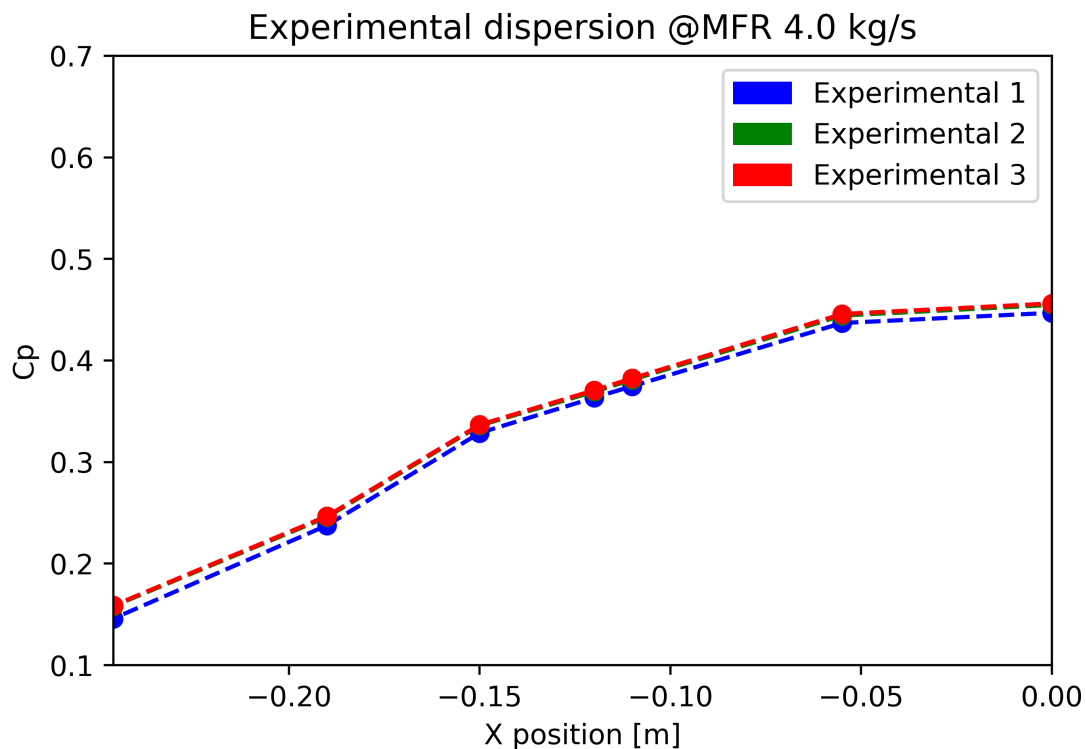


Figure 3.10: Experimental repeatability at $\text{MFR } 4.0 \text{ kg}\cdot\text{s}^{-1}$.

Figure 3.11 shows the C_p distribution from $3 \text{ kg}\cdot\text{s}^{-1}$ to $4 \text{ kg}\cdot\text{s}^{-1}$. This figure illustrates two distinct behaviors in the C_p distribution at the intake ramp. When high mass flow values are

present, the C_p increment between two mass flow rates appears to be proportional to the mass flow rate. However, for low mass flow rate values, C_p values tend to remain very close in the region between $-0.15\text{m} < x < -0.05\text{m}$. These nearby values could indicate a possible flow recirculation in that region; however, this cannot be verified solely with the curves obtained from the mean value of C_p .

An isentropic analysis was conducted to verify the coherence of the data obtained. This takes as a reference the transverse area at the AIP, the mass flow rate and freestream conditions. Figure 3.12 shows the curves obtained in comparison with experimental data. The transverse areas used for X values larger than -0.125 m were calculated directly from the CAD file. For values less than -0.125 m , the transverse areas considered were directly the streamtube in freestream conditions. However, taking this consideration into account, the effect of upstream flow on the streamtube is not taken into account, and therefore there is a discontinuity in C_p curves at $x = -0.125\text{ m}$. On the right side of the figure, the curves are smooth and coherent. It can be verified that a mass flow of $4\text{ kg}\cdot\text{s}^{-1}$ has a lower C_p value. This value grows inversely proportional to the mass flow rate, as experimental curves show. In general, the C_p values calculated by the isentropic approach are vertically displaced in reference to experimental curves. The isentropic approach does not take into account the loss of energy by viscosity effects or complex physical phenomena like flow separation. An examination of non-stationary data collected at the intake ramp may provide additional evidence of this change in flow behavior.

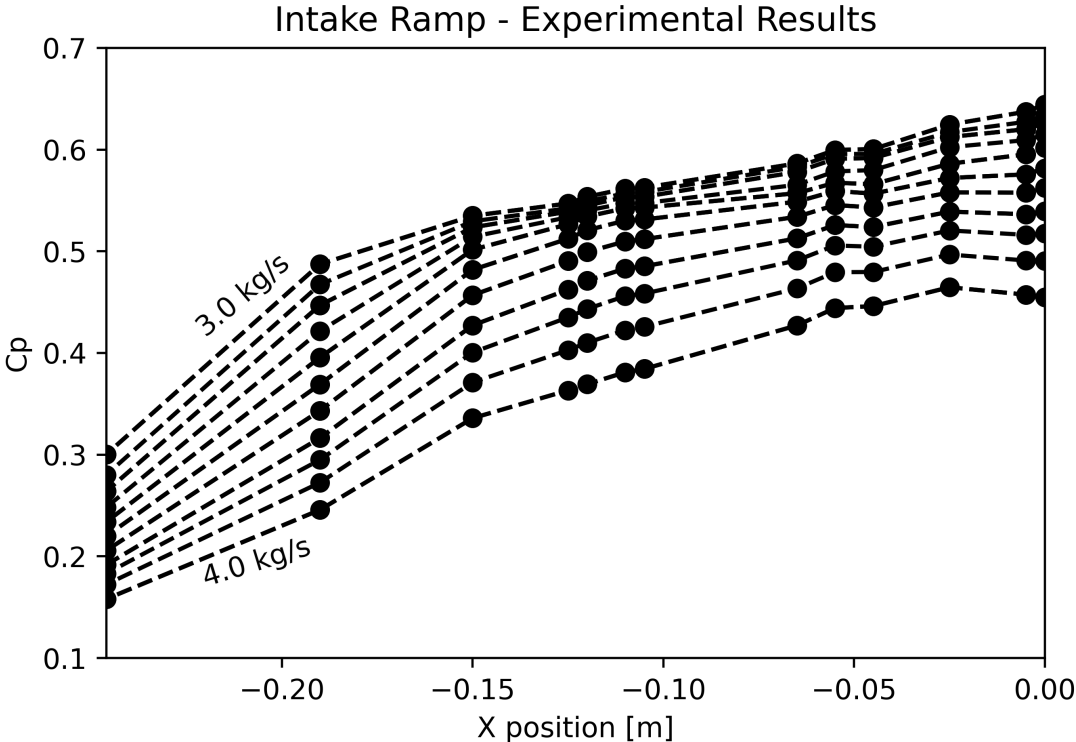


Figure 3.11: Experimental C_p distribution at intake ramp each $0.1\text{ kg}\cdot\text{s}^{-1}$ from $3\text{ to }4\text{ kg}\cdot\text{s}^{-1}$

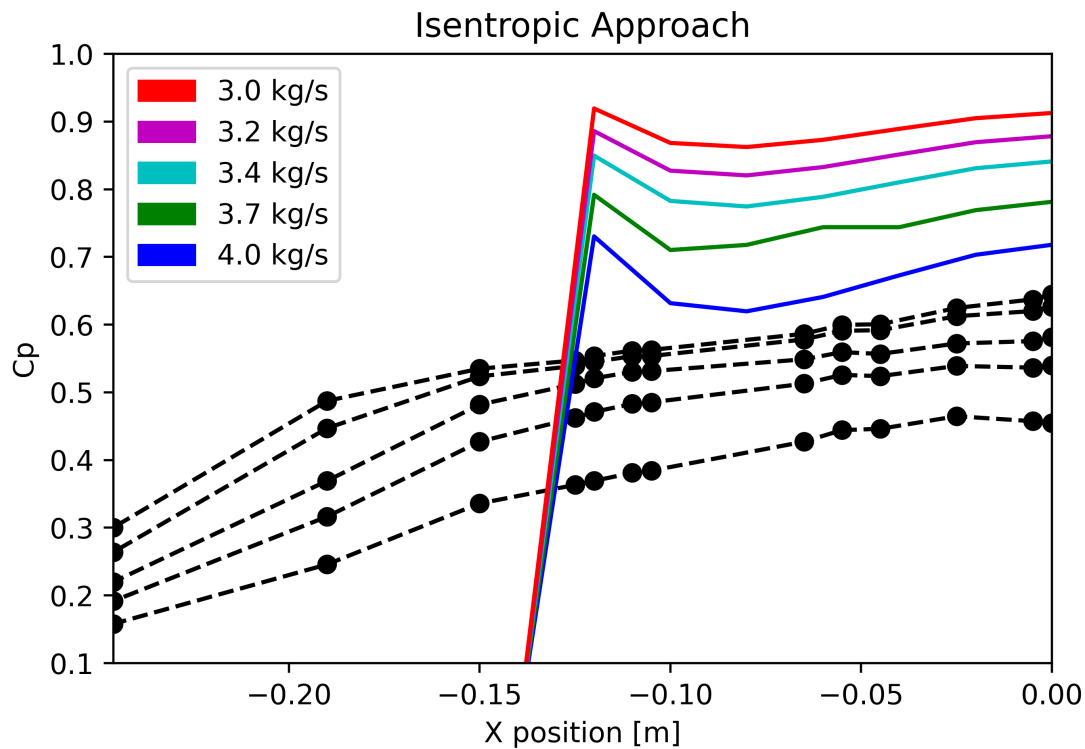


Figure 3.12: Comparison between the experimental data and an isentropic approach.

3.5.2 Unsteady values analysis

The signals analyzed in this section come from the Kulites (see table 3.2 for their location). These sensors are located on the intake ramp and have an acquisition frequency of 20kHz. Figure 3.22 shows the statistics calculated for different mass flow rate values.

As a first general behavior to highlight, the mean value of C_p for all sensors tends to decrease when the mass flow increases. The highest C_p values are obtained for a mass flow rate of $3.0\text{kg}\cdot\text{s}^{-1}$. This behavior was expected since when the mass flow increases, the velocity also increases, and subsequently the static pressure decreases. In addition, the intake ramp reduces the flow velocity due the increase of transversal area, therefore the downstream sensors will have a slightly higher C_p value. Both behaviors have already been shown in figure 3.11, which represents the mean values of C_p . It can also be observed that the sensor k103 gives a mean value abnormally high and not representative of the intake ramp physics.

In addition, the reduction in static pressure for high mass flow rates may also be attributed to the loss of energy resulting from viscous effects in the boundary layer. In cases where the flow has the potential to separate, there is an exchange of momentum between the free stream and the boundary layer. In cases where flow separation is not expected, all of this total pressure loss is concentrated in the lower regions of the boundary layer.

Statistics k101

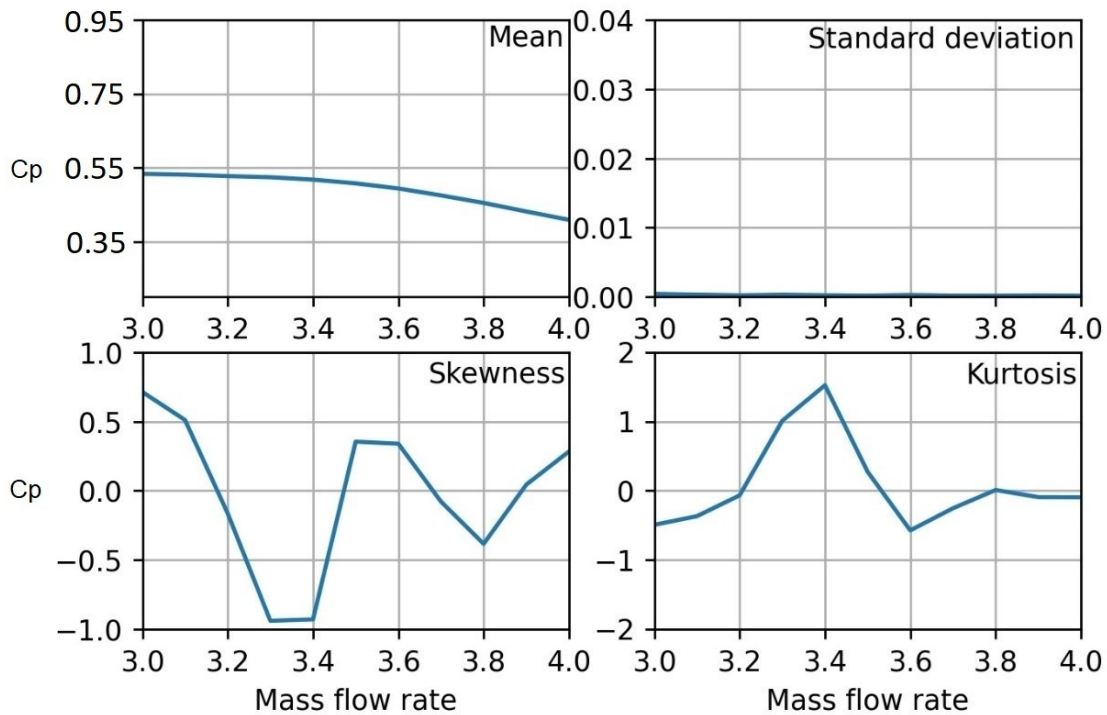


Figure 3.13: (a) k101 sensor statistics

Statistics k102

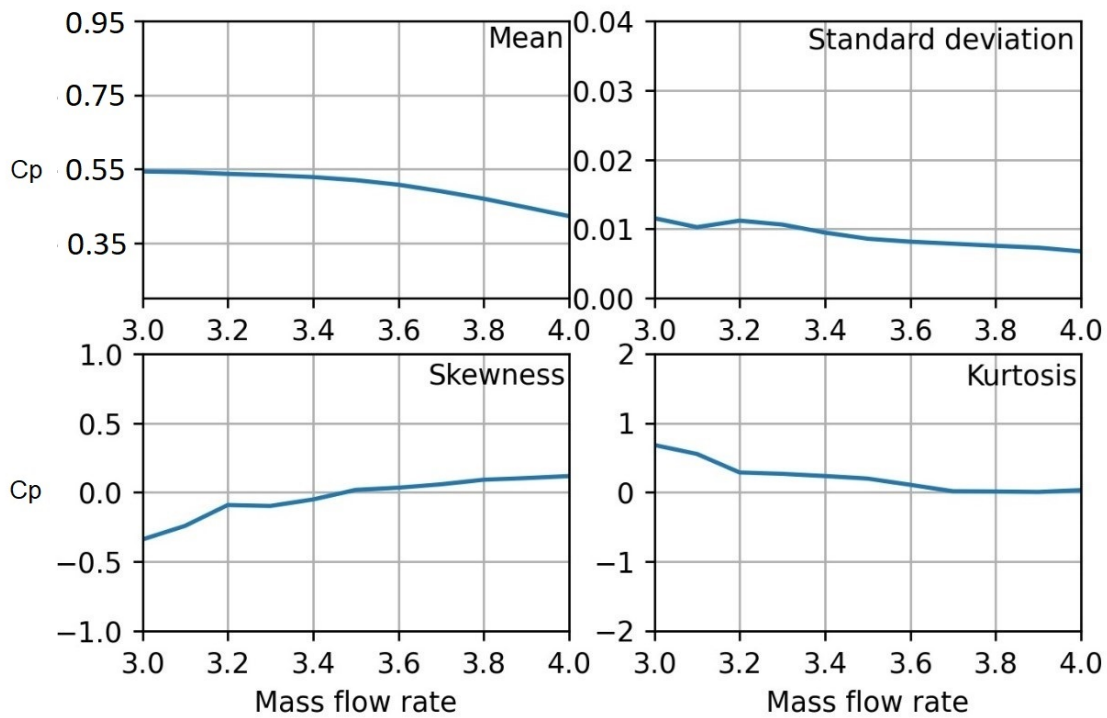


Figure 3.14: (b) k102 sensor statistics

Figure 3.15: Kulite sensors at intake ramp statistics.

Statistics k103

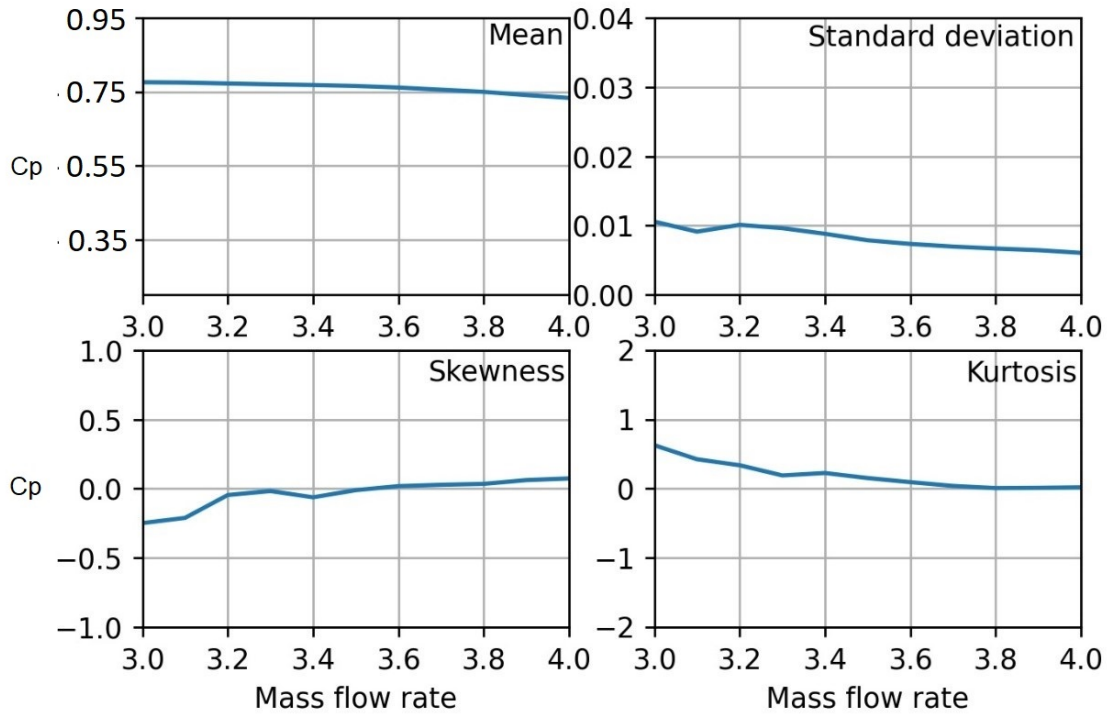


Figure 3.15: (c) k103 sensor statistics

Statistics k104

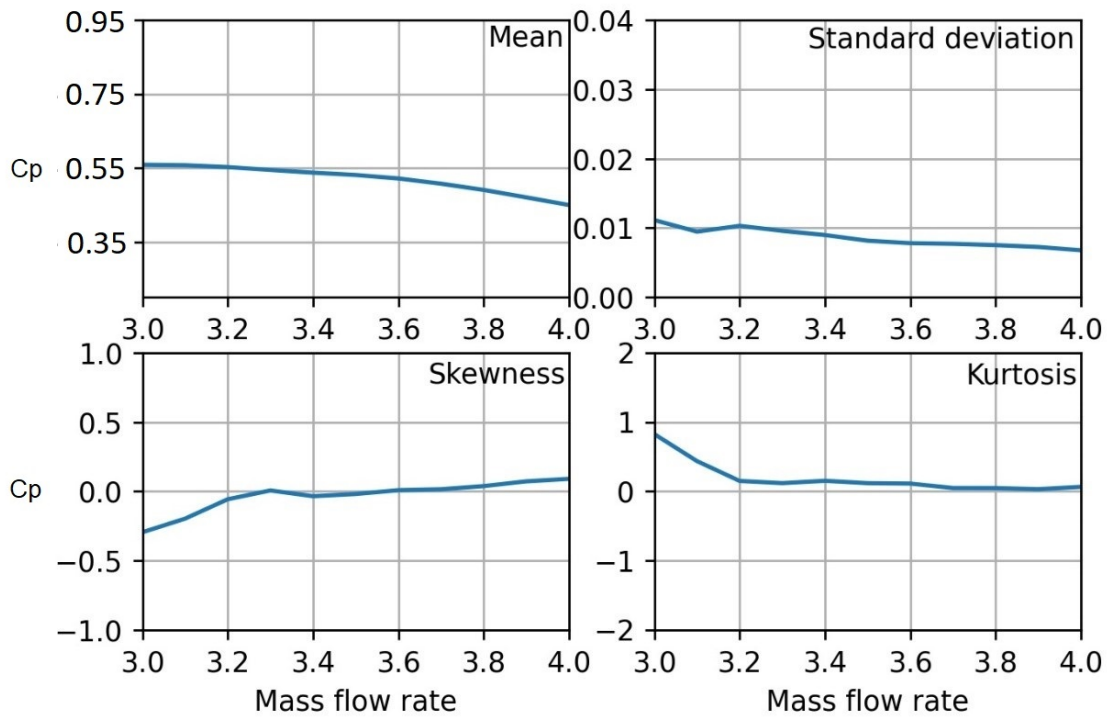


Figure 3.16: (d) k104 sensor statistics

Figure 3.17: Kulite sensors at intake ramp statistics. (cont.)

Statistics k105

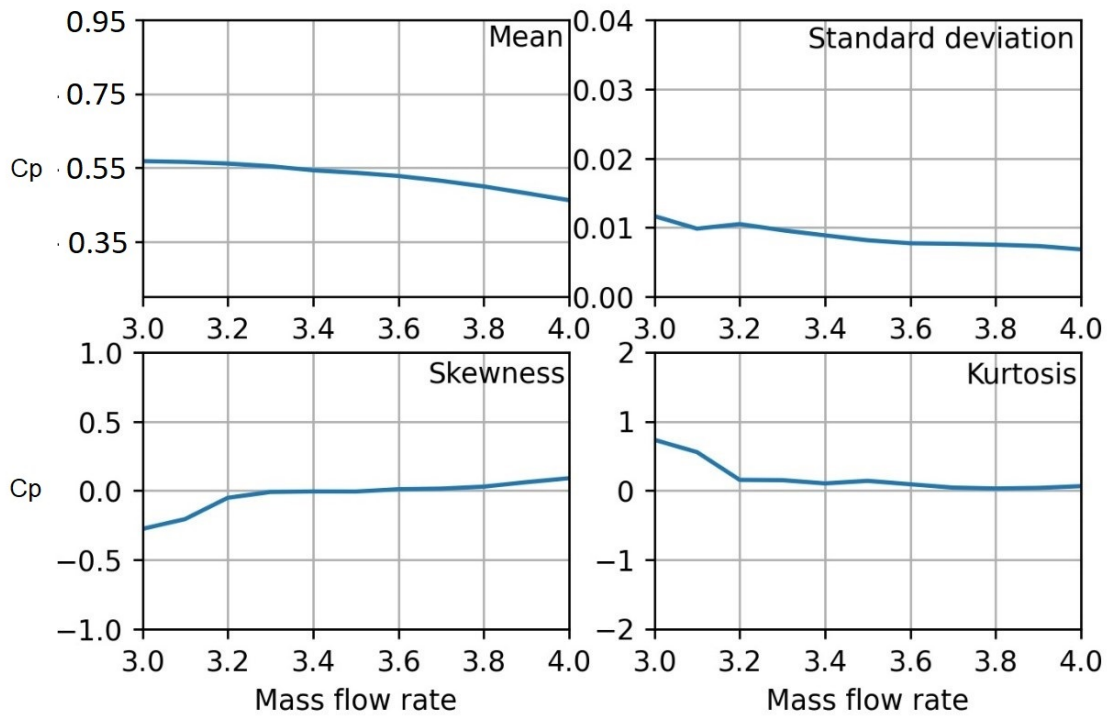


Figure 3.17: (e) k105 sensor statistics

Statistics k106

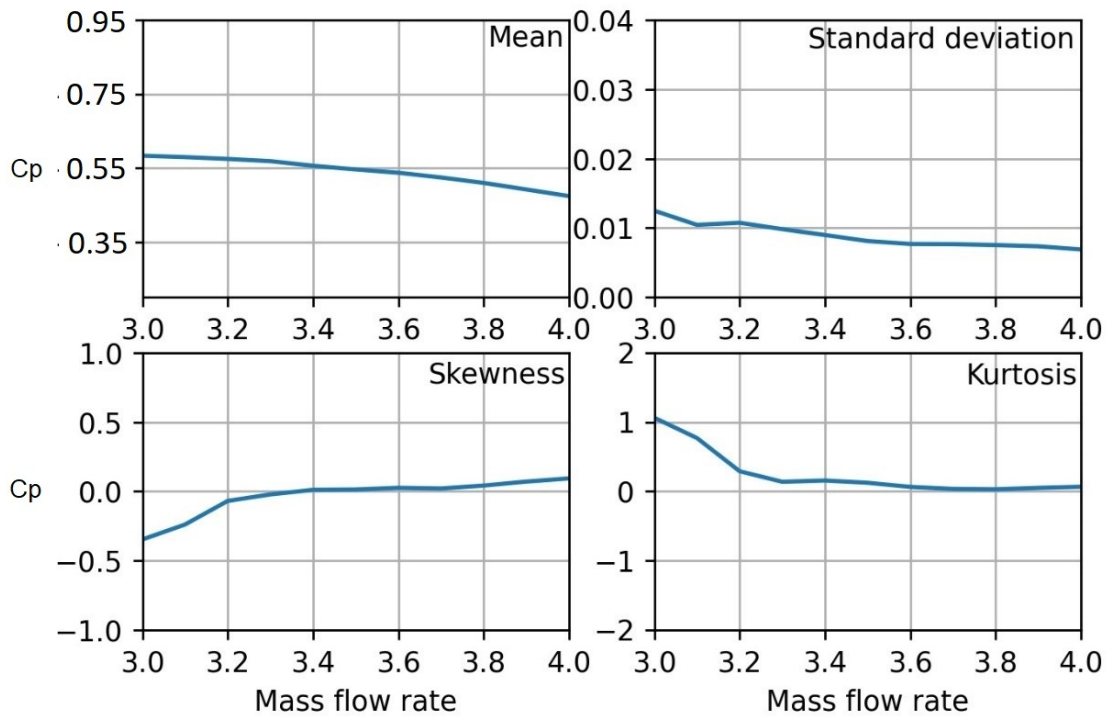


Figure 3.18: (f) k106 sensor statistics

Figure 3.19: Kulite sensors at intake ramp statistics. (cont.)

Statistics k107

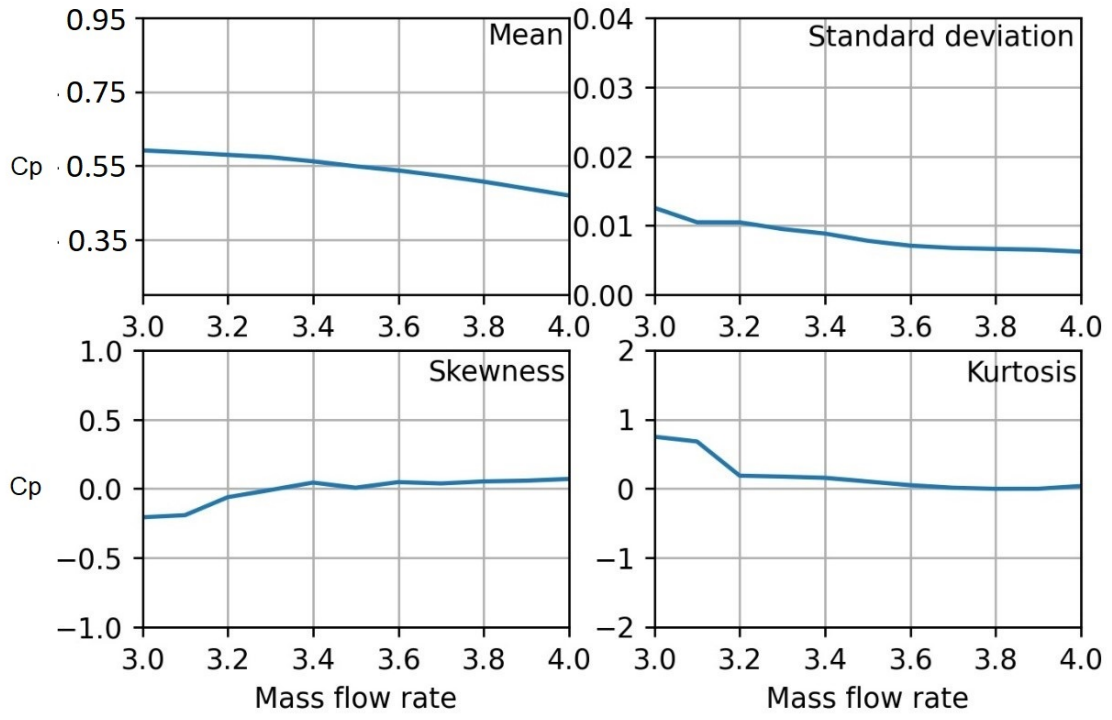


Figure 3.19: (g) k107 sensor statistics

Statistics k108

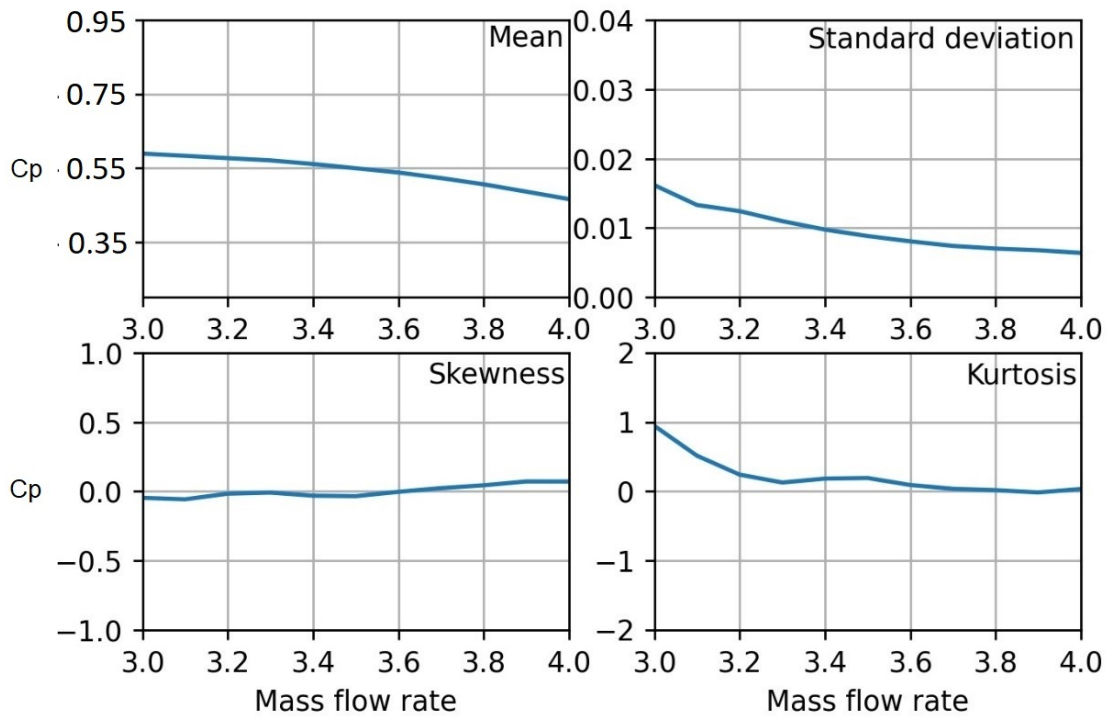


Figure 3.20: (h) k108 sensor statistics

Figure 3.21: Kulite sensors at intake ramp statistics. (cont.)

Statistics k109

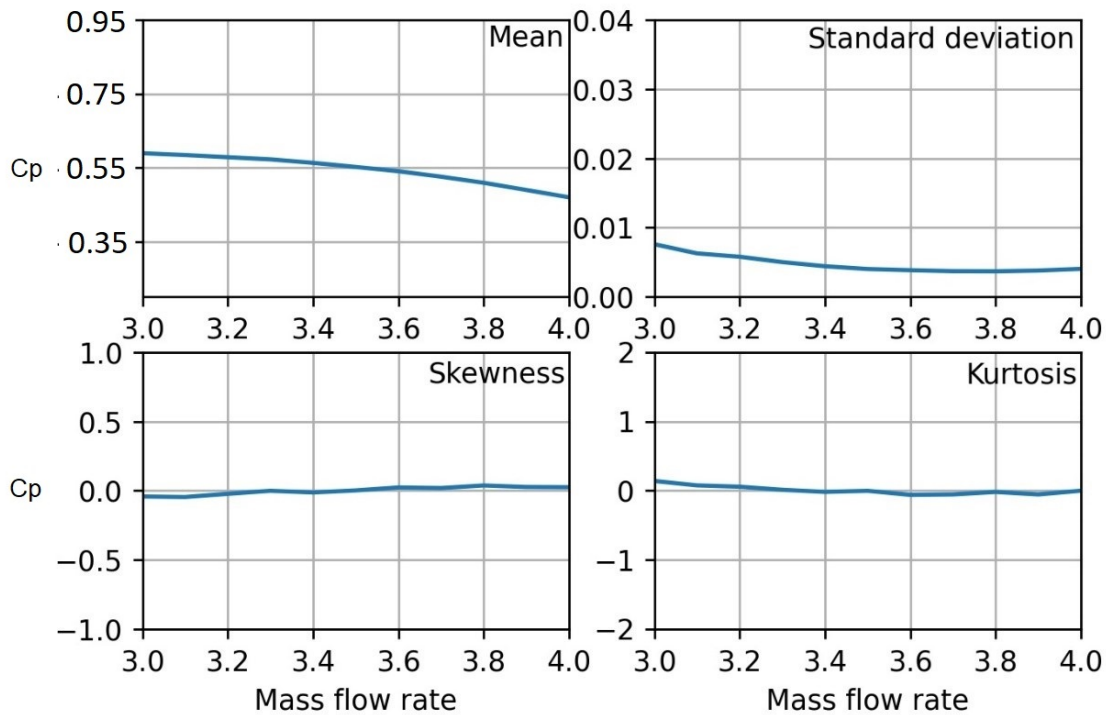


Figure 3.21: (i) k109 sensor statistics

Figure 3.22: Kulite sensors at intake ramp statistics. (cont.)

The standard deviation shows different behavior between the sensors. The sensor k101, placed at $x = -0.125\text{m}$, shows very low standard deviation values compared to the other sensors. The other sensors show very similar behaviors, decreasing inversely to the mass flow value, and having maximum values between 3.0 kg and $3.3 \text{ kg}\cdot\text{s}^{-1}$. The difference in the standard deviation reduction of the values obtained between the first sensor and the rest is noticeable. After a sensor verification, we have discovered that the oscillation amplitudes of the sensor k101 are not reliable.

The skewness and kurtosis values are highly influenced by the standard deviation. If this last parameter is low, skewness and kurtosis gives more extreme values. For low mass flow rates value the skewness exhibits a negative value, this mean that the signal has very intense valley values of short duration. For high mass flow rate values ($4 \text{ kg}\cdot\text{s}^{-1}$) the skewness is slightly positive, this means intense peaks of short duration. These skewness values can give some hint about the boundary layer state for a certain point and a certain mass flow value: when the flow is separated, there are some intense valleys, and when the flow is attached with a mass flow rate, there are intense peaks. The kurtosis value is around zero when there is no flow separation. For low mass flow rate, this value increases, showing a leptokurtic distribution. A high value of kurtosis indicates that the presence of extreme values (valley or peaks) with a higher probability.

One of the characteristics of turbulence that can be verified with the unsteady data is the transfer of energy from the larger to the smaller scales where the energy dissipates. The energy transfer mechanism is usually explained by the energy cascade, as shown in Figure 3.23. A notable feature of this energy cascade occurs in the inertial range, where energy has a slope of $-5/3$ on the logarithmic scale with respect to frequency.

In Figures 3.33, the power spectral density (PSD) was calculated for each sensor at ramp intake. The signals are noisy; therefore, Welch's method was used to visualize the spectra. The first analysis performed is data verification to see if its behavior resembles that expected in theory. Analyzing those figures shows that the experimental results, unlike the graph shown in Figure 3.23, exhibit a double slope. A possible hypothesis for this behavior could be an inverse turbulent energy cascade commonly found in 2D turbulent flows.

It should be noted that the measurements were taken on the surface of the ramp; therefore, the nature of turbulence in this region does not behave in the same way as in a region away from a surface. Probably within the boundary layer, turbulence behavior is quasi-bidimensional; therefore, energy transfer mechanisms change with respect to those mentioned above. In this type of flow, some kinetic energy is transported from smaller to larger eddies, as shown in Figure 3.24. In the other sense, there is a flow of enstrophy that goes from large eddies to smaller ones. In the range of inverse cascade of energy, the slope is similar to the previous case $-5/3$; however, in the range of enstrophy cascade, the slope changes to -3 . In Figures 3.33, dotted lines show slopes of $-5/3$ and -3 respectively. The sensors placed at the ramp clearly show this double-slope.

It is important to note that, although the inverse energy cascade is a concept associated with two-

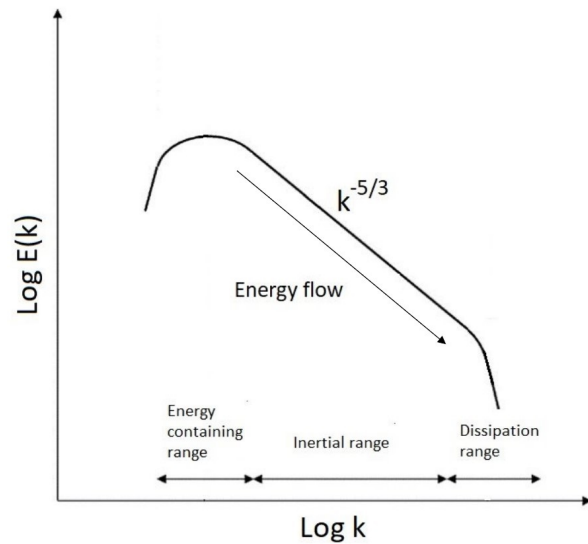


Figure 3.23: Turbulent energy cascade

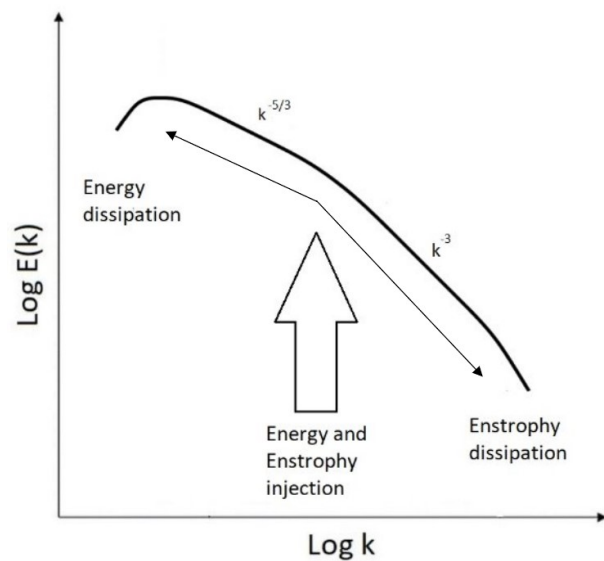


Figure 3.24: Inverse turbulent energy cascade

dimensional turbulence, there are studies that explore conditions under which similar phenomena could be observed in three-dimensional systems under certain constraints or forcings. However, these cases are exceptional and do not represent the typical behavior of three-dimensional isotropic turbulence. Some of these cases show quasi-two-dimensional behaviors, related to rotating flows [50] or flows confined in very thin layers [51]. The latter case would be more related to the behavior observed here. Other authors highlight the role played by helicity in the transfer process and show that 2D and 3D properties coexist naturally in all flows of nature [52]. The authors also share the general conclusion that these behaviors are not so deeply known and that more studies need to be developed in this regard. Some of the possible research avenues they propose are to investigate the interactions between 2D vortical modes and 3D potential modes, as well as to further investigate the role of helicity. These aspects go beyond the objectives of the thesis, however it is a phenomenon to be highlighted.

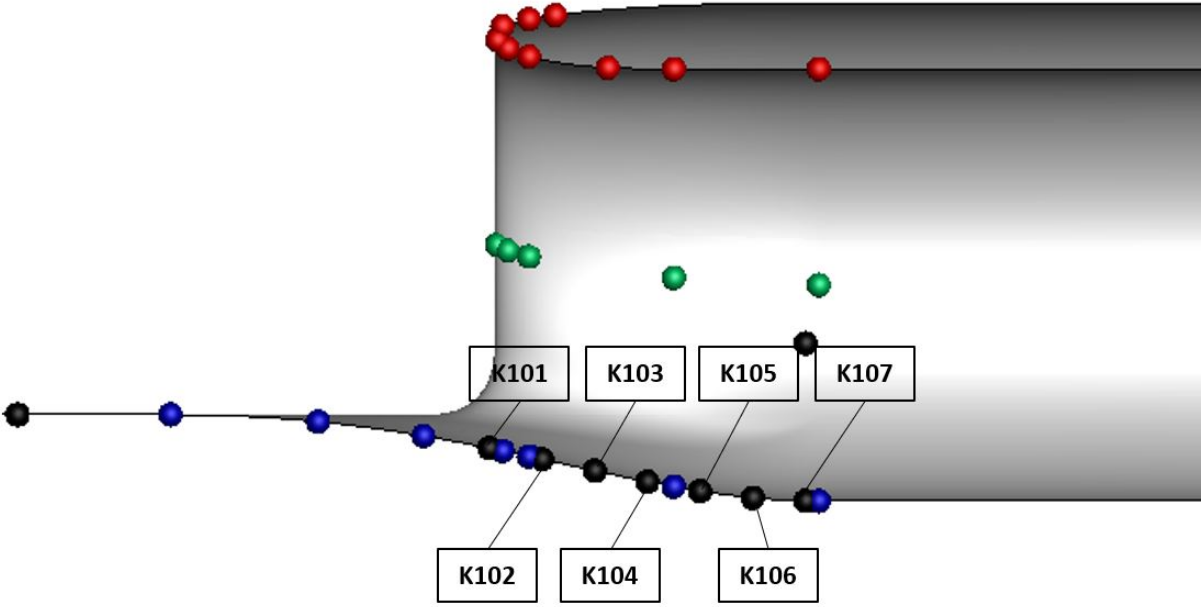


Figure 3.25: Kulite locations

Downstream, from k107, the plot seems more consistent along mass flow rate values; it should be emphasized that within boundary layer predominate local and characteristic effects of turbulence such as small-scale anisotropy and significant direct energy transfer between large- and small-scales. By advancing on ramp it can be seen that behavior approaches theory probably due to evolution of specific anisotropy in turbulence to more isotropic behavior. For high mass flow rate values, the aeroacoustics phenomena placed on the spectrum between 25-65Hz can be observed over the PSD plot. These phenomena cannot be fully identified due to the lack of other experimental measures. Probably the numerical analysis will allow to deepen a little more.

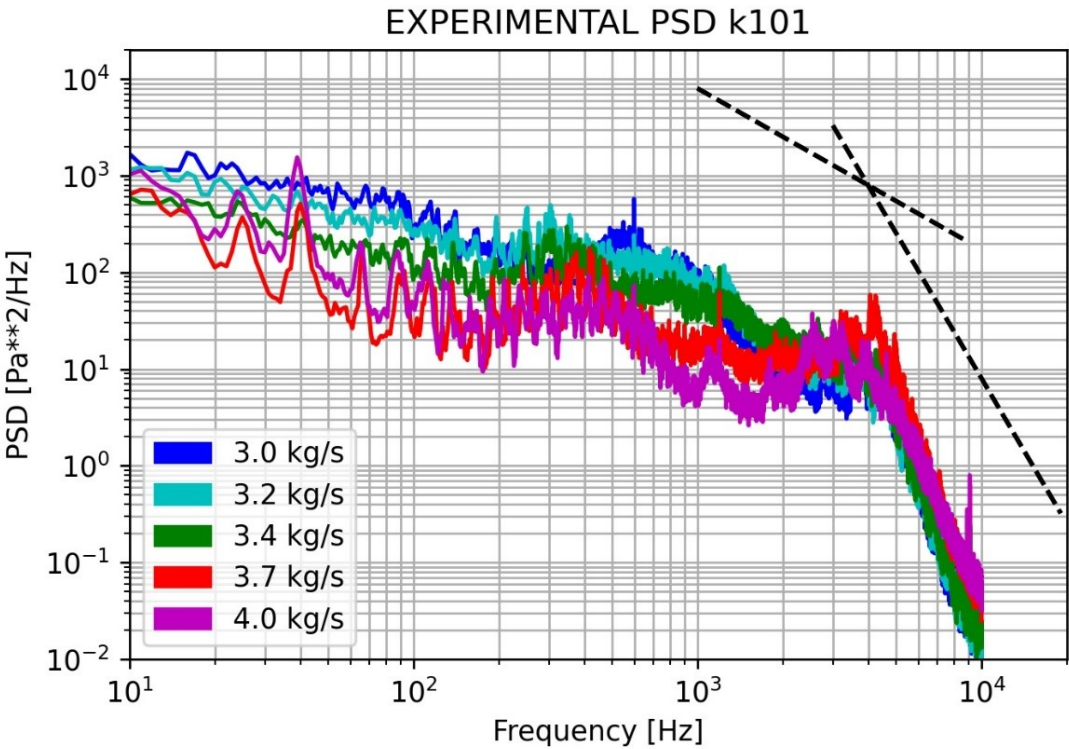


Figure 3.26: (a) k101

Figure 3.27: PSD of Kulite sensors on the intake ramp.

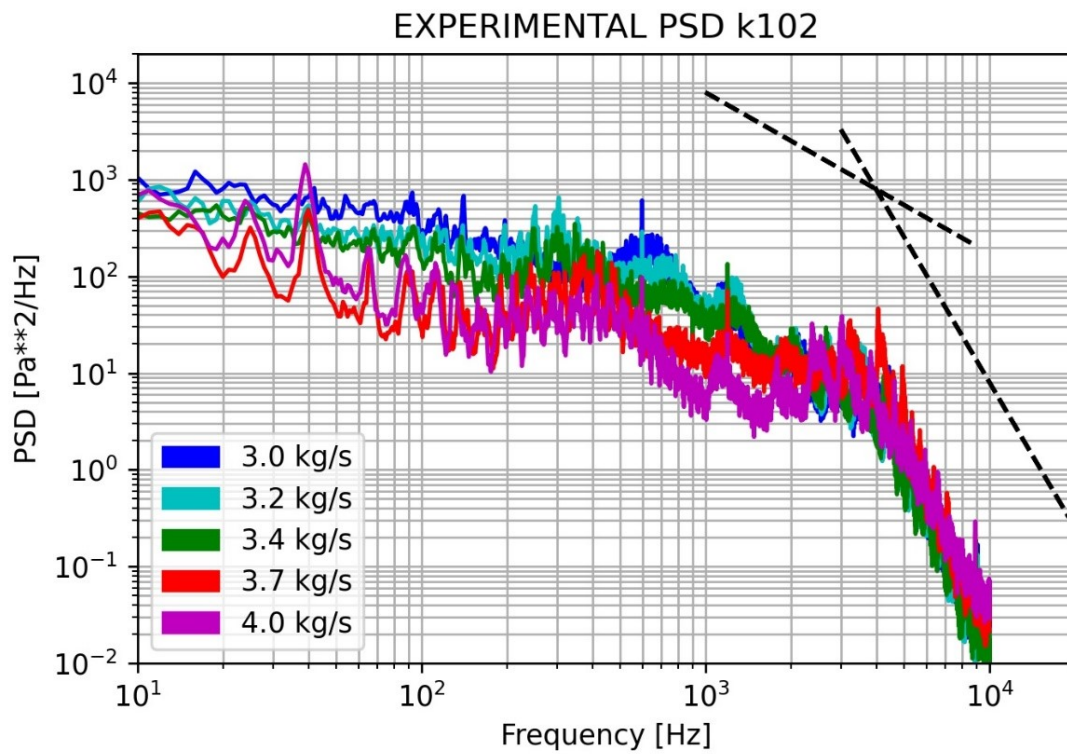


Figure 3.27: (b) k102

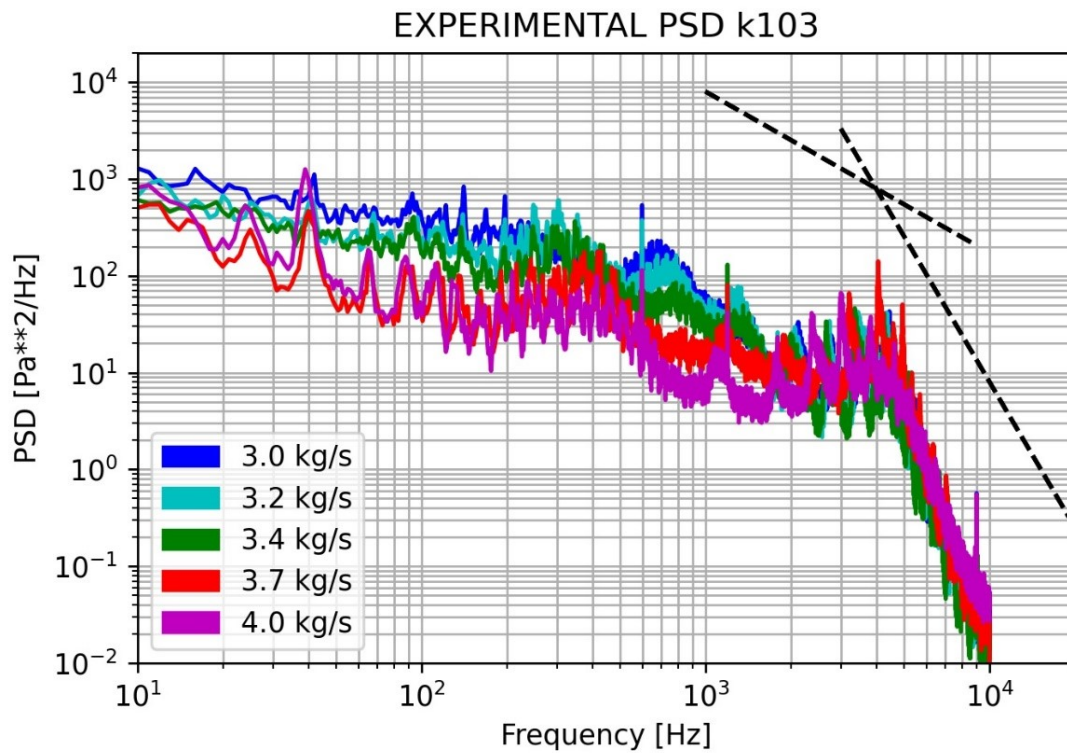


Figure 3.28: (c) k103

Figure 3.29: PSD of Kulite sensors on the intake ramp. (cont.)

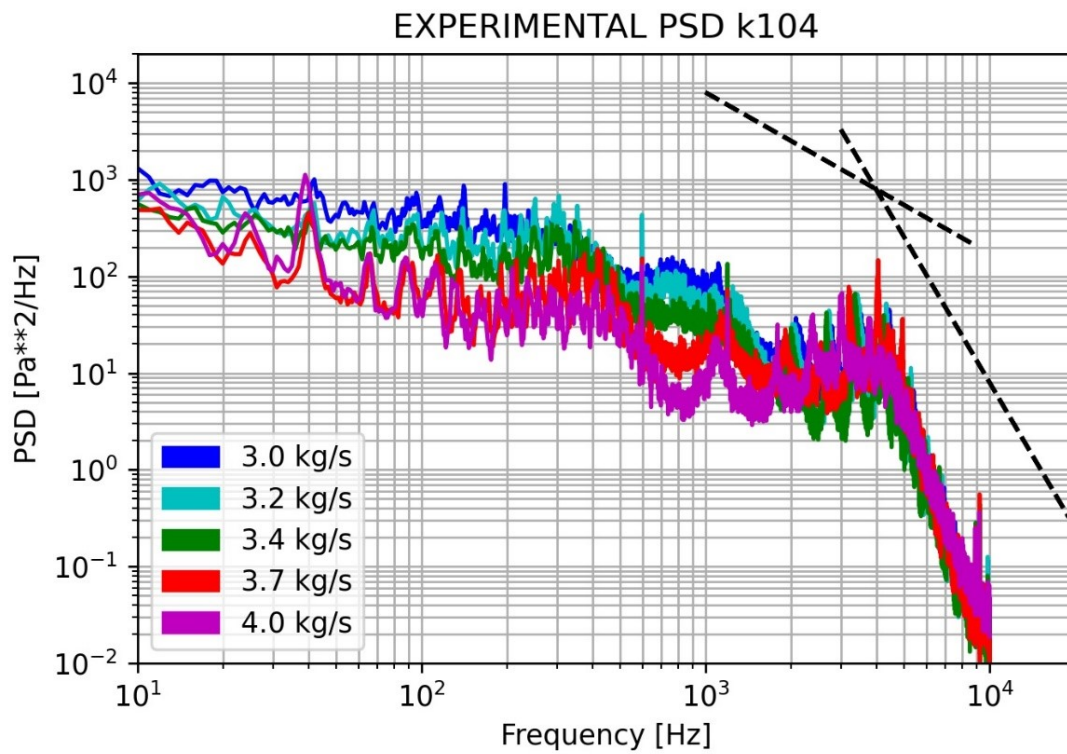


Figure 3.29: (d) k104

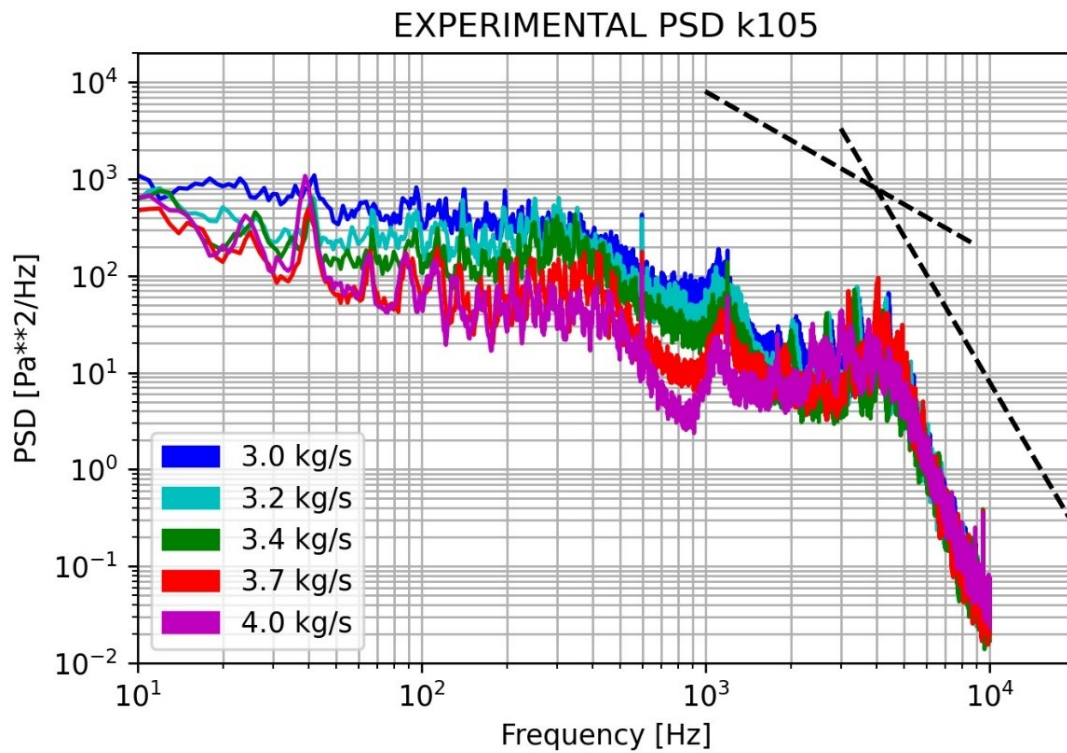


Figure 3.30: (e) k105

Figure 3.31: PSD of Kulite sensors on the intake ramp. (cont.)

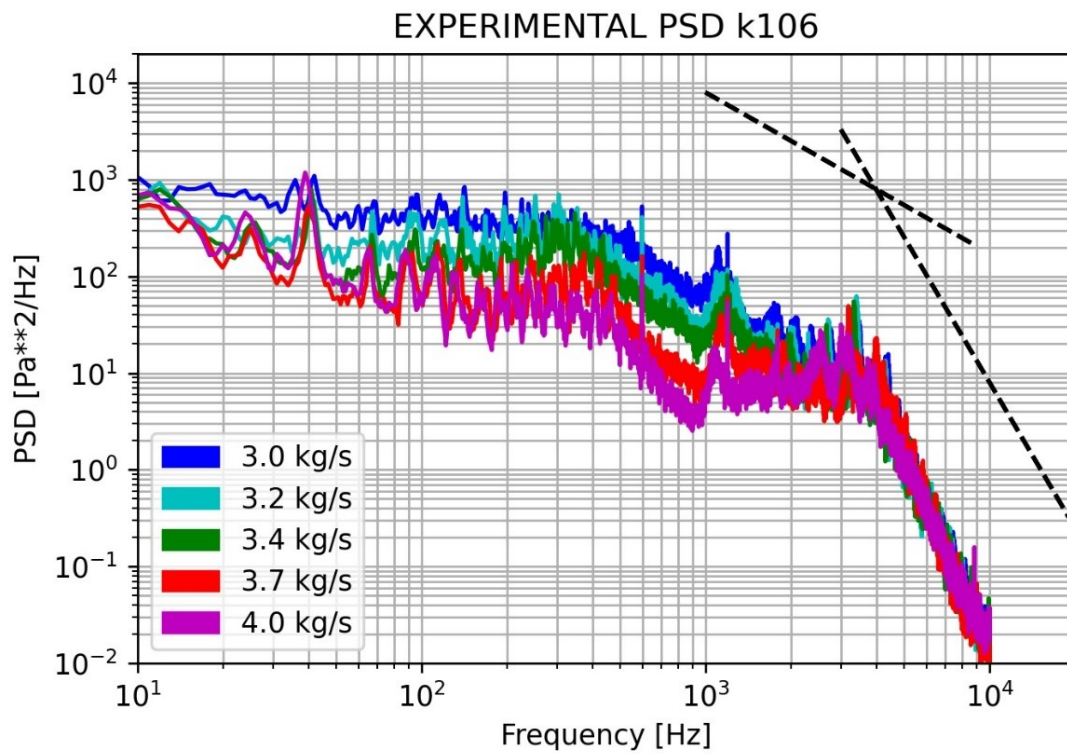


Figure 3.31: (f) k106

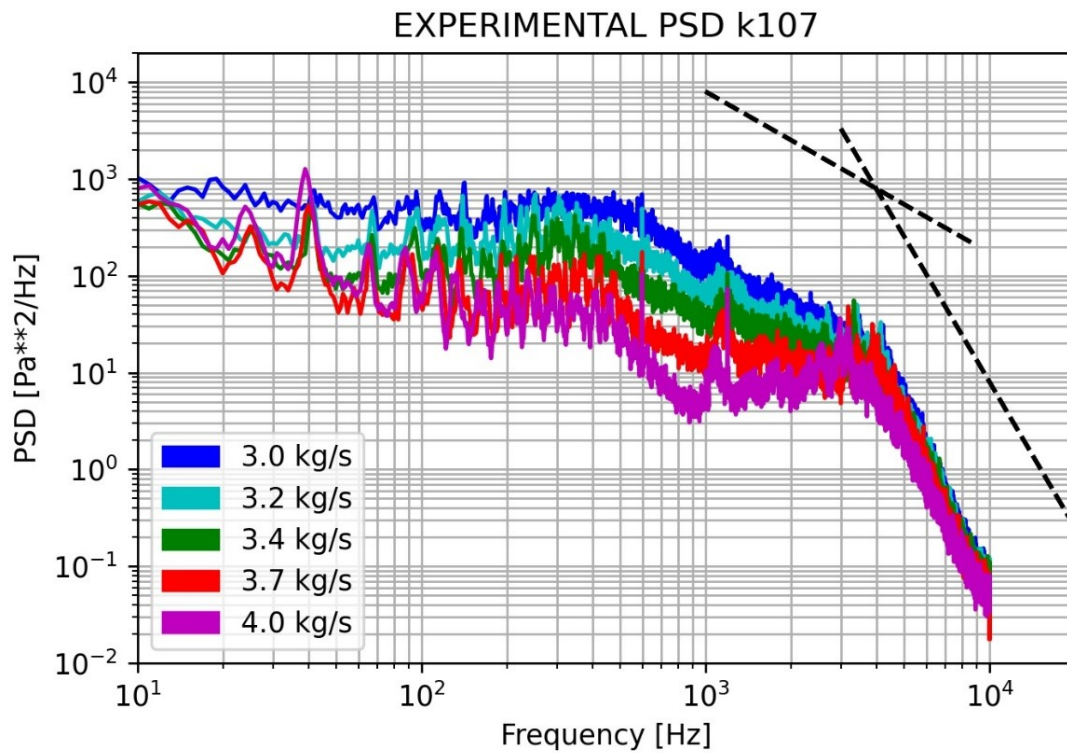


Figure 3.32: (g) k107

Figure 3.33: PSD of Kulite sensors on the intake ramp. (cont.)

3.6 Top-nacelle analysis

In this section, the pressure taps from PS104 to PS109 are analyzed. On the upper side of the nacelle, the behavior is similar to the ramp. As expected, the pressure increases when the velocity of flow ingested decrease. On this part of the nacelle, there is no flow separation. Figure 3.34 shows wall pressure distribution for mass flow rate values from $3.0 \text{ kg}\cdot\text{s}^{-1}$ to $4.0 \text{ kg}\cdot\text{s}^{-1}$. The C_p exhibits values exceeding unity due to compressibility effects. Notably, the most elevated C_p values are localized around the stagnation line. The mass flow rate significantly impacts the pressure distribution across the nacelle. Typically, this distribution undergoes variation as the mass flow rate fluctuates. However, precise determination of the stagnation line position remains challenging with experimental data, primarily due to the discretization of pressure sensors along the nacelle wall.

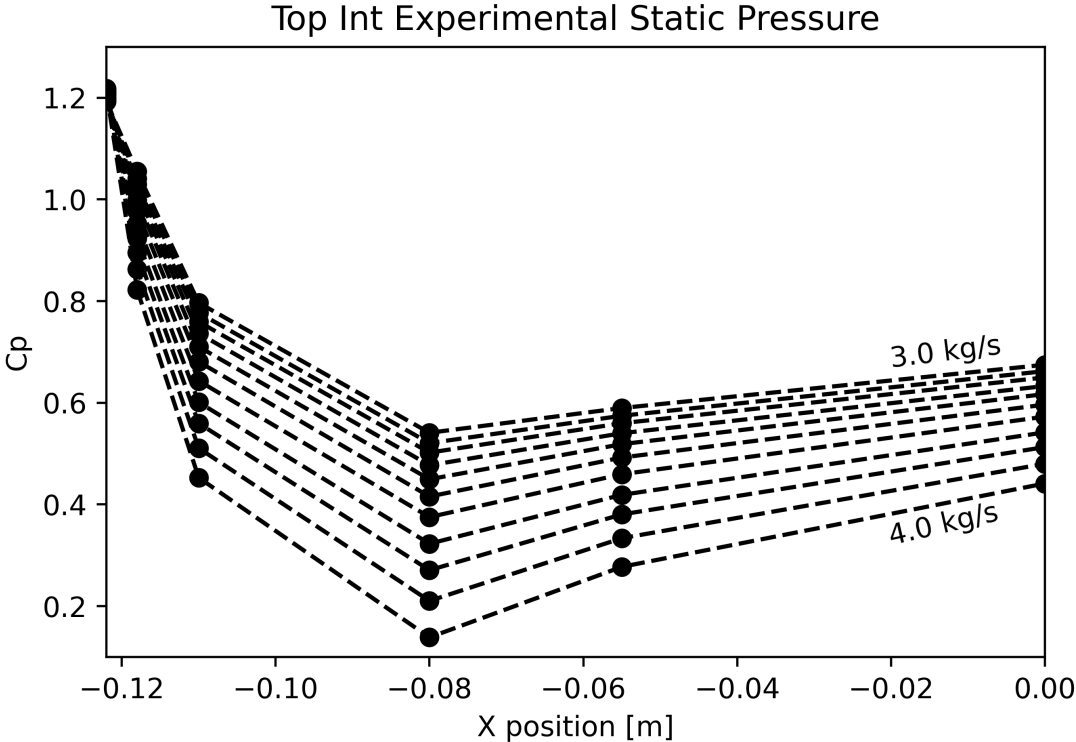


Figure 3.34: Cp distribution over the top-nacelle

3.7 Side-nacelle analysis

In this section the lateral sides of the nacelle are analysed. PS119 to PS124 and PS125 to PS130 describe the static pressure at left and right side respectively. Figures 3.35 and 3.36 show the evolution of Cp curve from a mass flow rate of $3.0 \text{ kg}\cdot\text{s}^{-1}$ to $4.0 \text{ kg}\cdot\text{s}^{-1}$. Like all other interior surfaces of the intake, the Cp value tends to decrease when the MFR increases.

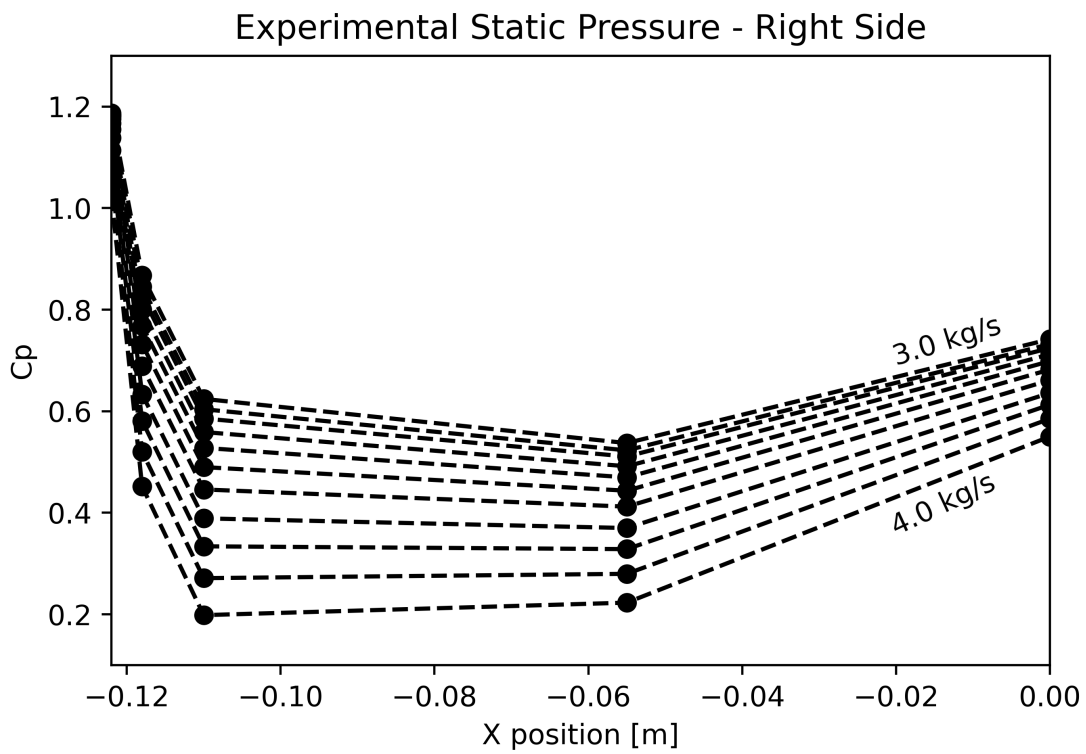


Figure 3.35: C_p distribution over the right-side of the nacelle.

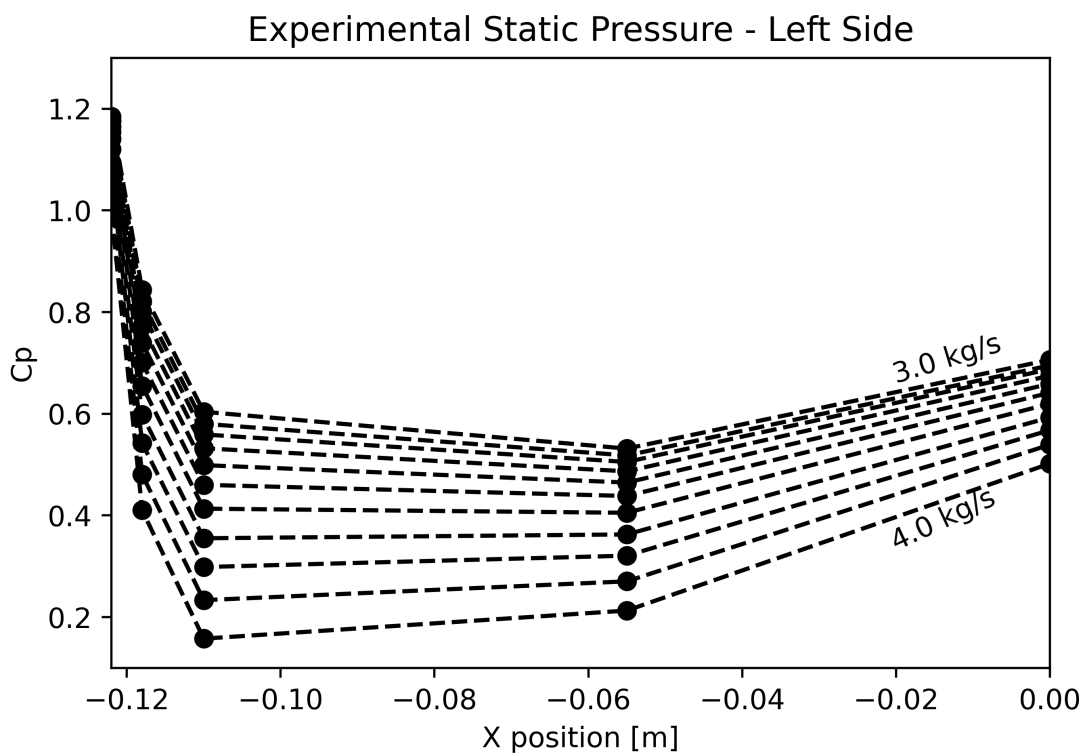


Figure 3.36: C_p distribution over the left-side of the nacelle

The experimental conditions chosen have a zero angle of sideslip. However, there is a slight offset between the right and left experimental curves, indicating that the conditions are not symmetrical. The physical phenomenon that generates this sideslip angle has not been fully identified in this analysis. Nevertheless, other experiences in the same wind tunnel have reported a similar phenomenon. For now, the analysis has been limited to estimating the apparent sideslip angle.

Figures from 3.37 to 3.39 show the curves obtained by numerical simulations. In all cases, the standard Spalart-Allmaras model is used, with a mass flow rate of $4.0 \text{ kg}\cdot\text{s}^{-1}$ and a sideslip angle between 0.25° and 1° . Analyzing the plots shows that the PS122 and PS128 sensors tend to give the same result even if the sideslip angle changes. Sensors located at values less than $x=5$ tend to be much more sensitive to small changes in sideslip angle. A qualitative comparison of the plots shows an apparent angle of sideslip in the experimental results of approximately 0.5° . This is based on the difference between both sides, as shown in Figure 3.38. This comparative analysis focuses exclusively on the disparity between the left and right curves, considering both numerical and experimental data. Generally, the numerical solution derived from the SA model exhibits C_p values that are marginally higher than those observed experimentally. A more detailed examination of these differences will be undertaken in subsequent chapters.

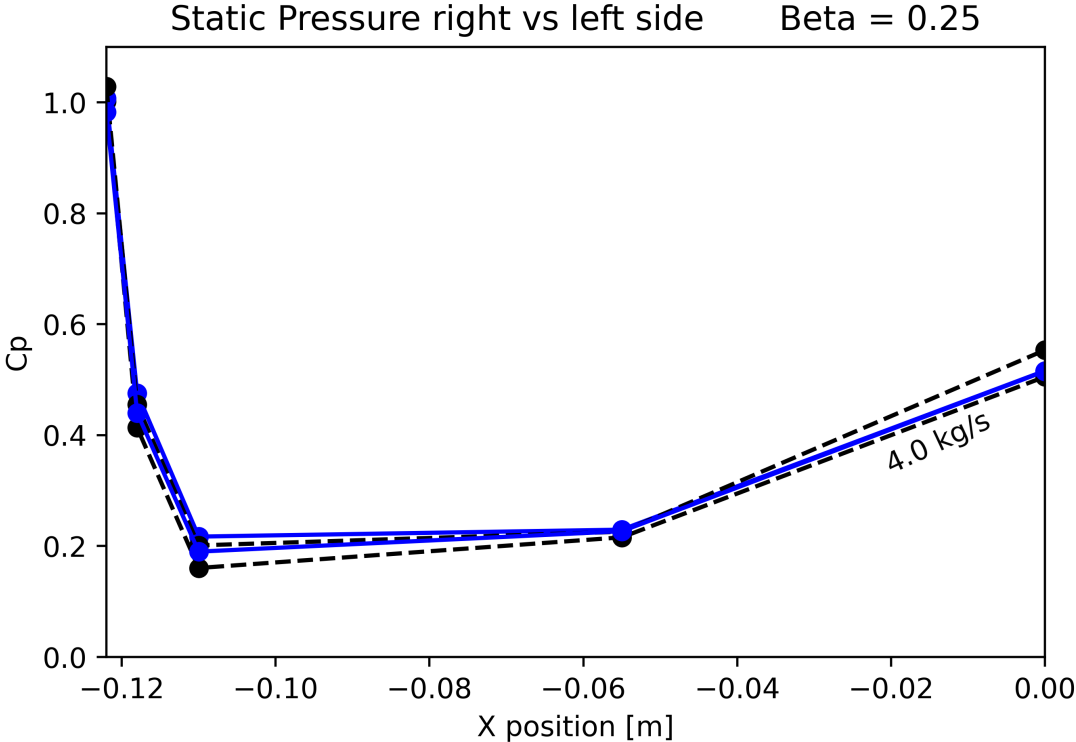


Figure 3.37: Sideslip comparison. $\beta = 0.25^\circ$

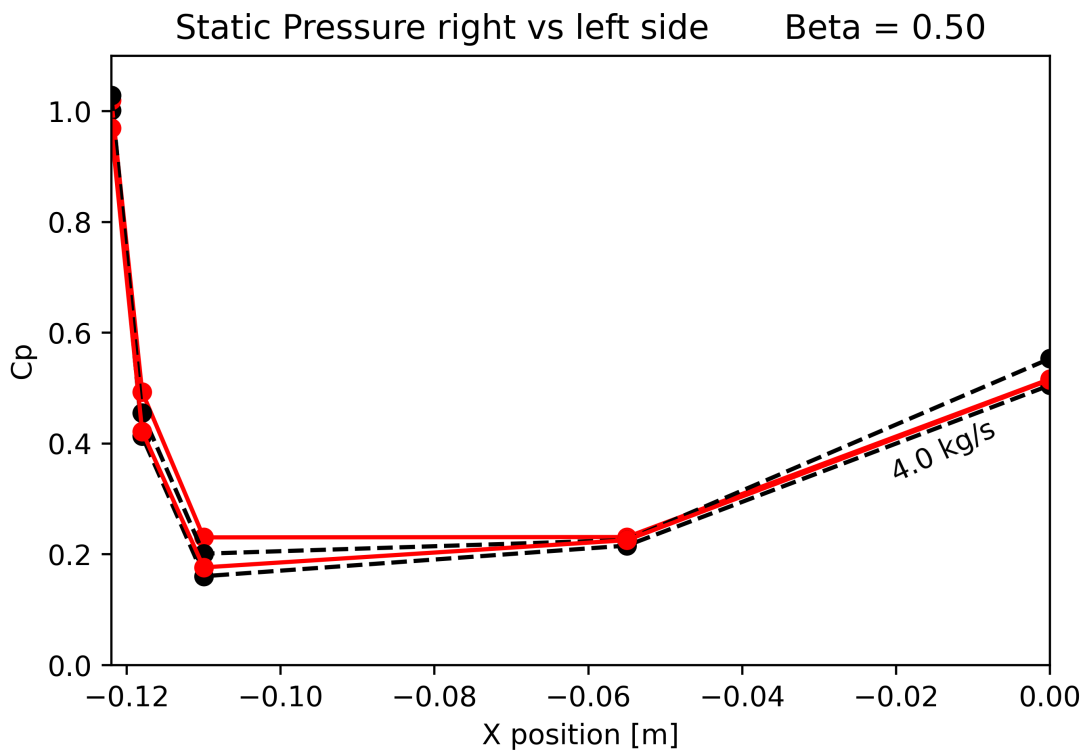


Figure 3.38: Sideslip comparison. $\beta = 0.5^\circ$

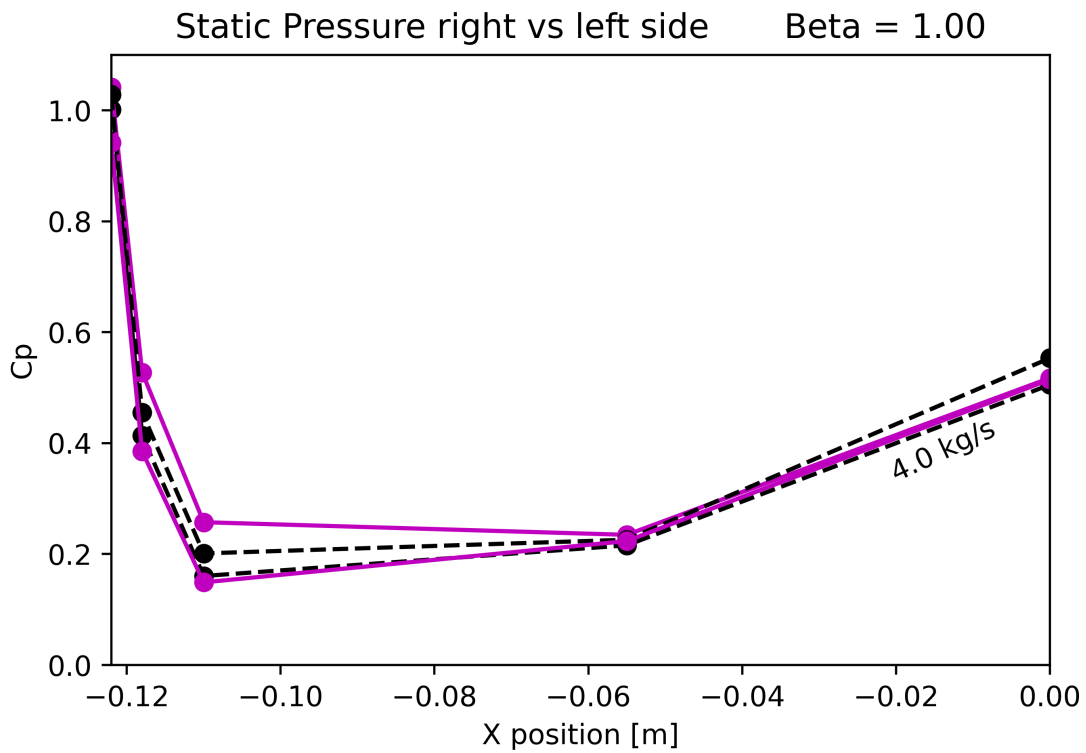


Figure 3.39: Sideslip comparison. $\beta = 1^\circ$

3.8 Rake analysis

3.8.1 Mean values analysis

The aim of this analysis is to examine the effects of boundary layer ingestion on the aerodynamic performance of the fan, especially the distortion at the Aerodynamic Interface Plane (AIP). To measure these effects, a multi-arm rake probe, depicted in figures 3.6 and 3.7, is employed. This rake has 8 arms and 5 rings, each with multiple pressure sensors. The radius of each ring is: $R1 = 77.76$ mm, $R2 = 68.51$ mm, $R3 = 57.56$ mm, $R4 = 44.54$ mm, $R5 = 25.10$ mm. The rake can be rotated by 22.5° to increase the number of measuring points for each radius and to capture the azimuthal variation of the flow.

Figure 3.40 shows the experimental values of the total pressure ratio P_i/P_{i0} at the AIP for different mass flow rates. P_{i0} is the total pressure at free stream conditions. In all cases, the upper half of the AIP is unaffected by the boundary layer thickening or a potential flow separation due to the unfavorable pressure gradient along the suction side of the duct. Furthermore, a common pattern observed is that the azimuthal region with total pressure loss is consistent across all mass flow rates. This region is located at the bottom, between 200° and 340° . Other authors have obtained similar experimental results [53]. Their results show symmetric flows in the x-z plane. They show a large region of streamwise flow separation which occurs within the duct. Duct curvature induced strong pressure driven secondary flows, which evolve into a large pair of counter-rotating vortices. These vortices convect the low momentum fluid of the boundary layer towards the center of the duct, degrading both the uniformity and magnitude of the total pressure profile. The ingestion of the boundary layer also causes a total pressure loss at the AIP regardless of the presence or absence of flow separation. As expected, the affected region is larger for cases where the flow is likely to be separated, extending to the most inner radii. For cases where the flow could be attached, the most external radii are more impacted by the pressure loss. The total pressure loss zone is more uniformly distributed for low mass flow rates, while it is more concentrated for high mass flow rates.

A similar pressure distribution is shown by other authors, obtained both experimentally [53] and numerically [54] [55]. A possible explanation for this phenomenon is that flow separation induces more energy exchange between the recirculation zone and the free stream due to mixing and turbulence. Conversely, when the flow is attached, there is less energy exchange and the total pressure loss tends to be confined to the boundary layer. In this case, the total pressure gradients are stronger and cause more adverse effects on the fan performance.

Figures 3.41 show the total pressure curves, normalized by P_{i0} , along azimuthal positions for different radial region. The total pressure profiles are not usually presented in the literature, however in the following chapters it will be of great importance when comparing the ability of each turbulence model to predict flow behavior, mainly its effect on the AIP.

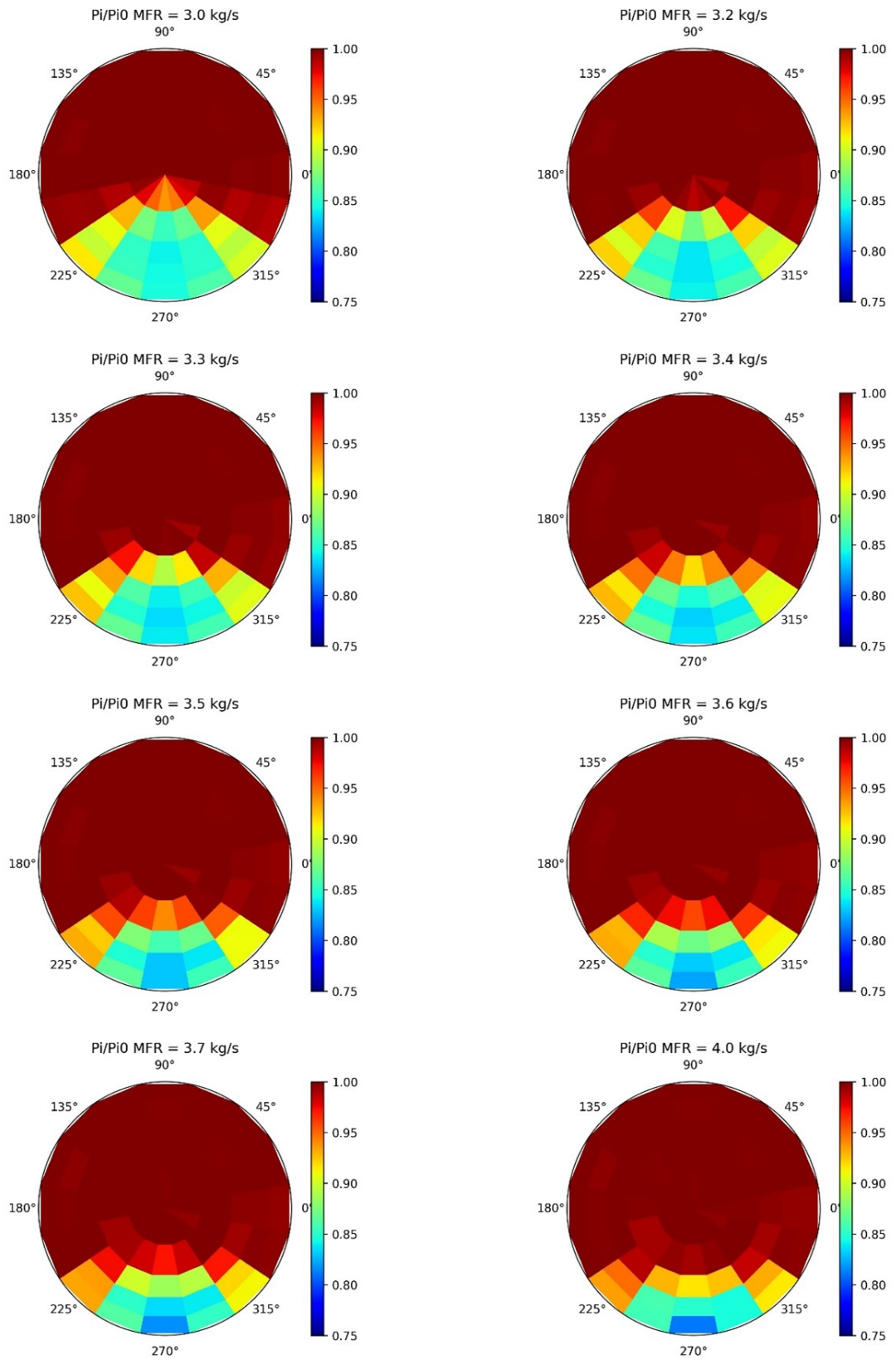


Figure 3.40: Total pressure loss at fan face for various mass flow rate values

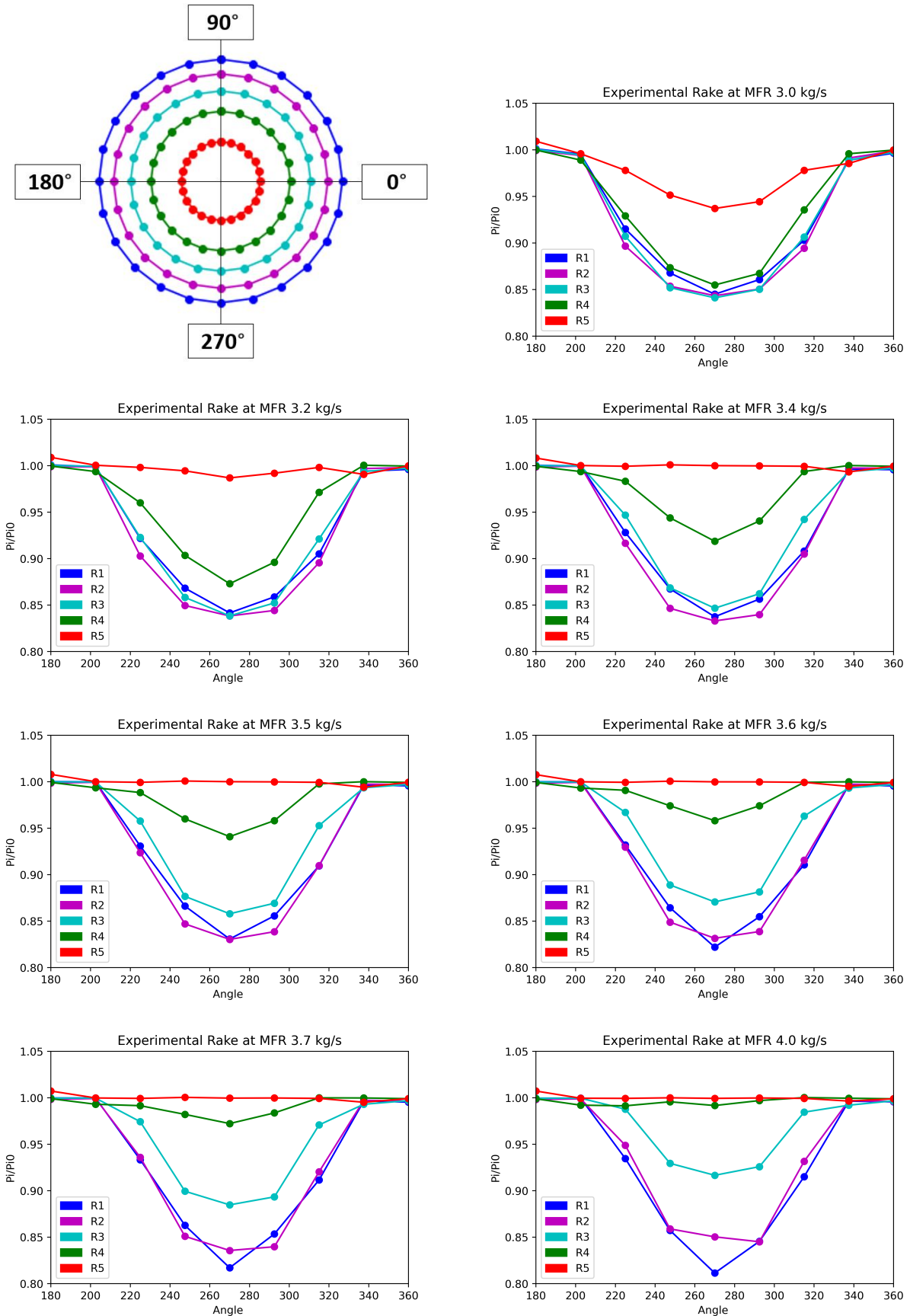


Figure 3.41: Distribution of the total pressure at the lower half of the fan face was investigated for different values of the mass flow rate.

3.8.2 Unsteady analysis

The same analysis is performed for the rake. The arms 3 and 7, located at the symmetry plane, are examined. The sampling frequency is identical to the kulites on the intake ramp. Figure 3.47 displays statistics computed for different mass flow rates.

There is a noticeable difference between the physics described by arm 3 and arm 7. The former is mainly situated in a region that is not affected by the total pressure loss due to boundary layer growth or potential flow separation. The mean value obtained by these sensors remains constant across all mass flow rates, indicating no influence. The standard deviation behaves similarly, with a slightly higher value at $3.2 \text{ kg}\cdot\text{s}^{-1}$. The skewness and kurtosis are close to zero for all points, except for point 3.5 when the mass flow rate is below $3.2 \text{ kg}\cdot\text{s}^{-1}$. In this case, both values increase, possibly influenced by the shear layer or flow separation.

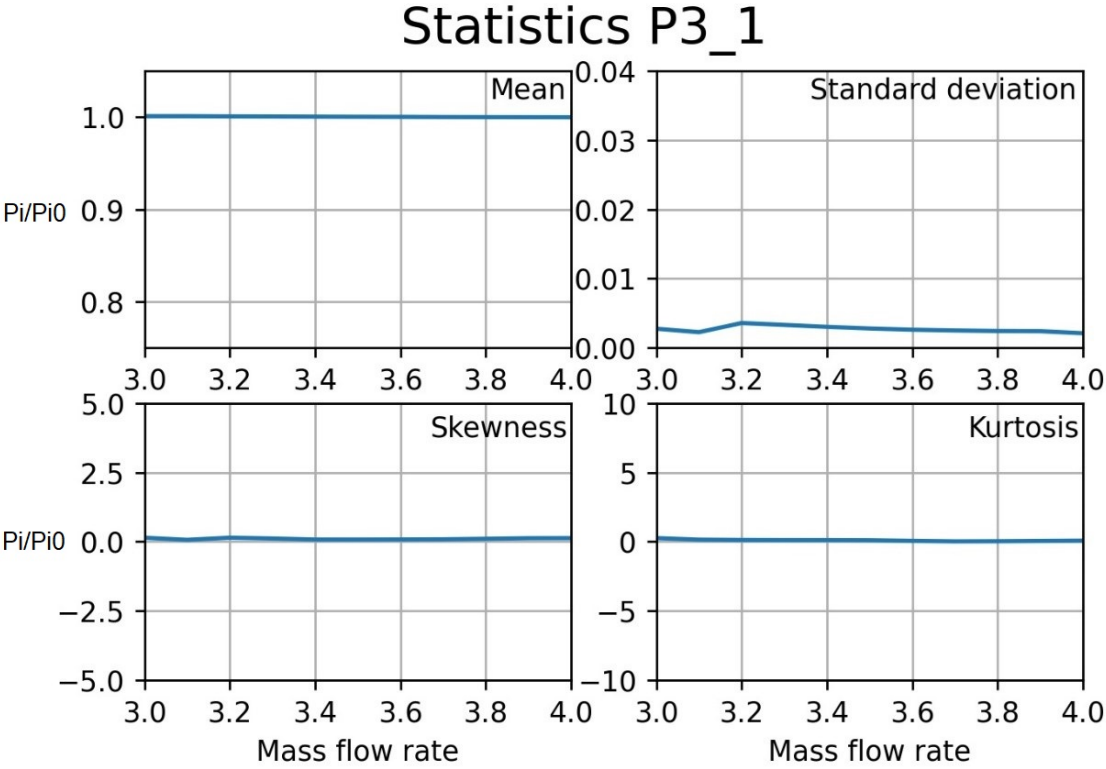


Figure 3.42: (a) Rake Sensor. Arm 3, point 1

Figure 3.43: Statistical analysis of rake sensors as function of mass flow rate.

Statistics P3_2

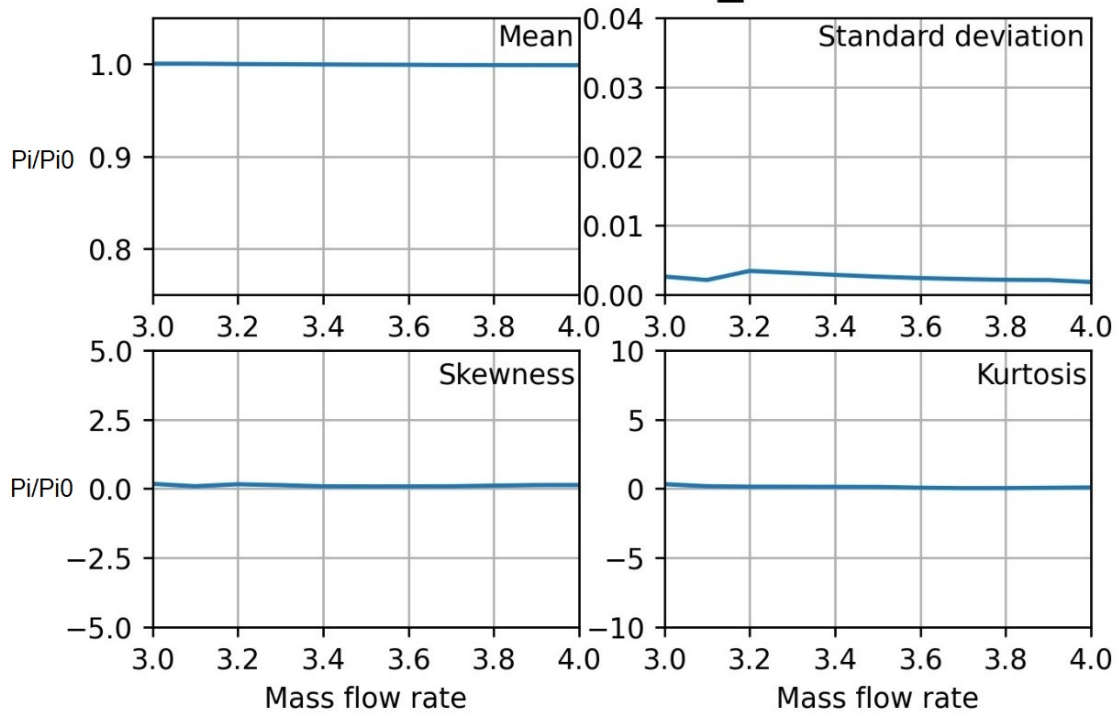


Figure 3.43: (b) Rake Sensor. Arm 3, point 2

Statistics P3_3

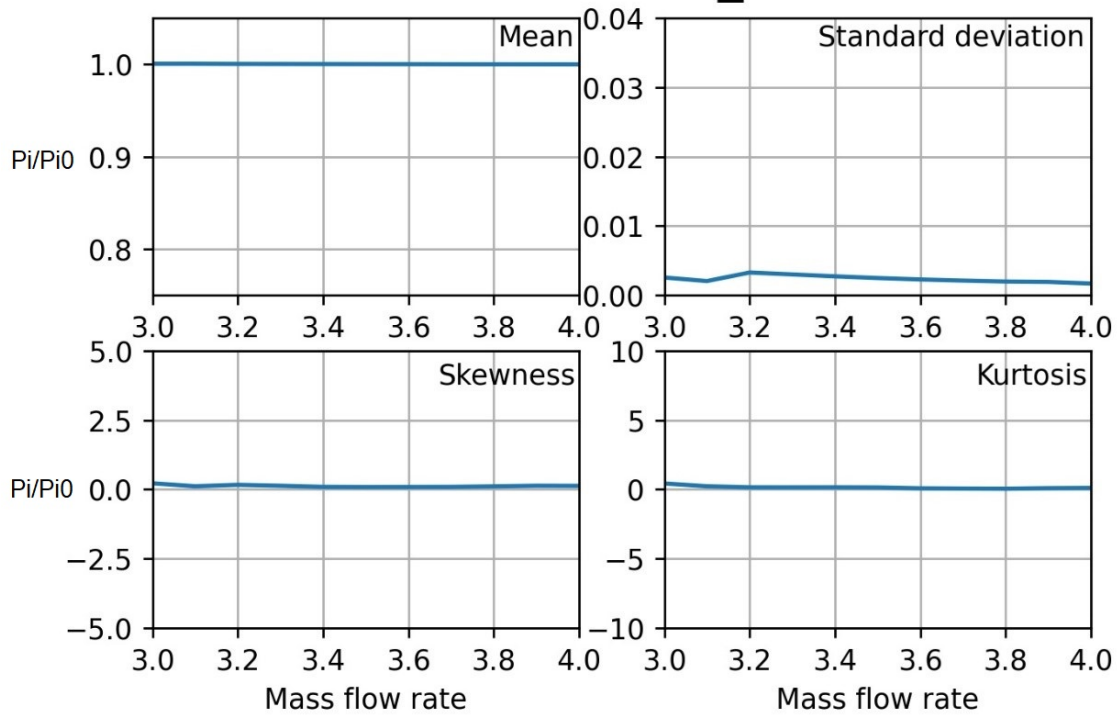


Figure 3.44: (c) Rake Sensor. Arm 3. point 3

Figure 3.45: Statistical analysis of rake sensors as function of mass flow rate. (cont.)

Statistics P3_4

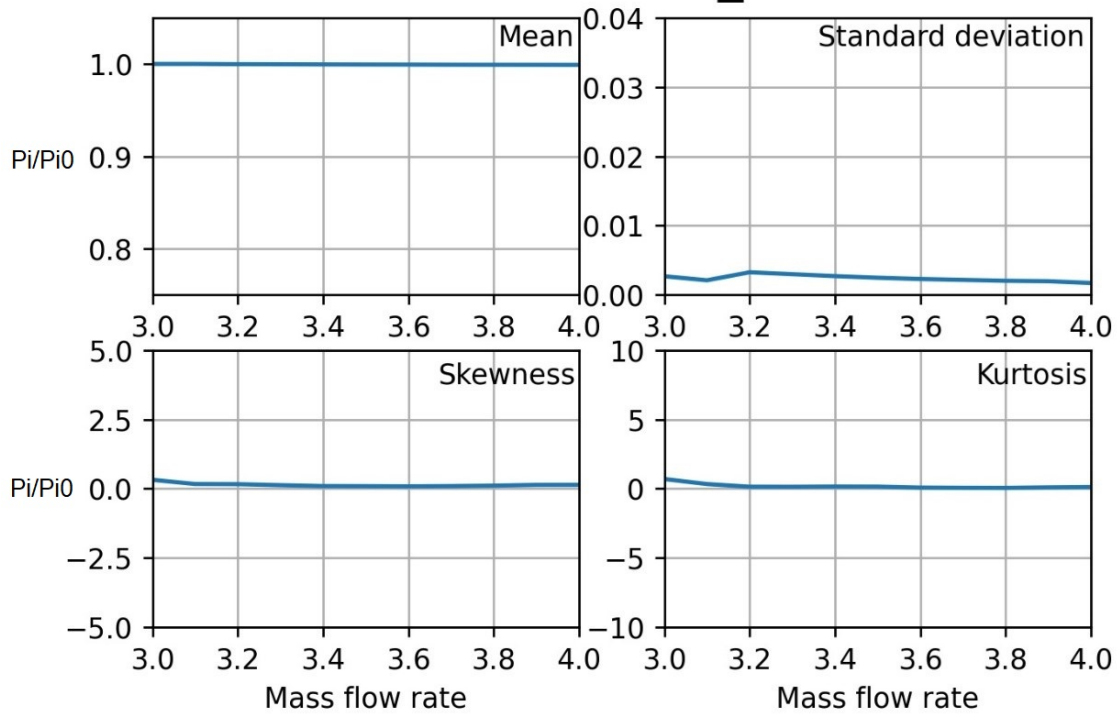


Figure 3.45: (d) Rake Sensor. Arm 3, point 4

Statistics P3_5

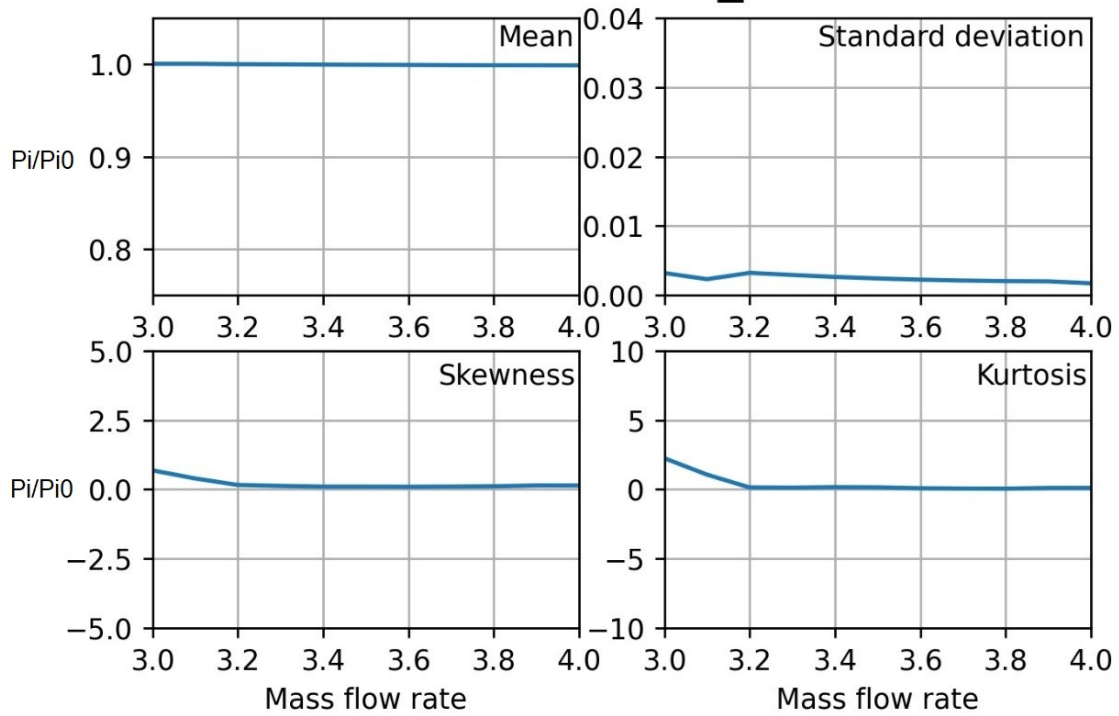


Figure 3.46: (e) Rake Sensor. Arm 3, point 5

Figure 3.47: Statistical analysis of rake sensors as function of mass flow rate. (cont.)

Arm 7 exhibits a distinct behavior from the previous case, as it is directly influenced by the total pressure loss and flow separation. The main statistical characteristics for these signals are displayed in Figure 3.53. The sensor in the most internal position experiences a reduction in the mean value of the total pressure at low mass flow rates. The lower the sensor, the more it is affected by the total pressure loss. For point P7_2, its value changes slightly, even at high mass flows. For point P7_1, the mean of the total pressure decreases with increasing mass flow, indicating a more concentrated loss of total pressure in the lower part. This is evident in figure 3.40.

The standard deviation can provide insights into the region where each sensor is located for a given mass flow rate. The highest values of the standard deviation occur in the shear layer. When the measurement is taken outside the shear layer and any recirculation zone, the typical values of the standard deviation are less than 0.005. This behavior is only observed for point P7_5, which is far enough from the ramp to not be affected by the shear layer or flow detachment. Moreover, for standard deviation values of around 0.01, it can be assumed that the measurements are taken in a recirculation zone or a region directly affected by boundary layer thickening, observed for point P7_1.

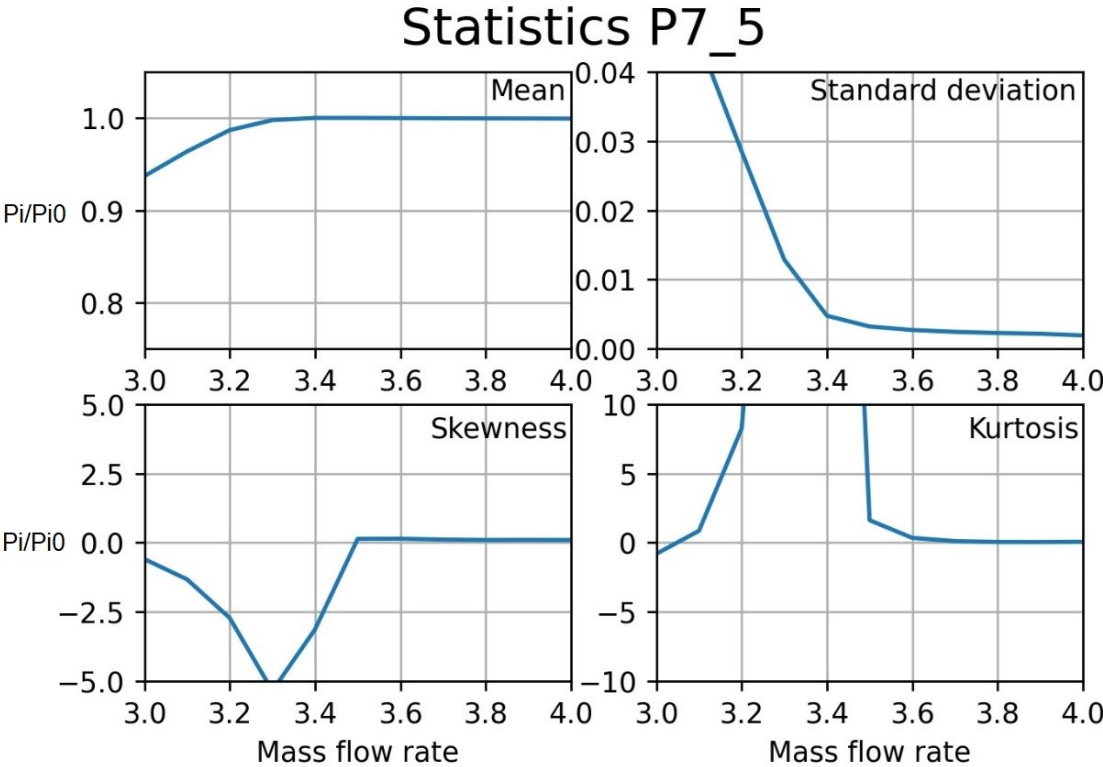


Figure 3.48: (a) Rake Sensor. Arm 7, point 5

Figure 3.49: Statistical analysis of rake sensors as function of mass flow rate.

Statistics P7_4

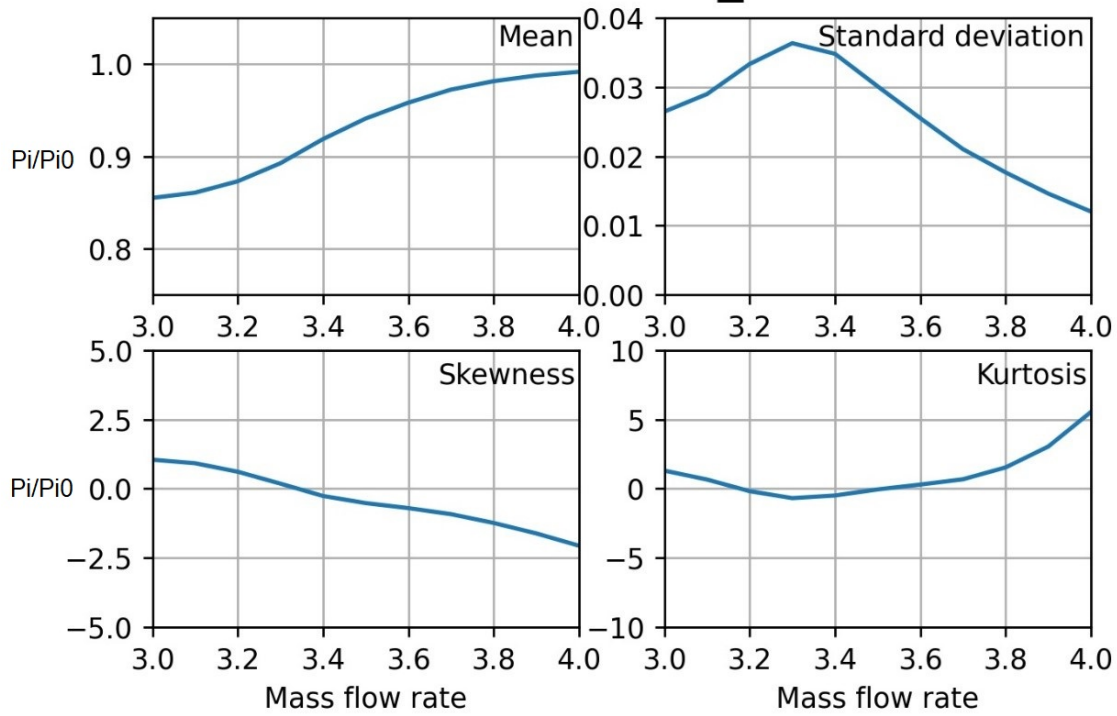


Figure 3.49: (b) Rake Sensor. Arm 7, point 4

Statistics P7_3

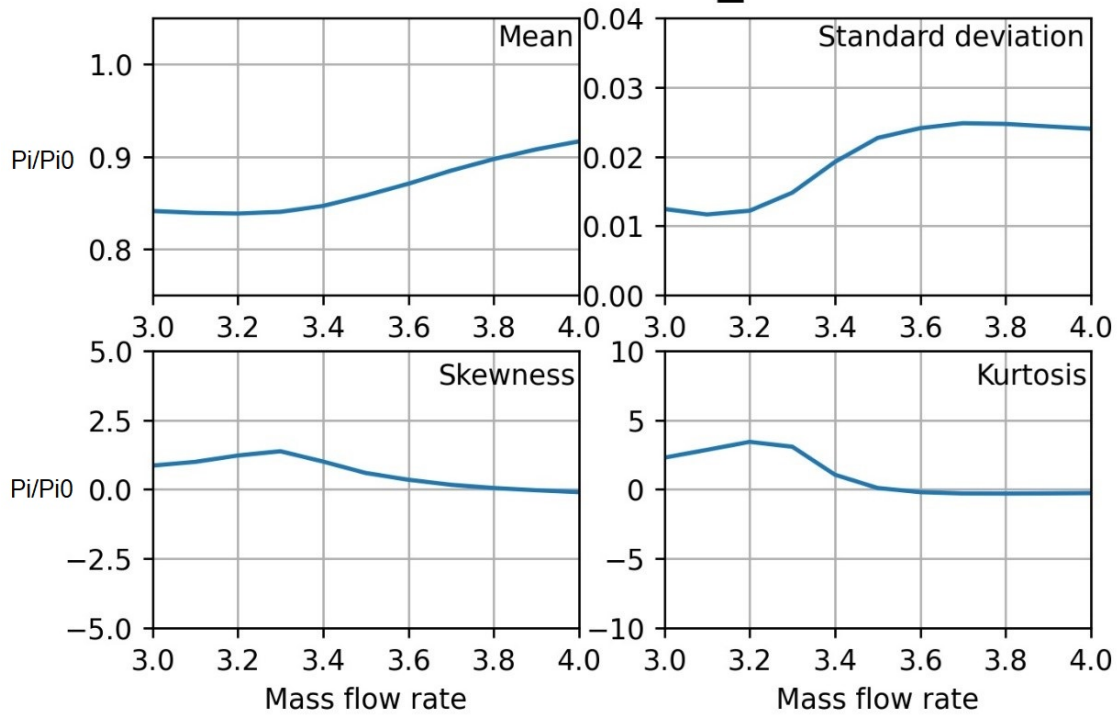


Figure 3.50: (c) Rake Sensor. Arm 7. point 3

Figure 3.51: Statistical analysis of rake sensors as function of mass flow rate. (cont.)

Statistics P7_2

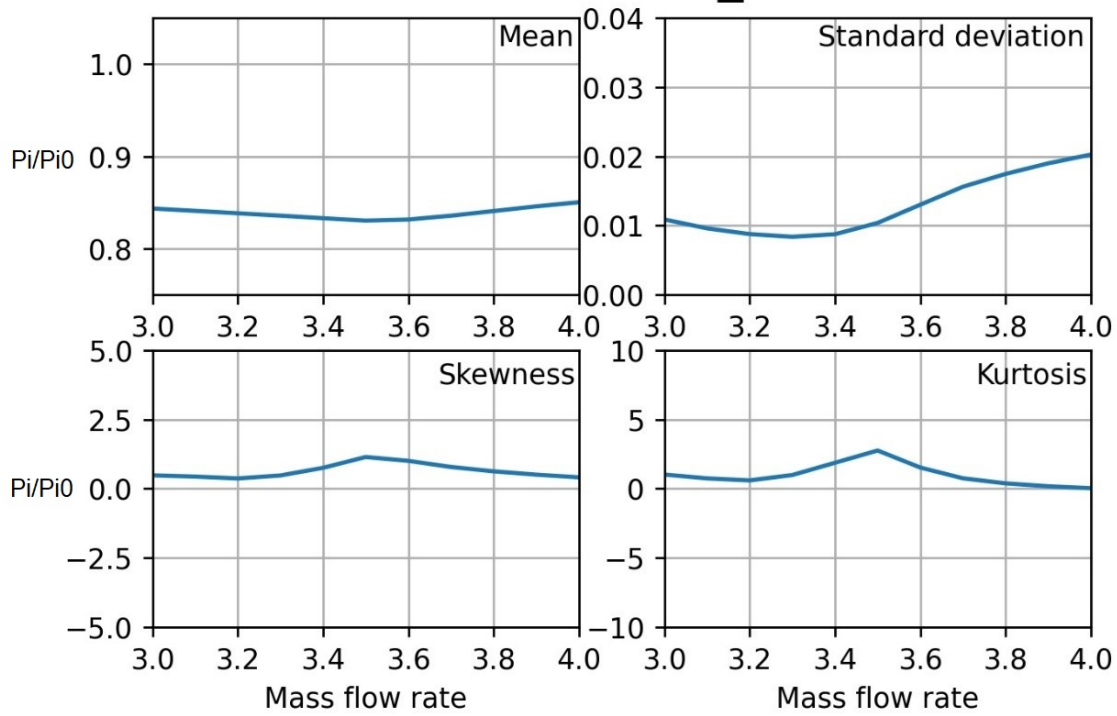


Figure 3.51: (d) Rake Sensor. Arm 7, point 2

Statistics P7_1

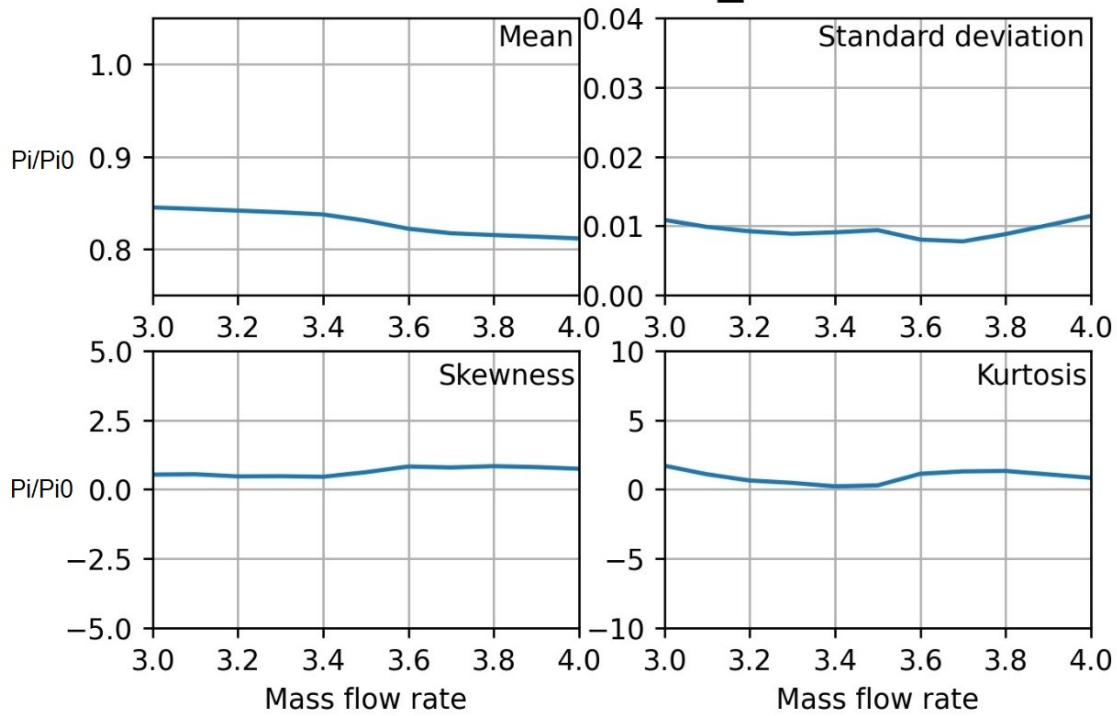


Figure 3.52: (e) Rake Sensor. Arm 7, point 1

Figure 3.53: Statistical analysis of rake sensors as function of mass flow rate. (cont.)

Skewness and kurtosis vary considerably across different sensors. For point P7_5, high values of skewness and kurtosis are observed at low mass flow rates, similar to point P3_5, indicating some effect caused by the shear layer. The skewness value tends to be negative when the sensor is situated in a boundary region between the unaffected flow and the shear layer, as shown by point P7_5 and part of P7_4. This implies that the signal has sharp and short-lived troughs. Conversely, when the measurement is taken in a recirculation zone or the shear layer, skewness values are slightly positive. Kurtosis tends to be very high in the shear layer and moderately positive in a recirculation area.

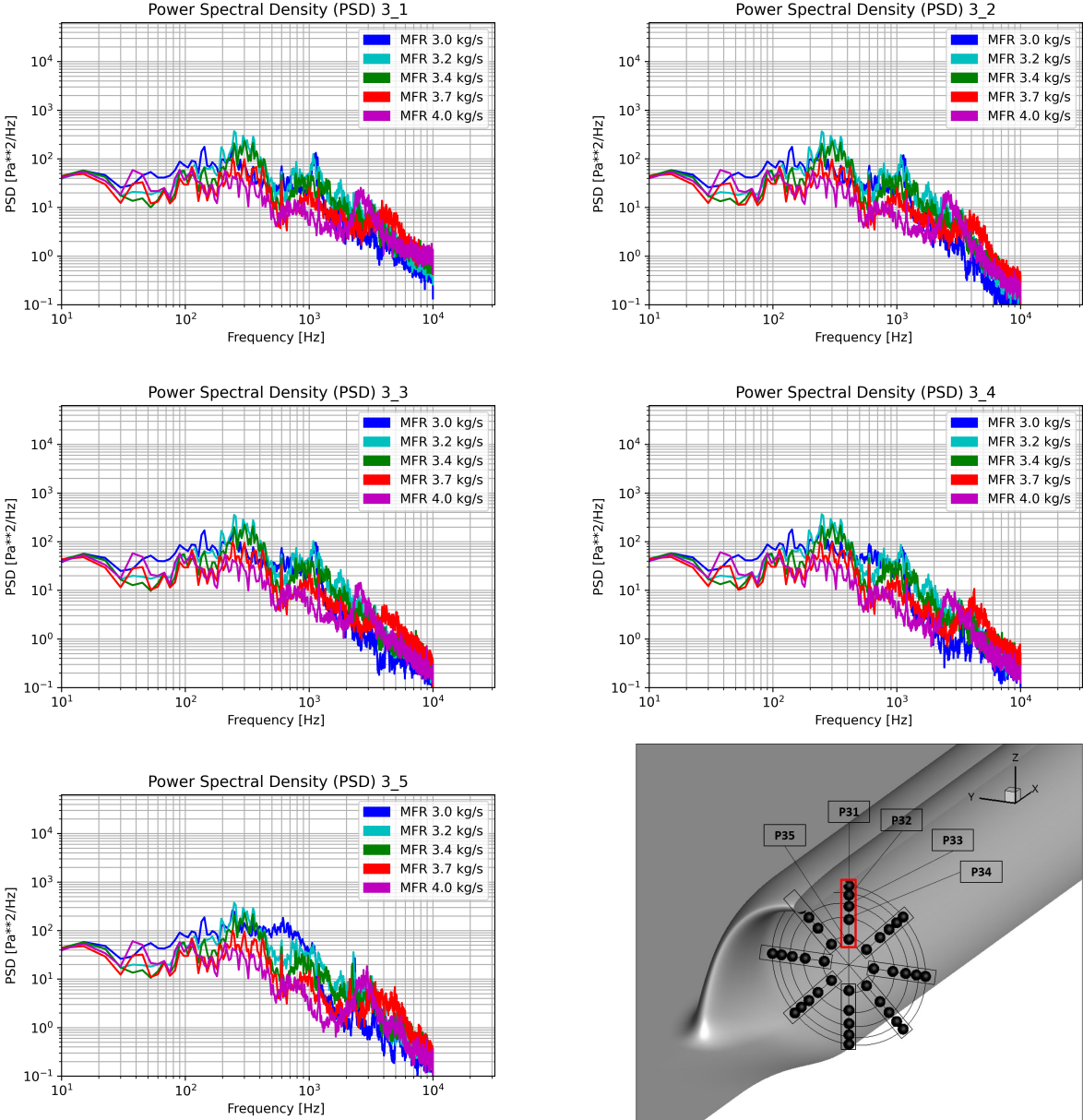


Figure 3.54: Power Spectral Density of arm 3 calculated for various mas flow rate values.

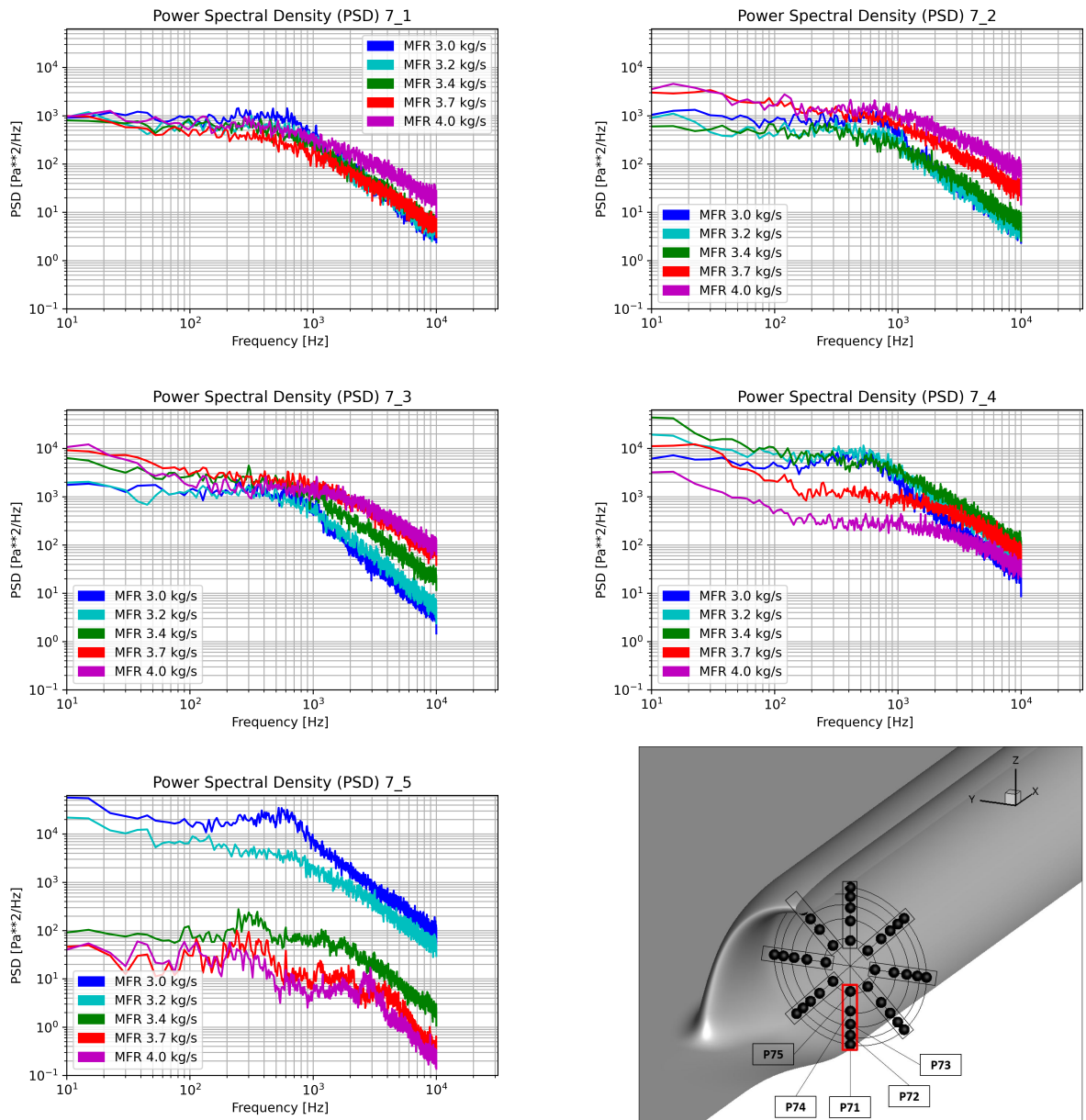


Figure 3.55: Power Spectral Density of arm 7 calculated for various mas flow rate values.

Figures 3.54 and 3.55 illustrate the calculated PSD for these sensors. As expected, the sensors located in arm 3 exhibit a lower turbulent kinetic energy than those in arm 7. Other authors have also observed this behavior [56] [57], the amount of turbulent kinetic energy increases when the measurement is taken within the shear layer. This difference is evident when we observe that the power density at low frequencies varies by an order of two with respect to the arm located in the recirculation zone. In general, it can be observed that all the plots, regardless of the location or mass flow rate at which the measurement was taken, tend to follow a slope of $-5/3$, which is consistent with the prediction in energy cascade theory as shown in Figure 3.23. The behavior of the signals also varies depending on the arm. For arm 3, behavior is highly influenced by acoustic phenomena. In arm 7, it can be seen that behavior is primarily driven by the development of turbulent structures generated by the thickness of the boundary layer, recirculation zone or shear layer. The latter tends to increase power density in the low power spectrum as can be seen in plots at point P7_3, P7_4 and P7_5.

3.9 Chapter summary and conclusions

The primary objective of this chapter was to present the experimental setup and analyze the results of the BLI intake that was tested in the Onera S3Ch wind tunnel. The model geometry, experimental sensors, and test conditions were defined. The only variable in the tests is the corrected mass flow rate ingested by the intake. Mach 0.82 conditions and atmospheric pressure remain constant for all tests. On the intake ramp, it was observed that the distribution of the time-averaged C_p decreases as the corrected mass flow increases, as expected. Furthermore, this distribution changes slightly for low mass flows, particularly in sensors between $x = -0.15$ m and $x = -0.10$ m, which tend to produce C_p values that are closer together than in the case of high mass flow. The unsteady analysis of these same sensors exhibits different behaviors, including aeroacoustic phenomena, the transfer of turbulent energy, and a double slope on PSD plot. The analysis of the sensors located on the sides of the inlet shows a slight side-slip, which has been observed and estimated at 0.5° . The sensors located at the top of the nacelle show a similar behavior to those located on the intake ramp; however, the distribution changes inversely proportional to the corrected MFR, evidencing that there is no change of physical phenomena in this area. Finally, the rake placed on the fan face has been analyzed. The results show that the region affected by the total pressure loss increases with decreasing corrected MFR; however, when MFR is high there is a much stronger loss of pressure in the lower part of the boundary layer. Statistical analysis of unsteady data shows a possible separated flow in the lower half of the rake for low MFR values. The PSDs for the sensors located in the upper half of the rake exhibit aeroacoustic phenomena; on the contrary, sensors located in the lower half exhibit a high level of turbulent kinetic energy in some cases supporting hypothesis of possible flow separation.

In this chapter, pressure measurements at the wall and from the rake have been analyzed. A high possibility of flow recirculation for low corrected MFR values has been revealed. Interesting conclusions about the distribution of total pressure loss in the AIP have been collected. These conclusions will be used to compare with numerical data and analyze distortion descriptors. Unfortunately, data from the PIV are not yet available, which would have provided many clues to identify other complex physical phenomena expected for this type of geometry. In the next chapters, numerical analyses will be performed using the same geometry under similar conditions. The objective is to compare with the experimental data in order to understand and improve the prediction of this engine intake concept.

Chapter 4

Analysis of Reynolds-averaged numerical simulations

Computational fluid mechanics (CFD) is a scientific field that can solve complex fluid analysis problems that are otherwise difficult or impossible to address by analytical or experimental methods. CFD offers several advantages, such as reducing experimentation costs, analyzing the flow field under various velocity and environmental conditions, manipulating variables and data with more flexibility and precision, identifying critical sources and potential geometric modifications that could enhance aerodynamic performance, and so on. However, CFD also has some limitations and sources of error. Firstly, CFD solutions depend on the accuracy of physical and mathematical models used to describe fluid behavior. Secondly, when solving equations on the computer, numerical errors are due to the approximations inherent in numerical models. These errors tend to decrease when refining the mesh, but they never vanish completely. Moreover, the quality of the initial or boundary conditions provided to the numerical model also affects the accuracy of the CFD solution.

During the last decades the CFD has evolved rapidly due to the advance in knowledge and ability to calculate a variety of applications. CFD models can be divided according to the strategy that is implemented when approximating the equations of Navier Stokes. Currently, most of the numerical simulations solve the Reynolds-Averaged Navier Stokes (RANS) equations. Some authors [58] indicate that current RANS simulations found their limit in their predictive capacity that is directly related to the approximations they apply. On the other hand, other authors [59] wonder if these limits really exist, and if so, they think that these limits are more related to the type of problem in question. In cases where problems are beyond current model capabilities, many believe that significant improvements can extend the accuracy and affordability of RANS computations to advance fluid dynamic design capabilities. In this chapter it is proposed to study, and compare with the bibliography, the physical phenomena linked to a BLI intake from the point of view of the CFD.

4.1 Reynolds-Averaged Navier-Stokes turbulence models

Computational Fluid Dynamics (CFD) modeling of turbulent flows for industrial applications has relied on Reynolds Averaged Navier Stokes (RANS) turbulence models for several decades. These models have evolved from algebraic to one and two equation formulations to cope with the increasing complexity of viscous wall bounded flows. RANS models have demonstrated robustness and accuracy for a broad range of turbulent flow applications, and they constitute the foundation of most engineering CFD simulations. This family of turbulence models is based on the Reynolds-Averaged Navier-Stokes equations, which are expressed in tensor notation as follows:

$$\frac{\partial \rho}{\partial t} + \frac{\partial}{\partial x_j}(\rho u_j) = 0 \quad (4.1)$$

$$\frac{\partial(\rho u_i)}{\partial t} + \frac{\partial}{\partial x_j}(\rho u_i u_j) = -\frac{\partial P}{\partial x_i} + \frac{\partial}{\partial x_j} \left[\mu \left(\frac{\partial u_i}{\partial x_j} + \frac{\partial u_j}{\partial x_i} \right) - \rho \overline{u'_i u'_j} \right] \quad (4.2)$$

$$\frac{\partial}{\partial x_j}(\rho e u_j) + \frac{\partial}{\partial t}(\rho e) = \frac{\partial}{\partial x_j}(u_j p) - \frac{\partial}{\partial x_j}(u_j \rho \overline{u'_i u'_j}) + Q \quad (4.3)$$

where ρ is the density, U is the mean velocity, P is the pressure, μ is the molecular viscosity, and $\overline{u'_i u'_j}$ is the Reynolds stress tensor. The Reynolds averaging process results in an additional stress term ($\rho \overline{u'_i u'_j}$). A possible approach to solving this equation is to formulate the stress terms as functions of the mean velocity terms. This issue is referred to as the closure problem.

4.1.1 Eddy Viscosity Models

Eddy viscosity models belong to a category of turbulence models that estimate the Reynolds stresses ($\rho \overline{\mathbf{u}'\mathbf{u}'}$). These models rely on the Boussinesq hypothesis, which was proposed in 1877, and postulates that the Reynolds stress tensor is correlated with the strain tensor of the mean flow. By analogy with a 2D Brownian motion, one can infer that the momentum is transported along the direction of the velocity gradient, and thus assume that the Reynolds stress is proportional to $\frac{\partial U_i}{\partial x_j}$ as expressed in equation 4.4. The proportionality constant μ_t is termed the turbulent viscosity. This term is artificial and regulates the intensity of diffusion. Applying the same analysis to a 3D flow, one can derive equation 4.5. In this equation κ denotes the turbulent kinetic energy and δ_{ij} represents the Kronecker's delta. The turbulent viscosity coefficient is determined according to each specific turbulent model.

$$-\rho \overline{\mathbf{u}'\mathbf{u}'} = \mu_t \frac{\partial U_i}{\partial x_j} \quad (4.4)$$

$$-\rho \overline{\mathbf{u}'\mathbf{u}'} = 2\mu_t \left(\frac{1}{2} \frac{\partial U_i}{\partial x_j} + \frac{1}{2} \frac{\partial U_j}{\partial x_i} - \frac{1}{3} \frac{\partial U_k}{\partial x_k} \delta_{i,j} \right) - \frac{2}{3} \rho \kappa \delta_{ij} = \tau_{ij} \quad (4.5)$$

Spalart-Allmaras one-equation model

The Spalart-Allmaras model is a one-equation model that solves a modeled transport equation for the kinematic eddy turbulent viscosity [60] [61]. It was designed specifically for aerospace applications involving wall-bounded flows and has been shown to give good results for boundary layers subjected to adverse pressure gradients. The model solves a transport equation for a kinematic viscosity-like variable ν , called Spalart-Allmaras variable. Its relation with the kinematic eddy viscosity is shown by equation 4.6.

$$\nu_t = \tilde{\nu} f_{\nu 1} \quad f_{\nu 1} = \frac{\chi^3}{\chi^3 + C_{\nu 1}^3} \quad \chi = \frac{\tilde{\nu}}{\nu} \quad (4.6)$$

The function $f_{\nu 1}$ is responsible for capturing a significant portion of the viscous damping effects. A single transport equation is solved for $\tilde{\nu}$, which is shown in vectorial form in equation 4.7. The transport equation comprises terms for the production, diffusion, and destruction of $\tilde{\nu}$.

$$\frac{\partial \tilde{\nu}}{\partial t} + \frac{\partial}{\partial x_j} (\nu \tilde{u}_j) = c_{b1} \tilde{S} \tilde{\nu} + \frac{1}{\sigma} [\nabla \cdot (\nu + \tilde{\nu}) \nabla \tilde{\nu} + c_{b2} (\nabla \tilde{\nu})^2] - c_{w1} f_w \left(\frac{\tilde{\nu}}{d} \right)^2 \quad (4.7)$$

The left-hand side of the equation contains the temporal derivative and the convection term. The right-hand side of the equation consists of three terms. The first term on the right-hand side represents the generation of turbulence. Turbulence is produced by shear (velocity-gradients) in the mean velocity profile. The shear rate tensor is represented by \tilde{S} , which is calculated by equation 4.8. The constant c_{b1} is calibrated to accurately represent turbulence production. Unlike other transport equations, the diffusion term has an additional non-linear term $c_{b2} (\nabla \tilde{\nu})^2$. This non-linear term, often written as a source term, provides more accuracy at the edge of the turbulent region where diffusion dominates [60]. The constant c_{b2} was calibrated to obtain a more accurate spreading of the wake profile. The final term on the right-hand side is the destruction term. The presence of a wall destroys turbulence through viscosity and inviscid blocking. The distance to the nearest wall is represented by d , and the function f_w tends to 0 as d tends to zero to prevent a divide-by-zero error. This function is calculated by equation 4.9. This term models the destruction of turbulence due to inviscid blocking only; viscous destruction of turbulence is accounted for in the definition of ν_t in equation 4.6. The viscous damping is accomplished through the function $f_{\nu 1}$.

$$\tilde{S} = \Omega + \frac{\tilde{\nu}}{\kappa^2 d^2} f_{v2} \quad S = \frac{1}{2} \left(\frac{\partial u_i}{\partial x_j} - \frac{\partial u_j}{\partial x_i} \right) \quad f_{v2} = 1 - \frac{\chi}{1 + \chi f_{v1}} \quad (4.8)$$

$$c_{w1} = \frac{c_{b1}}{\kappa^2} + \frac{1 + c_{b2}}{\sigma} \quad f_w = g \left[\frac{1 + c_{w3}^6}{g^6 + c_{w3}^6} \right]^{\frac{1}{6}} \quad g = r + c_{w2} (r^6 - r) \quad r = \min \left(\frac{\tilde{\nu}}{\tilde{S} \kappa^2 d^2}, 10 \right) \quad (4.9)$$

Table 4.1: Spalart-Allmaras model coefficients

σ	c_{b1}	c_{b2}	κ	c_{w2}	c_{w3}	c_{v1}
2/3	0.1355	0.622	0.41	0.3	2	7.1

Finally, the Spalart-Allmaras uses the kinematic turbulent viscosity calculated by equation 4.6 to propose a solution for the closure problem by the 4.10 relation.

$$\mu_t = \rho \nu_t \quad (4.10)$$

Spalart-Allmaras with Rotation/Curvature Correction

This is a revised version of the original Spalart-Allmaras model that aims to account for rotation and curvature effects [62]. The model is identical to the standard version, except that the production term, $c_{b1} \tilde{S} \tilde{\nu}$, is multiplied by the rotation function f_{r1} , which is defined by equation 4.11.

$$f_{r1} = (1 + c_{r1}) \frac{2r^*}{1 + r^*} [1 - c_{r3} \tan^{-1}(c_{r2} \tilde{r})] - c_{r1} \quad (4.11)$$

The non-dimensional term r^* and \tilde{r} are defined by equation 4.12. The strain rate tensor S_{ij} and the absolute-rotation tensor W_{jk} are calculated by equation 4.13. Objective measures of strain and rotation are then obtained as shown in equation 4.14. The model coefficients are presented in table 4.2.

$$r^* = \frac{\tilde{S}}{\tilde{W}} \quad \tilde{r} = \frac{2}{D^4} W_{ik} S_{jk} \left[\frac{\partial S_{ij}}{\partial t} + (\epsilon_{imn} S_{jn} + \epsilon_{jmn} S_{in}) \Omega_m \right] \quad (4.12)$$

$$S_{ij} = \frac{1}{2} \left(\frac{\partial U_i}{\partial x_j} + \frac{\partial U_j}{\partial x_i} \right) \quad W_{ij} = \frac{1}{2} \left[\left(\frac{\partial U_i}{\partial x_j} - \frac{\partial U_j}{\partial x_i} \right) + 2\varepsilon_{mji} \Omega_m \right] \quad (4.13)$$

$$\tilde{S} = (2S_{ij}S_{ij})^{1/2} \quad \tilde{W} = (2W_{ij}W_{ij})^{1/2} \quad D^2 = 0.5(\tilde{S}^2 + \tilde{W}^2) \quad (4.14)$$

Cr1	Cr2	Cr3
1.0	12.0	1.0

Table 4.2: Model coefficients for Spalart-Allmaras with rotation and curvature correction model

Spalart-Allmaras with Quadratic Constitutive Relation

In 2000, Spalart proposed the Quadratic Constitutive Relation (QCR) to improve the simulation of corner flows [63]. This method involves adding a second nonlinear term to the linear Reynolds stress tensor and can be used for any turbulence model that normally uses the Boussinesq relation. The additional term added to the linear Reynolds stress tensor to obtain a non-linear term is defined by equation 4.15. τ_{ij} are the turbulent stresses computed from the linear Boussinesq relation, S_{ij} is the strain tensor and O_{ij} is an antisymmetric normalized rotation tensor, all of which are defined by equations 4.16.

$$\tau_{ij,QCR} = \tau_{ij} - C_{cr1} (O_{ik} \tau_{jk} + O_{jk} \tau_{ik}) \quad (4.15)$$

$$\tau_{ij} = 2\mu_t S_{ij} \quad O_{ik} = \frac{(\partial u_i / \partial x_k) - (\partial u_k / \partial x_i)}{\sqrt{(\partial u_m / \partial x_n)(\partial u_m / \partial x_n)}} \quad (4.16)$$

The constant $C_{cr1} = 0.3$ is a preliminary and fully experimental value that was calculated by Spalart and calibrated in the outer region of a simple boundary layer. The calibration was done by requiring a fair level of anisotropy, where $u'^2 > w'^2 > v'^2$, which represents the stream-wise, spanwise and wall-normal Reynolds stresses respectively.

k- ω SST two-equations model

The SST k- ω turbulence model [64] is a two-equation eddy-viscosity model that is used for many aerodynamic applications. It is a hybrid model combining the Wilcox k- ω and the k- ε models. The k- ω model uses kinetic energy (k) and specific dissipation rate (ω) to estimate the

eddy viscosity (μ_t) by using the equation [4.17](#). The transport equations solved for this model are given by equations [4.18](#) and [4.19](#).

$$\mu_t = \frac{\rho a_1 k}{\max(a_1 \omega, \Omega F_2)} \quad (4.17)$$

$$\frac{\partial(\rho k)}{\partial t} + \frac{\partial(\rho u_j k)}{\partial x_j} = P_k - \beta^* \rho k \omega + \frac{\partial}{\partial x_j} \left[(\mu + \sigma_k \mu_T) \frac{\partial k}{\partial x_j} \right] \quad (4.18)$$

$$\frac{\partial(\rho k)}{\partial t} + \frac{\partial(\rho u_j k)}{\partial x_j} = \frac{\gamma}{\nu_t} P_k - \beta \rho \omega^2 + \frac{\partial}{\partial x_j} \left[(\mu + \sigma_\omega \mu_t) \frac{\partial \omega}{\partial x_j} \right] + 2(1 - F_1) \frac{\rho \sigma_{\omega 2}}{\omega} \frac{\partial k}{\partial x_j} \frac{\partial \omega}{\partial x_j} \quad (4.19)$$

The closure coefficients and auxiliary relations are presented in equations [4.19](#). Each constant is a combination of an inner (ϕ_1) and outer (ϕ_2) constant blended via equation [4.25](#). The blending functions are F_1 and F_2 . The production term is P_k represented by equation [4.23](#). In this case, a production limiter is used. The vorticity magnitude and the Reynolds stress are computed by equations [4.25](#) and [4.5](#), respectively. The model's constants are shown in table [4.3](#).

$$\phi = \phi_1 F_1 + \phi_2 (1 - F_1) \quad (4.20)$$

$$F_1 = \tanh \left[\left[\min \left[\max \left(\frac{\sqrt{k}}{\beta^* \omega d}, \frac{500 \nu}{d^2 \omega} \right), \frac{4 \sigma_{\omega 2} k}{CD_{k\omega} d^2} \right] \right]^4 \right] \quad (4.21)$$

$$F_2 = \tanh \left[\left[\max \left(\frac{2\sqrt{k}}{\beta^* \omega d}, \frac{500 \nu}{d^2 \omega} \right) \right]^2 \right] \quad (4.22)$$

$$P_k = \min \left(\tau_{ij} \frac{\partial U_i}{\partial x_j}, 20 \beta^* \rho k \omega \right) \quad (4.23)$$

$$CD_{k\omega} = \max \left(2 \rho \sigma_{\omega 2} \frac{1}{\omega} \frac{\partial k}{\partial x_j} \frac{\partial \omega}{\partial x_j}, 10^{-20} \right) \quad (4.24)$$

$$W_{ij} = \frac{1}{2} \left(\frac{\partial U_i}{\partial x_j} - \frac{\partial U_j}{\partial x_i} \right) \quad (4.25)$$

Table 4.3: Model coefficients for k- ω SST two-equations model

σ_{k1}	σ_{k2}	β_1	β_2	b^*	$\gamma_{\omega 1}$	$\gamma_{\omega 2}$	k	a_1
0.85	1	0.075	0.0828	0.09	0.5	0.856	0.41	0.31

4.1.2 Reynolds Stress Model

The Reynolds Stress Models (RSM) are higher level turbulence closures and represent the most complete classical turbulence model. The method of closure employed is usually referred to as a Second Order Closure. The Reynolds stress model involves the calculation of individual Reynolds stresses, $\overline{\rho u'_i u'_j}$, using differential transport equations. These individual Reynolds stresses are then used to obtain closure of the Reynolds-averaged momentum equation. RSM models are able to account for complex interactions in turbulent flow fields, such as the directional effects of the Reynolds stresses. All RSM models are based on the Reynolds stress transport equation.

SSG/LRR- ω Model

This model has been developed within the EU-project FLOMANIA[65]. The fundamental idea of the SSG/LRR- ω model is to combine the ε -based SSG model for the pressure strain correlation with the simpler model by Launder, Reece and Rodi (LRR)[66] near walls in the ω -based formulation of Wilcox[59]. Since the LRR-model can be written as a subset of the above SSG-model, the same blending of the Reynolds stress model coefficients $C_i, C_i^*, D^{(SD)}$ and $D^{(GD)}$ can be applied as to the coefficients of the ω -equation. Thus, all coefficients change consistently from LRR+ ω near walls to SSG+ ε at the boundary layer edge. The Reynolds transport stress equation used in this model is shown in 4.26, where ρ is the mean density and U_i represents the Cartesian components of the mean velocity vector. $\rho \tau_{ij}$ is the Cartesian components of the Reynolds stress tensor.

$$\frac{\partial(\rho \tau_{ij})}{\partial t} + \frac{\partial}{\partial x_k} (\rho \tau_{ij} U_k) = \rho P_{ij} + \rho \Pi_{ij} - \rho \varepsilon_{ij} + \rho D_{ij} \quad (4.26)$$

The components of the production term are given by equation 4.27. This production term does not need modeling, since all quantities are provided by the system of equations to be solved. The Cartesian components of the pressure-strain correlation are formally modeled according to Speziale, Sarkar and Gatski (SSG)[67], as shown in equation 4.28. The equation 4.29 show the specific kinetic turbulence energy and the Cartesian components of the anisotropy tensor. The set of equations 4.30 denotes the components of the simple strain rate tensor, the traceless strain rate tensor and the rotation tensor, respectively.

$$\rho P_{ij} = -\rho \tau_{ik} \frac{\partial U_j}{\partial x_k} - \rho \tau_{jk} \frac{\partial U_i}{\partial x_k} \quad (4.27)$$

$$\begin{aligned} \rho\Pi_{ij} = & - \left(C_1\rho\varepsilon + \frac{1}{2}C_1^*\rho P_{kk} \right) b_{ij} + C_2\rho\varepsilon \left(b_{ik}b_{kj} - \frac{1}{3}b_{kl}b_{kl}\delta_{ij} \right) + \left(C_3 - C_3^*\sqrt{b_{kl}b_{kl}} \right) \rho k S_{ij}^* \\ & + C_4\rho k \left(b_{ik}S_{jk} + b_{jk}S_{ik} - \frac{2}{3}b_{kl}S_{kl}\delta_{ij} \right) + C_5\rho k (b_{ik}W_{jk} + b_{jk}W_{ik}) \end{aligned} \quad (4.28)$$

$$k = \tau_{ii}/2 \qquad b_{ij} = \frac{\tau_{ij}}{2k} - \frac{1}{3}\delta_{ij} \quad (4.29)$$

$$S_{ij} = \frac{1}{2} \left(\frac{\partial u_i}{\partial x_j} + \frac{\partial u_j}{\partial x_i} \right) \qquad S_{ij}^* = S_{ij} - \frac{1}{3}S_{kk}\delta_{ij} \qquad W_{ij} = \frac{1}{2} \left(\frac{\partial u_i}{\partial x_j} - \frac{\partial u_j}{\partial x_i} \right) \quad (4.30)$$

The C_i and C_i^* are the model dependent coefficients. Dissipation is modeled by equation 4.30 as an isotropic tensor. The isotropic dissipation rate ε is provided indirectly by a transport equation for the specific dissipation rate ω . Two different models are available representing non-convective fluxes, simple gradient diffusion 4.32[68] or generalized gradient diffusion 4.33[69]. μ is the mean dynamic fluid viscosity, $D^{(SD)}$ and $D^{(GD)}$ represent respective model coefficients. In this case the generalized gradient diffusion model is used.

$$\rho\varepsilon_{ij} = \frac{2}{3}\rho\varepsilon \quad (4.31)$$

$$\rho D_{ij} = \frac{\partial}{\partial x_k} \left[\left(\mu\delta_{ij} + \frac{D^{(SD)}\rho k^2}{C_\mu\varepsilon} \right) \frac{\partial \tau_{ij}}{\partial x_k} \right] \quad (4.32)$$

$$\rho D_{ij} = \frac{\partial}{\partial x_k} \left[\left(\mu\delta_{kl} + D^{(GD)}\frac{\rho k\tau_{kl}}{\varepsilon} \right) \frac{\partial \tau_{ij}}{\partial x_l} \right] \quad (4.33)$$

Finally, the Menter's baseline equation 4.34[64] is employed for providing the isotropic dissipation rate 4.35, where $C_\mu = 0.09$. As the k- ω SST model, the coefficients are blended according to equation 4.25 between the bounding values associated with the ε equation[70] at the boundary layer edge ($F_1 = 0$), where the blending function is given by equation 4.36 based on the wall distance d . The corresponding values of the coefficients are given in Table 4.4. The corresponding bounding values are given in Table 4.5.

$$\frac{\partial(\rho\omega)}{\partial t} + \frac{\partial}{\partial x_k}(\rho\omega u_k) = \alpha_\omega \frac{\omega}{k} \frac{\rho P_{kk}}{2} - \beta_\omega \rho \omega^2 + \frac{\partial}{\partial x_k} \left[\left(\mu + \sigma_\omega \frac{\rho k}{\omega} \right) \frac{\partial \omega}{\partial x_k} \right] + \sigma_d \frac{\rho}{\omega} \max \left(\frac{\partial k}{\partial x_k} \frac{\partial \omega}{\partial x_k}, 0 \right) \quad (4.34)$$

$$\varepsilon = C_\mu k \omega \quad (4.35)$$

$$F_1 = \tanh \left[\min \left[\max \left(\frac{\sqrt{k}}{C_\mu \omega d}, \frac{500\mu}{\rho \omega d^2} \right), \frac{4\sigma_\omega^\varepsilon \rho k}{\sigma_d^\varepsilon \frac{\rho}{\omega} \max \left(\frac{\partial k}{\partial x_k} \frac{\partial \omega}{\partial x_k}, 0 \right) d^2} \right] \right]^4 \quad (4.36)$$

	α_ω	β_ω	σ_ω	σ_d
$\phi^{(\varepsilon)}$	0.44	0.0828	0.856	1.712
$\phi^{(\omega)}$	0.5556	0.075	0.5	0

Table 4.4: Bounding Values of ω -Equation Coefficients

	C_1	C_1^*	C_2	C_3	C_3^*	C_4	C_5	$D^{(SD)}$	$D^{(GD)}$
SSG	3.4	1.8	4.2	0.8	1.3	1.25	0.4	0.146	0.22
LRR	3.6	0	0	0.8	0	10.45	1.156	0.5	0.75

Table 4.5: Bounding Values of the SSG/LRR- ω Model Term Coefficients

4.2 Numerical simulations

A CFD campaign was performed to analyze the prediction capacity of turbulence models currently used in the industry. The chosen simulation setup is described in this section.

4.2.1 Geometry and mesh generation

The domain shape is composed of the BLI intake described in the previous chapter, table [3.1](#) and shown in Figure [3.2](#). The domain measures 6560mm in length and width and 3280mm in height, representing 40D and 20D respectively, where D is the fan diameter. Figure [4.1](#) shows the flow domain. A structured multiblock mesh composed of hexahedral elements is used. An O-H grid method topology is used for the interior of the nacelle. The exterior of the nacelle is formed by a mixture of C-grid topology near the nacelle and an O-grid one which extends

to the exterior. The geometry and the mesh have been created using Catia and ICEM-CFD respectively.

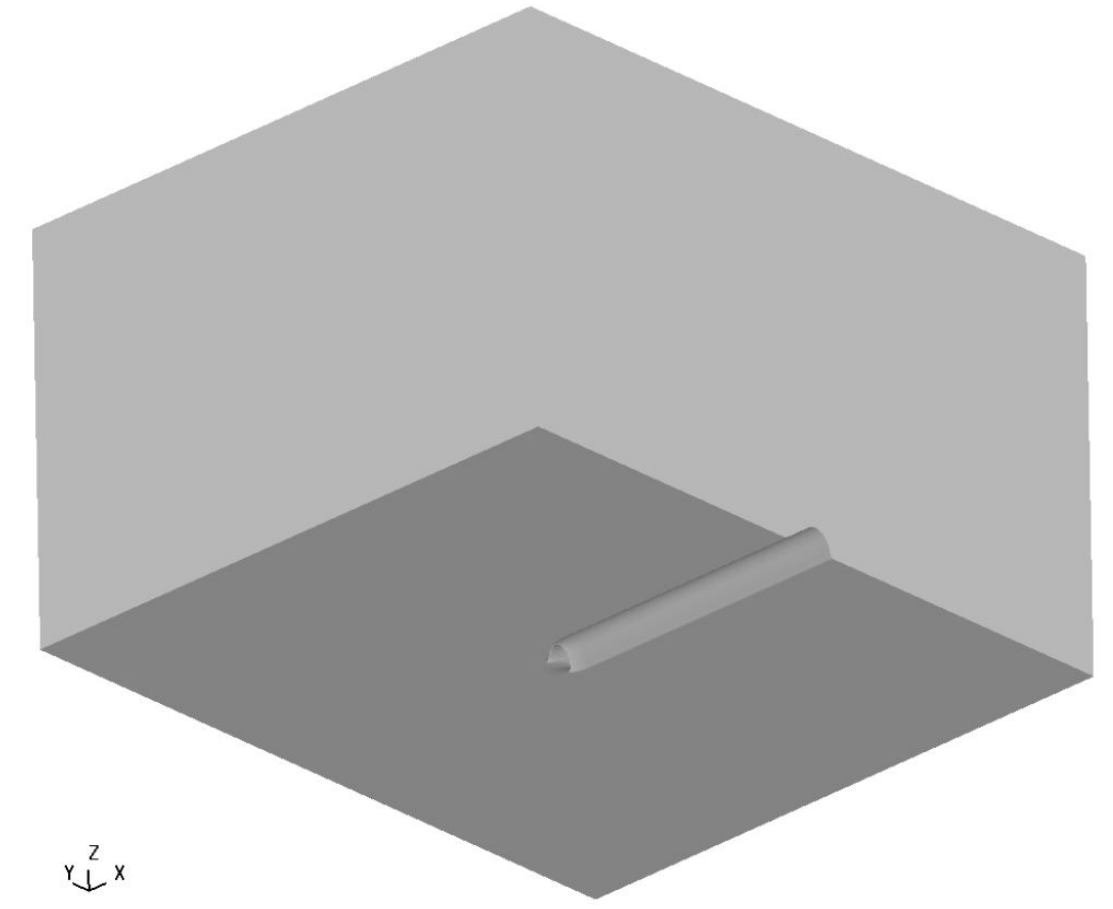


Figure 4.1: Computational domain

4.2.2 Simulation conditions and numerical setup

The numerical simulations have been performed using the ONERA-Safran elsA software [11], using the structured finite volume solver. For the RANS simulations, Jameson's second-order-accurate central scheme with artificial viscosity is used for the spatial discretization. The second and the fourth-order dissipation coefficients are equal to 0.5 and 0.016 respectively. The artificial viscosity reduction uses a e^2 value. For the turbulent equations, the Roe scheme coupled with Harten's formulation is used. Its coefficient value is 0.01. All the simulations are fully turbulent and a Courant–Friedrichs–Lewy number between 10 and 50 is used.

Reynolds-Average Navier-Stokes (RANS) computations have been performed using different turbulence models for closure: Spalart-Allmaras (SA) [60], Spalart-Allmaras with corrections or with Rotation/Curvature Correction (SA-RC) [62] or with QCR2000 correction [63] and the two-equation $k-\omega$ SST model [64]. A nonlinear eddy viscosity model, the SSG/LRR $-\omega$ Full Reynolds Stress Model (RSM) [71] has also been evaluated in this section.

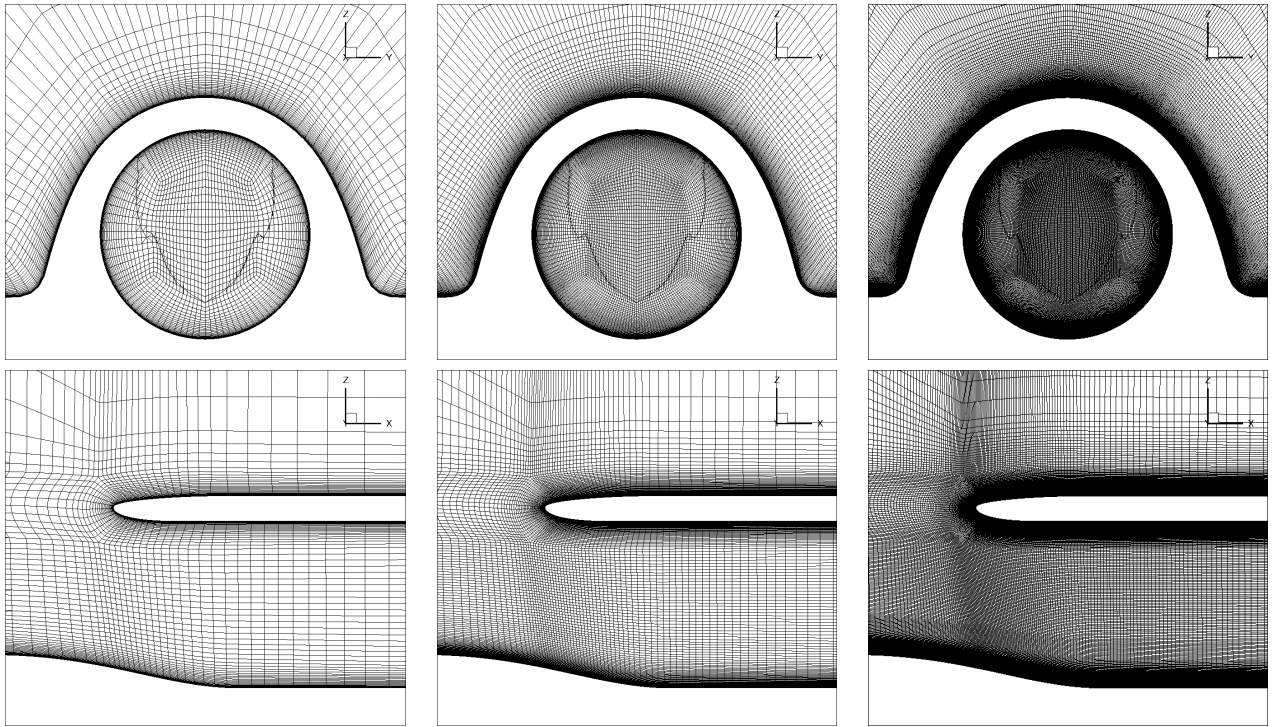


Figure 4.2: Different meshes analyzed (left: coarse, mid: normal, right: fine).

The flow conditions selected for the simulations are identical to those used in the wind tunnel test. A freestream condition is applied to the boundary of the flow domain, with a Mach number of 0.82 and a flow direction parallel to the flat plane with a zero-sideslip angle direction. A mass flow rate between $3 \text{ kg}\cdot\text{s}^{-1}$ to $4\text{kg}\cdot\text{s}^{-1}$ is imposed at the end of the extrusion of the engine inlet, far enough to ensure that it does not interfere with the flow behavior. The Reynolds number, taking the fan diameter as the reference length, is equal to 13.1 million.

Angle of attack	0°
Angle of sideslip	0°
Mach number	0.82
Reynolds number	13.1 million
Stagnation temperature	293 K
Turbulent Reynolds number	0.1
Mass flow rate	$3 \text{ kg}\cdot\text{s}^{-1} - 4\text{kg}\cdot\text{s}^{-1}$

Table 4.6: Flow and boundary conditions

4.2.3 Mesh convergence study

A mesh convergence study has been performed to ensure that the solution is independent of the mesh size. In this case, the standard Spalart-Allmaras model was used. A mass flow rate of $4 \text{ kg}\cdot\text{s}^{-1}$ was used. Three meshes were used: a coarse, normal and fine mesh, having 6 million,

25 million, and 100 million elements respectively. In this convergence analysis, the loss of total pressure at the AIP and a couple of distortion criteria were calculated. The figure 4.3 shows the relative error as a function of grid discretization. This relative error, using the finest grid as reference, was calculated by using the following equation:

$$\varepsilon(X) = \left(\frac{X_{grid2} - X_{grid1}}{X_{grid1}} \right) \cdot 100 + 1 \quad (4.37)$$

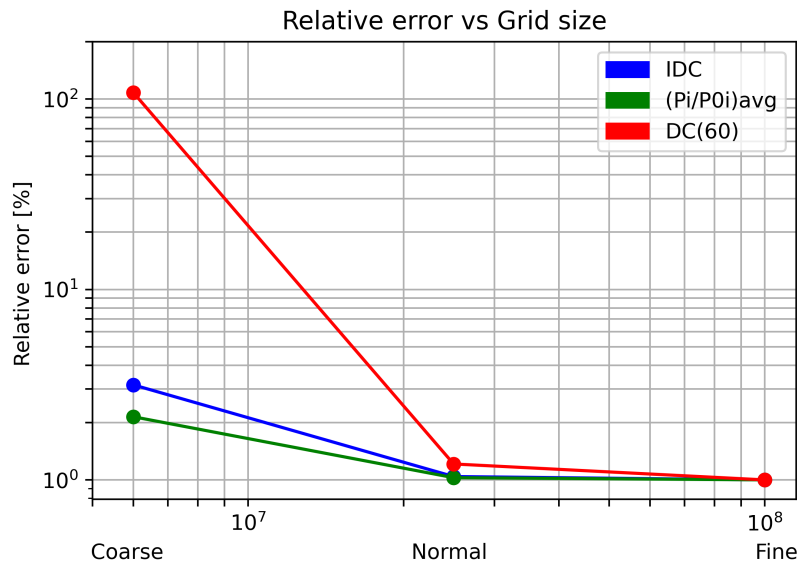


Figure 4.3: Relative error of distortion indices compared to grid size.

The pressure loss predicted by the coarse mesh is higher compared to the other meshes. The differences between the normal and fine meshes are close to zero. In the same figure, the IDC has been calculated using 2.8 for each mesh. In addition, the DC(60) has been also calculated by equation 2.7. In both cases the difference in results between normal and fine meshes is very small, being a little more accentuated for DC(60). The values obtained with the coarse mesh are further away from the rest.

In general, the difference between the normal and fine mesh is almost imperceptible. The relative error is very low and the results are considered to be independent of the mesh. Therefore, the normal mesh is used for all analyses.

4.2.4 Boundary layer thickness analysis

The boundary layer significantly influences the flow behavior of this type of intakes. To ensure simulation conditions are as similar as possible, it is necessary to adjust several parameters related to the boundary layer. The effect of the boundary layer has been experimentally analyzed in the previous section 3.4. The BLI intake ingests the boundary layer which has developed on

the upstream flat plate. The thickness of the boundary layer is modified by combining the "inviscid wall" and "viscous wall" boundary conditions. The thickness of the boundary layer increases with the increase of flow path over the "viscous wall" condition (see figure 4.4).

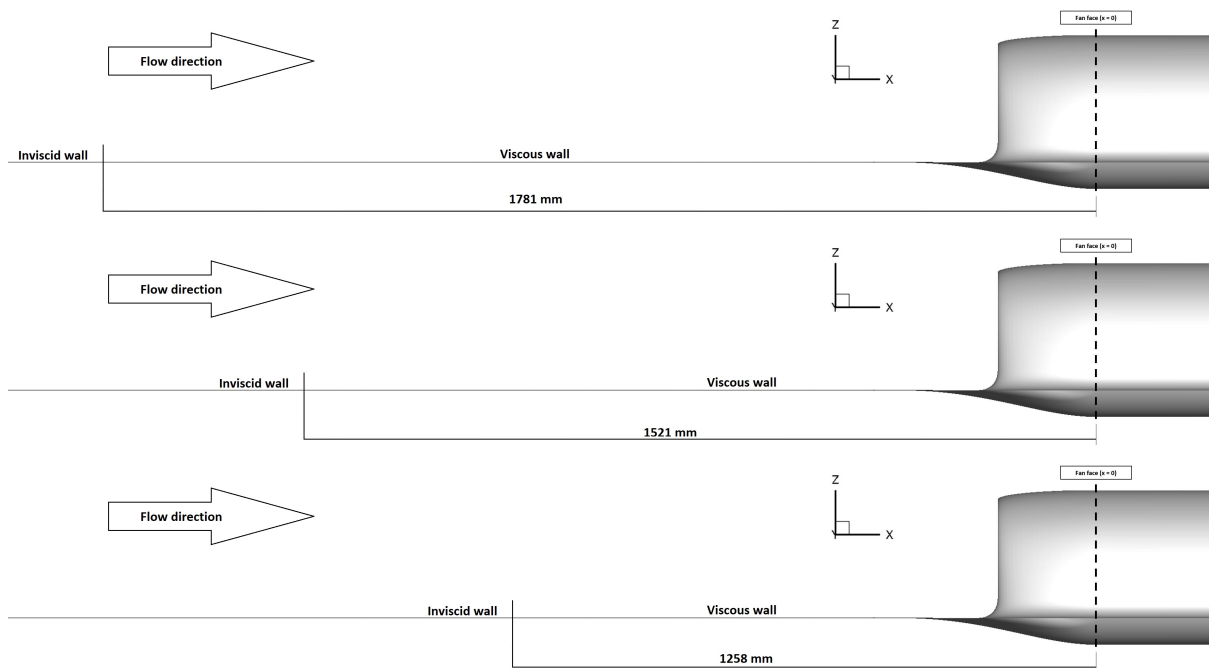


Figure 4.4: Boundary conditions on the flat plate for the different boundary layer thicknesses. Up: $\delta = 21.3$ mm. Center: $\delta = 16.1$ mm. Down: $\delta = 14.3$ mm.

The thickness of the boundary layer was measured at $x = -275$ mm, which is similar to the measurement taken in the experimental test as shown in figure 3.8. Figure 4.5 illustrates the comparison between the experimental and simulated boundary layers. The gray line represents the logarithmic law. It is important to verify that the boundary layer behavior matches the theory. The boundary layers profiles differ in the outer layer, this could indicate variations in the shape factor between the numerical and experimental boundary layer, as proposed by some authors [72] [73].

The thickness of the boundary layer is an important parameter to verify. Figure 4.6 illustrates the velocity profile of different boundary layers obtained from numerical simulations and the boundary layer measured in the tests. The boundary layer with a thickness of 16.1 mm, corresponding to the 1521 mm flat plate length, is the closest both in thickness value and shape to the experimental boundary layer. Therefore, this flat plate has been selected in this work.

In the next sections, we will examine the impact of the thickness of the boundary layer on physical phenomena and the distortion generated in the AIP. This analysis aims to elucidate the role of this parameter in this type of configuration.

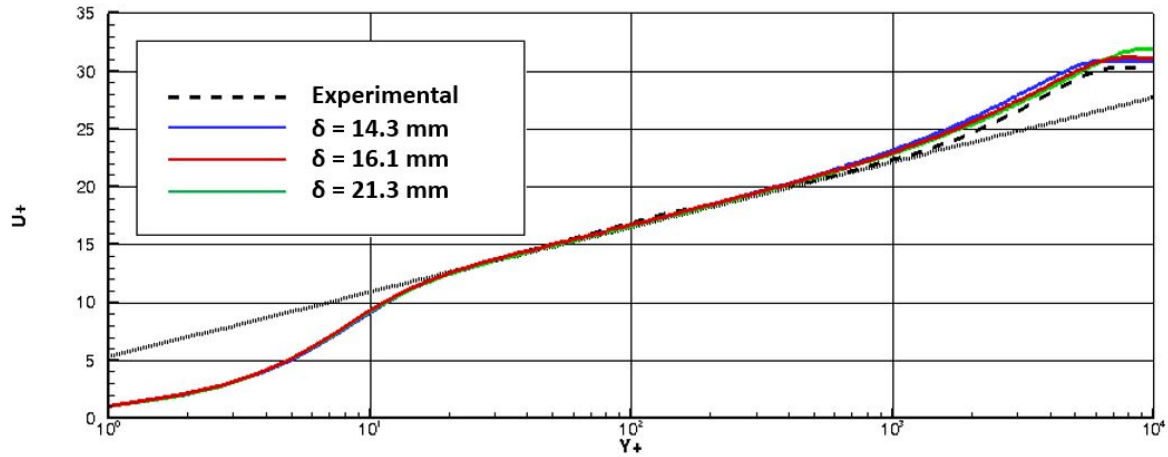


Figure 4.5: Comparison between numerical and experimental boundary layer profiles in log coordinates.

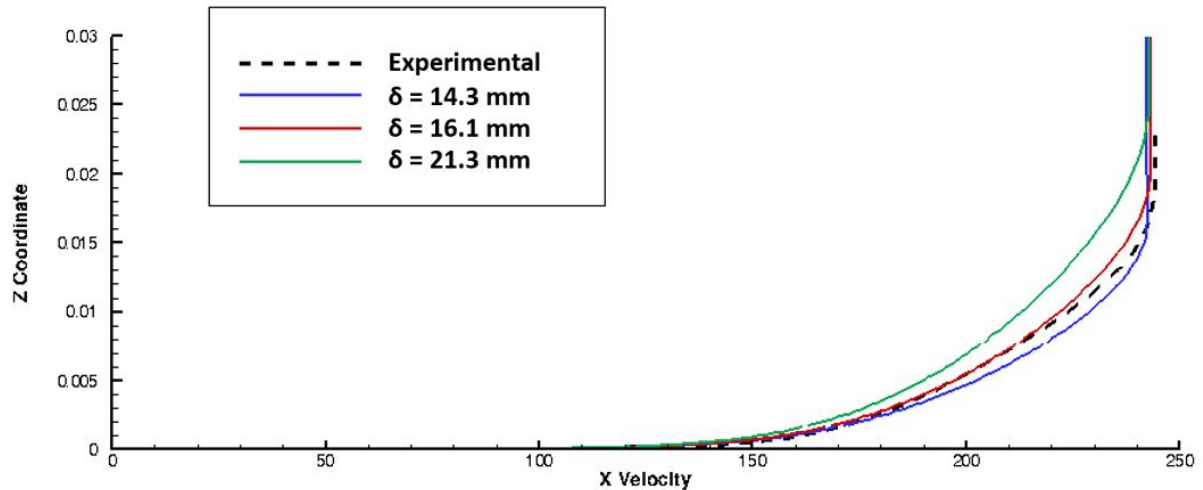


Figure 4.6: Comparison between numerical and experimental boundary layer profiles.

4.2.5 Simulation results analysis

In this section, we analyzed 35 simulations. The combination of turbulence models and MFR values used is shown in Tables 4.7 and 4.8. The convergence criteria for the numerical simulations is the residuals of the continuity equation and the turbulence equations. In all cases, these residuals were acceptable, less than 10^{-5} . Additionally, we used lift and drag values integrated on the nacelle surface as a physical parameter to monitor convergence. We present the results of the simulations for each turbulence model for the lowest mass flow in Figure 4.7. The figure illustrates several physical phenomena, including flow separation (denoted by the blue region), loss of total pressure in AIP and counter-rotating vortices.

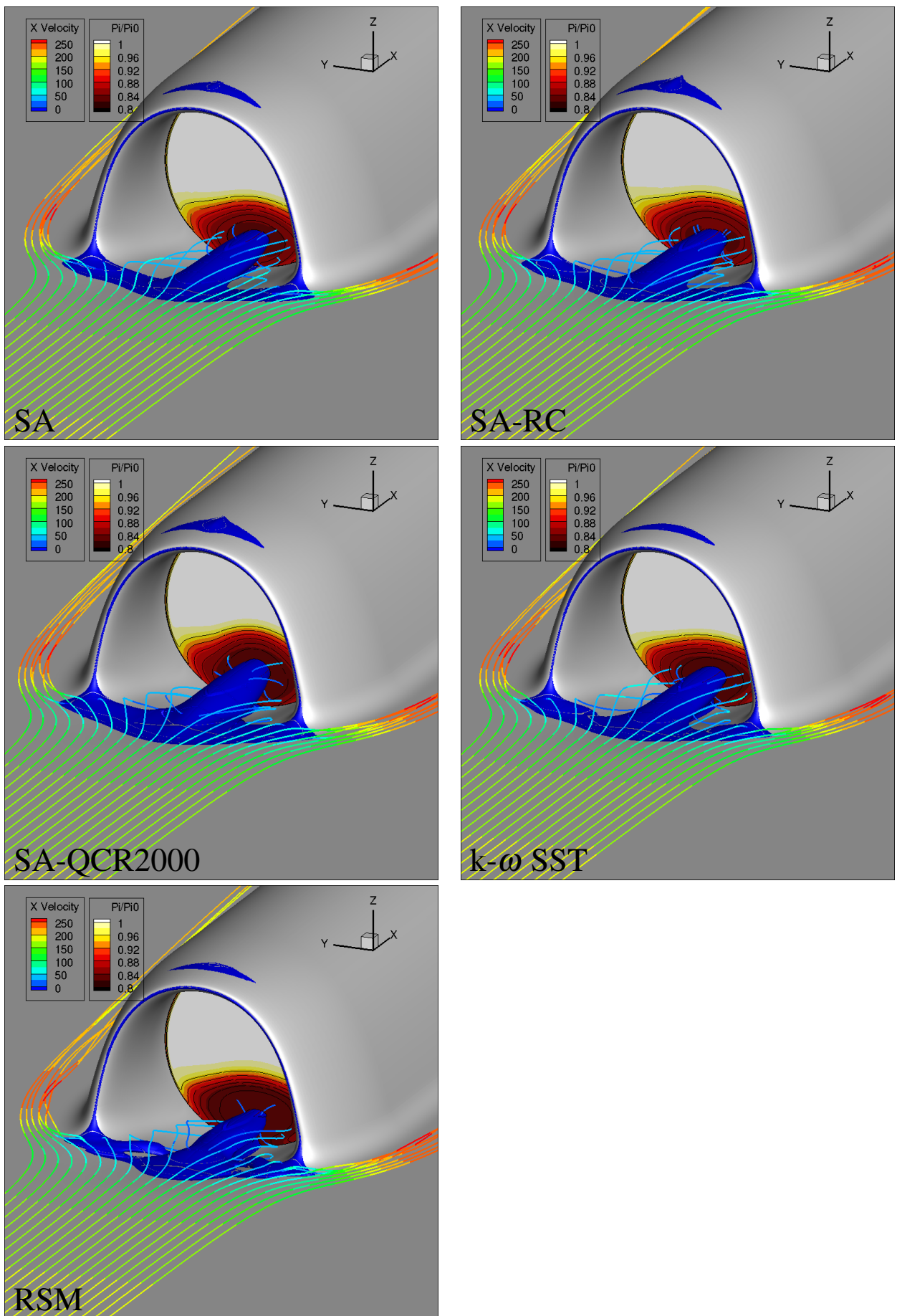


Figure 4.7: Flow separation and vortices for $MFR = 3.0 \text{ kg}\cdot\text{s}^{-1}$.

Turbulence model
Spalart-Allmaras (SA)
Spalart-Allmaras with Rotation/Curvature Correction (SA-RC)
Spalart-Allmaras with Quadratic Constitutive Relation (SA-QCR2000)
k- ω SST Model (SST)
SSG/LRR- ω Model (RSM)

Table 4.7: Turbulence models studied.

Mass flow rate (MFR) [kg·s⁻¹]
3.0
3.2
3.4
3.5
3.6
3.7
4.0

Table 4.8: MFR values studied.

Separation analysis

Flow separation is evident in both the inner and outer regions of the nacelle. The separation observed in the upper outer portion is ascribed to the influence of a shock wave. Notably, the most extensively studied separation phenomenon pertains to the internal flow, particularly in scenarios characterized by low mass flow rates. In this case, the main reason for the separation is the adverse pressure gradient created by the reduction of the flow velocity due to the ramp shape at the engine intake. This separation is also affected by the vortices generated at the inlet. To detect the flow separation, the skin friction coefficient (C_f) over the intake ramp is analyzed. While this is formally true only for 2D cases, in the present scenario, we consider it permissible to approximate due to the symmetry present in both the geometry and flow conditions. The skin friction coefficient is calculated using equation 4.38, where τ_w represents the local wall shear stress and q represents the free-stream dynamic pressure.

$$C_f = \frac{\tau_w}{q} = \frac{\tau_w}{\frac{1}{2}\rho_\infty u_\infty^2} \quad (4.38)$$

The skin friction coefficient distribution is computed for two spanwise sections. The selected y values are 0mm (symmetry plane) and 30 mm. The skin friction coefficient distribution on $y = 0$ mm and $y = 30$ mm is shown in Figures 4.8 and 4.9, respectively.

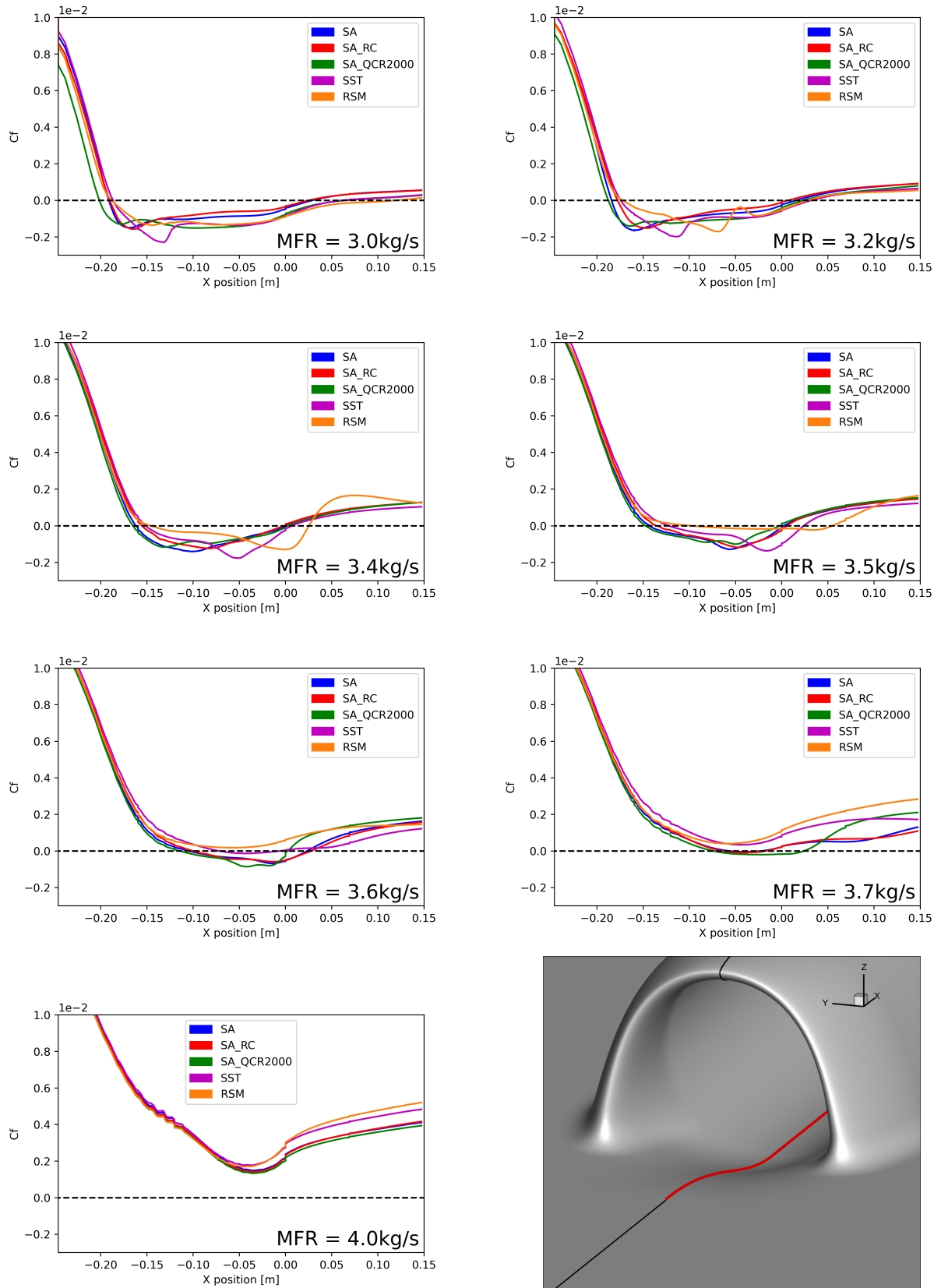


Figure 4.8: Skin friction coefficient on the intake ramp, $y = 0$ mm.

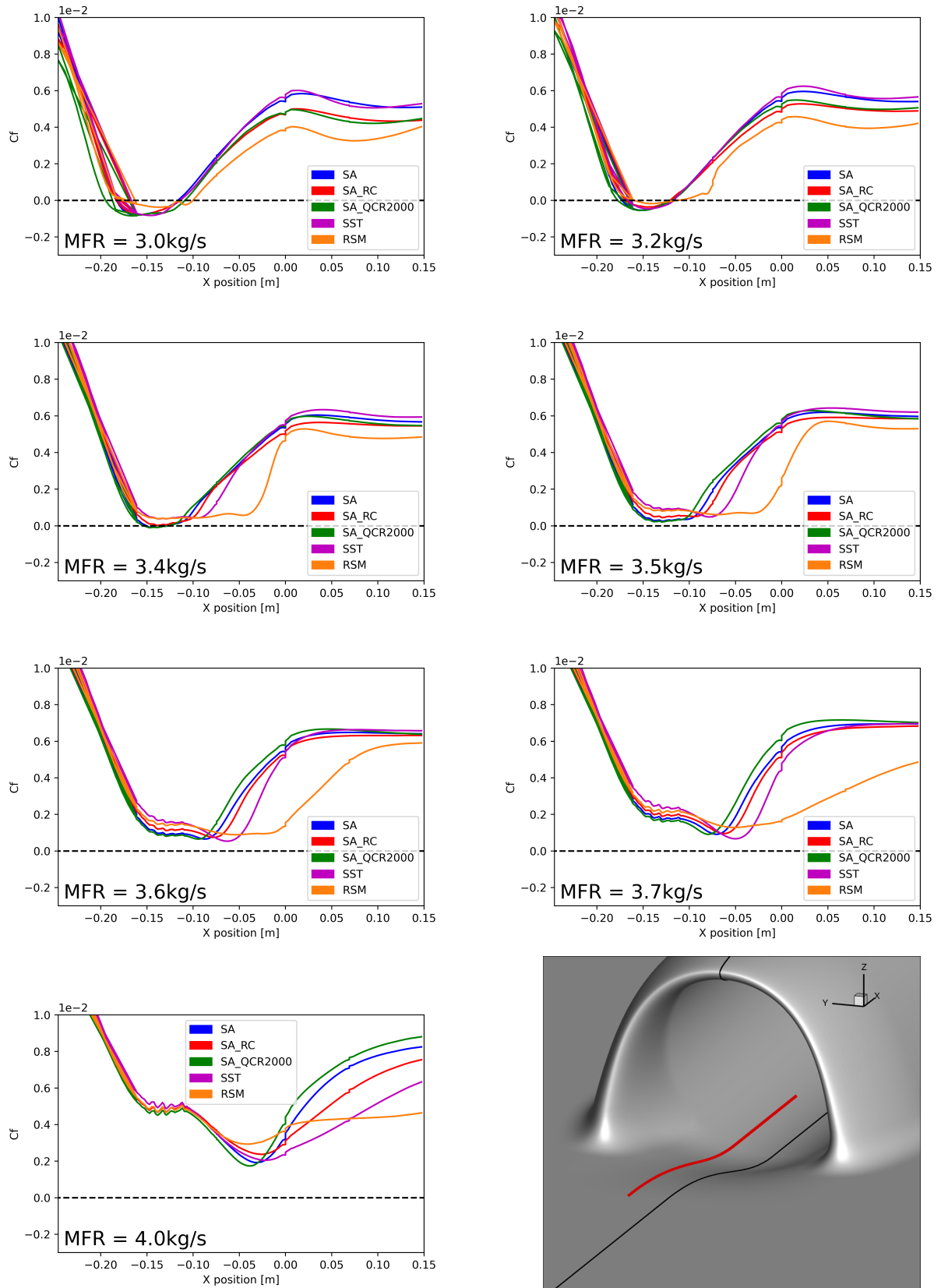


Figure 4.9: Skin friction coefficient on the intake ramp, $y = 30$ mm.

The plots show that the mass flow rate value for which the boundary layer separation appears varies between $3.7 \text{ kg}\cdot\text{s}^{-1}$ and $3.5 \text{ kg}\cdot\text{s}^{-1}$ according to the turbulence model.

First, it is interesting to analyze the differences between each turbulence model before the separation. The explanation for these differences is the topology of the detached flow region. Figures 4.8 and 4.9 clearly show that the shape of the separated flow region varies between the models, and this variation influences the upstream flow. For the cases where there is no separation, the difference between each model is much lower, however there are still some differences due the pressure gradients on the intake ramp.

Looking at the values in the plane $y = 0 \text{ mm}$, it can be observed that the SA-QCR2000 model tends to predict a separation which occurs upstream of the other models for all mass flow rate values. Furthermore, it can be observed that the RSM model predicts reattachment more downstream than the other models. The RSM predicts a flow separation for a mass flow rate value lower than $3.5 \text{ kg}\cdot\text{s}^{-1}$, $k-\omega$ for $3.6 - 3.5 \text{ kg}\cdot\text{s}^{-1}$ and SA family from $3.7 - 3.5 \text{ kg}\cdot\text{s}^{-1}$. Tables 4.9-4.12 show separation and reattachment location for each model. NA means that the flow is attached.

MFR [$\text{kg}\cdot\text{s}^{-1}$]	SA [mm]	SA-RC [mm]	SA-QCR2000 [mm]	SST [mm]	RSM [mm]
3.0	-192.3	-189.1	-200	-185.3	-186.2
3.2	-182.1	-175.2	-185.7	-171.9	-171.9
3.4	-160	-153	-163.6	-149.1	-148.6
3.5	-140.6	-134.7	-145.5	-121.5	-97.5
3.6	-103.8	-100	-113.4	-71.6	NA
3.7	-55.8	-63.1	-73.2	NA	NA
4.0	NA	NA	NA	NA	NA

Table 4.9: Location of the separation point on the intake ramp according to the skin friction coefficient, $y = 0 \text{ mm}$.

MFR [$\text{kg}\cdot\text{s}^{-1}$]	SA [mm]	SA-RC [mm]	SA-QCR2000 [mm]	SST [mm]	RSM [mm]
3.0	28.8	22.1	65.1	61.2	118.9
3.2	12.4	6.1	22.1	28.8	25.4
3.4	0.1	-2.9	0.1	6.1	22.1
3.5	0.0	3.1	-2.9	22.1	53.6
3.6	22.1	25.5	0.0	-8.7	NA
3.7	-23.1	-20.2	22.1	NA	NA
4.0	NA	NA	NA	NA	NA

Table 4.10: Location of the reattachment point on the intake ramp according to the skin friction coefficient, $y = 0 \text{ mm}$.

Vortices analysis

The vortices generated are an important physical phenomenon to be analysed in this type of configuration. The most convenient way to quantify these vortices is through vorticity. This

MFR [$\text{kg}\cdot\text{s}^{-1}$]	SA [mm]	SA-RC [mm]	SA-QCR2000 [mm]	SST [mm]	RSM [mm]
3.0	-161	-179.9	-183.2	-179.8	-176.4
3.2	-170	-166.9	-176.4	-163.9	-158.1
3.4	-149.9	NA	-152.6	NA	NA
3.5	NA	NA	NA	NA	NA
3.6	NA	NA	NA	NA	NA
3.7	NA	NA	NA	NA	NA
4.0	NA	NA	NA	NA	NA

Table 4.11: Location of the separation point on the intake ramp according to the skin friction coefficient, $y = 30$ mm.

MFR [$\text{kg}\cdot\text{s}^{-1}$]	SA [mm]	SA-RC [mm]	SA-QCR2000 [mm]	SST [mm]	RSM [mm]
3.0	-116.7	-114.3	-109.4	-115.5	-100.6
3.2	-122.3	-121.2	-118.9	-117.8	-113.1
3.4	-130	NA	-127.3	NA	NA
3.5	NA	NA	NA	NA	NA
3.6	NA	NA	NA	NA	NA
3.7	NA	NA	NA	NA	NA
4.0	NA	NA	NA	NA	NA

Table 4.12: Location of the reattachment point on the intake ramp according to the skin friction coefficient, $y = 30$ mm.

quantity provides a convenient framework for understanding a variety of complex flow phenomena, such as the formation and motion of vortex rings. The vorticity vector is defined by equation [4.39](#)

$$\vec{\omega} = \vec{\nabla} \times \vec{u} \quad (4.39)$$

The vorticity magnitude calculated at the fan face is shown in Figures [4.10](#). The distribution of vorticity in the SA family cases is very similar. The regions with the strongest vorticity are located on the lower side of the fan face, contrary to the $k-\omega$ SST model for which the largest vorticity values are obtained near the center of the intake. A similar behavior is found for the RSM model. The maximum vorticity values are predicted by the same two models and thus tends to predict stronger vortices, even with an attached boundary layer.

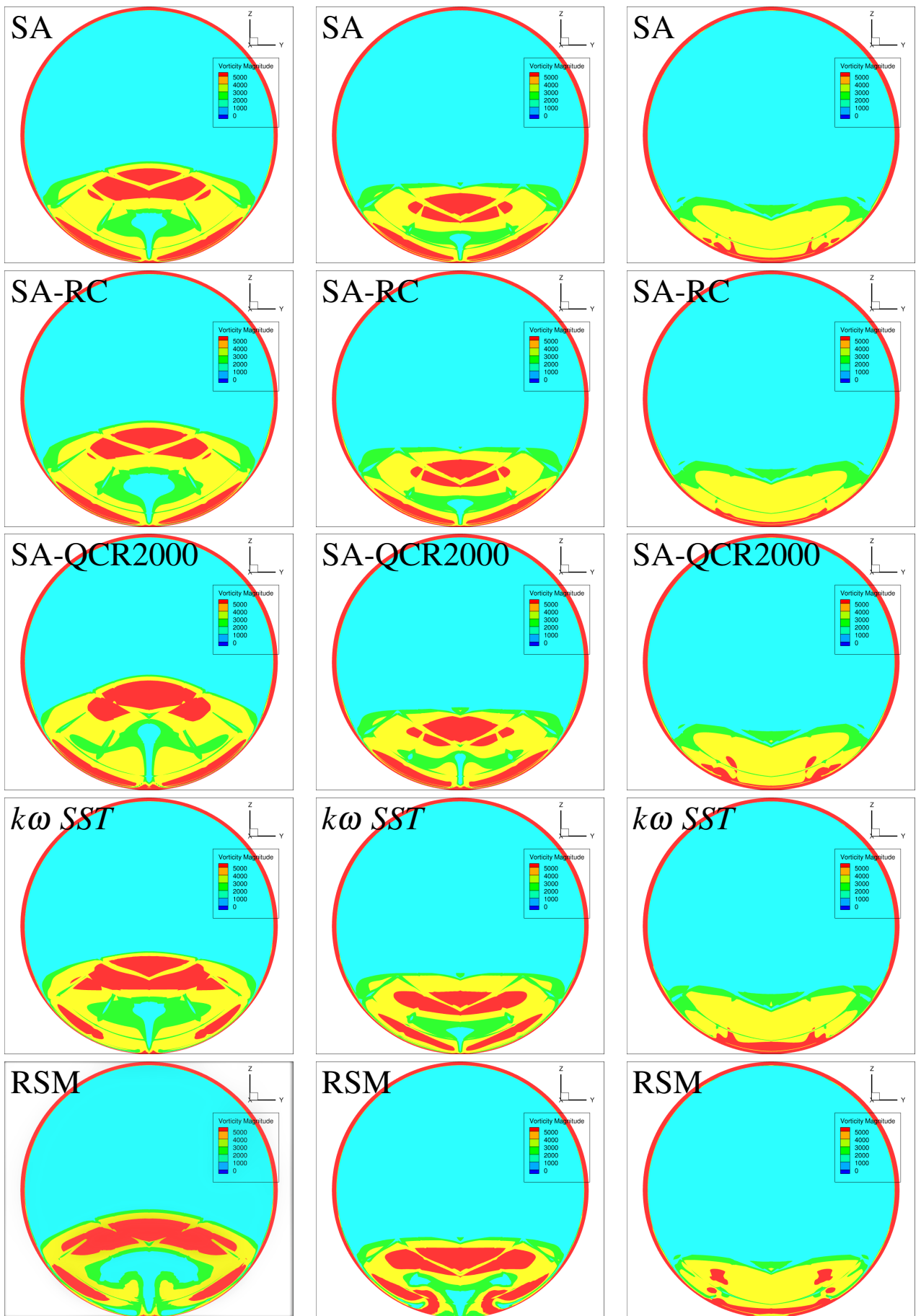


Figure 4.10: Vorticity field at fan face for each turbulence model. Left: $3.0 \text{ kg}\cdot\text{s}^{-1}$, center: $3.4 \text{ kg}\cdot\text{s}^{-1}$, right: $4.0 \text{ kg}\cdot\text{s}^{-1}$

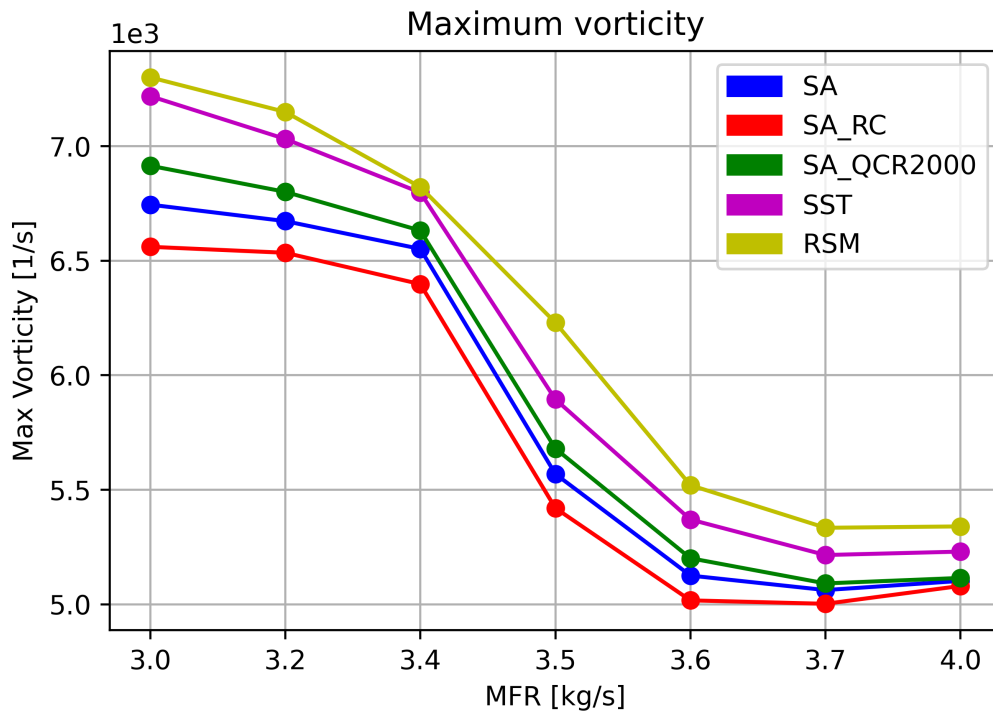


Figure 4.11: Evolution of the maximum vorticity value with the MFR value at the AIP for each turbulence model along MFR

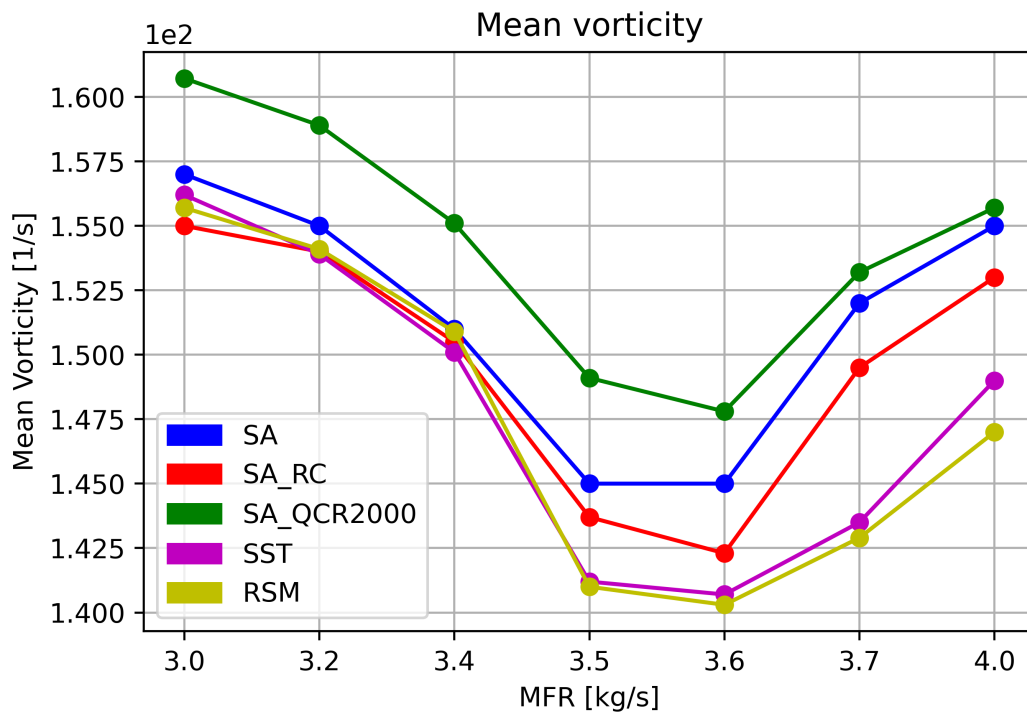


Figure 4.12: Evolution of the mean vorticity value with the MFR value at the AIP for each turbulence model along MFR

The vorticity values are calculated solely on the plane located at the fan face. The values located less than 5mm from the wall are not taken into account to avoid the influence of the boundary layer, in which there are large velocity gradients. Figure 4.11 illustrates the maximum value calculated in the described region. The RSM model, followed by $k-\omega$ SST, exhibit stronger vorticity values in all cases. The SA, SA-RC and SA-QCR2000 models exhibit some differences in their maximum vorticity values when the flow is separated, but these differences are minimal when the flow is attached.

Figure 4.12 shows the mean value of vorticity in the same plane as figure 4.11. In all cases, the mean value of vorticity in the plane is minimal just around the mass flow rate for which separation occurs. In all cases, the mean value of the $k-\omega$ SST and RSM models are lower than for other models. This is more evident when the flow is attached. Interestingly, all models of turbulence, with the exception of SA-QCR200, tend to give rather similar average values.

4.3 Effects of flow parameters

4.3.1 Boundary layer thickness

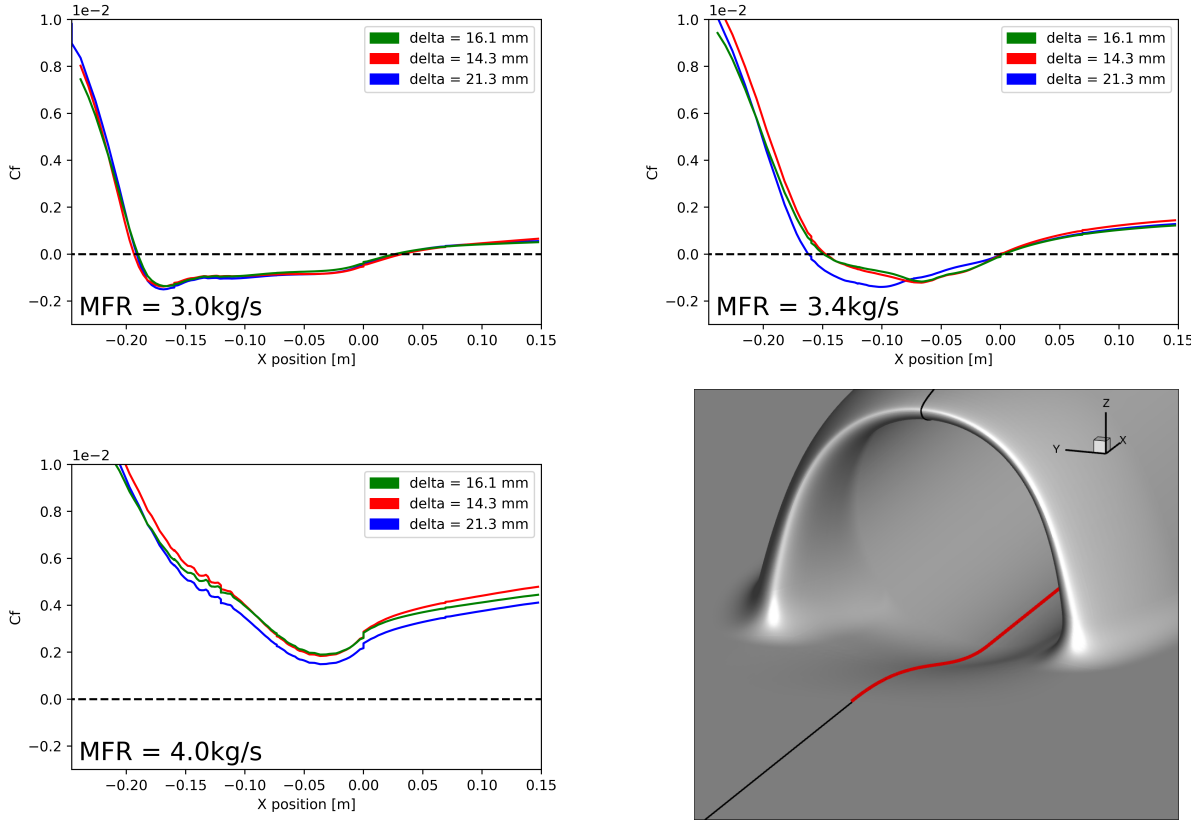


Figure 4.13: Skin friction coefficient on the intake ramp for different boundary layer thicknesses, $y = 0$ mm.

For the purpose of this analysis, three different thicknesses of boundary layer were utilized, one greater and one smaller than the one used previously. The remaining flow conditions were kept constant. The turbulence model employed in this case was the Spalart-Allmaras SA. Figure 4.13 illustrates the skin friction coefficient of these simulations for a mass flow rate of 3.0, 3.4, and 4.0 kg·s⁻¹. In all cases, a slight change in the boundary layer thickness did not seem to significantly affect this value. Furthermore, a thick boundary layer was observed to exhibit lower skin friction values, while a thick boundary layer slightly advance the flow separation. These small changes in both the skin friction coefficient and the flow separation point are directly related to the exchange of energy occurring within the boundary layer.

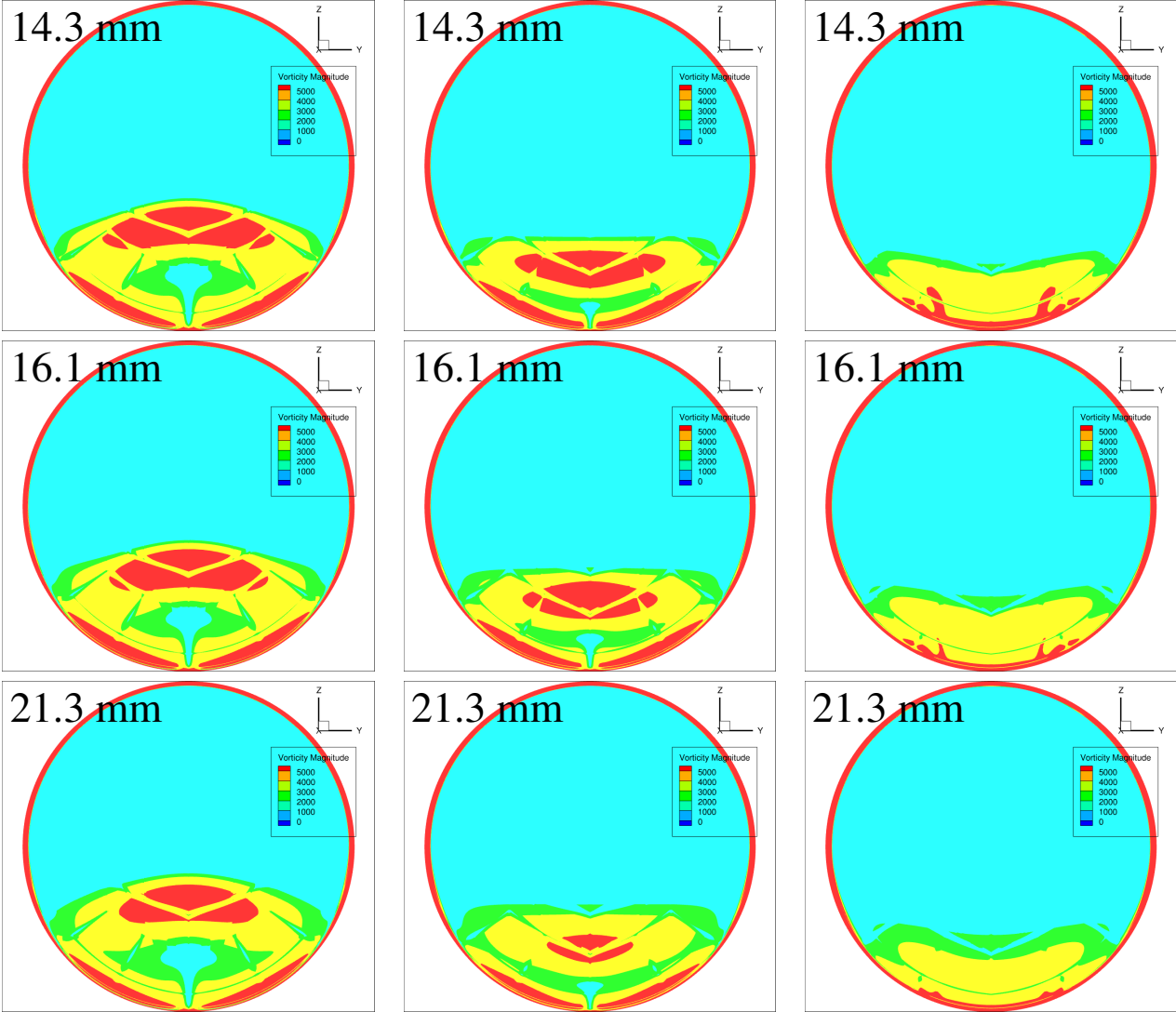


Figure 4.14: Vorticity field at fan face for each boundary layer thickness. Left: 3.0 kg·s⁻¹, center: 3.4 kg·s⁻¹, right: 4.0 kg·s⁻¹

The vorticity magnitude for different boundary layer thicknesses at mass flow rates of 3.0, 3.4, and 4.0 kg·s⁻¹ is presented in Figure 4.14. The results indicate that the magnitude of vorticity is inversely proportional to the thickness of the boundary layer. Specifically, a thicker boundary

layer exhibits less vorticity magnitude at the AIP compared to the thinner boundary layer. This difference in vorticity can be attributed to the intensity of the vortices, which are partly linked to secondary flow. A thicker boundary layer results in a larger length in which the velocity change between the free flow and the innermost part of the boundary layer, thereby decreasing the intensity of the secondary flow. This behavior is observed even in cases without flow separation.

4.3.2 Mach number

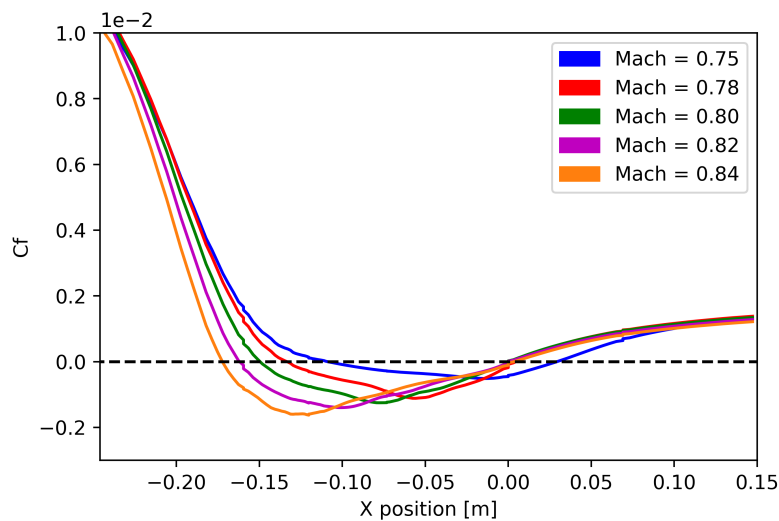


Figure 4.15: Skin friction coefficient on the intake ramp for different boundary layer thicknesses, $y = 0 \text{ mm}$ at $3.4 \text{ kg}\cdot\text{s}^{-1}$.

This subsection examines the impact of the Mach number on the coefficient of friction and the magnitude of vorticity at the AIP, similarly to the previous analysis. The Mach number was varied between 0.75 and 0.84 for a mass flow rate of $0.34 \text{ kg}\cdot\text{s}^{-1}$. Figure 4.15 illustrates the distribution of the skin friction coefficient along the intake ramp. The Mach effect is evident, with the friction coefficient decreasing as Mach number decreases, as expected. Furthermore, it can be observed that increasing the Mach number also leads to flow separation over the intake ramp.

Regarding the vorticity magnitude, Figure 4.16 shows that clear effects are caused by variations in Mach number. Specifically, an increase in Mach number results in an increase in the intensity of counteractive vortices, leading to higher vorticity values at the AIP.

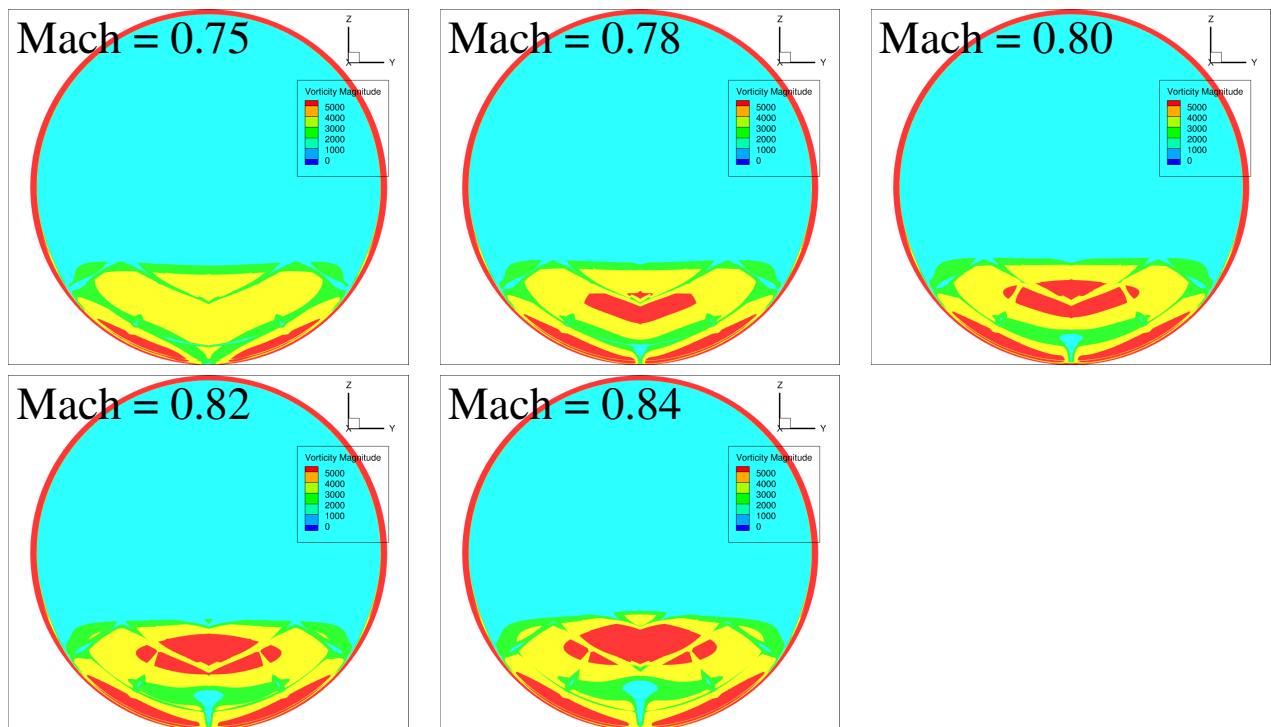


Figure 4.16: Effect of Mach number on vorticity field at fan face for each Mach condition at $3.4 \text{ kg}\cdot\text{s}^{-1}$.

4.4 Chapter summary and conclusions

This chapter describes part of the numerical analyses carried out to understand the physical phenomena in a BLI inlet and their changes according to different MFR values. In the first part, different turbulence models are presented highlighting their mathematical details. An analysis of the dependency of the results from the mesh density was carried out, using the total pressure loss in the AIP as a comparison parameter and a pair of distortion indices. Mesh convergence was demonstrated, with very small variations, from a mesh of 25 million elements.

A set of 35 simulations were carried out, which included five different turbulence models and seven MFR values, the latter varying between $3 \text{ kg}\cdot\text{s}^{-1}$ and $4 \text{ kg}\cdot\text{s}^{-1}$. As a general behavior, it was found that there is a flow separation at the intake ramp for low MFR values. There is a transition region between separated and attached flow, which varies slightly depending on the turbulence model. For high mass flow rates, the flow is fully attached at the entrance ramp and the differences between the different turbulence models are minimal. As expected from the literature, there is a presence of counter-rotating vortices in all simulations, which are secondary flow effects and horseshoe vortices.

The recirculation zone mainly affects the central zone of the intake ramp. The height at which flow detachment occurs varies slightly between different turbulence models, with models from the SA family generally exhibiting premature detachment compared to other models. It should

be noted that the SA-QCR2000 model tends to predict a more extensive recirculation zone compared to the other turbulence models. The RSM model tends to predict separation for mass flow rates lower than $3.4 \text{ kg}\cdot\text{s}^{-1}$, the $k\text{-}\omega$ SST for values less than $3.6 \text{ kg}\cdot\text{s}^{-1}$, and the SA family for values less than $3.7 \text{ kg}\cdot\text{s}^{-1}$.

The maximum values of vorticity in the AIP tend to increase with the flow separation size, being maximum for values close to $3 \text{ kg}\cdot\text{s}^{-1}$ in all models. These maximum values tend to decrease inversely with the value of MFR, showing a slight increase when the flow is fully attached to the inlet ramp, as shown in Figure 4.11. The maximum vorticity is predicted by the RSM model, followed by the $k\omega$ -SST and finally the SA family, with the SA-RC model predicting the lowest vorticity values. The mean vorticity values in the AIP show different results, with the SA-QCR2000 model showing quite a difference compared to the rest in these values. When the flow is detached, the rest of the models show similar values, but greater differences are found when the flow is attached to the intake ramp. The minimum mean values are predicted by the RSM model. These results indicate that probably the vortices generated by the RSM model are stronger and more concentrated than those of other models, while the SA family tends to diffuse vorticity values a little more.

In this chapter, we analyzed the impact of various parameters on the flow behavior in a BLI intake, including the thickness of the boundary layer and the Mach number in the free stream. Our analysis revealed that a thicker boundary layer tends to increase skin friction coefficient values over the intake ramp. Furthermore, it was observed that a thicker boundary layer leads to an early separation compared to other boundary layer thicknesses. Additionally, an increase in boundary layer thickness was found to decrease the vorticity magnitude in AIP.

Only the main physical phenomena involved in the BLI inlet were studied and compared from a CFD point of view. In the next chapters, it is proposed to study certain physical phenomena more specifically, such as total pressure loss in the AIP, distortion criteria and the study of some non-stationary physical phenomena through the use of hybrid RANS/LES hybrid simulations. An even more detailed analysis will also be carried out to compare the set of numerical results with experimental results.

Chapter 5

Analysis of the ZDES simulations

As shown in the previous chapter, the impact of the turbulence model on the solution is large, and the ability of each model to accurately predict physical phenomena varies. The same problem solved using different turbulence modelling can yield different solutions, as illustrated in Figure 5.1.

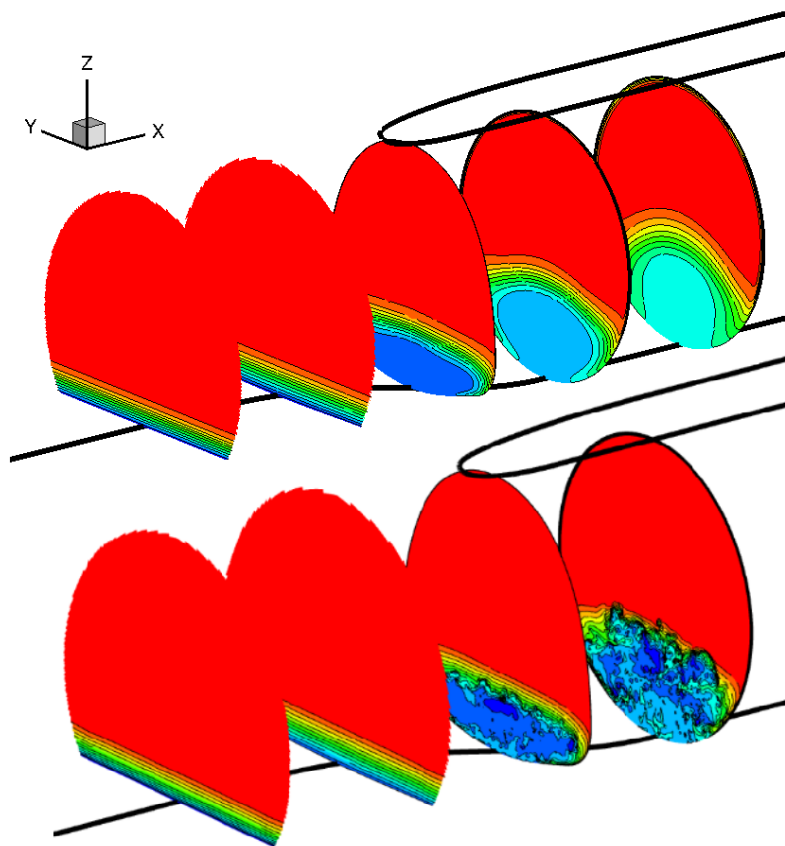


Figure 5.1: Total pressure loss along the BLI intake. Top: Spalart-Allmaras model. Bottom: ZDES mode 2 model.

The RANS closure models used in the previous sections are modelling the full turbulence spectrum. Those models are accurate when there is no flow separation but they prove not reliable for separated flows. For this type of flows, scale-resolving simulations (DNS, LES or hybrid RANS/LES) are expected to provide more accurate results. In this chapter we continue with the analysis of the BLI model, numerical simulations by using the Zonal Detached Eddy Simulation (ZDES) model, which is an hybrid RANS/LES model.

5.1 Scale-resolving simulations

RANS modelling is the most common and widespread approach in industrial applications. The RANS models provide time-averaged solutions by modeling all turbulence scales. This family of turbulence models has been utilized in previous chapters. All RANS models have some limitations due to the modelling assumptions used to derive the mathematical formulation of the model, it is becoming increasingly clear that certain classes of flows are better covered by models in which all or a part of the turbulence spectrum is resolved in at least a portion of the numerical domain. Such methods are termed Scale-Resolving Simulation (SRS) models. The main families of the SRS models are the Large Eddy Simulation (LES) and Direct Numerical Simulation (DNS).

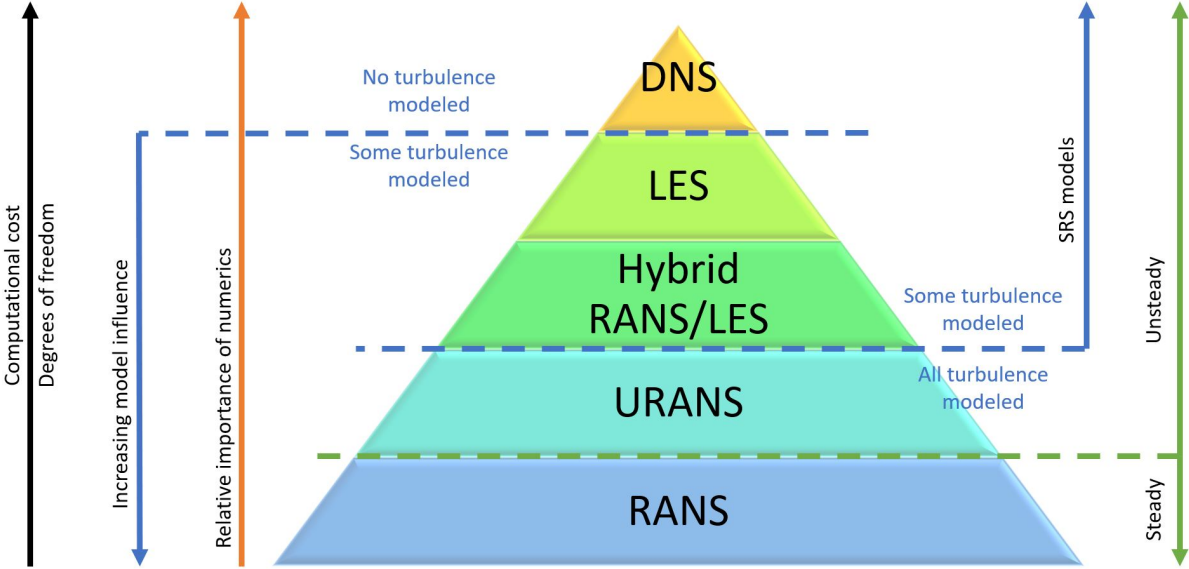


Figure 5.2: Hierarchy of different levels of turbulence modeling.

Figure 5.2 shows a general scheme of the turbulence models. The computational cost a CFD simulation increases from RANS to DNS as the number of degrees of freedom required to solve the flow increases. As a consequence of the computational cost, scale resolving approaches like DNS and LES are generally applied to simple geometries and moderate Reynolds numbers, while hybrid RANS/LES and RANS can be applied to complex industrial problems.

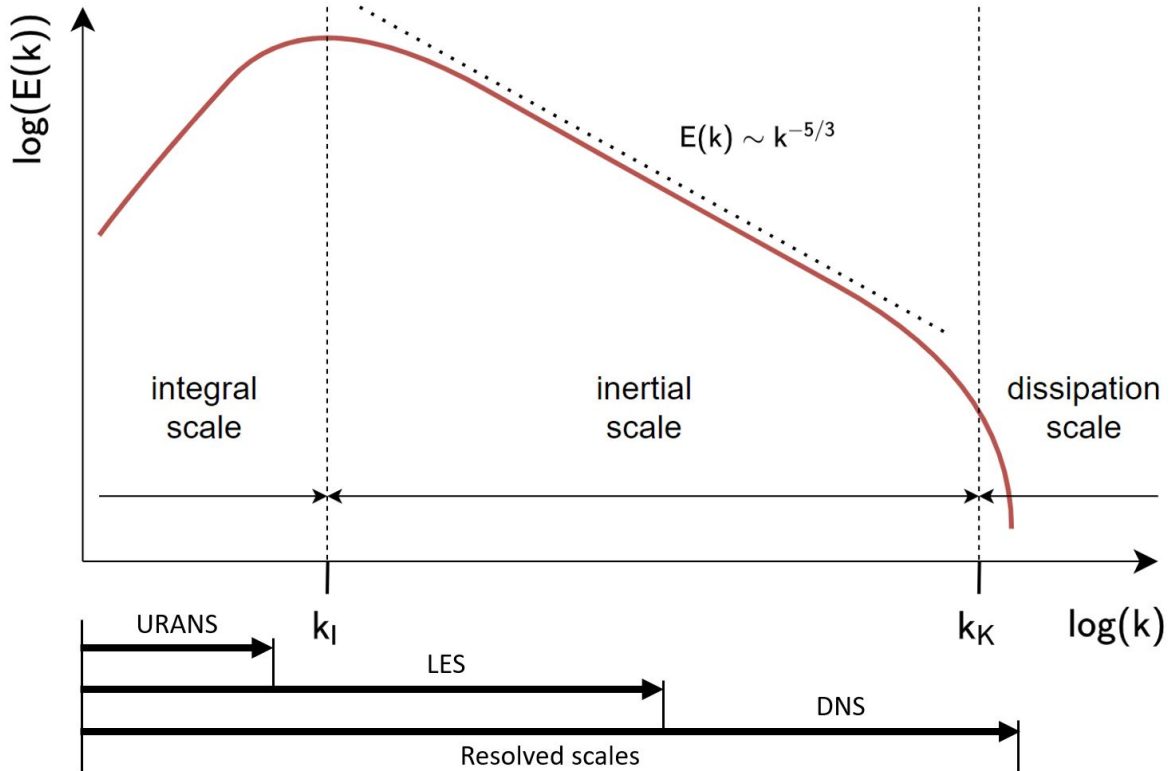


Figure 5.3: Energy distribution and scales in turbulence modeling.

There are two main motivations for using SRS models in favor of RANS formulations. The first reason for using SRS models is the need for additional information that cannot be obtained from the RANS simulation. Examples include acoustic phenomena or any other time dependant physical phenomena. The second reason for using SRS models is related to accuracy. It is known that RANS models have their limitations in accuracy in certain flow situations. RANS models have shown their strength essentially for attached flows, where the calibration according to the law-of-the-wall provides a sound foundation for further refinement. For free shear flows, the accuracy of RANS models is much lower. There is a wide variety of such flows, ranging from simple self-similar flows such as jets, mixing layers and wakes to impinging flows, flows with strong swirl, massively separated flows and many more. Considering that RANS models typically already have limitations covering the most basic self-similar free shear flows with one set of constants, there is little hope that even the most advanced Reynolds Stress Models (RSM) will eventually be able to provide a reliable foundation for all such flows [74] [75].

5.1.1 Direct Numerical Simulation (DNS)

A direct numerical simulation (DNS) is a simulation in computational fluid dynamics in which the Navier-Stokes equations are numerically solved without any turbulence model. This means that the whole range of spatial and temporal scales of the turbulence are resolved, as shown

in figure 5.3. DNS is the most accurate CFD method, as it does not introduce any modeling or approximation of the flow. However, DNS is also the most expensive CFD method, as it requires a very high computational cost and data analysis effort, therefore, this method is only used in very simplified academic cases [76].

5.1.2 Large Eddy Simulation (LES)

In LES, the smallest scales of turbulence are spatially filtered out while the largest, most energy containing scales are resolved directly. Due to the nature of turbulence, at a very small scale, the flow structures tend to be similar to each other even in different applications. This allows the use of simpler turbulence models that tend to be more universal and can be applied to several applications with a reduced requirement of model tuning [77].

Similarly to RANS modelling, in LES turbulence models aim at resolving the unknown terms in the filtered Navier-Stokes equations, called the Sub-grid Scale stresses. The term comes from the fact that in most LES models, the filtering of the equations is obtained at mesh size level, relegating the modelling to flow scales smaller than the grid size. LES modelling offers increased range of applicability and increased fidelity of the solution but all of this comes with an increased computational cost due to the time step requirements, as we can no longer consider the flow steady, and increased mesh resolution required to capture more details of the flow.

5.1.3 Hybrid RANS/LES models

A hybrid RANS/LES method combines the main benefits of both turbulence model families. The method provides the precision of Large Eddy Simulation models in regions where it is needed, while maintaining a relatively low computational cost. This allows for its implementation in some industrial applications. Hybrid RANS/LES methods modify existing Reynolds-averaged closures to provide scale-resolving functionality in regions of the computational domain with sufficient grid resolution to support the resolution of turbulent structures. In practice, this usually involves an attempt to resolve some fraction of the turbulence in free shear flows and possibly the outer portion of turbulent boundary layers.

A large percentage of hybrid RANS/LES models can be represented as some sort of blend between the equations governing the Reynolds-averaged and spatially-filtered Navier-Stokes equations or a sub-set of equations. Some hybrid formulations involve a blending of the modeled turbulent viscosity [78] [79], while others suggest a blend of the turbulent length scale [80]. While not all hybrid RANS/LES models are designed to provide a wall-modeled LES functionality, several formulations have been developed with this simulation strategy in mind. However, it should be emphasized that for any hybrid RANS/LES formulation to function as an effective wall-modeled LES, the underlying grid must provide a level of grid resolution that can capture a high fraction of the turbulence energy in the outer portion of the boundary layer.

This requirement forces the use of more isotropic grid elements within the boundary layer as compared with hybrid RANS/LES formulations that treat the entire boundary layer as a RANS region.

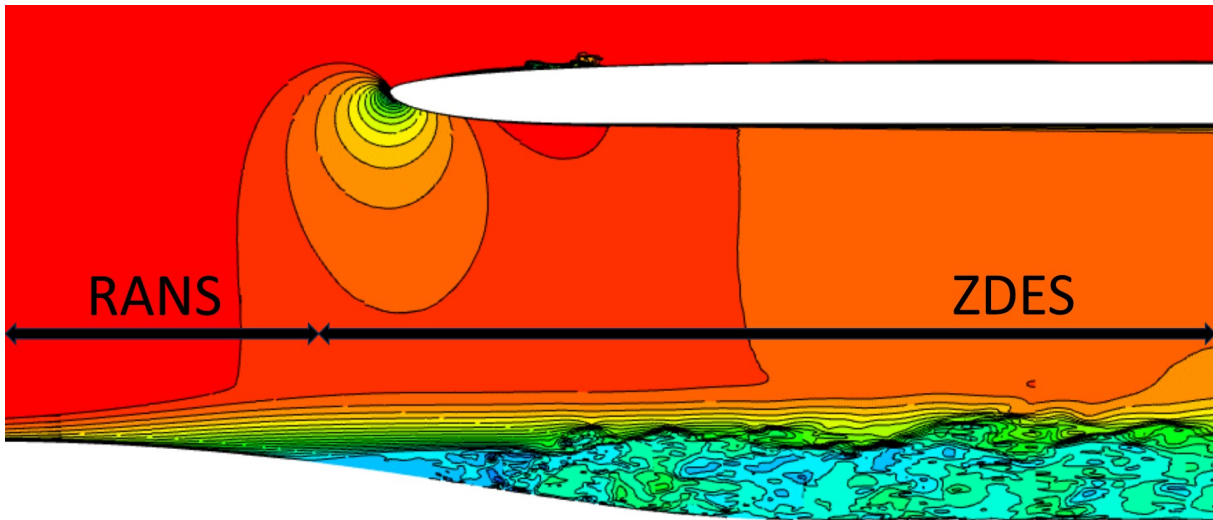


Figure 5.4: Illustration of the zonal solving with ZDES by the visualisation of flow velocity at the intake.

5.2 Zonal Detached Eddy Simulations

As explained in last section, it is possible to find a balance between costs and precision in RANS/LES hybrid methods. These methods are known to adopt RANS behavior within the boundary layer and LES behavior in the free field, reducing the cost of resolving turbulent flow. A very detailed presentation of the existing models is presented in [81].

Depending on the desired precision, a variable part of the boundary layer is then modeled by RANS method. When only the first 10 percent of the boundary layer from the wall (internal area) is modeled, we can assimilate the hybrid method to an LES with wall law (Wall-Modeled LES, WMLES), and we're talking about zonal approach. Conversely, when the entire thickness of the boundary layer is to be modeled, then it is a global approach.

In 1997, a global approach called Detached-Eddy Simulation was proposed [82]. However, two limits to its nominal operation have been identified. The first one results from gray zones where the model switches from RANS behavior to LES operation. In these regions of the calculation domain, located at the outer boundary of the attached boundary layers, the modeled turbulence is destroyed by the model but this destruction occurs over a non-zero distance. The resolved content does not grow fast enough because the RANS branch has a stabilizing behavior as long as modeled content remains, which generates a global turbulence deficit. The second limit

identified consists of a delay in the development of instabilities producing resolved turbulence in free shear layers, for example in the case of detachment of the boundary layer. This delay is due to the continued activity of the RANS model, which dampens fluctuations, during the transition to LES mode.

Recent studies have made it possible to propose a global model that prevents the two risks mentioned above. The Zonal Detached Eddy Simulation (ZDES) is a method developed since the beginning of the 2000s at ONERA [83]. It proposes four modes of operation that can be used simultaneously within the same simulation. Thus, in mode 0, the ZDES behaves identically to the Spalart and Allmaras model (SA) [60]. Modes 1 and 2 are global hybrid approaches, initially distinguished by different sub-grid scales and a manual and automatic specification respectively of the LES [84], branch passage zones, similar to DES97 [82] and DDES [85]. The mode 3 is a Wall-Modeled Large Eddy Simulation model (WMLES) [86]. All the aforementioned modes utilize a solitary transport equation for the variable $\tilde{\nu}$, which is also employed by the Spalart-Allmaras family of models. Recently, a significant improvement to the ZDES mode 2 has been proposed [87]. This improvement guarantees the protection of the entire boundary layer thickness while simultaneously allowing for the development of rapid instabilities in case of passage in branch LES. Figure 5.5 shows the different ZDES modes. The behaviors of these models have been scrutinized, validated and analyzed by numerous studies [88][89][90][91], and more recently in diverse applications, such as axial compressor studies [92], study of launchers and burners [93][94], characterization of behavior of the boundary layer [95][96][97], acoustic studies [98], characterization of distortion in air inlets [99], etc.

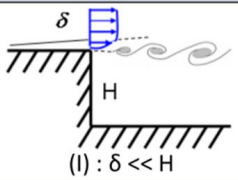
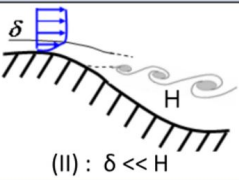
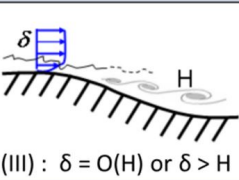
Zonal Detached Eddy Simulation (ZDES)			
	Mode 1	Mode 2	Mode 3
Flow category	 (I) : $\delta \ll H$	 (II) : $\delta \ll H$	 (III) : $\delta = O(H)$ or $\delta > H$
Applications	Base flow, free shear flows, spoilers, steps, slat/flap cove, etc.	Buffet, flaps, duct flows, nacelle intake, etc.	Corner flows, turbulent boundary layer, separation onset on high lift devices, shallow separations, etc.

Figure 5.5: Classification of typical flow problems and associated ZDES modes ((credit:ONERA)).

Currently, ZDES mode 2 is the only hybrid RANS/LES method that enables robust automatic processing of boundary layers by the RANS model, including the wake zone and independent of the mesh. Therefore, this mode has been selected for the present industrial application. The mathematical model is based on the Spalart-Allmaras model [60], so the ZDES adds a transport equation for the variable $\tilde{\nu}$ to the RANS equations. The production and dissipation

terms associated with this new transport equation are described in equations [5.1](#).

$$P_{\tilde{v}} = c_{b1}\rho\tilde{S}\tilde{v} \quad D_{\tilde{v}} = c_{w1}\rho f_w^{(II)} \left(\frac{\tilde{v}}{\tilde{d}^{(II)}} \right) \quad (5.1)$$

The hybrid characteristic distance, $\tilde{d}^{(II)}$ is a wall distance function n , as shown in equation [5.2](#). The sub-grid scale ($\tilde{\Delta}^{(II)}$) is defined in function of the mesh local properties, as shown in equation [5.3](#). The Δ_{max} refers to the largest dimension of the current mesh cell, while Δ_{ω} is the square root from the section of the same cell orthogonally to the local vorticity vector [\[84\]](#) [\[100\]](#).

$$\tilde{d}^{(II)} = n - f_p \max \left(0; n - C_{DES} \tilde{\Delta}^{(II)} \right) \quad (5.2)$$

$$\tilde{\Delta}^{(II)} = (1 - \Upsilon_{\Delta}) \Delta_{max} + \Upsilon_{\Delta} \Delta_{\omega} \quad (5.3)$$

$$\Upsilon_{\Delta} = 1_{f_d(r_d) > f_{d,0}} \cdot 1_{1 - [1 - f_{P,2}(r_c, \zeta_{\tilde{v}})] f_R(\zeta_{\Omega}) > f_{d,0}} \quad (5.4)$$

In addition, the definition of the sub-grid scale $\tilde{\Delta}^{(II)}$ uses the Boolean test shown in [5.4](#). The function $f_{\omega}^{(II)}$ is defined in equation [5.5](#). Similar to the sub-grid scale, the function $f_{\omega}^{(II)}$ also uses a Boolean test defined in [5.6](#).

$$f_{\omega}^{(II)} = (1 - \Upsilon_w) f_w + \Upsilon_w [(1 - \Upsilon_{\Delta}) \cdot 100 + \Upsilon_{\Delta} f_w^I] \quad (5.5)$$

$$\Upsilon_w = 1_{f_d(r_d) > 1 - f_{d,0}} \cdot 1_{1 - [1 - f_{P,2}(r_d, \zeta_{\tilde{v}})] f_R(\zeta_{\Omega}) > 1 - f_{d,0}} \quad (5.6)$$

The protection function is constructed using three auxiliary functions: f_d (originally from DDES), $f_{P,2}$ and f_R . Its role is to differentiate between areas where the model must adopt a RANS behavior ($f_P = 0$) and those where it is desirable to have an LES branch switch ($f_P = 1$), as shown in equation [5.7](#). The auxiliary functions are shown in equations [5.8](#) [5.9](#) [5.10](#).

$$f_P = f_d(r_d) [1 - [1 - f_{P,2}(r_d, \zeta_{\tilde{v}})] f_R(\zeta_{\Omega})] \quad (5.7)$$

$$f_d(r) = 1 - \tanh \left[(C_1 r)^{C_2} \right] \quad (5.8)$$

$$f_{P,2}(r, \varsigma) = \frac{f_d(\beta r)}{f_d(r)} f_d(\varsigma) \quad (5.9)$$

$$f_R(\varsigma) = \begin{cases} 1 & \text{if } \varsigma \leq C_4, \\ \frac{1}{1 + \exp\left[\frac{-6\alpha}{1-\alpha^2}\right]} & \text{if } C_4 < \varsigma \leq \frac{4}{3}C_4 \text{ with } \alpha = \frac{\frac{7}{6}C_4 - \varsigma}{\frac{1}{6}C_4} \\ 0 & \text{if } \varsigma > C_4 \end{cases} \quad (5.10)$$

In order to protect the viscous sublayer, the parameter r_d is utilized and calculated through equation 5.11. The protection of the wake zone ($\varsigma_{\tilde{v}}$) is calculated according to equation 5.12. The inhibitory function of the wake when the boundary layer detaches (ς_{Ω}) is calculated according to equation 5.13.

$$r_d = \frac{\tilde{v} + \nu}{\kappa^2 n^2 \sqrt{\sum (\partial_{x_j} u_i)^2}} \quad (5.11)$$

$$\varsigma_{\tilde{v}} = \frac{C_3 \max\{0; -\partial_n \tilde{v}\}}{\kappa n \sqrt{\sum (\partial_{x_j} u_i)^2}} \quad (5.12)$$

$$\varsigma_{\Omega} = \partial_n \Omega \sqrt{\frac{\tilde{v}}{\left[\sqrt{\sum (\partial_{x_j} u_i)^2}\right]^3}} \quad (5.13)$$

To avoid unwanted LES branch passes caused by numerical errors associated with the vorticity gradient reconstruction, the f_R inhibition function may be restricted to 1 in regions where the intensity of vorticity is low relative to the overall rate of fluid deformation 5.14.

$$f_{R,lim}(\varsigma_{\Omega}) = \begin{cases} f_R(\varsigma_{\Omega}) & \text{if } \Omega \geq \zeta \sqrt{\sum (\partial_{x_j} u_i)^2} \\ 0 & \text{otherwise} \end{cases} \quad (5.14)$$

C_1	C_2	C_3	C_4	$f_{d,0}$	β	ζ
8	3	25	0.03	0.8	2.5	0.8

Table 5.1: Zonal-Detached Eddy Simulation (ZDES) mode 2 numerical parameters

$$\tilde{S} = \Omega + \frac{\tilde{v}}{\kappa^2 n^2} f_{v,2}^{(II)} \quad (5.15)$$

The functions and parameters defined are calculated using the constants provided in Table 5.1.

Similar to the Spalart and Allmaras model (1992), a modified shear value is used to define the term turbulence production. This shear value is calculated using Equation 5.15. The $f_{v,i}^{(II)}$ function are calculated with the Boolean test previously presented.

5.3 BLI intake simulation using ZDES mode 2

This section applies previously developed knowledge and methods to simulate the boundary layer ingestion (BLI). The first step is to identify the physical phenomena to simulate. Both Chapter 3 and Chapter 4 obtained numerical and experimental results of this same configuration. In both analyses, flow separation in the intake ramp caused by the pressure gradient was observed. The simulations indicate that this flow separation is coupled with the formation of counter-rotating vortices, which are the confluence of horseshoe vortices and secondary flow due to the curvature of the intake ramp.

In other studies using S-ducts, it has been found that 90% of the turbulent kinetic energy has its spectral content between 0-900 Hz, which corresponds to a Strouhal number ranging up to 2.2 [5]. Concerning distortion at the AIP, some studies have found two main frequencies at $St = 0.42$ and 0.32 associated with the lateral movement of streamwise vortices and vertical perturbations ranging between $St = 0.26 - 1.0$ [101].

Similar results have been found in the analysis of the unsteady total pressure field [102]. The cases of the S-duct show similar physical phenomena, however it must be clarified that the velocity to adimensionalize the frequencies in the S-ducts is the one obtained in the AIP. In our case, the velocity obtained in the AIP is directly related to the mass flow rate. This velocity may vary between 116 and $155 \text{ m}\cdot\text{s}^{-1}$ for 3.0 and $4.0 \text{ kg}\cdot\text{s}^{-1}$ respectively. The flow separation occurs in the lower side of the intake, as shown in figure 5.6. This information is used to define the grid resolution for the LES region, defined in figure 5.7.

Grid cell size Δ plays as a threshold between modelled and resolved scales. The mesh resolution has been defined taking into account the physical phenomena discussed above. ZDES approaches require a dedicated mesh, complying with LES requirements in terms of refinement and mesh quality in areas where the phenomenon to be simulated in ZDES occurs, in this case the main event is the flow separation and shear layer at the intake ramp. The parameter to determine a grid size based on our physical phenomena is the shear layer momentum thickness (δ_w), shown in figure 5.8 and described by equation 5.16.

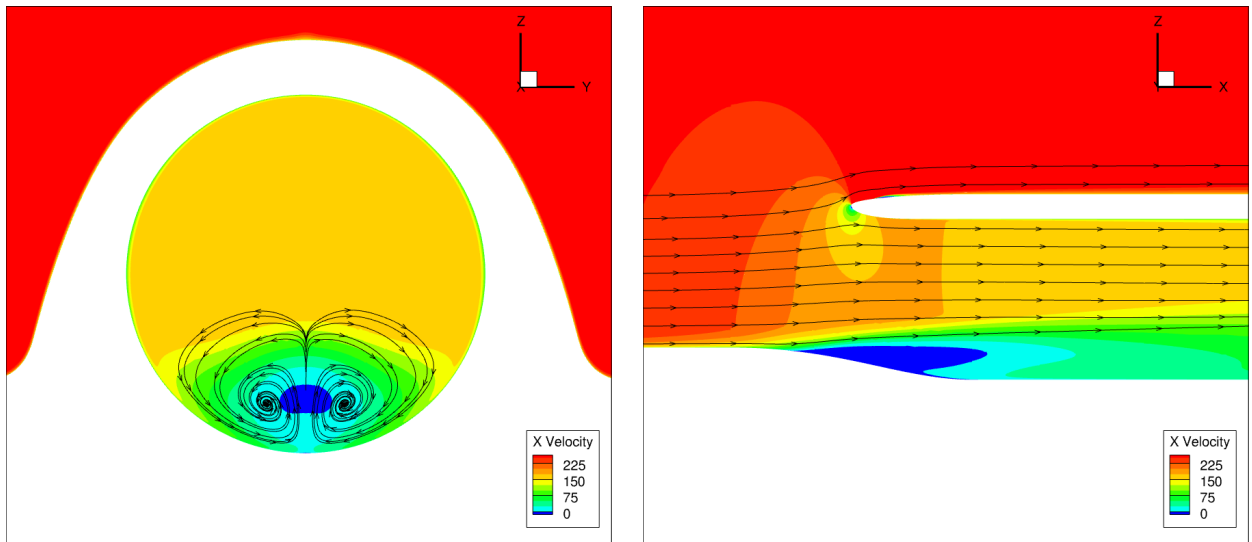


Figure 5.6: The axial velocity was obtained using the Spalart-Allmaras model (SA) for a mass flow rate of $3.0 \text{ kg}\cdot\text{s}^{-1}$. The dark blue region indicates the recirculation zones. The left image shows the axial velocity distribution in the Aerodynamic Interface Plane (AIP), while the right image shows the axial velocity distribution in the symmetry plane.

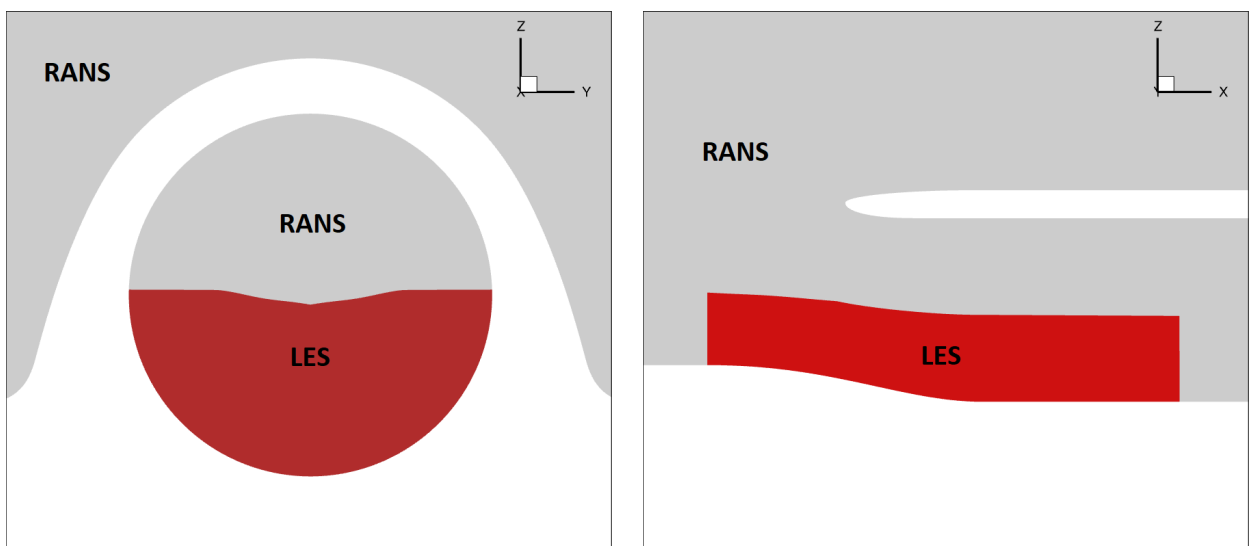


Figure 5.7: The region to refine in preparation for the Zonal Detached Eddy Simulation (ZDES) method is shown in red. The left image shows the region to refine in the Aerodynamic Interface Plane (AIP), while the right image shows the region to refine in the symmetry plane.

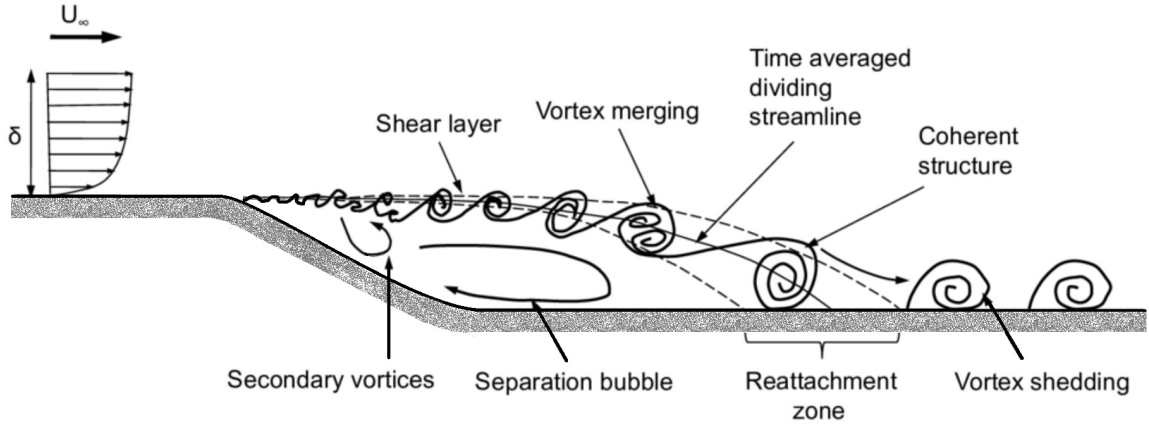


Figure 5.8: The flow over a curved intake ramp is characterized by the presence of unsteady physical phenomena that result from the separation of the boundary layer from the surface of the ramp. These unsteady phenomena include vortex shedding, flow separation, and reattachment.

$$\delta_w = \frac{U^+ - U^-}{\max \frac{\partial U}{\partial z}} \quad (5.16)$$

$$\Delta_x = \Delta_y = \frac{\delta_w}{2} \quad \Delta_z = \frac{\delta_w}{15} \quad (5.17)$$

The values of U^+ , U^- and $\max \frac{\partial U}{\partial z}$ were obtained from RANS solutions using the Spalart-Allmaras turbulence model at $3.0 \text{ kg}\cdot\text{s}^{-1}$. U^+ corresponds to the velocity above the shear layer, U^- corresponds to the velocity below the shear layer, and $\max \frac{\partial U}{\partial z}$ is the maximum variation of the mean velocity along the axis normal to the surface. The maximum grid size to capture the desired physical phenomena is shown in Equation 5.17. The value obtained for δ_w is 15 mm. According to Equation 5.17, Δ_z has an approximate value of 1 mm. A good practice for Large Eddy Simulations is to have a mesh that is as isotropic as possible. This means that the aspect ratio between the lengths of a mesh element should be as similar as possible. Therefore, the dimensions Δ_x and Δ_y are sized according to the value obtained for Δ_z . The Δ grid size chosen for this region is 0.5 mm.

The mesh used for the ZDES simulation is shown in Figure 5.9. The mesh is of the chimera type, with a refined region added to the original mesh. The rest of the mesh is topologically similar to the one used in the RANS simulations. This chimera method interpolates the values between the refined and the original region. Flow domain dimensions and edge conditions do not change with respect to RANS cases. The chosen mass flow rate values for the ZDES simulations corresponds to separated flow cases: $3.0 \text{ kg}\cdot\text{s}^{-1}$ and $3.4 \text{ kg}\cdot\text{s}^{-1}$.

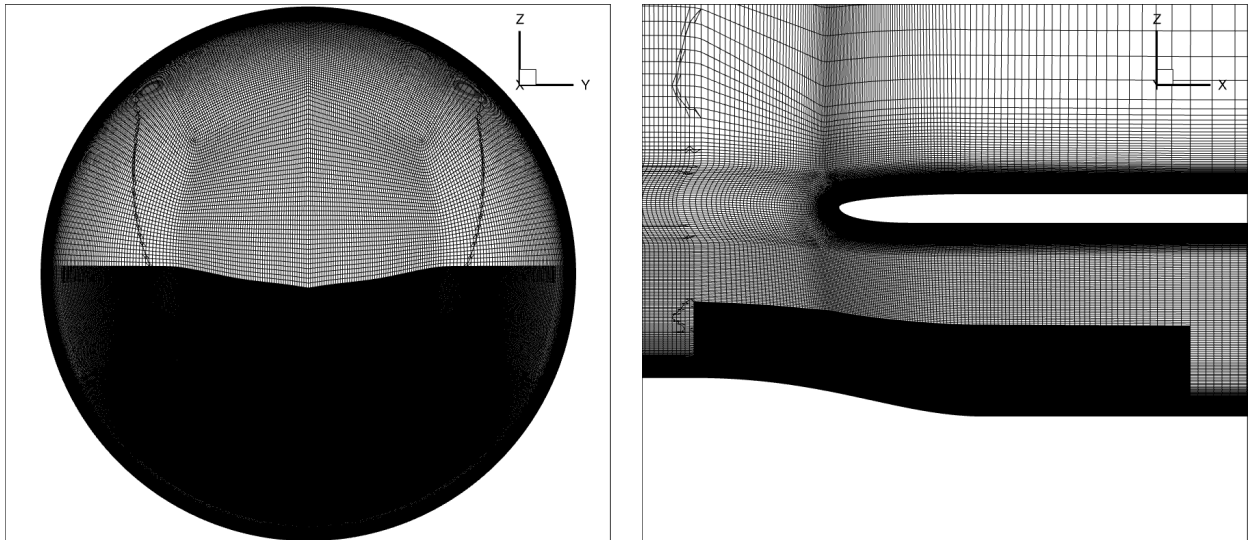


Figure 5.9: The Zonal Detached Eddy Simulation (ZDES) method employs a refined mesh with elements of maximum size 0.5 mm in each direction within a specific region. Left: AIP plane. Right: symmetry plane.

First, the solution has been converged on the new mesh using the Spalart-Allmaras model. Subsequently, the ZDES model was activated. For this simulation, a central AUSM + (P) scheme without artificial viscosity was used with a third-order limiter. The other numerical parameters were similar to those selected in RANS simulations.

In this study, we have selected a time step of $5 \cdot 10^{-7}$ seconds that satisfies the CFL condition and theoretically enables the capture of physical phenomena up to 1 GHz. However, it should be noted that the sample rate is defined at 100 kHz, which is significantly higher than the frequency range of physical phenomena described in the literature. Additionally, the inner loop consists of 5 sub-iterations, which is sufficient to ensure a one order of magnitude decrease of the residuals. The simulated total time is 0.1 second, which corresponds to 200000 time steps after the transient phase of the ZDES.

The extractions of the simulation consisted of 11 normal planes in axial and tangential directions, along with 150 probes located at various locations throughout the flow domain. The sampling rate for planes was 10 kHz, while that for probes was 100 kHz.

Figure 5.10 illustrates the instantaneous solutions for the two mass flow rates exported in different planes. In both simulations, flow separation occurs over the intake ramp with the lowest MFR having the strongest separation as expected. The total pressure and velocity field are impacted as shown in figure 5.10. In the following sections, the turbulent behavior is analyzed in more detail. This includes their role in the energy generated by the turbulent structures, as well as their impact on distortion in the AIP.

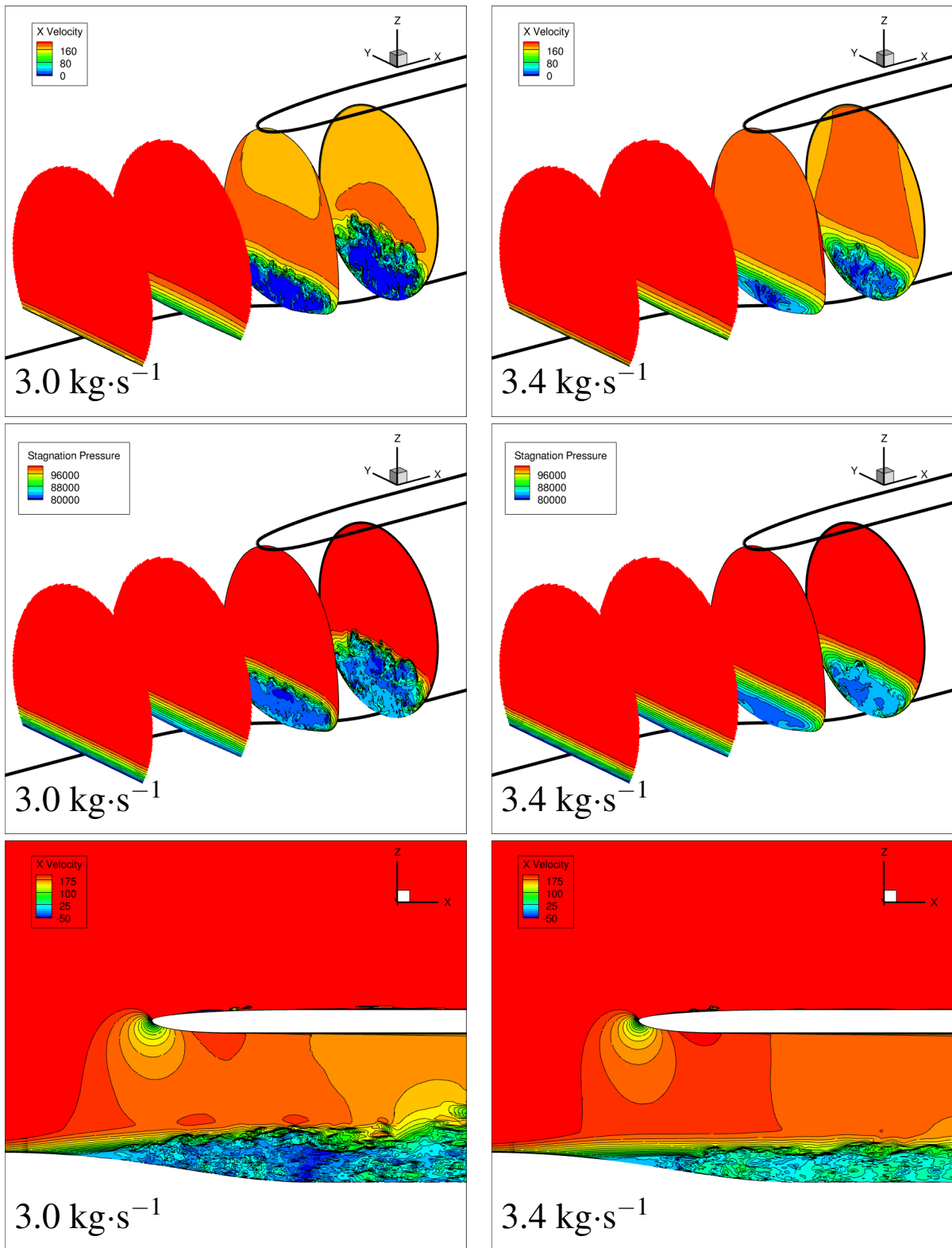


Figure 5.10: Instantaneous flow behavior predicted by the ZDES model. Left: $3.0 \text{ kg}\cdot\text{s}^{-1}$. Right : $3.4 \text{ kg}\cdot\text{s}^{-1}$. Up: Axial velocity in different planes. Center: Total pressure in different planes. Down: Axial velocity in the symmetry plane.

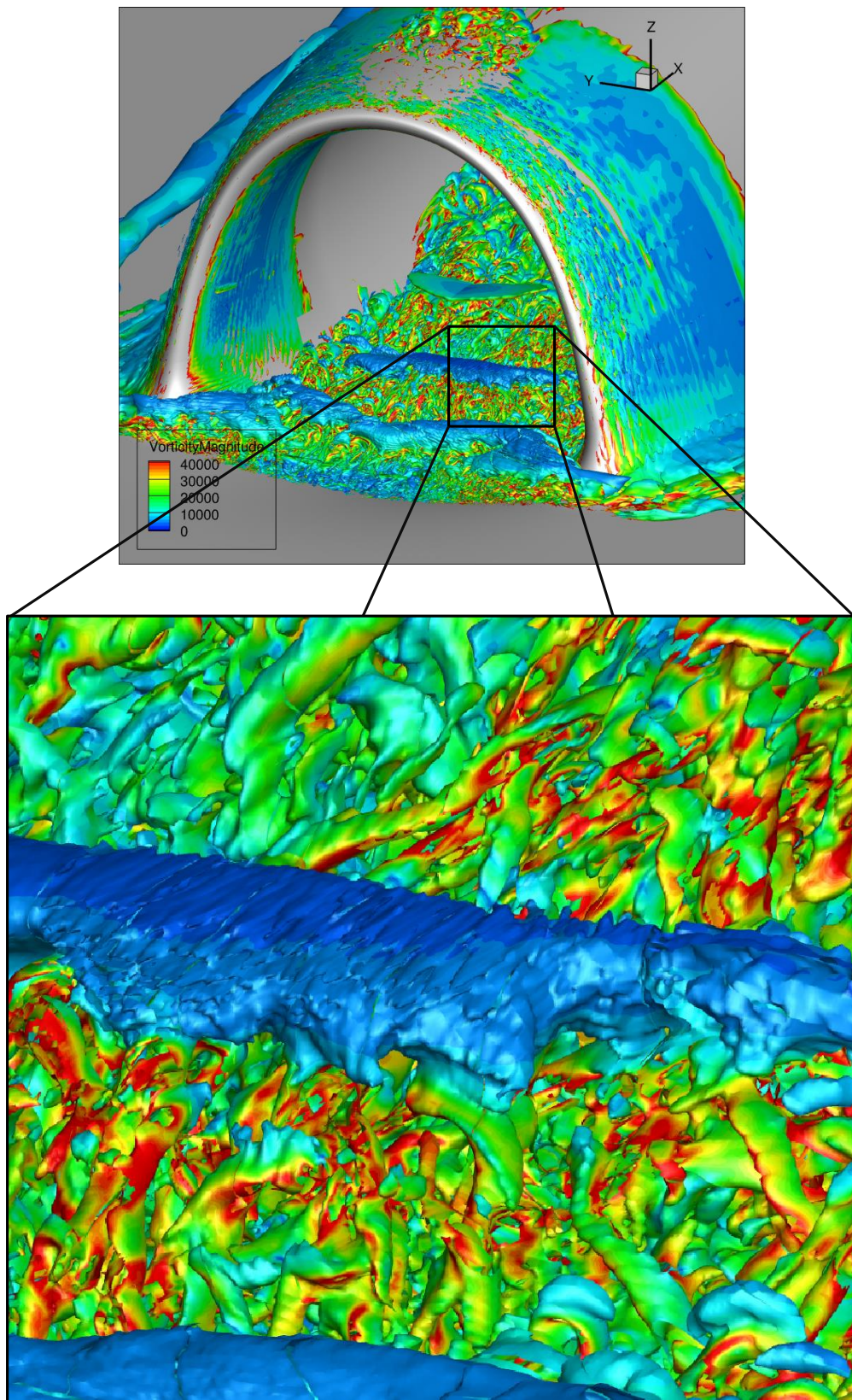


Figure 5.11: Turbulent structures visualized using an isovalue of Q Criterion for a mass flow rate of $3.0 \text{ kg}\cdot\text{s}^{-1}$. The color scale represents the vorticity magnitude.

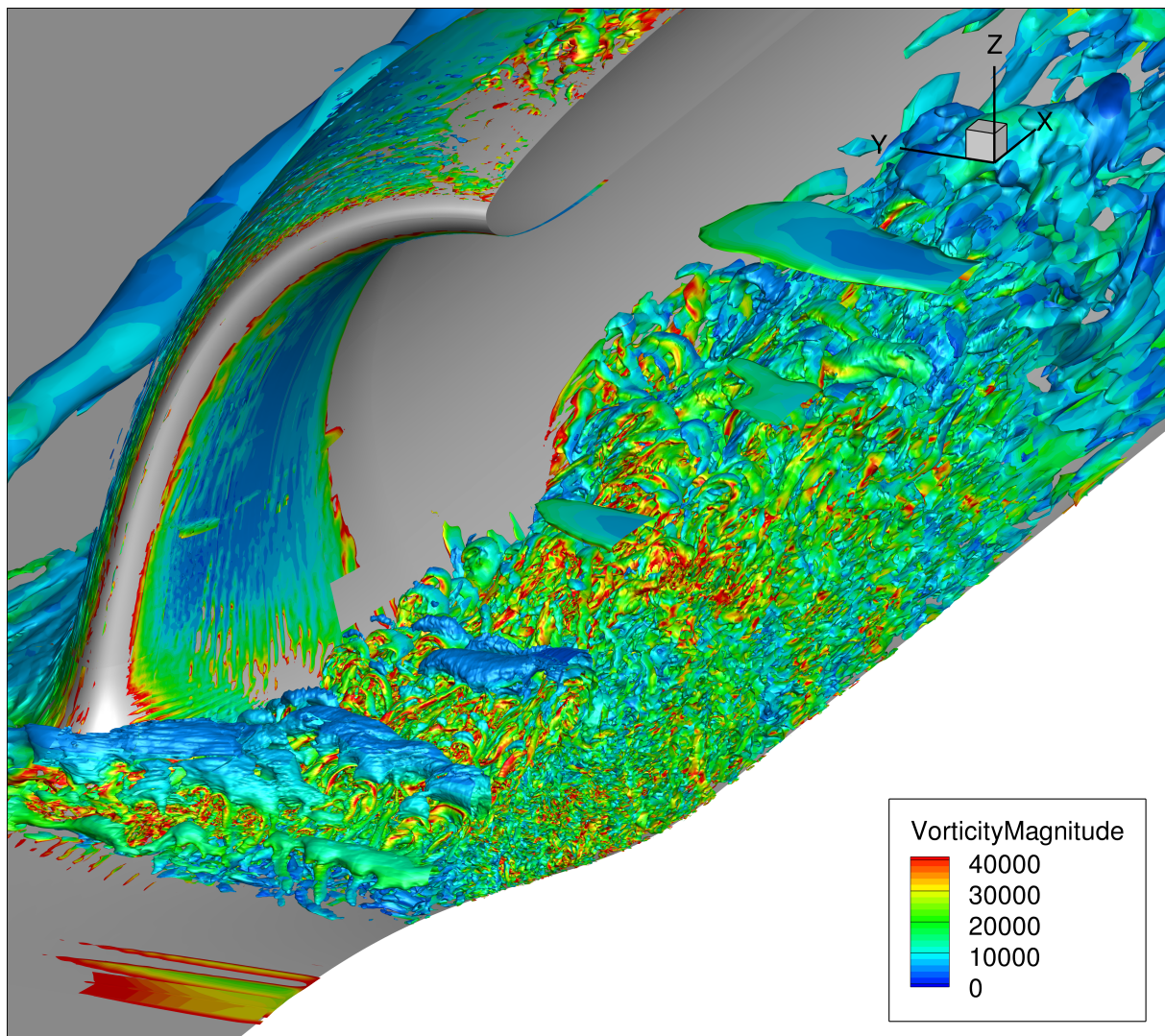


Figure 5.12: Turbulent structures cut by the symmetry plane showing the turbulence behaviour near the wall. The turbulence structures are visualized using an isovalue of Q Criterion for a mass flow rate of $3.0 \text{ kg}\cdot\text{s}^{-1}$.

Figures [5.11](#) and [5.12](#) illustrate the turbulence structures along the intake ramp. The first figure emphasizes turbulent structures by highlighting their upper part corresponding to the shear layer while the second figure makes a cut in the symmetry plane allowing identification of their behavior in the recirculating region. Vortex roll-up is visible in the shear layer as well as hairpin vortices. In the next section, the signals from different sensors are analyzed. The probe locations are the same as the Kulites in [3.25](#).

Signal analysis for sensors over the intake ramp

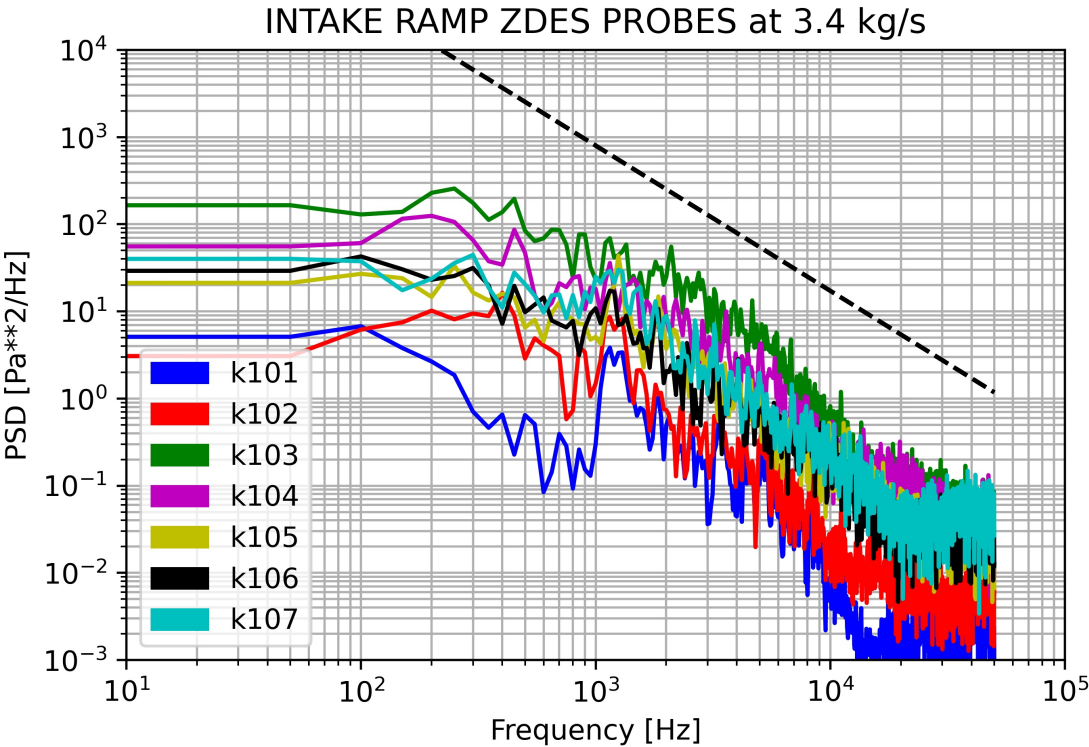
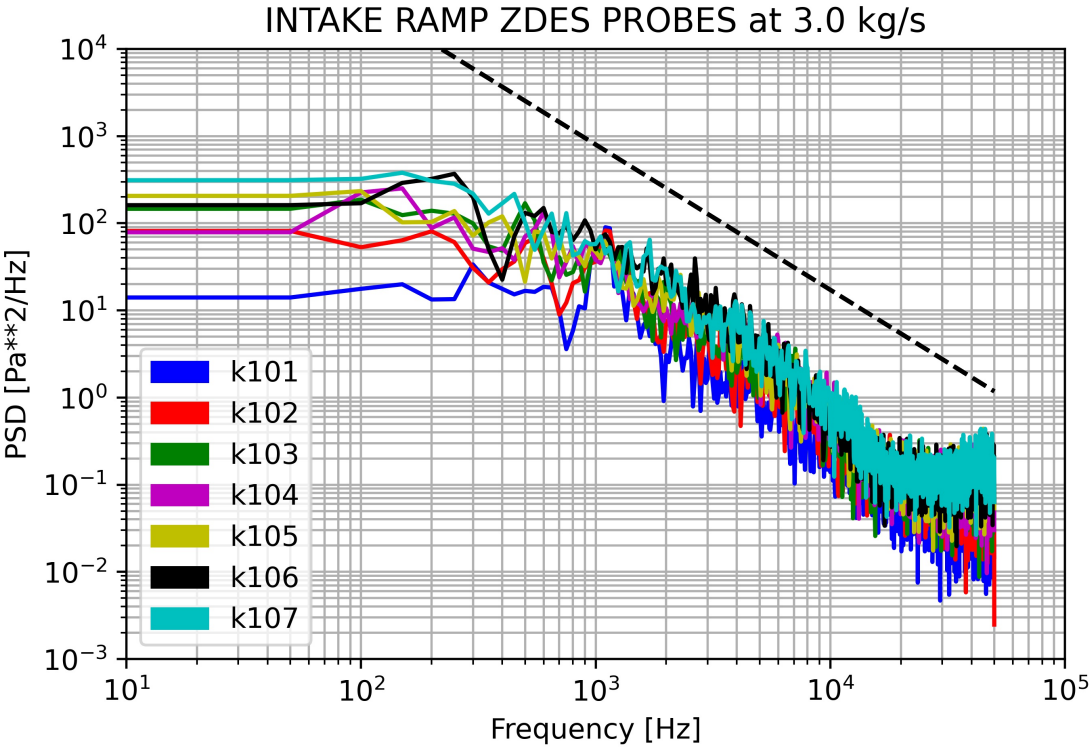


Figure 5.13: Power Spectral Densities (PSD) calculated for the probes placed over the intake ramp. The dotted line represents the -5/3 characteristic turbulent slope. Up: 3.0 kg·s⁻¹. Down: 3.4 kg·s⁻¹.

The plots presented in Figure 5.13 illustrate the spectral and distribution of energy. Two distinct behaviors are observed depending on the case analyzed. In the first case, corresponding to a mass flow of $3.0 \text{ kg}\cdot\text{s}^{-1}$, all pressure spectra are quite similar for the probes along the intake ramp. They exhibit a typical turbulent behavior with a slope of $-5/3$, as shown in Figure 3.23. All probes exhibit the same behavior, except for probe k101, which is located in the most upstream position but still on the intake ramp. This probe exhibits a bump around 1250 Hz, which could be related to some physical phenomenon. The probe is situated within the recirculation region, and its behavior is correlated with the position of the separation due to the MFR. The same frequency is also likely associated with oscillations of the shear layer, as illustrated in Figure 5.11.

The second case is characterized by a mass flow rate of $3.4 \text{ kg}\cdot\text{s}^{-1}$ and exhibits some dispersion in the energy levels between each probe. The first two probes in the direction of flow (k101 and k102) show a peak at 1250 Hz close to the one observed for a mass flow rate of $3.0 \text{ kg}\cdot\text{s}^{-1}$. As distance increases from these probes, sensors tend to exhibit a more classical turbulent behavior.

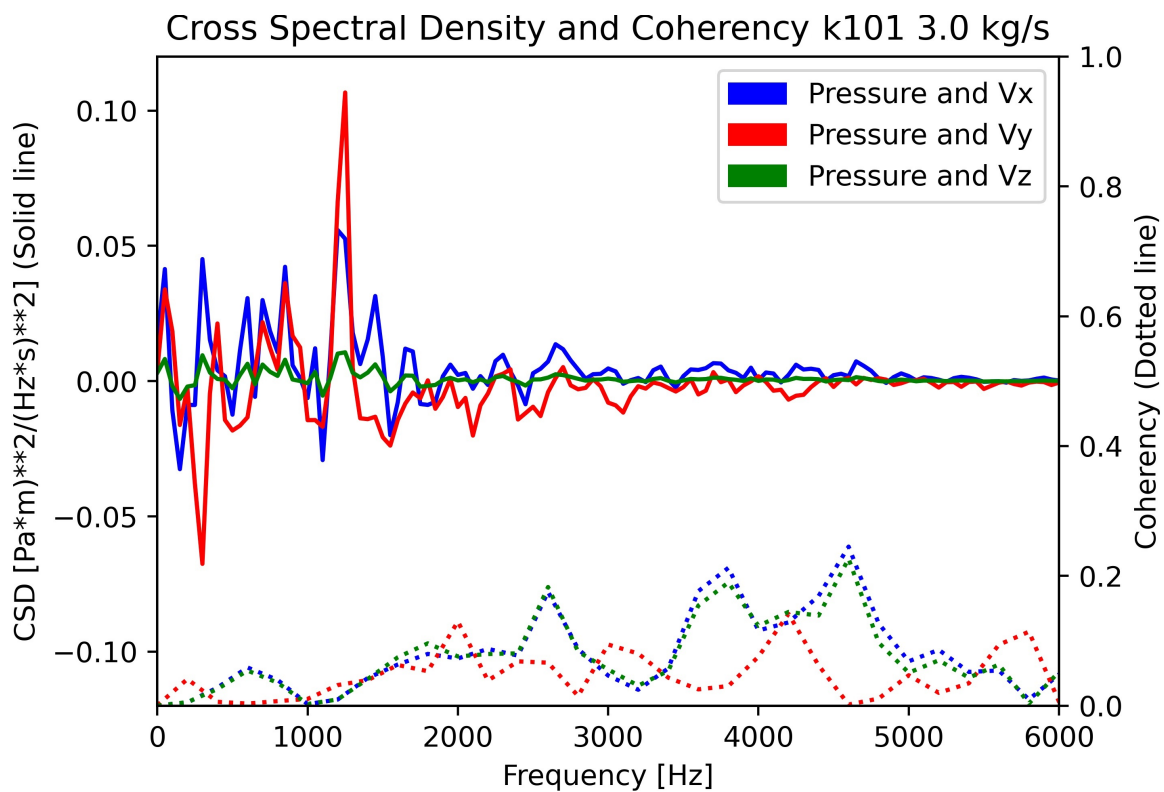


Figure 5.14: Cross Spectral density value between pressure and velocities signals from probe k101 at $3.0 \text{ kg}\cdot\text{s}^{-1}$. The right axis shows the CSD, represented by solid lines. The left axis shows the coherency, represented by dotted lines.

Figure 5.14 shows the CSD value obtained from pressure and velocity signals for k101 at $3.0 \text{ kg}\cdot\text{s}^{-1}$. In both cases (mass flow rates of $3.0 \text{ kg}\cdot\text{s}^{-1}$ and $3.4 \text{ kg}\cdot\text{s}^{-1}$), Cross Spectral Density between pressure and velocities for the k101 probe shows a peak of energy around the 1250 Hz

spectrum. However, the coherency between the pressure signal and the signals of the velocity components seems to be rather weak. This frequency corresponds to a Strouhal number of 0.854.

Signal analysis for sensors located at the AIP

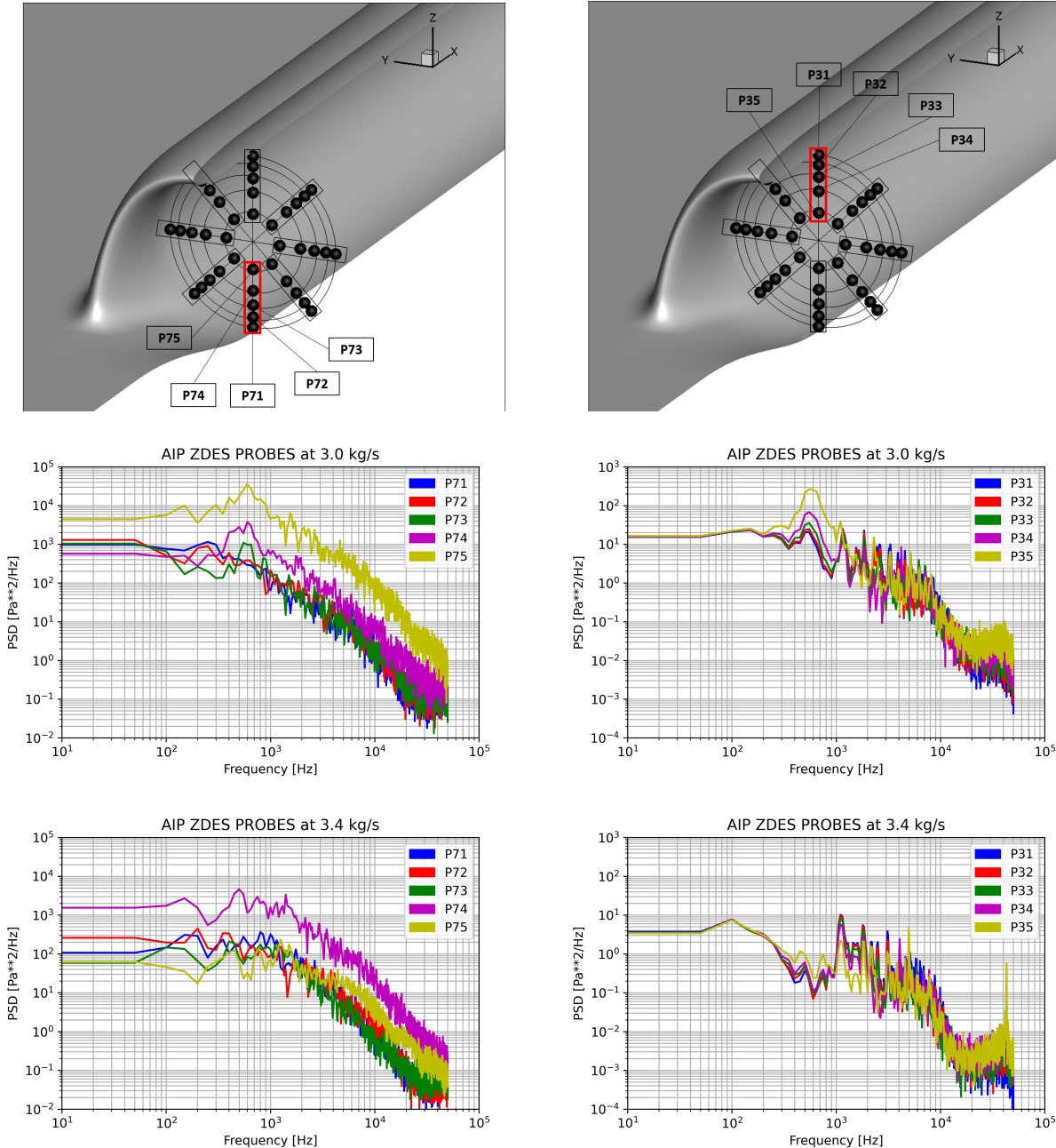


Figure 5.15: Power Spectral Densities for the sensors located on the vertical arms of the rake placed at the AIP. Left: lower arm 7 affected by the flow recirculation. Right: upper arm 3 located outside the recirculation zone.

The AIP is influenced by various physical phenomena, including flow recirculation, counter-rotating vortices, and some acoustic resonance effects. First, the vertical axis of the AIP is

analyzed, which includes arms 3 and 7. The latter is affected by the flow separation. In figure 5.15, the distributions of energy in the spectrum for these two arms are illustrated. In the left column, arm 7 shows an energy distribution characteristic of a completely turbulent flow. However, probes located in the innermost radius position show an increase in this turbulent kinetic energy, which reveals information about the shear layer. This energy is maximum for point P75 and P74 in cases of MFR $3.0 \text{ kg}\cdot\text{s}^{-1}$ and $3.4 \text{ kg}\cdot\text{s}^{-1}$, respectively. For the case of $3.0 \text{ kg}\cdot\text{s}^{-1}$ all probes show a peak of energy near 600 Hz. The pressure spectra corresponding to arm 3 are presented in the right column. For these probes a bump is clearly visible around 550-600 Hz. This bump is hypothesized to be associated with the frequency generated by vortices within the shear layer and the size of the recirculation region, which act as a cavity generating acoustic resonance. This resonance is propagated along the fluid domain. It is noteworthy that this observation is particularly pronounced for the probe located in the shear layer. For $3.4 \text{ kg}\cdot\text{s}^{-1}$, the PSD shows different peaks at 1200 Hz, 1800 Hz and their harmonics corresponding to a Strouhal numbers of 1.4 and 2.2.

The cross-spectral densities obtained using pressure and velocities are depicted in figures 5.16 and 5.17. The former displays the results for arm 7. A high coupling between axial velocity and pressure for point P75 can be observed in the frequency range of 450-600 Hz. A similar behavior is found for probe P74 for $3.4 \text{ kg}\cdot\text{s}^{-1}$, where there is a large coupling of pressure and axial velocity at 450 Hz. In both cases, this coupling is significant up to frequencies even greater than 1000 Hz. For these points, the graphs also show a much stronger coherency between the pressure and axial velocity signals compared to the other velocity components. The rest of the probes show relatively little coupling in the frequency domain. Most of these small couplings occur at low frequencies, with the exception of case $3.4 \text{ kg}\cdot\text{s}^{-1}$, which shows some coupling with axial velocity around 1250 Hz. It can also be mentioned that within the circulating region, the coherency shown between the pressure signal and vertical velocity is moderate, slightly higher than the rest of the components.

Concerning the upper arm 3, a coupling for the $3.0 \text{ kg}\cdot\text{s}^{-1}$ simulation between pressure and axial velocity for 600 Hz can be highlighted, which is maximal for the probe the closest to the shear layer. It is also possible to observe a less pronounced coupling between pressure and lateral and vertical velocities for the frequencies of 450 Hz and 650 Hz, respectively. Both vertical and axial velocities exhibit significant coherency with the pressure signal in this case. This coherency is accentuated around 500-600 Hz, although it is also high for higher frequencies. It should be noted that as one approaches the mixing layer, the coherency with the axial velocity becomes more important than with other variables. The analysis for $3.4 \text{ kg}\cdot\text{s}^{-1}$ shows a much smaller coupling, an axial velocity/pressure coupling at 100 Hz present in all probes can be highlighted.

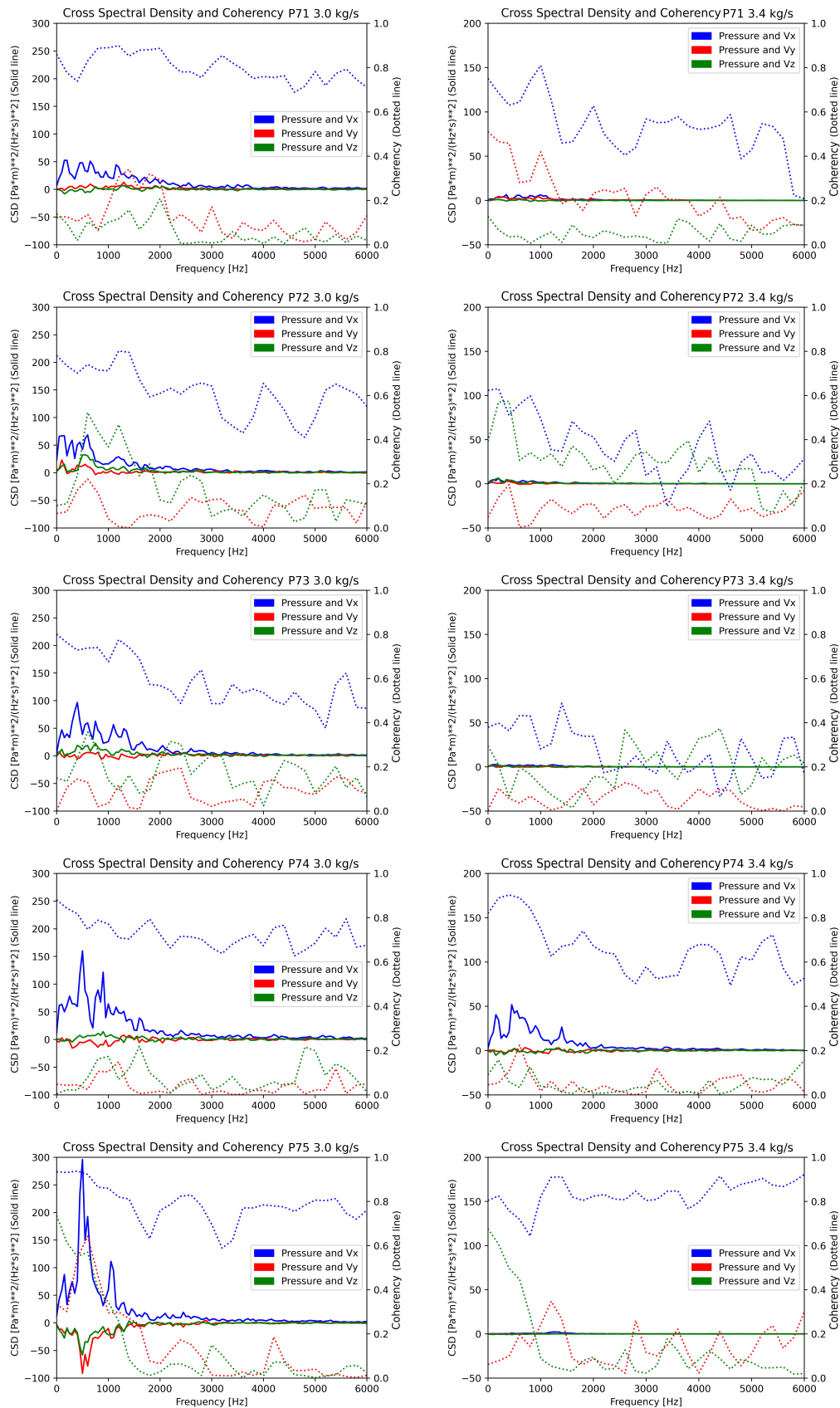


Figure 5.16: Cross Spectral density value between pressure and velocities for probes placed on arm 7. Left: $3.0 \text{ kg}\cdot\text{s}^{-1}$. Right: $3.4 \text{ kg}\cdot\text{s}^{-1}$. The right axis shows the CSD, represented by solid lines. The left axis shows the coherency, represented by dotted lines.

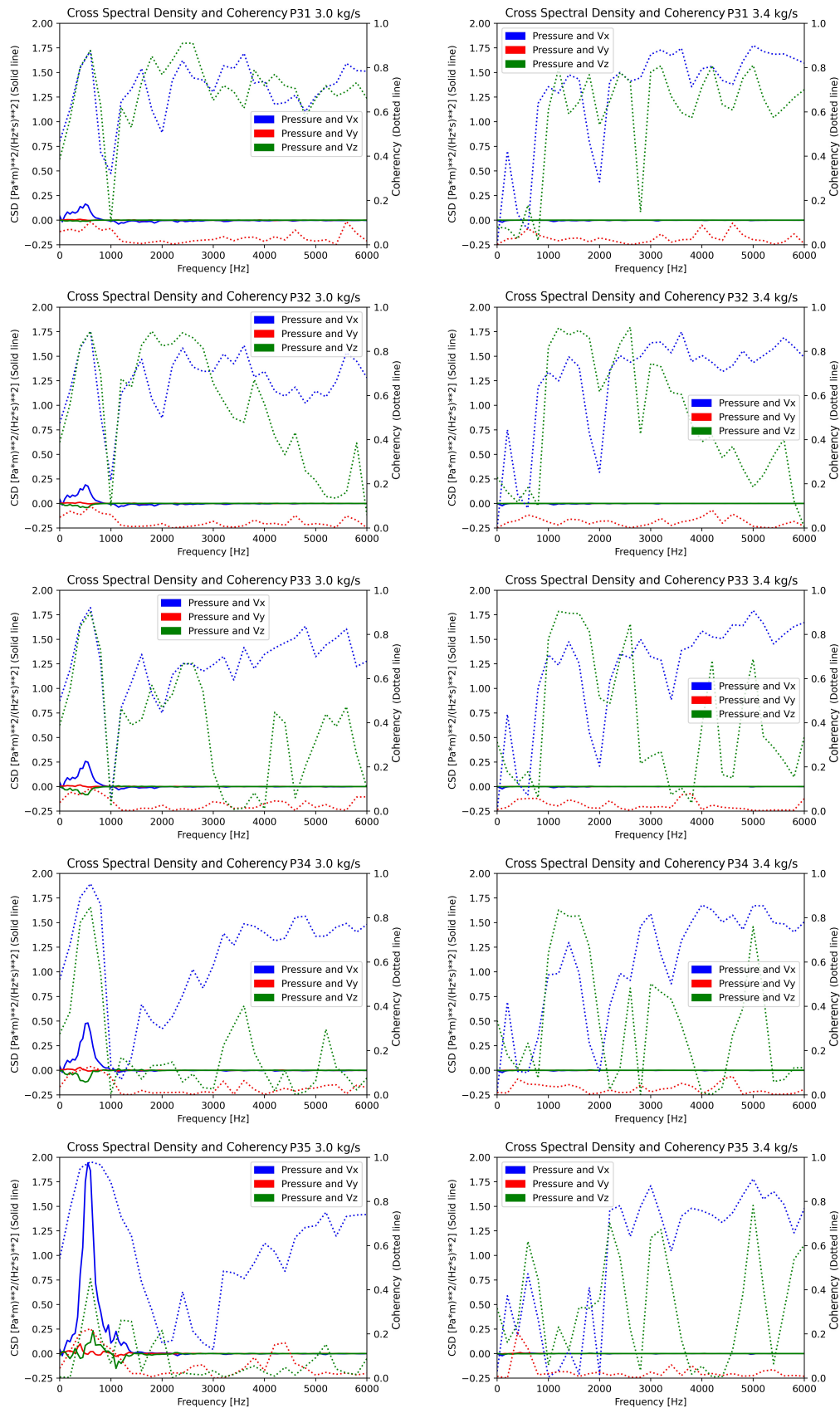


Figure 5.17: Cross Spectral density value between pressure and velocities for probes placed on arm 3. Left: $3.0 \text{ kg}\cdot\text{s}^{-1}$. Right: $3.4 \text{ kg}\cdot\text{s}^{-1}$. The right axis shows the CSD, represented by solid lines. The left axis shows the coherency, represented by dotted lines.

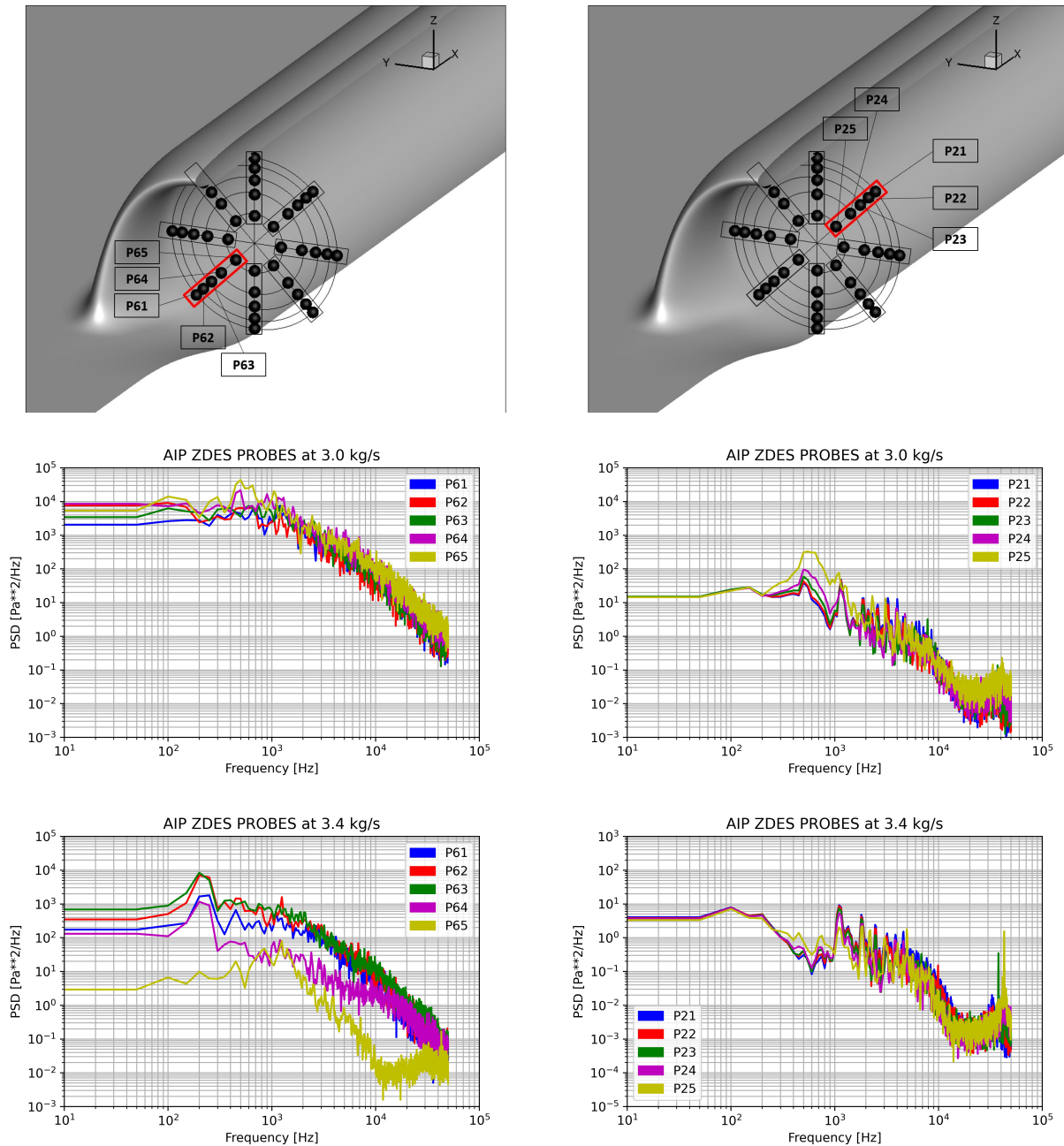


Figure 5.18: Power Spectral Densities for probes located on the diagonal arms of the rake placed at the AIP. Left: lower-diagonal arm affected by the flow recirculation. Right: upper-diagonal arm located outside the recirculation zone.

In addition, an other coupling with vertical velocity at 1100 Hz can be observed. A small coupling with lateral velocity at 700 Hz can be seen for the probe the closest to the shear layer. In this case the coherency seems to be more important for high frequencies, denoting coherency of moderate to high for both axial and vertical velocity components.

Figure 5.18 shows the PSD calculated on arms 2 and 6, corresponding to the diagonal at the AIP. For arm 6, at $3.0 \text{ kg}\cdot\text{s}^{-1}$, it can be observed that for probes P61 to P63, there is no resonance and the PSD corresponds to a turbulent spectrum.

The P64 and P65 probes are located outside this turbulent zone, showing behaviors more related to acoustic phenomena with a bump around 500-600 Hz for the case of $3.0 \text{ kg}\cdot\text{s}^{-1}$. For $3.4 \text{ kg}\cdot\text{s}^{-1}$ case, the lower arm shows a bump around 200-300 Hz, corresponding of $St = 0.25$, which had not been observed in the analysis of the vertical axis and could be related to the counter-rotating vortices. Some authors found similar Strouhal number associated to vortex shedding phenomena for similar applications [5]. This bump of energy is maximal for probes near to the vortex core and shear layer. Arm 2 exhibits an aeroacoustic behavior similar to other cases, with a peak at 1250 Hz.

Figures 5.19 and 5.20 depict the cross-spectral density and coherency for arms 2 and 6. There is a high coherency between the pressure signals and axial velocity in the whole spectrum for arm 6. The cross-spectral density for this arm shows a high level of energy, especially for probe P65 at $3.0 \text{ kg}\cdot\text{s}^{-1}$. This higher correlation density is found at 500 Hz. The rest of the probes for the same case exhibit similar behaviors, in addition to showing a certain energy density in the spectrum at 100-300 Hz, especially in the regions farther from the center of the AIP. Regarding the simulation of $3.4 \text{ kg}\cdot\text{s}^{-1}$, a maximum cross density can be observed with axial and lateral velocity at 200 Hz for probe P62. There is also some energy density at 1250 Hz for the same probe under the same conditions. Far away from mixing layer, the coherency between pressure and vertical velocity is moderate, the coherency with lateral velocity is low.

Arm 2 presents a different scenario from Arm 6. The probes in both cases are located in a region that is not affected by flow recirculation or vortices. The cross-spectral density analysis reveals that there is a high coherency between the axial velocity and pressure signals around 500-600 Hz when the flow rate is $3.0 \text{ kg}\cdot\text{s}^{-1}$. This coherency tends to increase as the probes approach the shear layer. In contrast, other energy densities are found at 100 Hz for a flow rate of $3.4 \text{ kg}\cdot\text{s}^{-1}$; however, these energy densities are much smaller than those predicted by $3.0 \text{ kg}\cdot\text{s}^{-1}$ case.

The analysis of arms 1 and 5 of the rake is presented in Figure 5.21. Theoretically, there is symmetry in both the geometry and the flow field, which should result in similar behaviors in both arms. The behavior of the energy density in the spectral domain changes depending on the mass flow. For the data obtained at $3.0 \text{ kg}\cdot\text{s}^{-1}$, the behavior is mostly turbulent, with maximum concentrations of energy between 500-600 Hz. For $3.4 \text{ kg}\cdot\text{s}^{-1}$, the behavior is different. The energy density distribution shows mostly aeroacoustic phenomena, among which a significant amount of energy can be observed around 200 Hz, as well as 1250 Hz and 1900 Hz.

The cross-spectral density for these arms is shown in Figures 5.22 and 5.23. For the case at $3.0 \text{ kg}\cdot\text{s}^{-1}$, arm 5 shows an important coherency between the pressure signals, axial velocity, vertical velocity, and to a lesser extent, the lateral velocity between the frequencies of 450-600 Hz. This coherency is important even up to 1000 Hz. For values greater than 3000 Hz, only the axial velocity shows a high coherency with pressure signal.

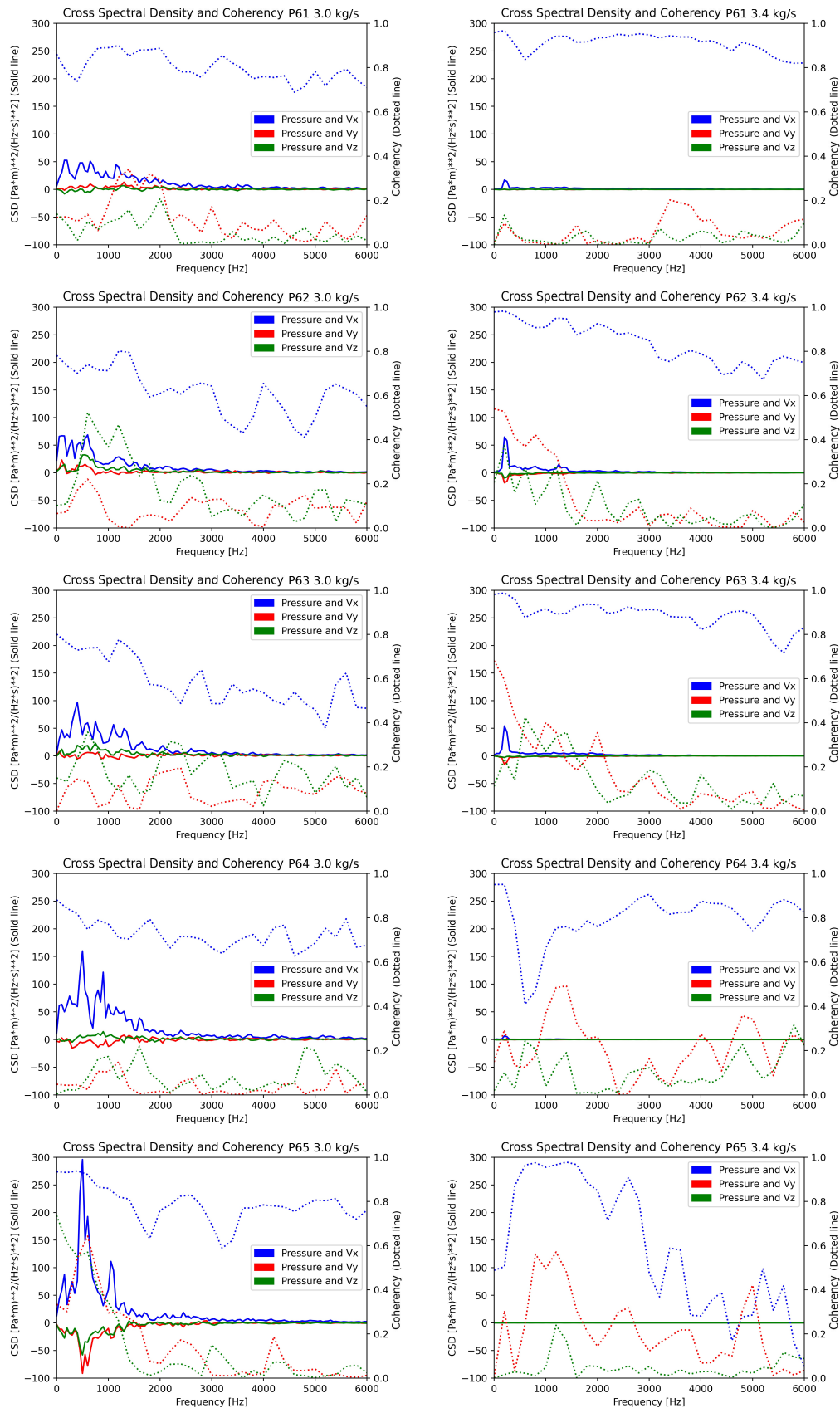


Figure 5.19: Cross Spectral density value between pressure and velocities for probes placed on arm 6. Left: $3.0 \text{ kg}\cdot\text{s}^{-1}$. Right: $3.4 \text{ kg}\cdot\text{s}^{-1}$. The right axis shows the CSD, represented by solid lines. The left axis shows the coherency, represented by dotted lines.

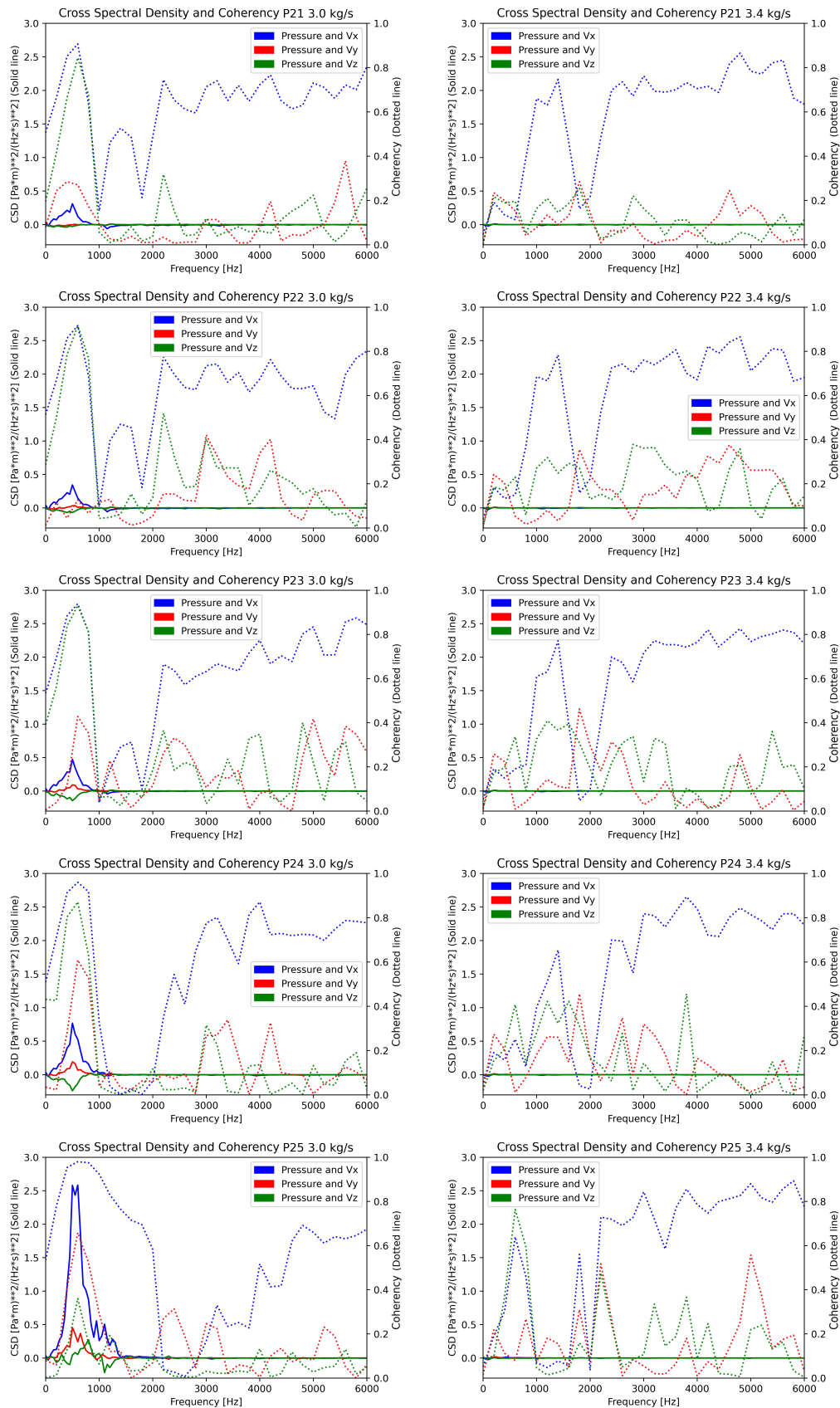


Figure 5.20: Cross Spectral density value between pressure and velocities for probes placed on arm 2. Left: $3.0 \text{ kg}\cdot\text{s}^{-1}$. Right: $3.4 \text{ kg}\cdot\text{s}^{-1}$. The right axis shows the CSD, represented by solid lines. The left axis shows the coherency, represented by dotted lines.

For the case of $3.4 \text{ kg}\cdot\text{s}^{-1}$, the amount of energy is significantly lower due to the fact that we are located outside the mixing layer. Analogous to the preceding scenario, the most significant coherency is observed in frequencies lower than 1000 Hz. The axial velocity exhibits a substantial coherency for frequencies from 3000 Hz. The lateral velocity displays some peaks throughout the spectrum. The vertical velocity manifests coherency solely in frequencies below 1000 Hz. This coherency of signals increases as we approach the center of the AIP. The probes located near the the center shows a greater distribution in the coherency of signals, showing a link between pressure and axial velocity around 450 Hz.

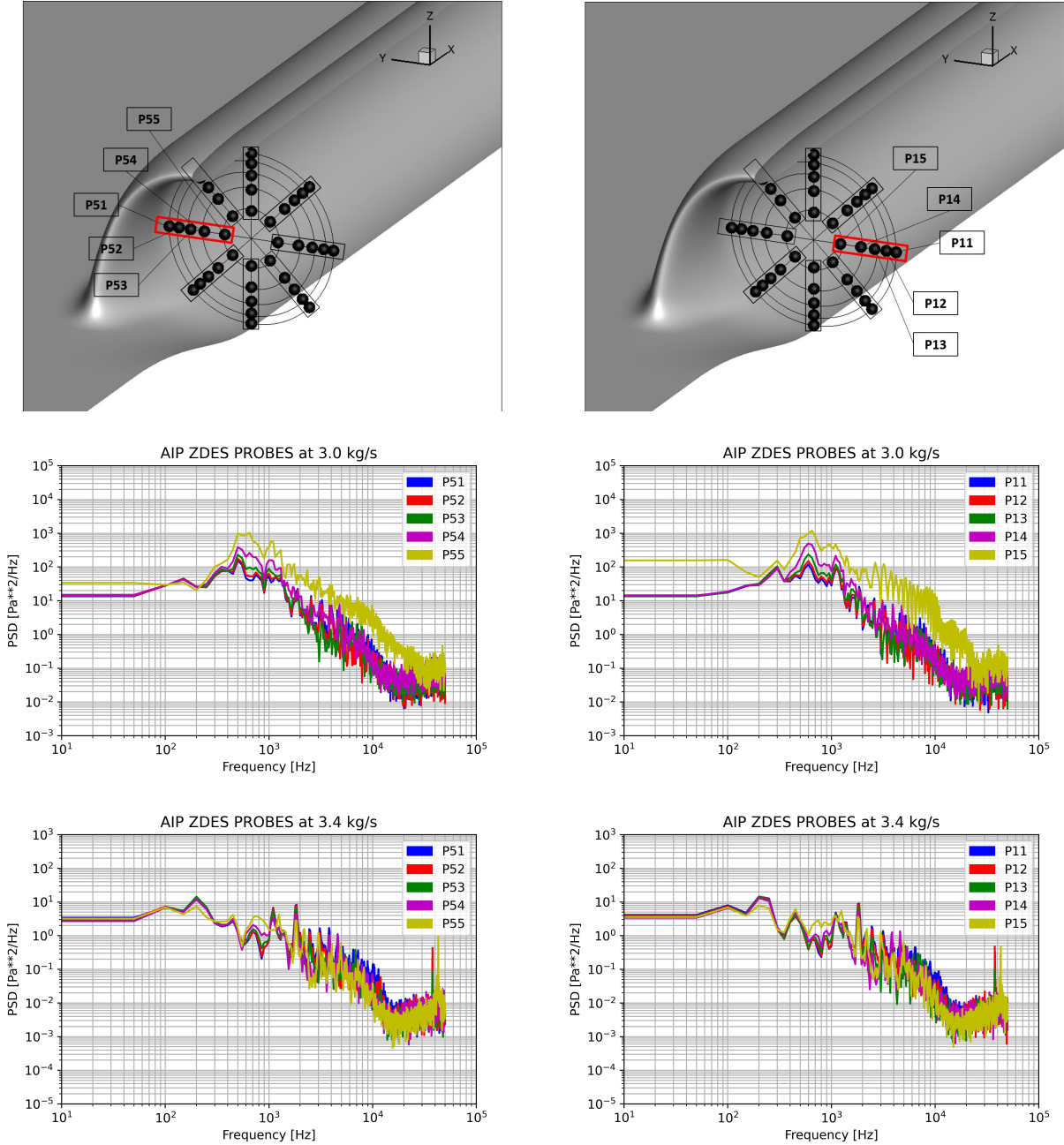


Figure 5.21: Power Spectral Densities for the probes on the horizontal arms of the rake placed at the AIP. Left: left side arm. Rigth: rigth side arm.

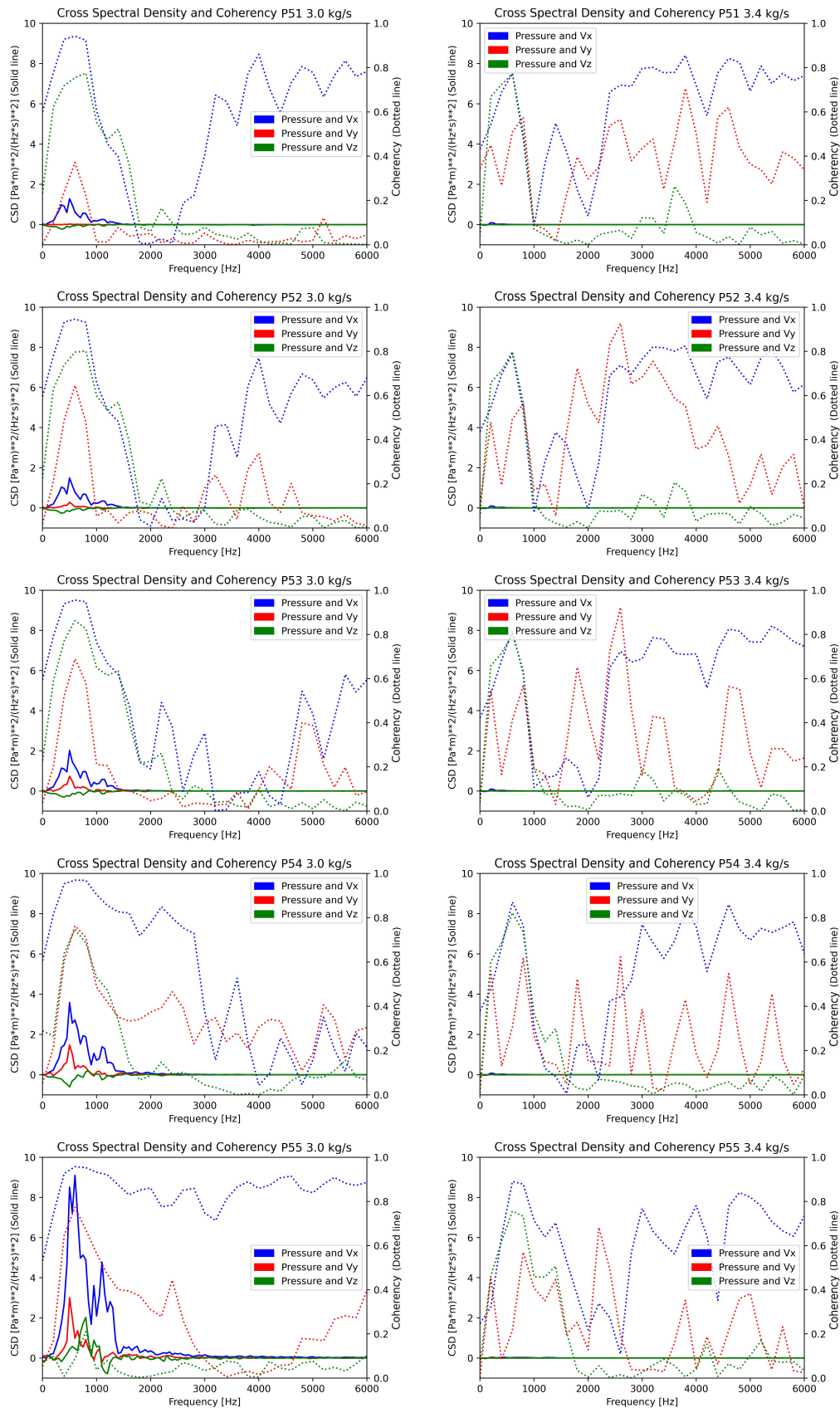


Figure 5.22: Cross Spectral density value between pressure and velocities for probes placed on arm 5. Left: $3.0 \text{ kg}\cdot\text{s}^{-1}$. Right: $3.4 \text{ kg}\cdot\text{s}^{-1}$. The right axis shows the CSD, represented by solid lines. The left axis shows the coherency, represented by dotted lines.

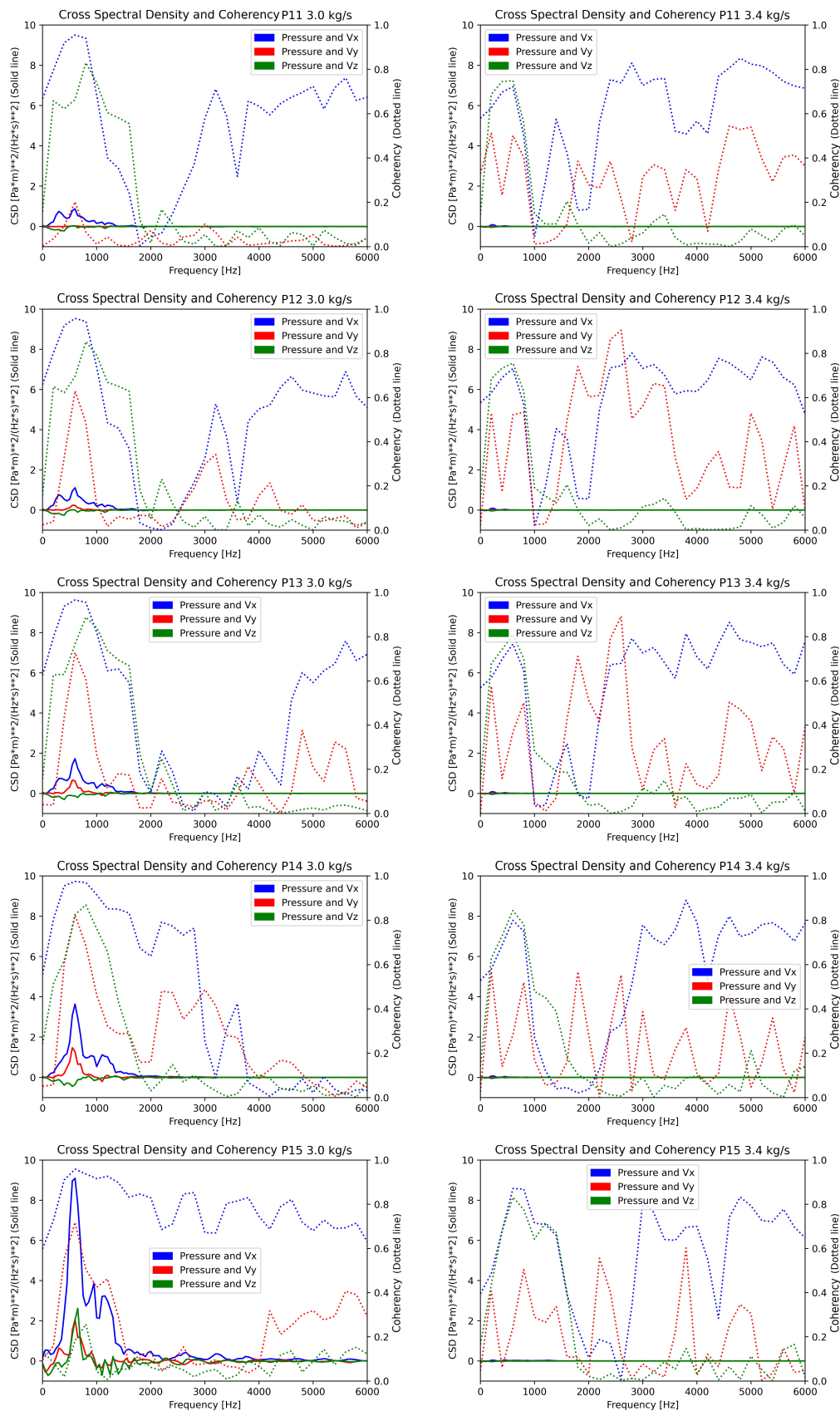


Figure 5.23: Cross Spectral density value between pressure and velocities for probes placed on arm 1. Left: $3.0 \text{ kg}\cdot\text{s}^{-1}$. Right: $3.4 \text{ kg}\cdot\text{s}^{-1}$. The right axis shows the CSD, represented by solid lines. The left axis shows the coherency, represented by dotted lines.

The behavior for arm 1 is quite similar to arm 5, showing a high energy at 450 Hz and 200 Hz for cases of $3.0 \text{ kg}\cdot\text{s}^{-1}$ and $3.4 \text{ kg}\cdot\text{s}^{-1}$ respectively. At $3.0 \text{ kg}\cdot\text{s}^{-1}$, the coherency of the axial and vertical velocity, with the pressure, is particularly high for frequencies below 1000 Hz. The lateral velocity also exhibits some consistency in these values for points approaching the center of the AIP. In the remaining spectrum, only the axial velocity exhibits coherency. Regarding the case of $3.4 \text{ kg}\cdot\text{s}^{-1}$, the behavior is similar to the one observed for arm 5, with the coherency with the axial velocity being the most conspicuous. The following section offers a more detailed discussion about the possible physical phenomena present.

5.3.1 Spectral analysis discussion

In the last section, the results obtained by the ZDES (mode 2) simulation were analyzed, in particular from an spectral point of view, both at the entrance ramp and at the AIP. There are some frequencies that were mentioned more than others which will be analyzed here.

The analysis of the solution obtained in the case of $3.4 \text{ kg}\cdot\text{s}^{-1}$ is presented first. The flow field of the solution shows a turbulent behavior in all directions. Some vortex structures can be seen in the various images of instantaneous solutions shown in Figure 5.24. This behavior occurs around 230 Hz, which can also be accentuated, above all, on probes k103 and k104, as shown in the graphs in Figure 5.13. In this same case, oscillations of the axial velocity are observed within the shear layer. These oscillations are coupled with oscillations in the vertical velocity, resulting in the generation of large vortices that are normal to the lateral plane and propagate outside the recirculation zone. The frequency of these oscillations is between 500-600 Hz and is mainly captured by probes located inside or near the shear layer. On the left side of the figure 5.25, a zone of increased axial velocity is observed, which crosses a region where axial velocity decreases. The behavior described is also shown by the instantaneous solutions depicted in Figure 5.15. The cross spectral density between the pressure and axial velocity is shown in figure 5.16. For the diagonal arms, physical phenomena stand out in the 200-230 Hz frequency bandwidth, associated with vertical and lateral velocities. This lateral oscillatory movements are probably related to the same evidenced by the intake ramp.

The behavior for the case of $3.0 \text{ kg}\cdot\text{s}^{-1}$ is quite similar, with the difference that the vortices normal to the lateral plane appear to be more energetic, therefore their effects tend to spread more even outside the recirculation zone. The frequency of these vortices is around 550 Hz. Figure 5.16 shows the coupling between the axial velocity and the pressure oscillations. In the lower part of the recirculation zone it also shows a horizontal oscillating motion, which is shown at a frequency slightly lower than for the case of $3.4 \text{ kg}\cdot\text{s}^{-1}$, around 150-200 Hz, as shown in figure 5.13.

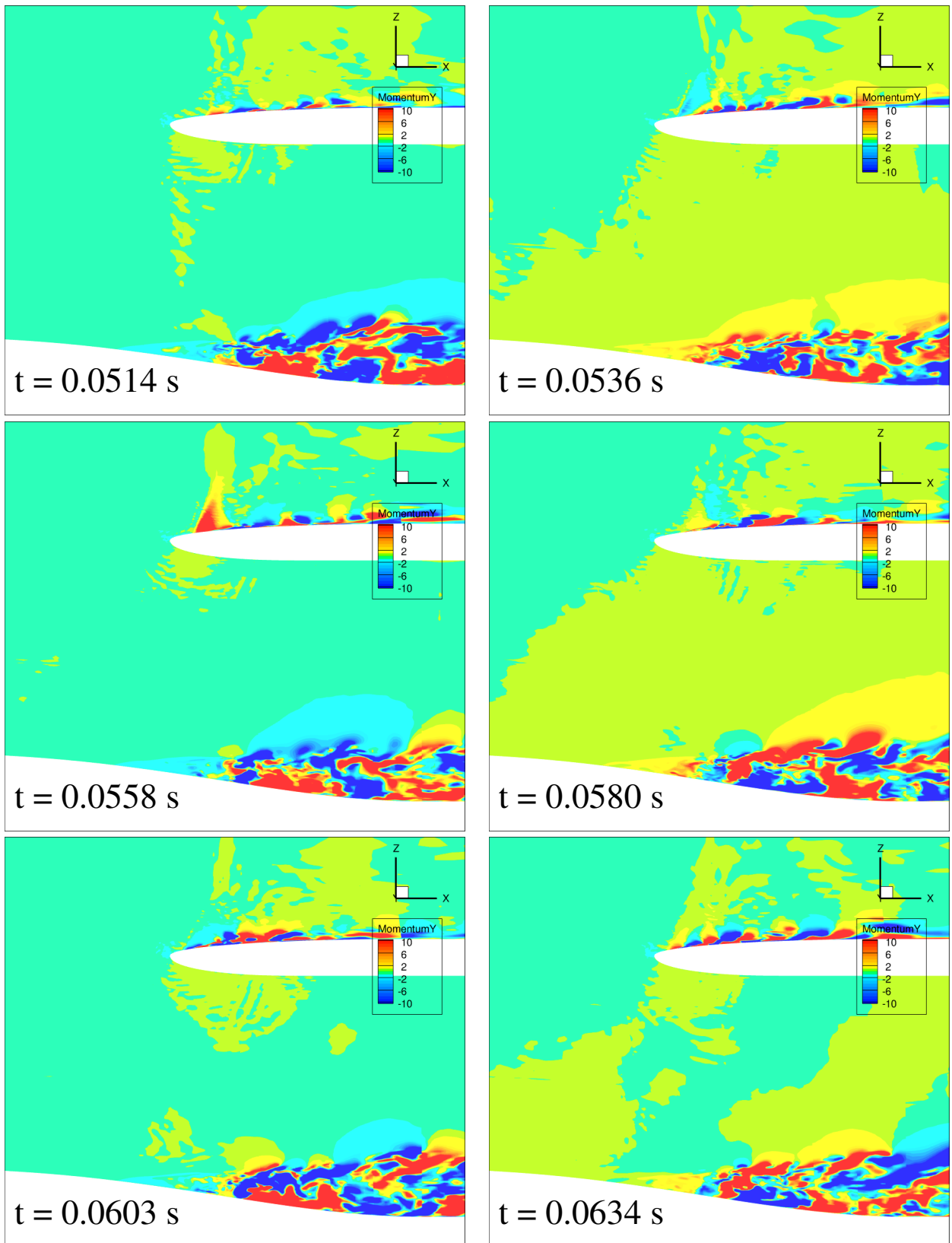


Figure 5.24: Instantaneous flow field predicted by the ZDES model. The images show the lateral velocity with a sampling frequency of 450 Hz. Left: $3.0 \text{ kg} \cdot \text{s}^{-1}$. Right : $3.4 \text{ kg} \cdot \text{s}^{-1}$.

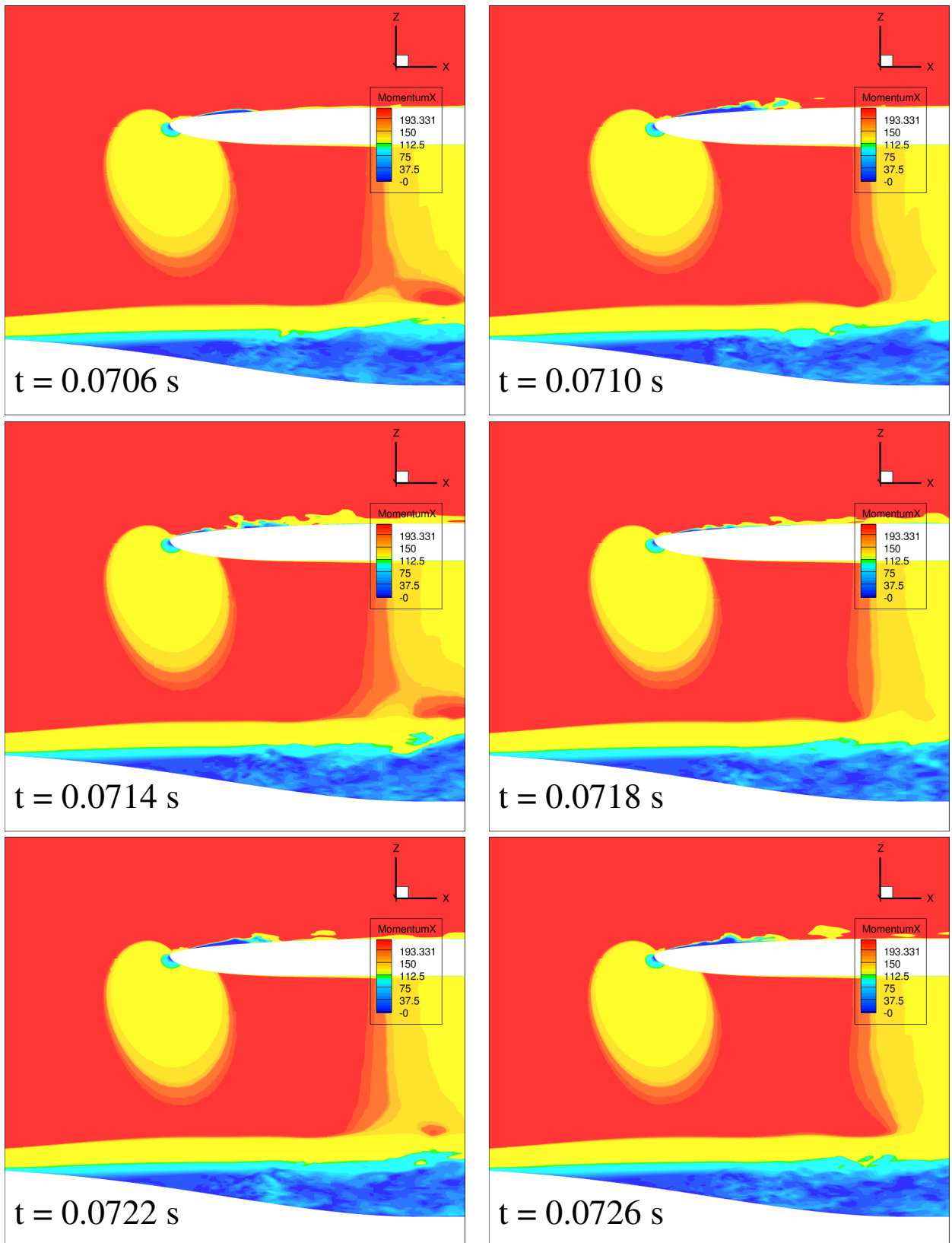


Figure 5.25: Instantaneous flow field predicted by the ZDES model at the symmetry plane . The images show the axial velocity with a sampling frequency of 2500 Hz. Left: $3.0 \text{ kg}\cdot\text{s}^{-1}$. Right : $3.4 \text{ kg}\cdot\text{s}^{-1}$.

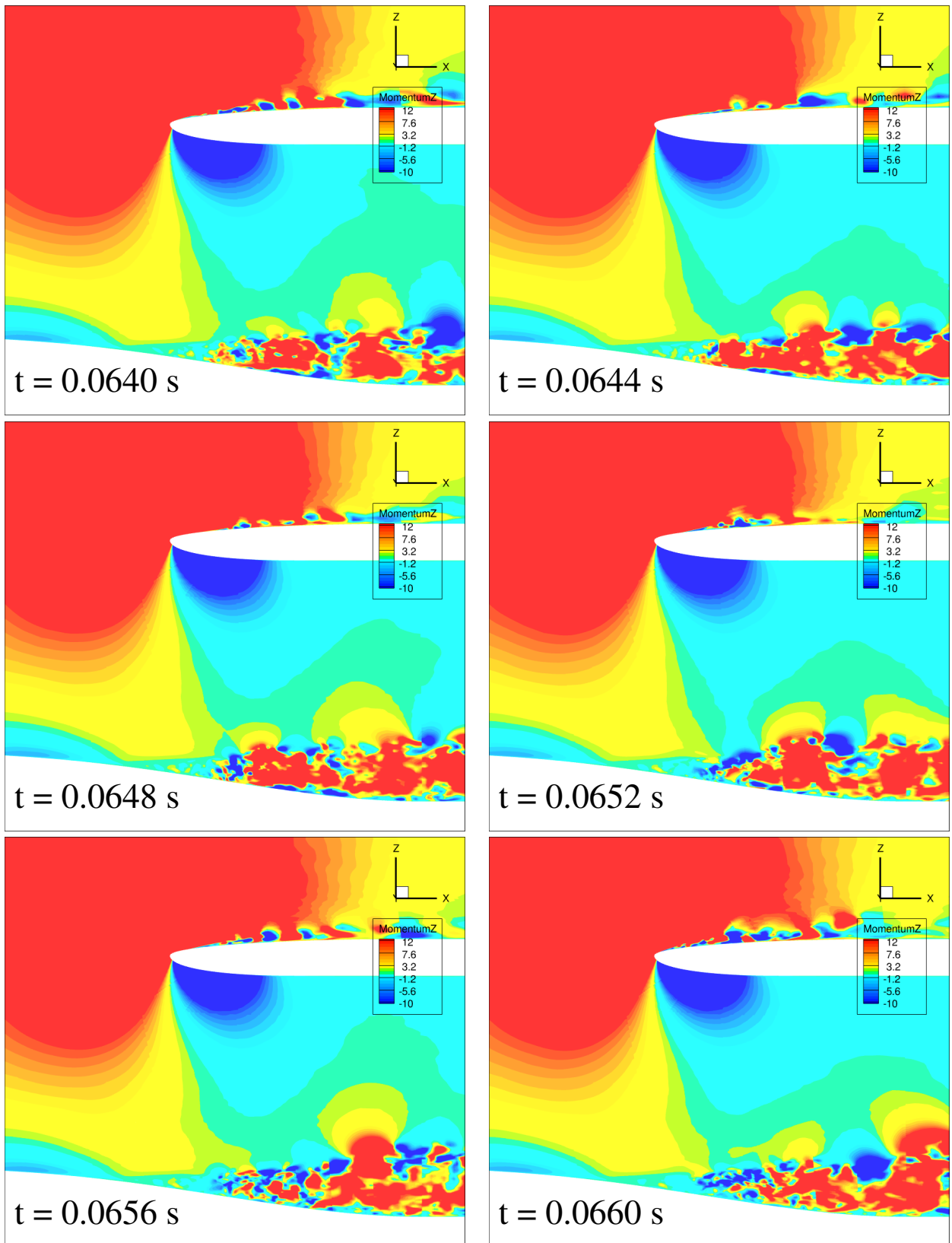


Figure 5.26: Instantaneous flow field predicted by the ZDES model at the symmetry plane. The images show the vertical velocity with a sampling frequency of 2500 Hz. Left: $3.0 \text{ kg} \cdot \text{s}^{-1}$. Right : $3.4 \text{ kg} \cdot \text{s}^{-1}$.

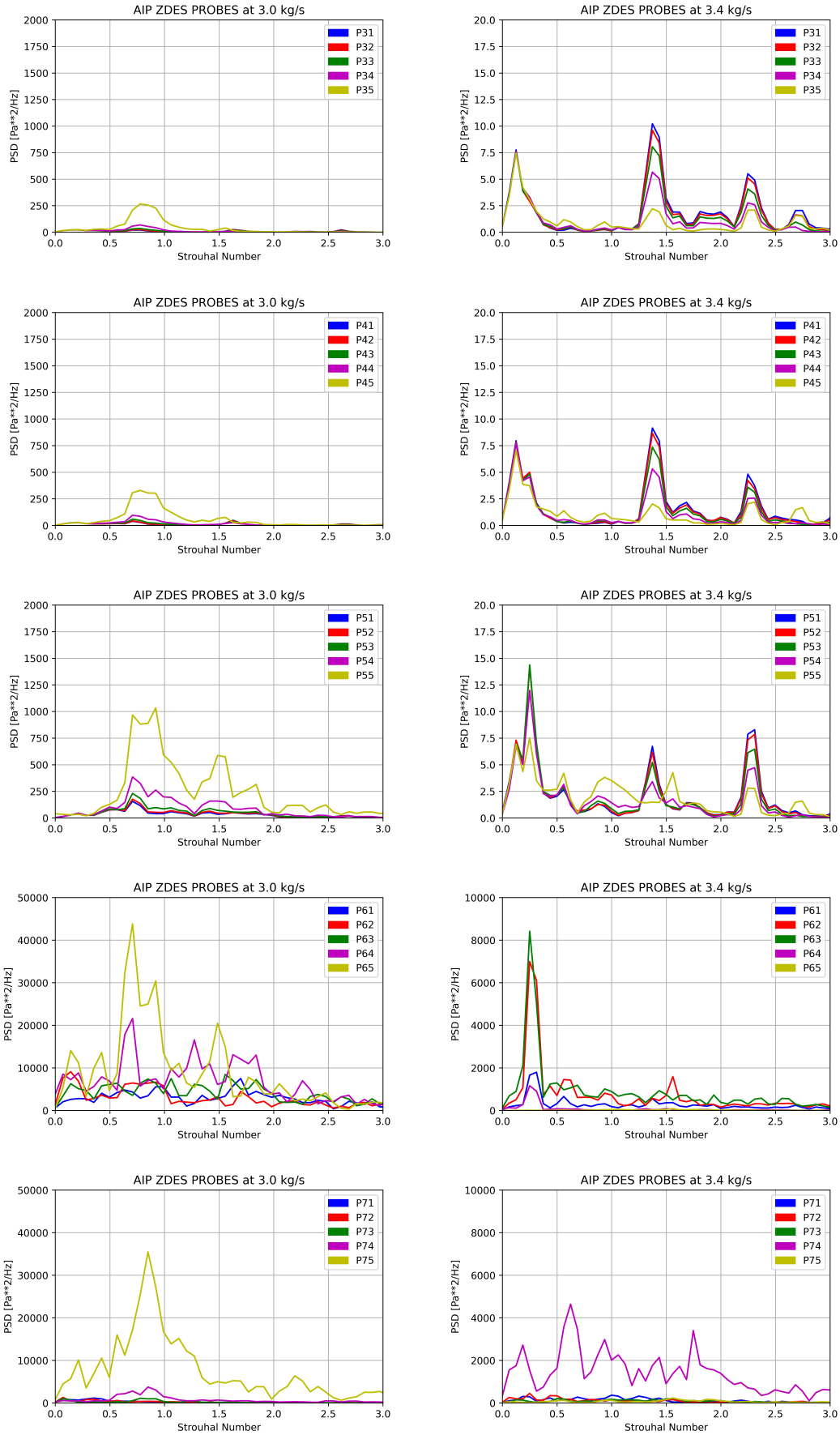


Figure 5.27: PSD and Strouhal number for probes located on the AIP. Left: $3.0 \text{ kg}\cdot\text{s}^{-1}$. Right: $3.4 \text{ kg}\cdot\text{s}^{-1}$.

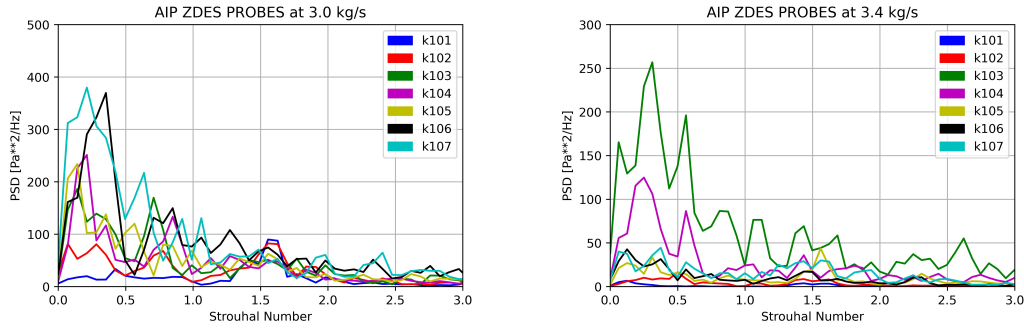


Figure 5.28: PSD and Strouhal number for probes located on the entrance ramp. Left: $3.0 \text{ kg}\cdot\text{s}^{-1}$. Right: $3.4 \text{ kg}\cdot\text{s}^{-1}$.

Energy density is presented in Figures 5.27 and 5.28, with frequencies translated into Strouhal numbers. Initially, it was anticipated that a correlation between the physical phenomena would be found, likely manifesting in the same Strouhal number value. However, upon examination of the aforementioned plots, it is evident that the correlation is minimal. Instead, consistency is more pronounced for the probes located on the intake ramp.

The spectral analysis conducted at the AIP reveals minimal correlation between physical phenomena. For a mass flow rate of $3.0 \text{ kg}\cdot\text{s}^{-1}$, a high level of energy can be observed for a Strouhal number around 0.7 and 0.9, this is observed in the left side of figure 5.27. The latter are associated with vertical oscillations of the shear layer around 550 Hz. For the case of $3.4 \text{ kg}\cdot\text{s}^{-1}$, it is more difficult to discriminate a dominant density for most sensors within the recirculation zone. Strouhal numbers related to lateral movements can be seen for the diagonal arms. In the lower part, this event is also noted but is overlapped by others. Oscillations at $St = 0.6$ can also be observed for this same arm, related to the oscillations of the shear layer at 500-600 Hz.

At the AIP, physical phenomena with Strouhal values between 0.7 and 0.9 typically predominate in the part not affected by recirculation for the case of $3.0 \text{ kg}\cdot\text{s}^{-1}$. In contrast, for the case of $3.4 \text{ kg}\cdot\text{s}^{-1}$, there is a greater variety of phenomena, particularly aeroacoustics, which are presented in values of 0.2, 1.4 and 2.2 for the Strouhal number, as shown on the right of figure 5.27.

Over the intake ramp, the Strouhal numbers of both cases appear to be more consistent, concentrating the higher energy density around $St = 0.3$, which is associated with lateral oscillations that occur just after flow separation. These oscillations appear on sensors k106 and k107 for the case of $3.0 \text{ kg}\cdot\text{s}^{-1}$ and on k103 and k104 for the case of $3.4 \text{ kg}\cdot\text{s}^{-1}$.

5.4 Chapter summary and conclusions

In this chapter, we have analyzed the BLI inlet using more complex numerical models and analyzing the physical behavior over time. The first part of the chapter explains the theoretical foundations of Zonal Detached Eddy Simulation (ZDES) and its relationship with other families.

The ZDES model 2, which is an automatic mode, has been used for the simulation. The mesh used for the RANS computations has been modified by adding a refined region inserted thanks to the chimera method. The cell size in this LES region was dimensioned according to the expected phenomena. The instantaneous solutions that show the flow separation predicted by RANS models were analyzed and discussed. The signals extracted from the probes were analyzed, showing a turbulent distribution of turbulent kinetic energy along the spectrum.

A spectral analysis was also performed in both simulations with the objective of discriminating possible physical phenomena. This spectral analysis was performed on both the intake ramp and the AIP. These spectral analyses were based on the computation of Power Spectral Densities (PSD) and Cross Spectral Densities (CSD).

For the case of $3.0 \text{ kg}\cdot\text{s}^{-1}$, the probes located on the intake ramp revealed a lateral movement of the recirculation zone in the frequency range of 150-200 Hz, corresponding to $St = 0.25$. Additionally, just before separation point, the first probes show phenomena with a frequency of 1250 Hz, equivalent to $St = 1.76$, probably related to aeroacoustic phenomena. For the same case, an analysis of the probes located at the AIP reveals a high level of turbulent kinetic energy in the shear layer, especially for the P75 probe. In the same region, a peak at 600 Hz ($St = 0.85$) is observed, which is correlated with high coherency with all velocity components.

The case of $3.4 \text{ kg}\cdot\text{s}^{-1}$ exhibits certain differences from the previous one. It should be emphasized that the separation for this case is much smaller than the previous one, therefore certain differences may arise in the physical phenomena. The most similar results are found on the intake ramp, just after the separation point where the pressure oscillations show a significant level of kinetic energy correlated with the vertical velocity oscillations. This correlation occurs for a frequency of 230 Hz, corresponding to $St = 0.25$. At the AIP, for the case of $3.4 \text{ kg}\cdot\text{s}^{-1}$, the energy level is higher and a peak at 500 Hz is observed. This peak is correlated with the velocity components and corresponds to $St = 0.62$. Some peaks are also observed for frequencies ranging from 100 to 1250 Hz. These are found in probes located in the recirculation zone. For this case, a significant amount of energy can also be observed at the frequency of 230 Hz but captured by the probes located in the arms. This measurement can confirm a possible coupling between the lateral movements of the recirculation zone and the counter-rotating vortices.

The unsteady phenomena in regions not directly affected by flow recirculation appear to be more

pronounced for the case of $3.4 \text{ kg}\cdot\text{s}^{-1}$, exhibiting peaks in values corresponding to Strouhal numbers of 0.2, 1.4 and 2.2. For the case of $3.0 \text{ kg}\cdot\text{s}^{-1}$, pressure waves originating from the shear layer are visible and they have a Strouhal number between 0.7 and 0.9.

Some authors found similar frequencies and Strouhal number associated with a shedding phenomenon, most of them located below 300 Hz [5]. Some lateral and longitudinal perturbations were also associated with frequencies of 0.40 and 0.75, respectively. They also demonstrated that Reynolds and Mach number variations have only a minor effect on the unsteady characteristics of these flow fields [101]. Other studies [103] have also concluded that the main mechanisms responsible for disturbances are related to counter-rotating vortices, they are alternately generated around the separation region at a Strouhal number of $St=0.53$. This is consistent to phenomena observed in our studies, giving a Strouhal between 0.62-0.85 depending on the MFR. The behaviors found in this chapter, specially the shedding frequencies related with physical phenomena, are consistent with the literature. However, it should be emphasized that both the flow conditions (Mach number, etc.) and the geometry are different and this could explain the observed differences. A more comprehensive analysis of the behavior of distortion at the AIP will be performed in the following chapters.

Chapter 6

Comparison of numerical results with experimental data

The simulation and prediction of complex flows like the one occurring in a BLI intake is one of the present issues facing the industry. For BLI engines placed at the rear of the fuselage, usually a double curvature ramp intake is used. The flow characteristics at the intake resemble those seen in an S-duct. This kind of geometry has been the subject of several Computational Fluid Dynamics (CFD) analyses, both to assess design modifications [8] and to compare with experimental results [104]. In comparison with the experimental data, these previous assessments show a large dispersion that is dependent on the numerical methodology used and, more importantly, the turbulence model chosen. These inaccuracies might be a significant hurdle to the development of a concept when investigating highly optimized or creative designs. Some authors [9] have even recommended abandoning RANS model research in favor of focusing on scale-resolving simulations, such as LES or hybrid RANS/LES, and standardizing its use in industrial applications.

The associated physical phenomena, as well as the flow field behaviors have been described and analyzed in the previous chapters. This chapter compares the experimental results with those obtained numerically, both in RANS and ZDES. The main differences found in the different sensors located on the geometry are analyzed and evaluated, in addition to analyzing the loss of total pressure loss at the AIP. In the first section we study the wall pressure measurements, both on the entrance ramp and on the lateral and upper walls of the nacelle. An analysis is then performed at the AIP, mainly to estimate the total pressure loss and the size of the affected regions. Finally, the pressure signals from the different sensors are analyzed in order to compare the evolution of the turbulent kinetic energy and the possible aeroacoustic phenomena evidenced in the previous chapter on the ZDES simulations.

6.1 Intake Ramp analysis

This section analyzes the wall pressure distribution on the intake ramp. Pressure tap locations are given in Table 3.6, from PS111 to PS117. To compare with the experimental data, values are displayed in terms of wall pressure coefficient computed using equation 3.12. The repeatability (Figure 3.10) of the data obtained in the wind tunnel tests has already been analyzed in Chapter 3.

The standard Spalart-Allmaras and $k-\omega$ SST models are two largely used turbulence models in the industry. They are commonly used to design and simulate aeronautical components. Additionally, two common corrections for the Spalart-Allmaras model, known as the Quadratic Constitutive Relation (QCR2000) and Rotation and Curvature Correction (RC), are evaluated. Finally, a combined Speziale-Sarkar-Gatski/Launder-Reece-Rodi Reynolds-stress model (RSM) is also evaluated. All these models have been presented in Chapter 4. Figures 6.1-6.5 show the comparison of numerical and experimental curves for each RANS turbulence model. In addition, this section also analyzes the results from the two ZDES simulations at $3.0 \text{ kg}\cdot\text{s}^{-1}$ and $3.4 \text{ kg}\cdot\text{s}^{-1}$ already shown in Chapter 5.

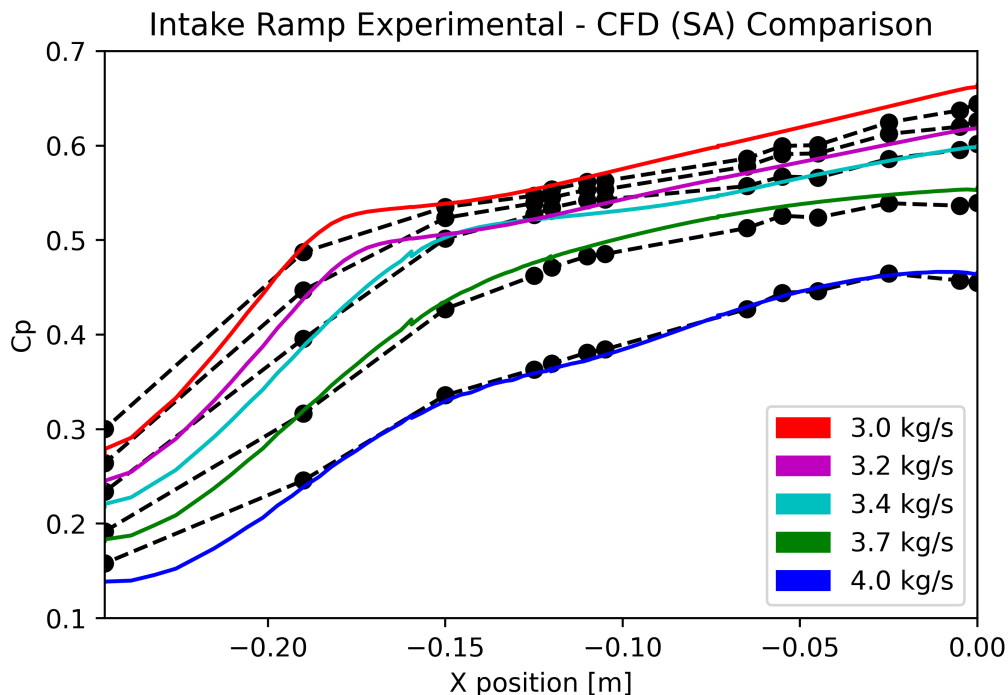


Figure 6.1: Comparison of wall pressure coefficient (C_p) along the intake ramp for various mass flow rate (MFR) values between experimental and numerical data obtained from the Standard Spalart-Allmaras model (SA).

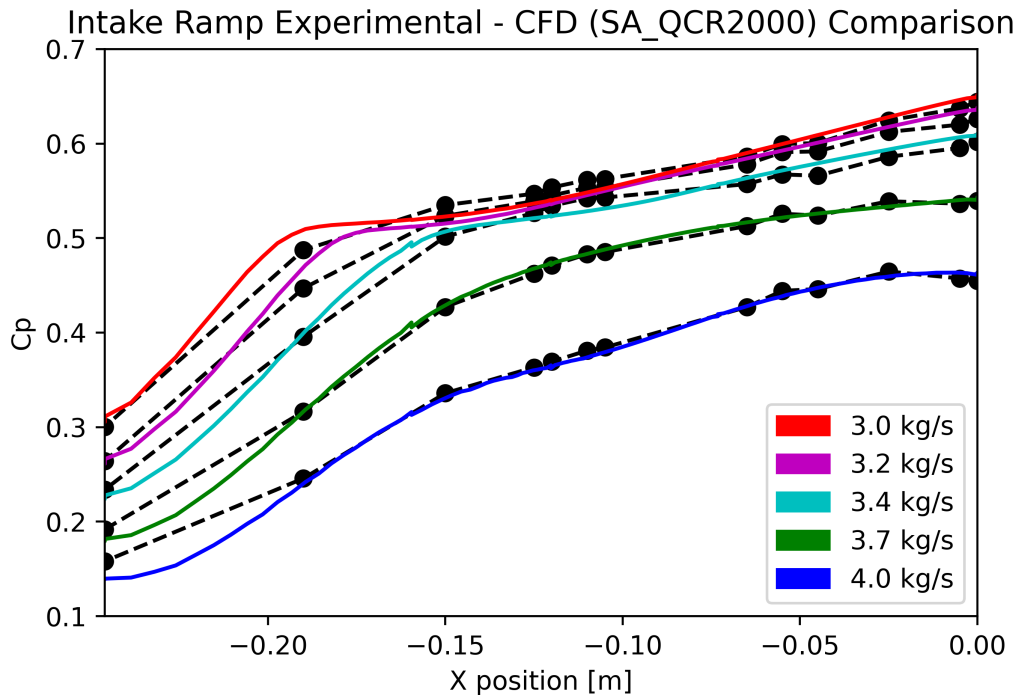


Figure 6.2: Comparison of wall pressure coefficient (C_p) along the intake ramp for various mass flow rate (MFR) values between experimental and numerical data obtained from Spalart-Allmaras model with quadratic constitutive relation (SA-QCR2000).

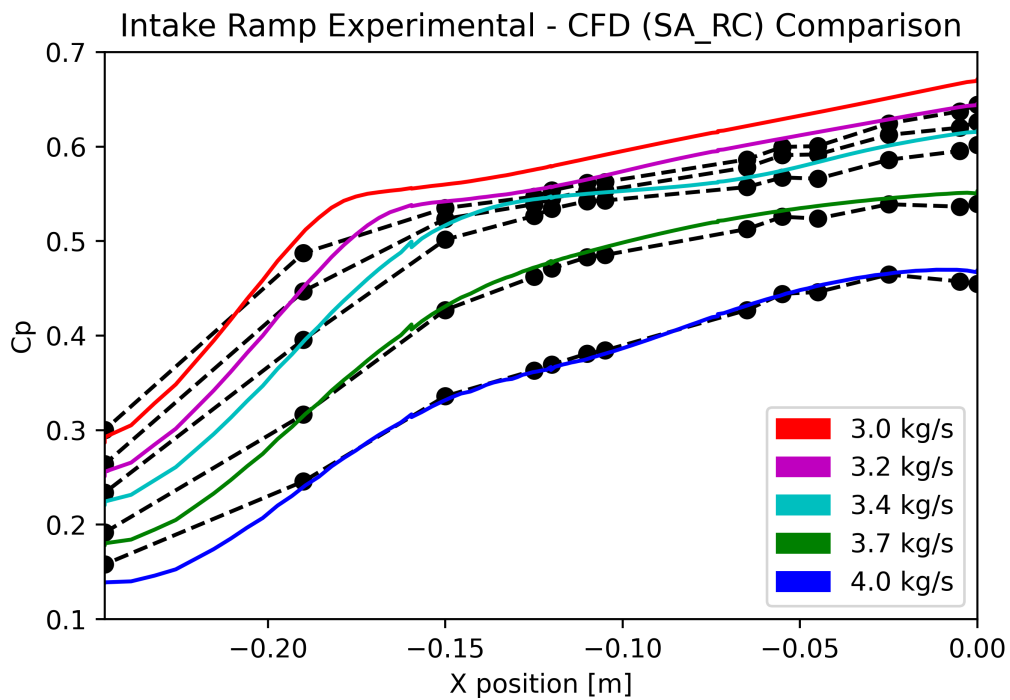


Figure 6.3: Comparison of wall pressure coefficient (C_p) along the intake ramp for various mass flow rate (MFR) values between experimental and numerical data obtained from Spalart-Allmaras model with rotation and curvature correction (SA-RC).

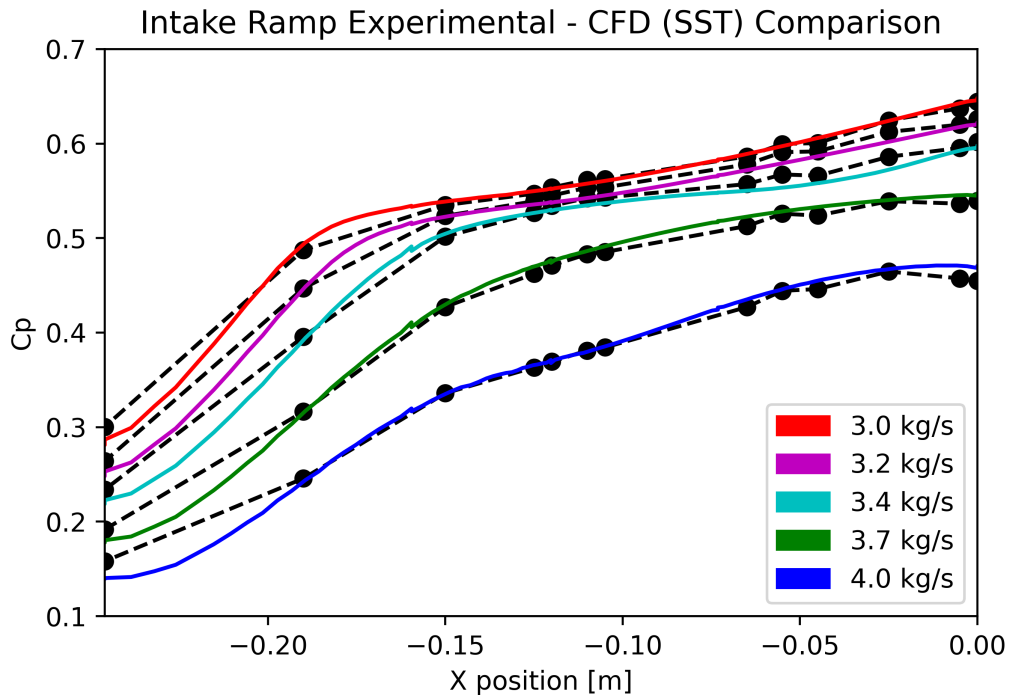


Figure 6.4: Comparison of wall pressure coefficient (C_p) along the intake ramp for various mass flow rate (MFR) values between experimental and numerical data obtained from $k-\omega$ SST model.

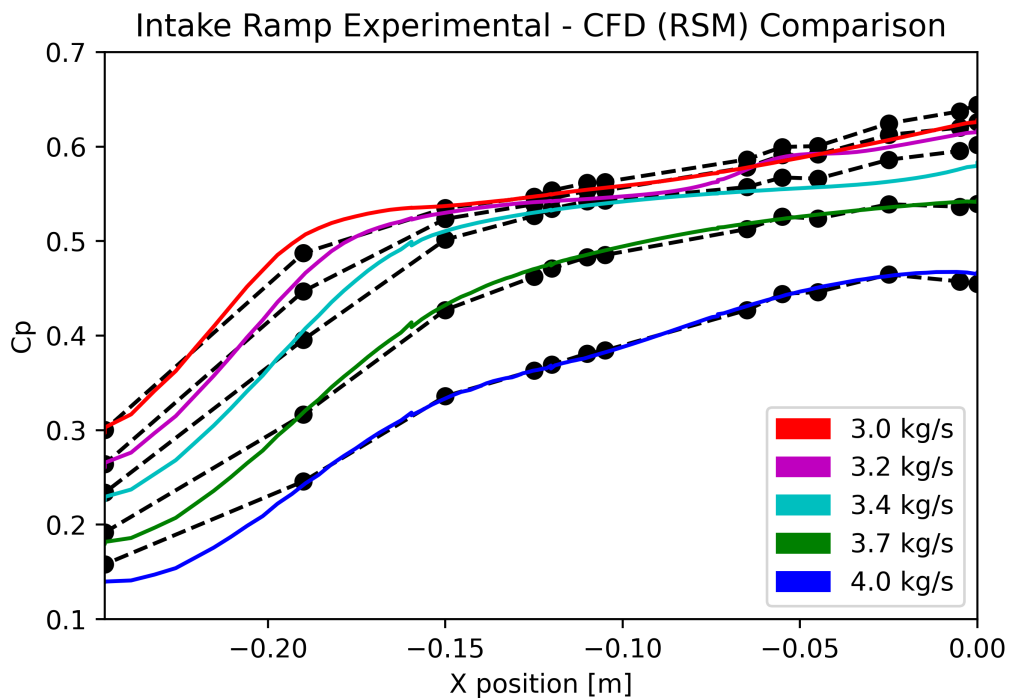


Figure 6.5: Comparison of wall pressure coefficient (C_p) along the intake ramp for various mass flow rate (MFR) values between experimental and numerical data obtained from Speziale-Sarkar-Gatski/Launder-Reece-Rodi differential Reynolds-stress model (RSM).

All turbulence models are more or less close to the curves obtained experimentally. It is difficult to state which model is the closest to the experimental data. The following images (see Figures 6.6-6.12) compare the different turbulence models for each mass flow rate case. For the case of $3.0 \text{ kg}\cdot\text{s}^{-1}$ and $3.4 \text{ kg}\cdot\text{s}^{-1}$, the mean value obtained by the ZDES has been added to the plots.

While details of physical phenomena cannot be evidenced by seeing the C_p curves, however studies of our CFD simulations, made on chapter 4 and 5, show that all turbulence models predict a flow separation for low mass flow values. Figures 6.6, 6.7, and 6.8 show the cases for mass flow rate between $4.0 \text{ kg}\cdot\text{s}^{-1}$ and $3.6 \text{ kg}\cdot\text{s}^{-1}$; in these cases, there is very slight separation or no flow separation according to the model. The curves of each turbulence model do not show major differences between them. They closely align with the experimental curve, exhibiting minimal deviations. However, a notable discrepancy emerges at $x = -0.25 \text{ m}$. In this instance, turbulence models consistently yield lower values for the C_p . Several factors may contribute to this disparity, including variations in boundary layer shape, the influence of wind tunnel walls, etc. In subsequent sections, we shall explore a couple of hypotheses to elucidate the origins of this observed discrepancy.

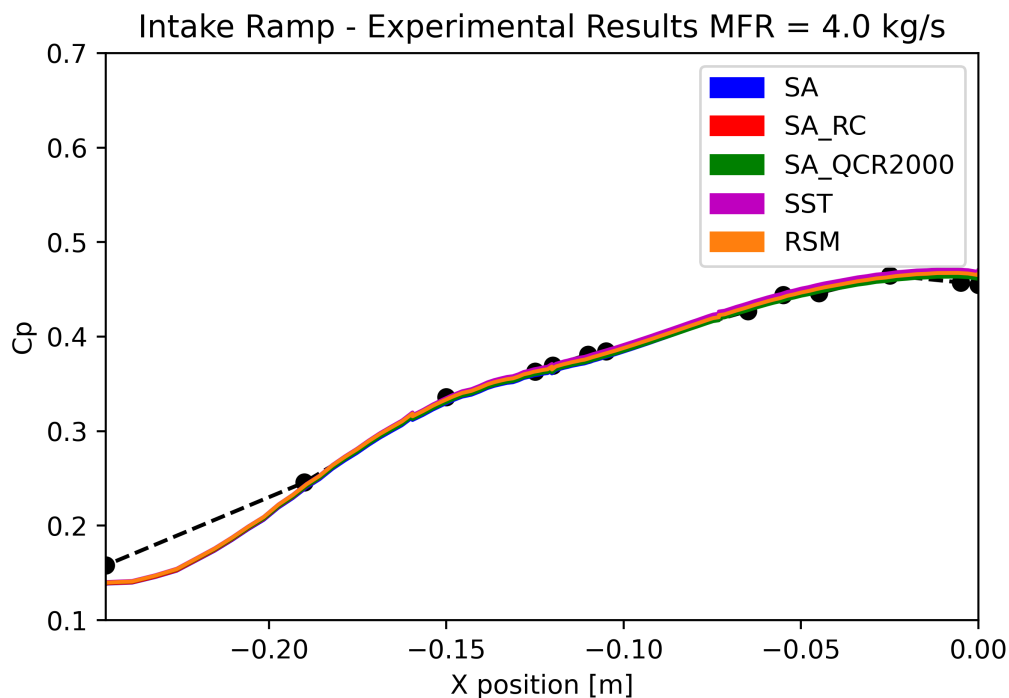


Figure 6.6: Comparison of wall pressure coefficient (C_p) along the intake ramp for various turbulence models at a mass flow rate (MFR) of $4.0 \text{ kg}\cdot\text{s}^{-1}$. In this case there is no flow separation.

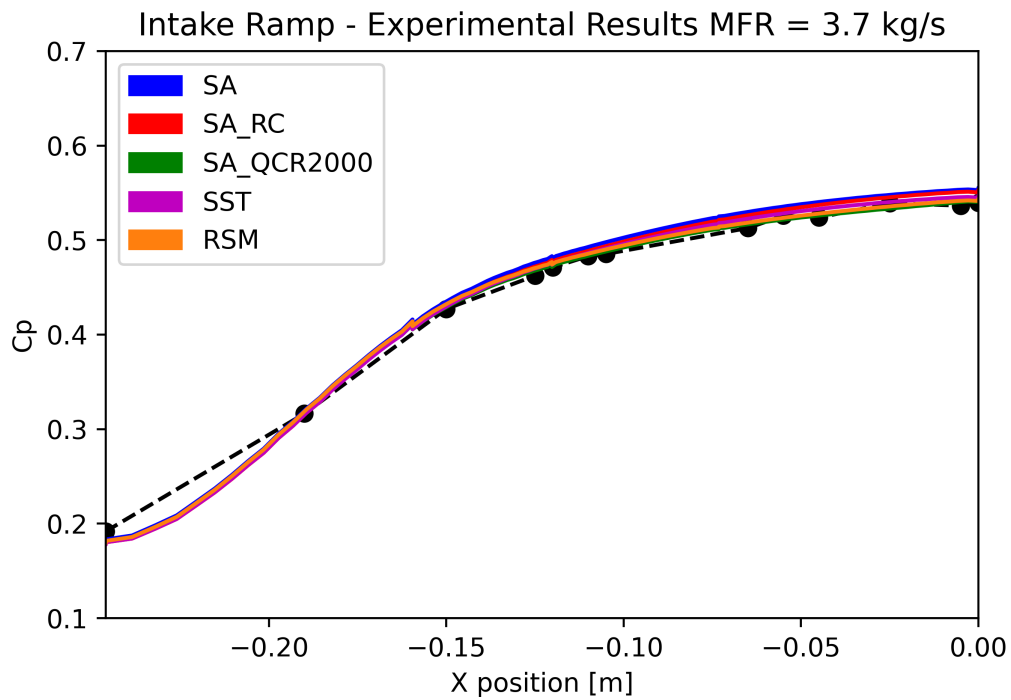


Figure 6.7: Comparison of wall pressure coefficient (C_p) along the intake ramp for various turbulence models at a mass flow rate (MFR) of $3.7 \text{ kg}\cdot\text{s}^{-1}$. In this case there is no flow separation.

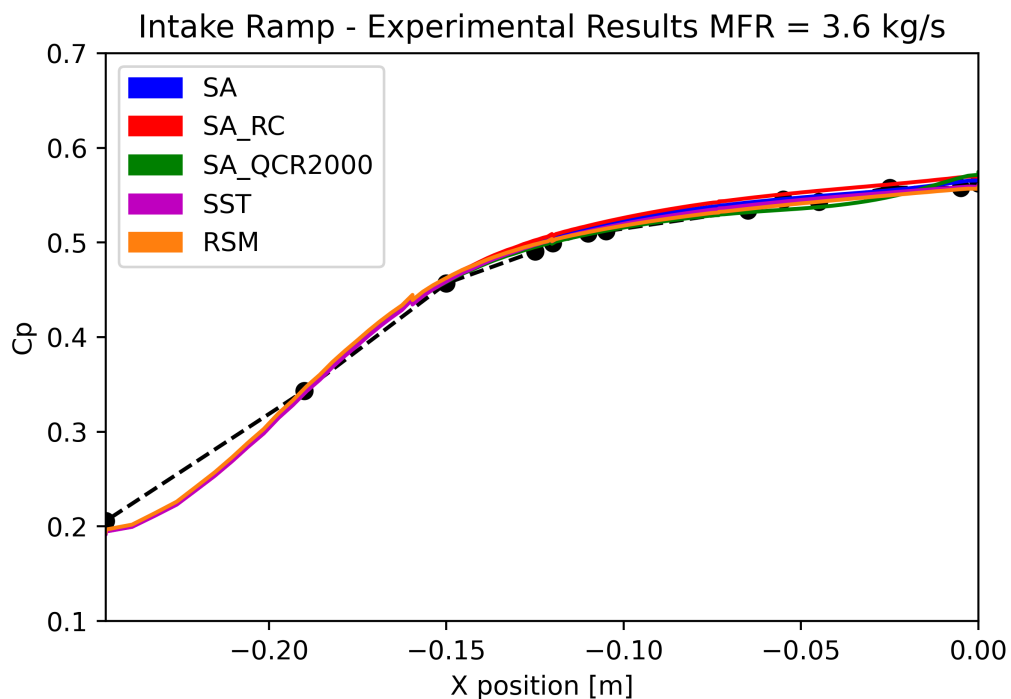


Figure 6.8: Comparison of wall pressure coefficient (C_p) along the intake ramp for various turbulence models at a mass flow rate (MFR) of $3.6 \text{ kg}\cdot\text{s}^{-1}$. In this case there is no flow separation.

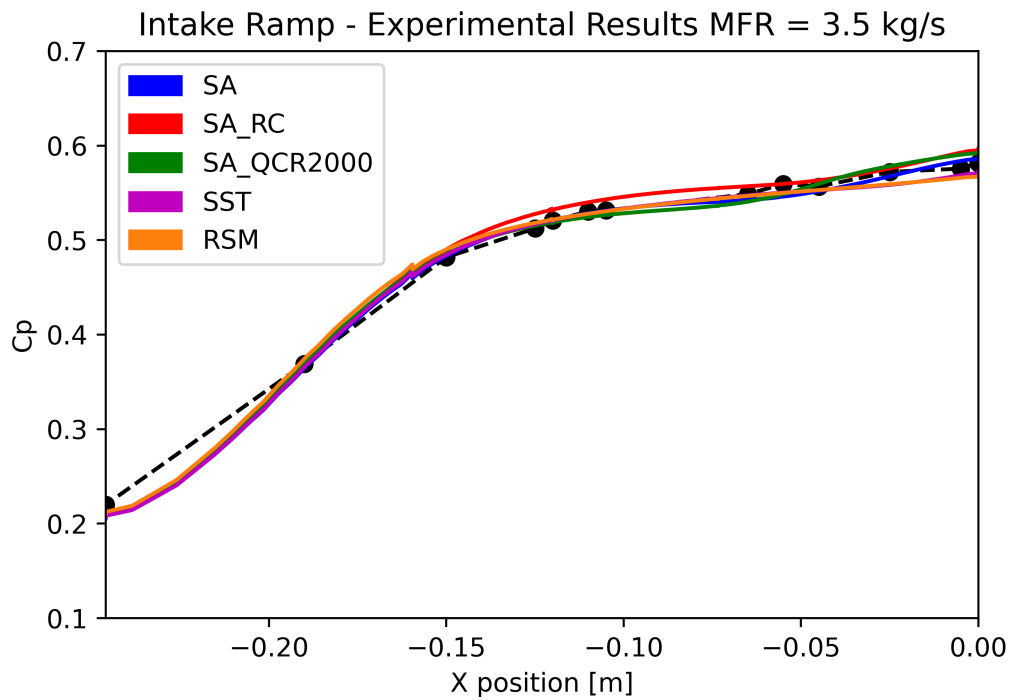


Figure 6.9: Comparison of wall pressure coefficient (C_p) along the intake ramp for various turbulence models at a mass flow rate (MFR) of $3.5 \text{ kg}\cdot\text{s}^{-1}$. In this case there is a slight flow separation.

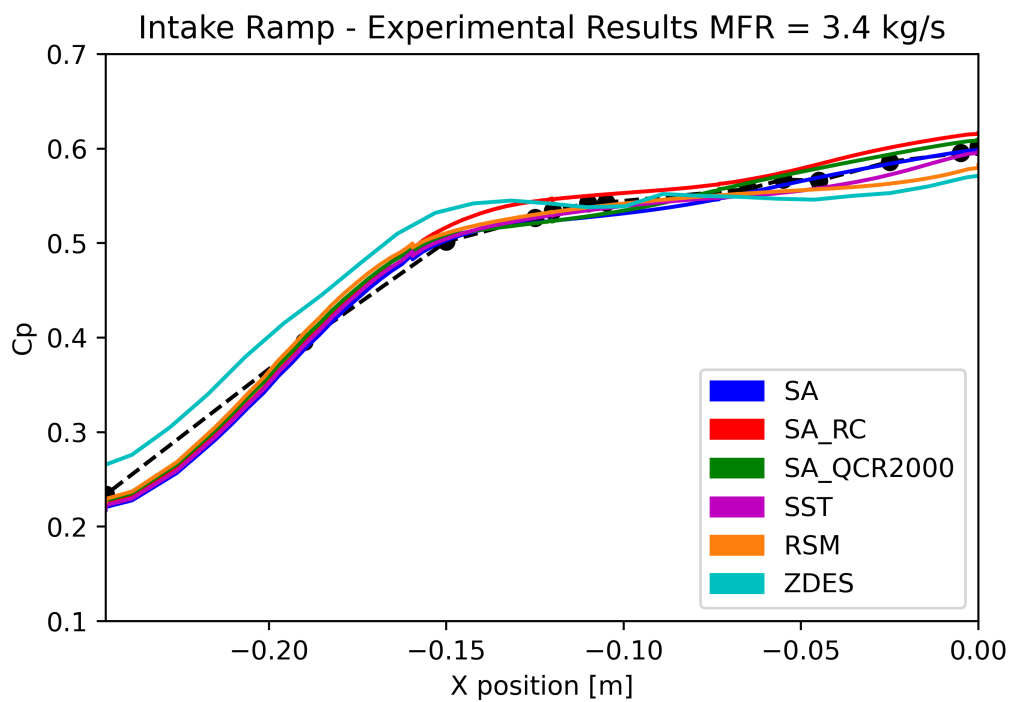


Figure 6.10: Comparison of wall pressure coefficient (C_p) along the intake ramp for various turbulence models at a mass flow rate (MFR) of $3.4 \text{ kg}\cdot\text{s}^{-1}$. In this case there is a flow separation.

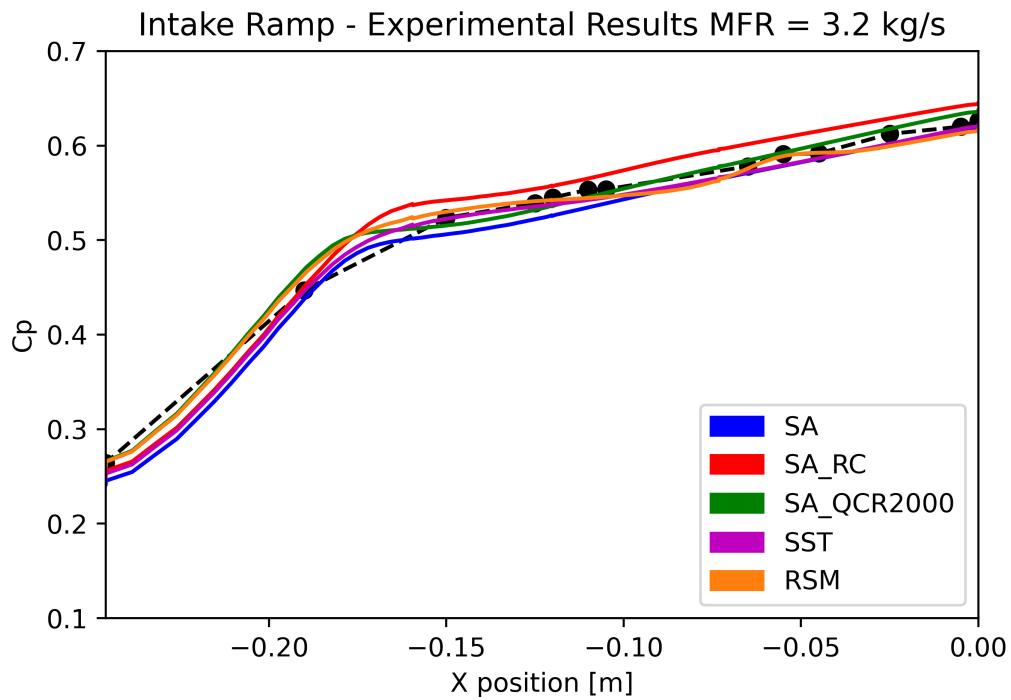


Figure 6.11: Comparison of wall pressure coefficient (C_p) along the intake ramp for various turbulence models at a mass flow rate (MFR) of $3.2 \text{ kg}\cdot\text{s}^{-1}$. In this case there is a flow separation.

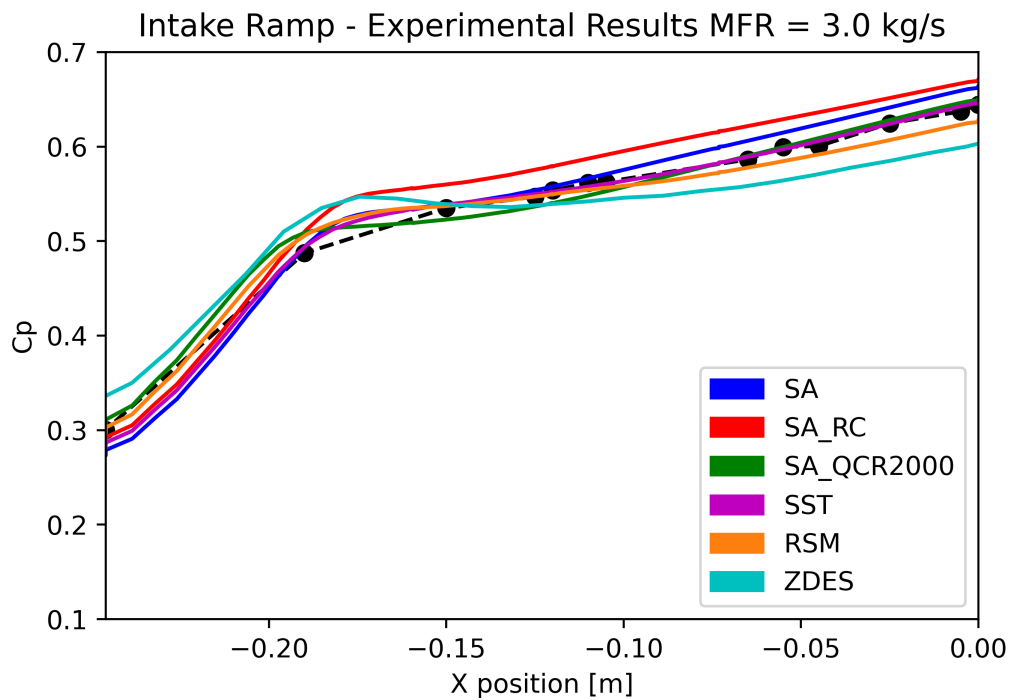


Figure 6.12: Comparison of wall pressure coefficient (C_p) along the intake ramp for various turbulence models at a mass flow rate (MFR) of $3.0 \text{ kg}\cdot\text{s}^{-1}$. In this case there is a flow separation.

Figures 6.9-6.12 show the cases for which there is a flow separation at the intake ramp, which occurs for x values between -0.20 m to -0.15 m. The mass flow rate from which the flow separation appears may vary according to the turbulence model, although for values less than 3.5 $\text{kg}\cdot\text{s}^{-1}$ all turbulence models predict a separation bubble. In general, the simulations demonstrate a favorable predictive capability along the ramp. RSM and $k-\omega$ SST models exhibit a good agreement with experimental data in regions where flow separation manifests. However, in the lower segment of the ramp, a better accuracy is achieved through the utilization of the SA-QCR2000 and the $k-\omega$ SST models.

For the case with the most intense separation ($\text{MFR} = 3.0$ $\text{kg}\cdot\text{s}^{-1}$), the $k-\omega$ SST model is in better agreement with the experiment for the whole intake ramp than other models. Nevertheless, the discrepancies observed in comparison with other models are not substantially significant. The SA models tend to over-predict the pressure on the wall along the intake ramp. When the flow is fully separated, the SA-QCR2000 model appears to have a improvement in prediction compared to other SA models. In general, the SA-RC model tends to give the least accurate prediction. For this MFR value, the ZDES does not improve the pressure estimation.

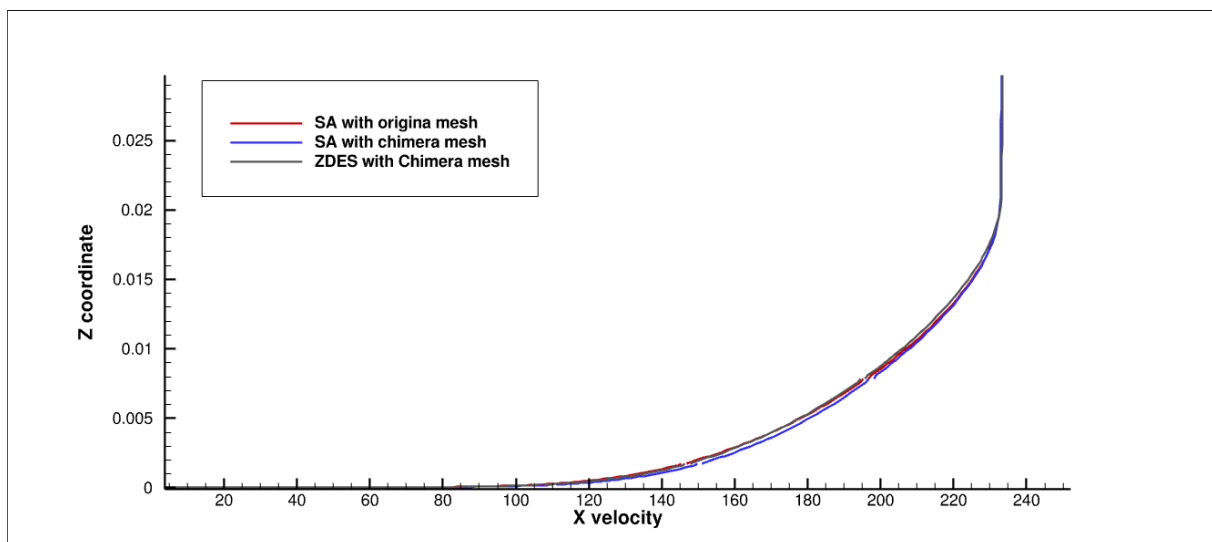


Figure 6.13: Comparison of boundary layer profile for ZDES and SA simulations at 3.0 $\text{kg}\cdot\text{s}^{-1}$.

According to the results for both ZDES runs, the pressure at the beginning of the intake ramp is overestimated. The overestimation of the pressure could be due to differences in the boundary layer shape or the use of a mesh with a chimera method. The boundary layer profile of both meshes used in the SA and ZDES is depicted in Figure 6.13. The boundary layer is measured at $x = -0.275$ m. The profiles obtained from both simulations are similar, indicating that there are no significant differences between them. The C_p distribution over the intake wall is illustrated in Figure 6.14. The plot reveals that there are significant differences between the pressure distributions obtained from the two meshes. The Spalart-Allmaras (SA) model with chimera mesh tends to overestimate the C_p at the beginning of the intake ramp, similar to what was

observed in the ZDES. However, from the flow separation, its behavior diverges from the ZDES model, showing much more similarity to that obtained with the original mesh, but with some vertical displacement .

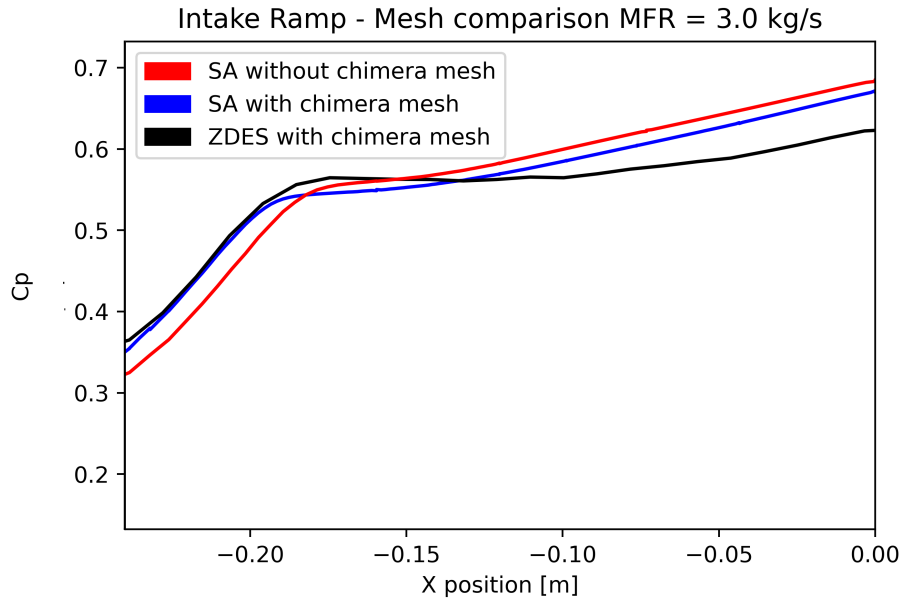


Figure 6.14: Comparison of wall pressure coefficient (C_p) along the intake ramp for ZDES and SA simulations at $3.0 \text{ kg}\cdot\text{s}^{-1}$.

MFR [$\text{kg}\cdot\text{s}^{-1}$]	SA [m]	SA-RC [m]	SA-QCR [m]	SST[m]	RSM [m]	ZDES [m]
3.0	-0.192	-0.189	-0.200	-0.185	-0.186	-0.205
3.2	-0.183	-0.176	-0.186	-0.173	-0.169	NS
3.4	-0.160	-0.153	-0.164	-0.149	-0.141	-0.169
3.5	-0.140	-0.131	-0.144	-0.118	-0.086	NS
3.6	-0.0991	-0.096	-0.110	-0.066	X	NS
3.7	X	-0.056	-0.068	X	X	NS
4.0	X	X	X	X	X	NS

Table 6.1: Location of the separation point for different MFR values and turbulence models (the origin is located at the AIP)

Table 6.1 shows the location of flow separation predicted by each model. None of the turbulence models predicts separation for the $4.0 \text{ kg}\cdot\text{s}^{-1}$ case, which is consistent with the curve shown in Figure 6.6, where all turbulence models have exactly the same pressure curve on the ramp. In Figures 6.7 and 6.8, there are small differences in curves, especially around $x = -0.05$. The different variants of Spalart-Allmaras and $k\text{-}\omega$ SST predict small recirculation bubbles around

that value, while the RSM model is totally attached. From $3.4 \text{ kg}\cdot\text{s}^{-1}$, all turbulence models tend to predict a strong flow separation. In general, models of the Spalart-Allmaras family tend to predict separation earlier than other models. The $k\text{-}\omega$ SST and RSM models tend to predict later and smaller separation. Looking at pressure curves, the $k\text{-}\omega$ SST model tends to be in better agreement with the experimental data. All turbulence models show slight dispersion when flow begins to separate, but this last model is the most accurate.

6.2 Top-nacelle analysis

The analysis in this section uses sensors from PS104 to PS109. At the upper side of the nacelle, behavior is similar to that of the ramp. As expected, pressure increases when velocity of ingested flow decreases. For this part of the nacelle, there is no flow separation; however, some influence of wind tunnel walls may be expected. Figure 3.34 shows experimental C_p curves for mass flow rate values from $3.0 \text{ kg}\cdot\text{s}^{-1}$ to $4.0 \text{ kg}\cdot\text{s}^{-1}$. Figures 6.15-6.21 show C_p curves for each mass flow rate and turbulence models.

For high mass flow rates, there is not so much dispersion of the curves predicted by each turbulence model. Some dispersion of the curves can be appreciated in cases where flow begins to separate, more clearly for mass flows less than $3.4 \text{ kg}\cdot\text{s}^{-1}$. This separation occurs only on the ramp; however, its effects can be seen in the whole flow field ingested by the engine. In such instances, it is generally observed that turbulence models tend to underestimate the C_p at lower MFR. Contrary to the ramp, the SA-RC model appears to yield a prediction that is marginally more proximate to the experimental data. At $3.0 \text{ kg}\cdot\text{s}^{-1}$, the curve delineated by the SA-RC model is evidently distinct from those predicted by alternative models; nevertheless, these variances are not deemed to be of substantial difference.

The stagnation point on the nacelle is a parameter that can influence the distribution of pressure over the nacelle. It is generally expected that this parameter should change as the mass flow rate varies. However, due to the discretization of pressure sensors on the wall, it is difficult to estimate the position of this point with precision using experimental data. Numerical data can be used to easily find this point. The set of plots in Figures 6.22 and 6.23 show the C_p curves for both interior and exterior surfaces for all turbulence models used. The upper part shows the curves for a mass flow rate of $4.0 \text{ kg}\cdot\text{s}^{-1}$, while the lower part shows them for a mass flow rate of $3.0 \text{ kg}\cdot\text{s}^{-1}$.

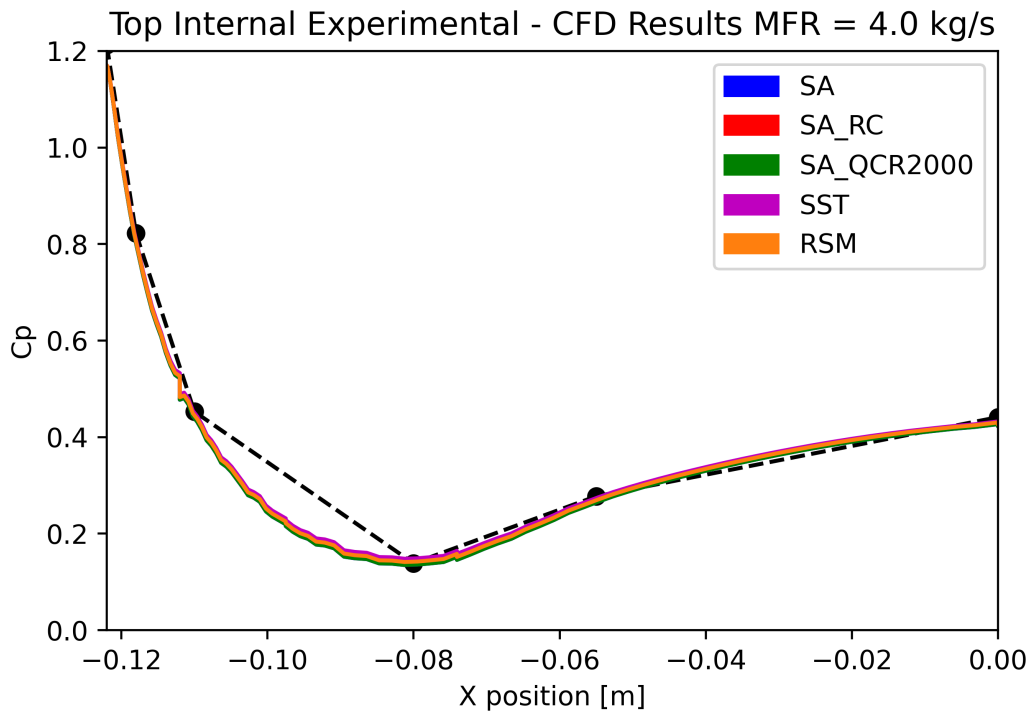


Figure 6.15: Comparison of wall pressure coefficients (C_p) along top upper side nacelle for various turbulence models at $4.0 \text{ kg}\cdot\text{s}^{-1}$.

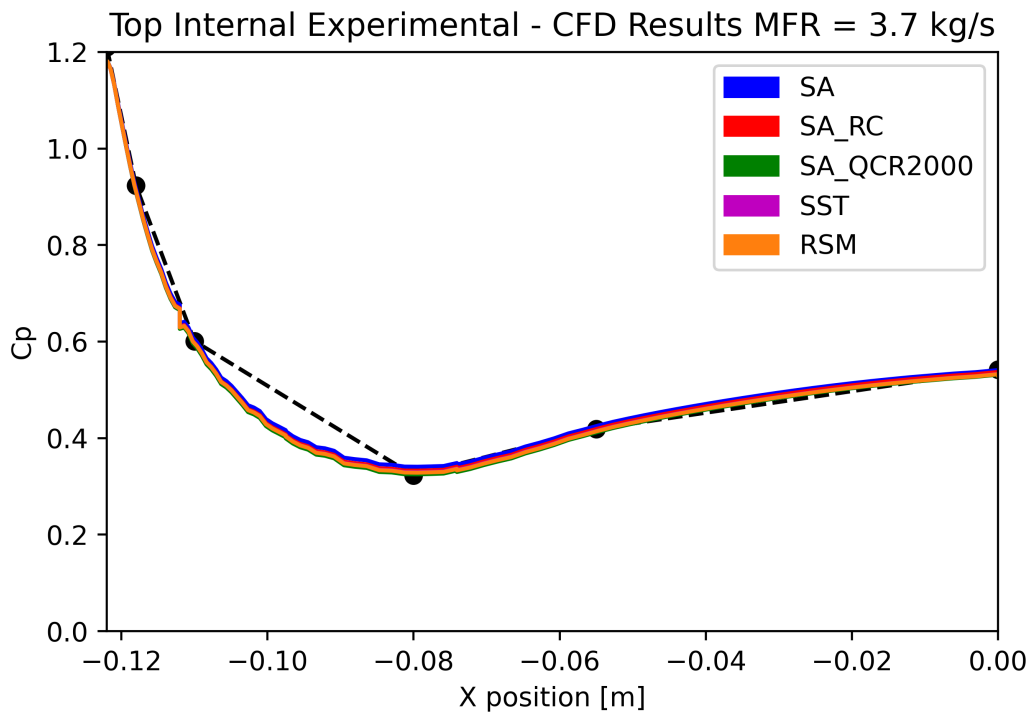


Figure 6.16: Comparison of wall pressure coefficients (C_p) along top upper side nacelle for various turbulence models at $3.7 \text{ kg}\cdot\text{s}^{-1}$.

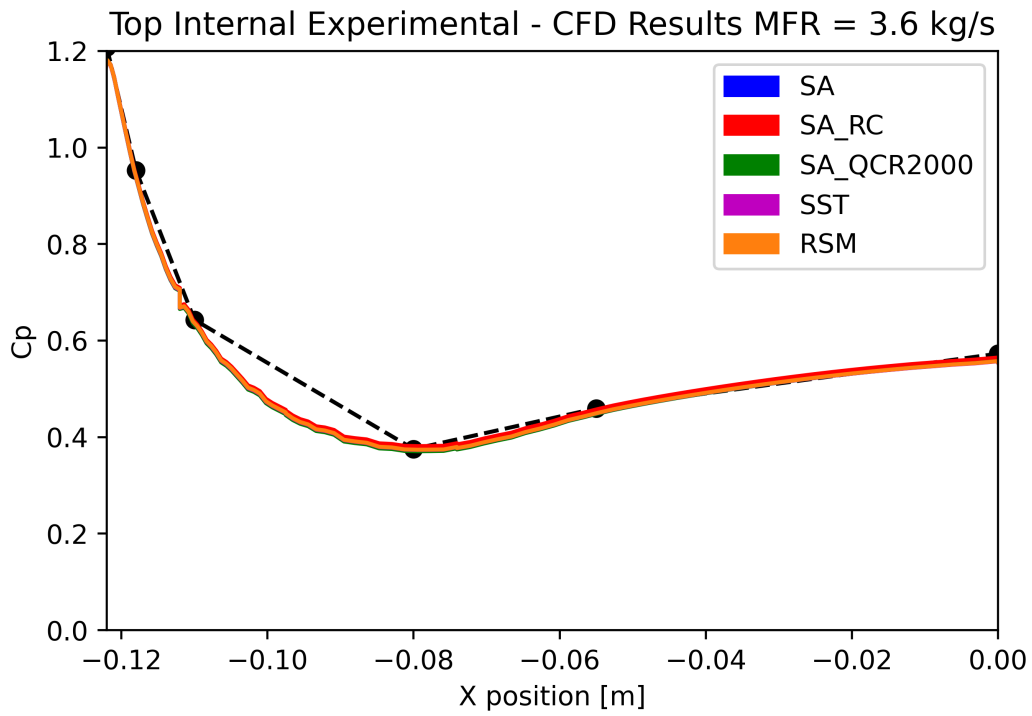


Figure 6.17: Comparison of wall pressure coefficients (C_p) along top upper side nacelle for various turbulence models at $3.6 \text{ kg}\cdot\text{s}^{-1}$.

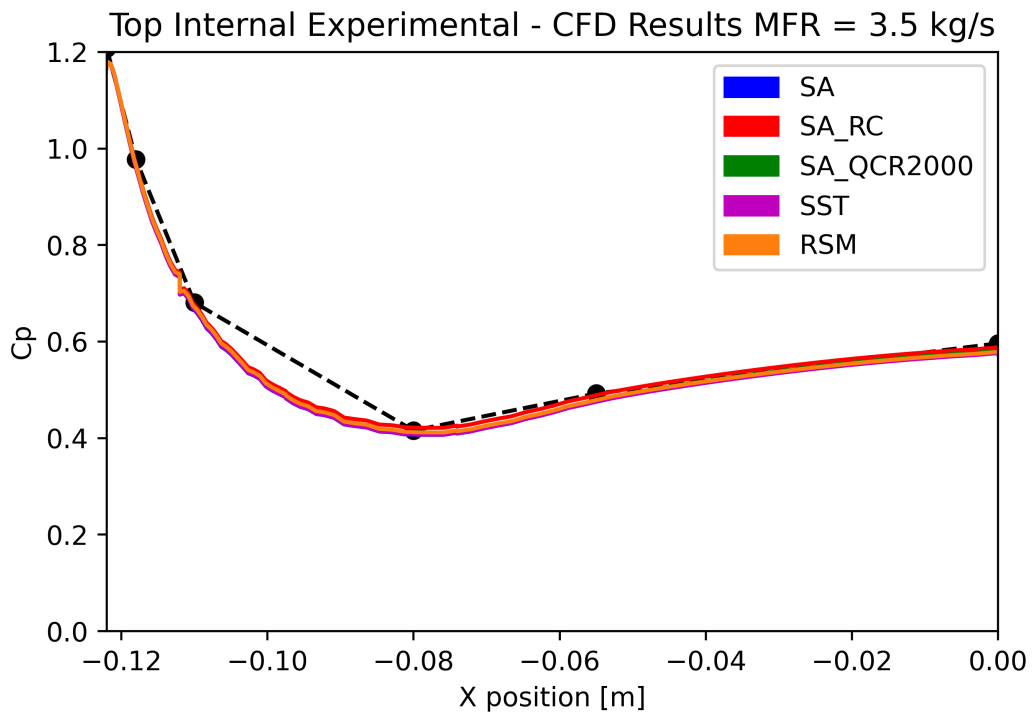


Figure 6.18: Comparison of wall pressure coefficients (C_p) along top upper side nacelle for various turbulence models at $3.5 \text{ kg}\cdot\text{s}^{-1}$.

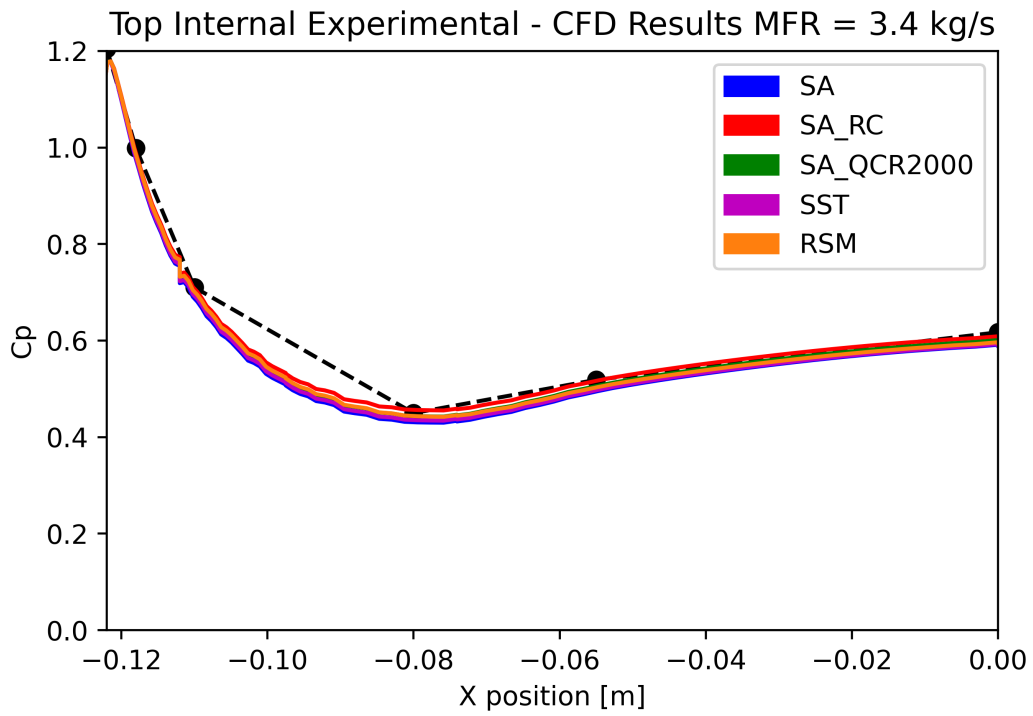


Figure 6.19: Comparison of wall pressure coefficients (C_p) along top upper side nacelle for various turbulence models at $3.4 \text{ kg}\cdot\text{s}^{-1}$.

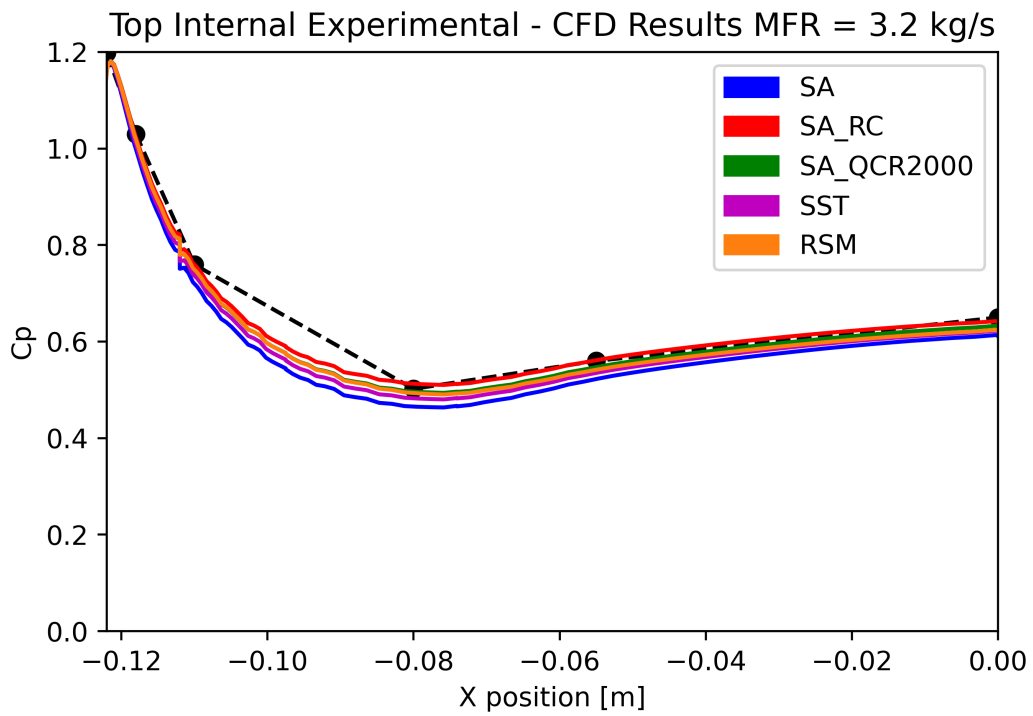


Figure 6.20: Comparison of wall pressure coefficients (C_p) along top upper side nacelle for various turbulence models at $3.2 \text{ kg}\cdot\text{s}^{-1}$.

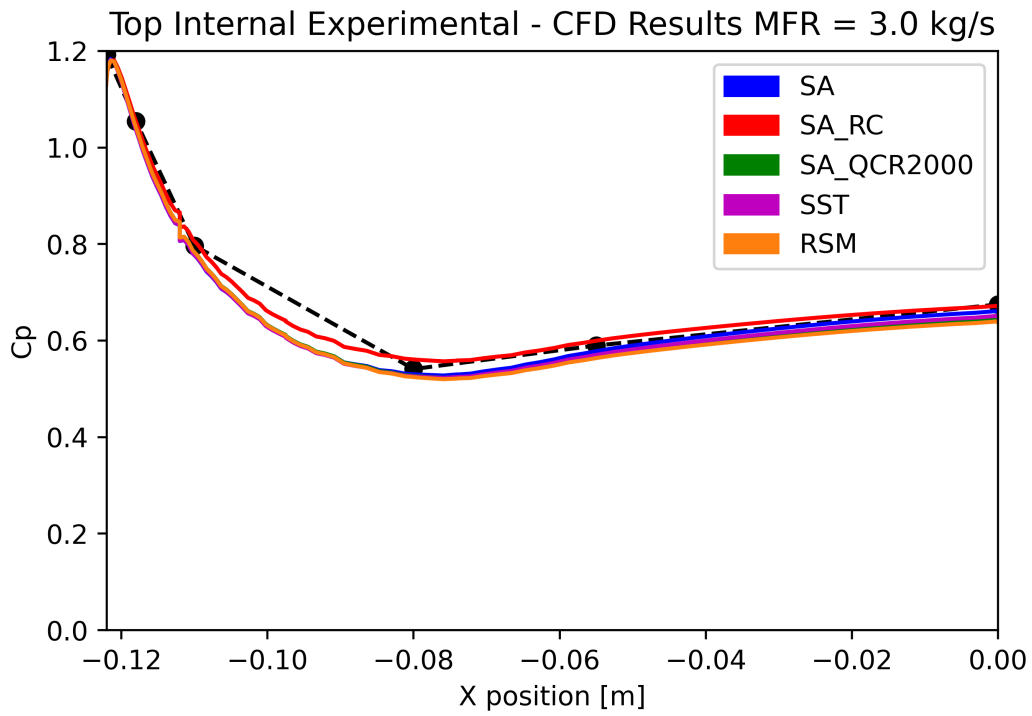


Figure 6.21: Comparison of wall pressure coefficients (C_p) along top upper side nacelle for various turbulence models at $3.0 \text{ kg}\cdot\text{s}^{-1}$.

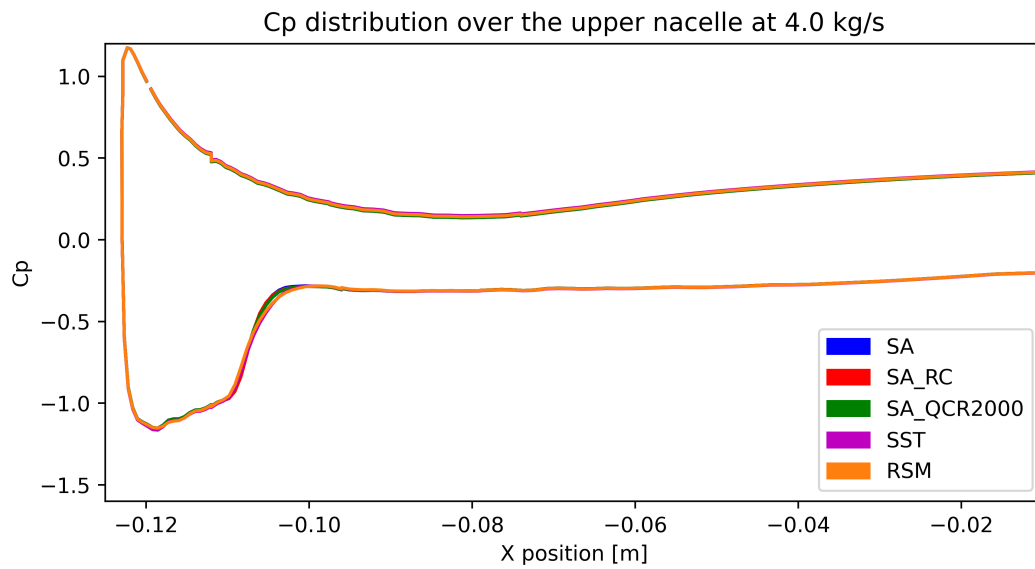


Figure 6.22: Wall pressure coefficient over the upper nacelle surface for different numerical turbulence models at $4.0 \text{ kg}\cdot\text{s}^{-1}$.

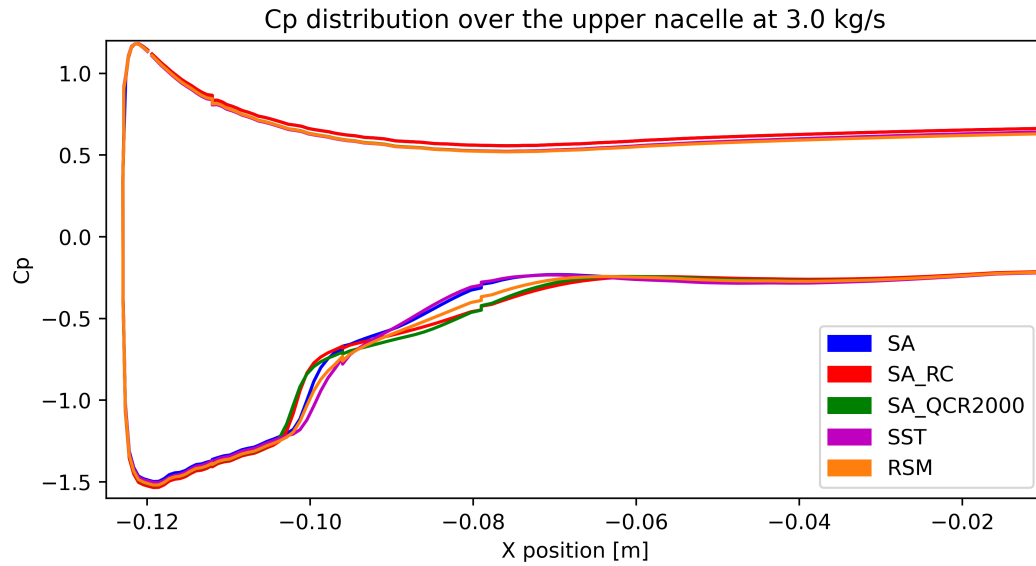


Figure 6.23: Wall pressure coefficient over the upper nacelle surface for different numerical turbulence models at $3.0 \text{ kg}\cdot\text{s}^{-1}$.

As previously shown, there is not a significant difference between the models on the interior side. In all cases, the stagnation point is located inside the nacelle, slightly displaced from the leading edge. There is no variance in the position of the stagnation point predicted by each turbulence model for the same mass flow rate case. In the case with flow separation, a significant data dispersion is noticeable. This data dispersion is primarily evident in the interior of the nacelle, which is indirectly influenced by the flow detachment and, as a result, alters the pressure field. Furthermore, a dispersion can be observed on the outer surface of the nacelle, which is caused by the presence of a shock wave. This last is even observed in the case with the highest mass flow.

6.3 Side-nacelle analysis

In this section the lateral sides of the nacelle are analysed. PS119 to PS124 and PS125 to PS130 describe the static pressure at left and right side respectively. Figures 6.24 to 6.28 show the evolution of Cp curve from a mass flow rate of $3.0 \text{ kg}\cdot\text{s}^{-1}$ to $4.0 \text{ kg}\cdot\text{s}^{-1}$.

All numerical models are in good agreement with the experimental data. Nonetheless, it is observed that the side-slip angle's effect, generated by the wind tunnel and quantified in Chapter 3, amplifies the differences between numerical and experimental data. Moreover, it is discernible that models which yield superior predictions on the ramp are inclined to underestimate the Cp on both sides for lower mass flow rate values. This tendency is exemplified by models such as the $k-\omega$ SST, RSM, and SA-QCR2000. Conversely, the SA-RC model, which demonstrates a lower accuracy on the ramp, exhibits an overestimation of Cp values for these cases.

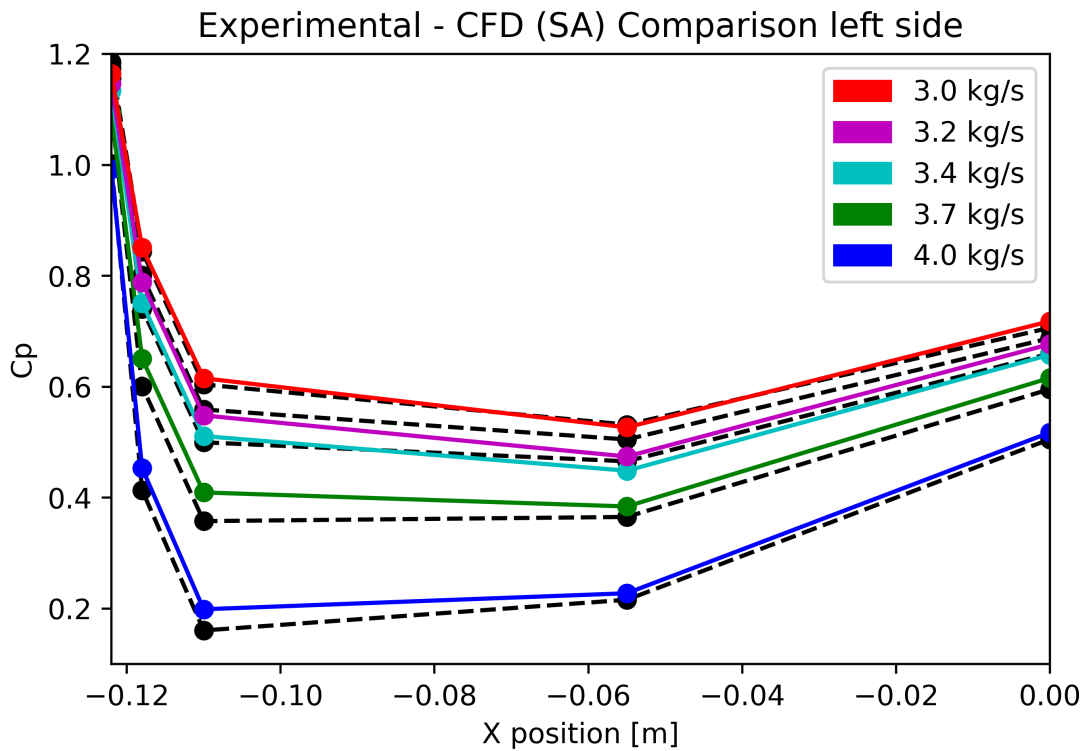
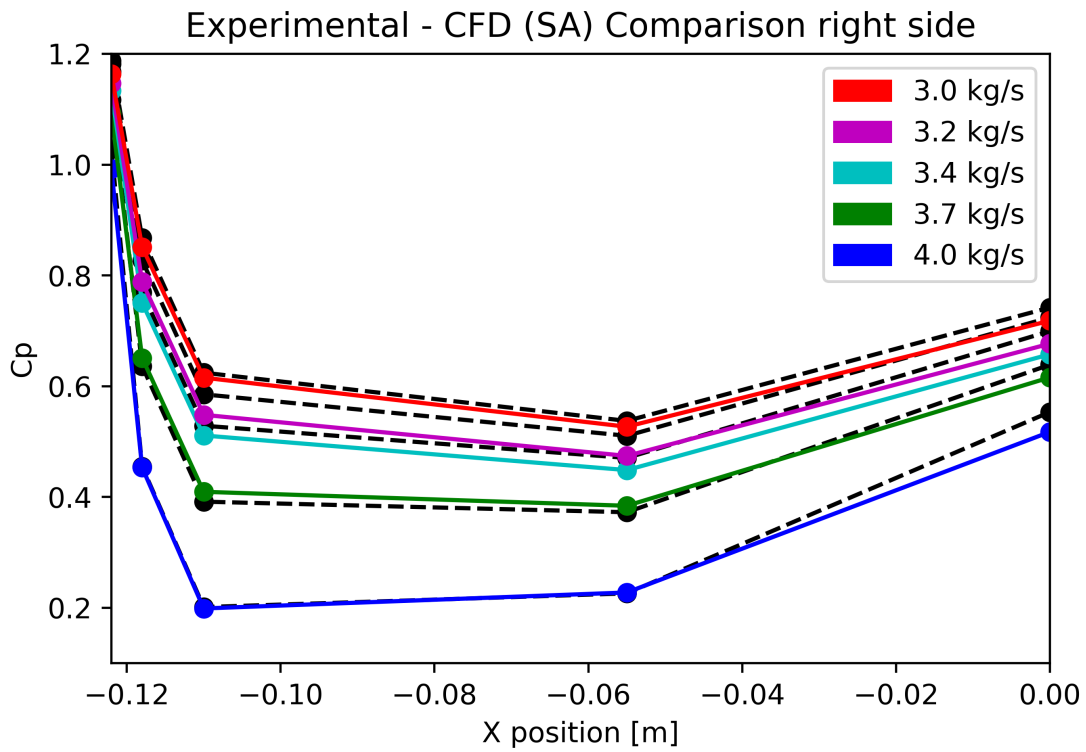


Figure 6.24: Comparison of wall pressure coefficients (C_p) over side-nacelle surfaces between experimental and numerical data obtained from Standard Spalart-Allmaras (SA) model. Up: right-side. Down: left-side.

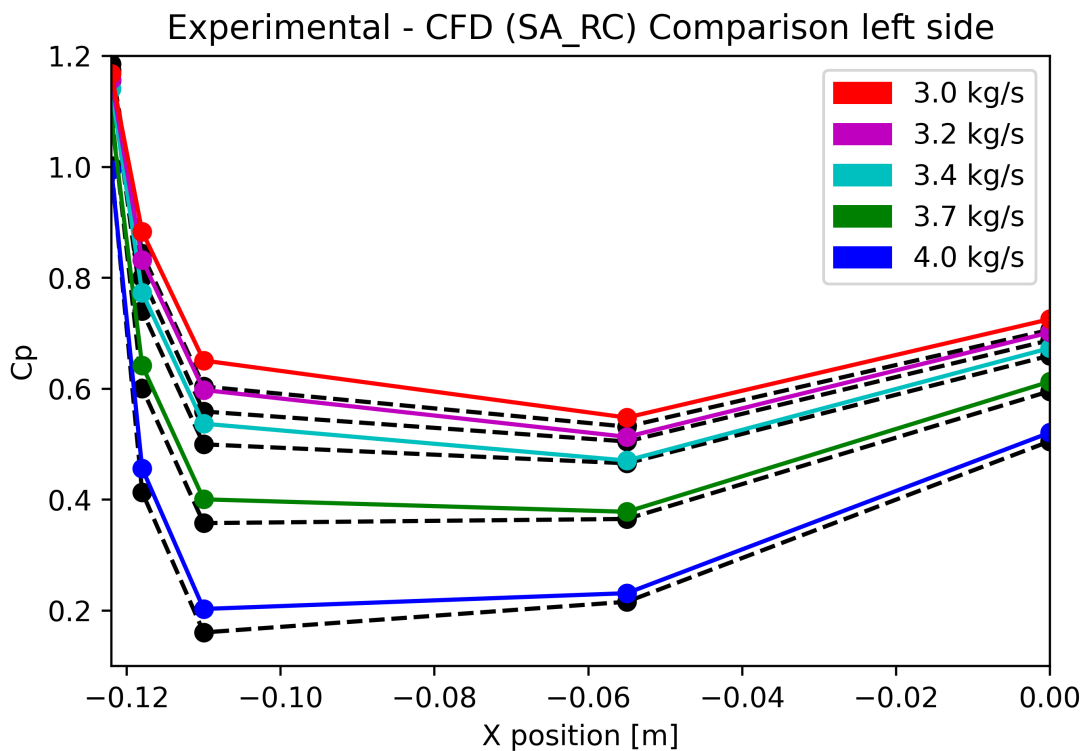
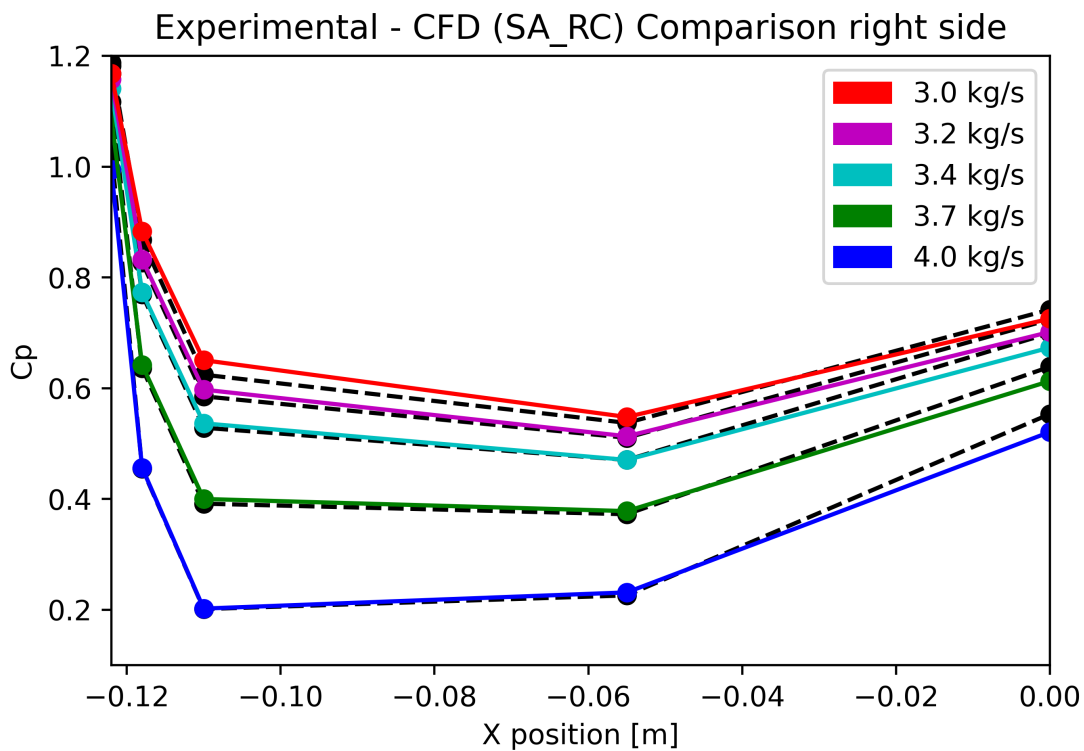


Figure 6.25: Comparison of wall pressure coefficients (C_p) over side-nacelle surfaces between experimental and numerical data obtained from Spalart-Allmaras model with rotation and curvature correction (SA-RC). Up: right-side. Down: left-side.

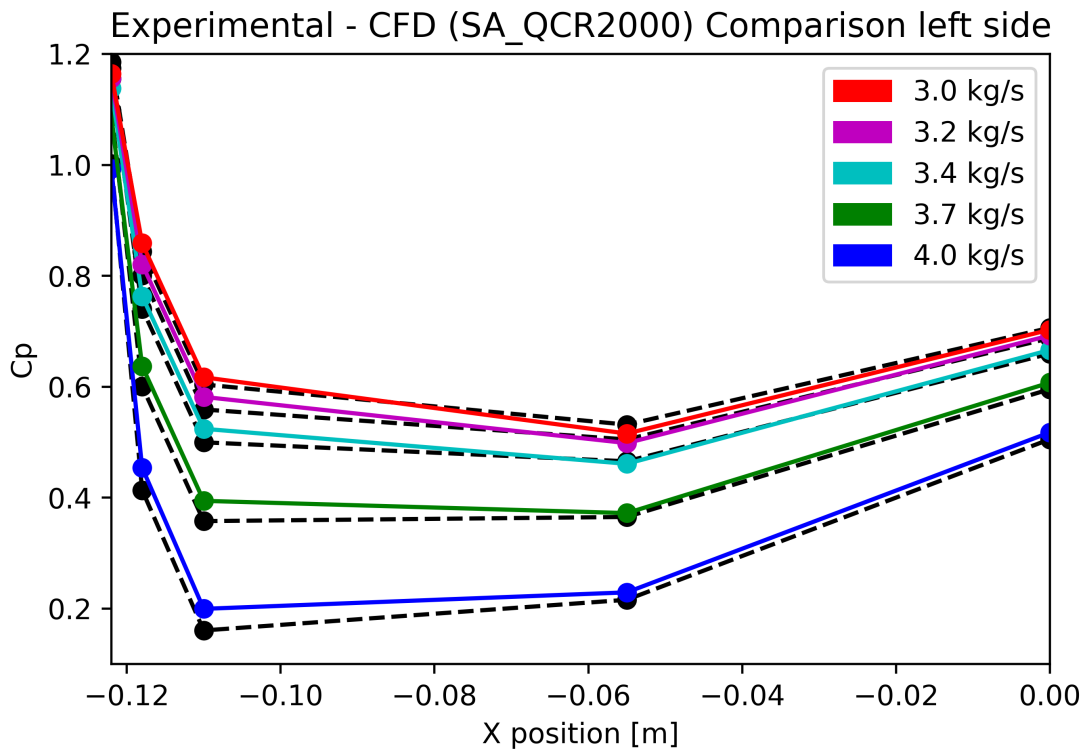
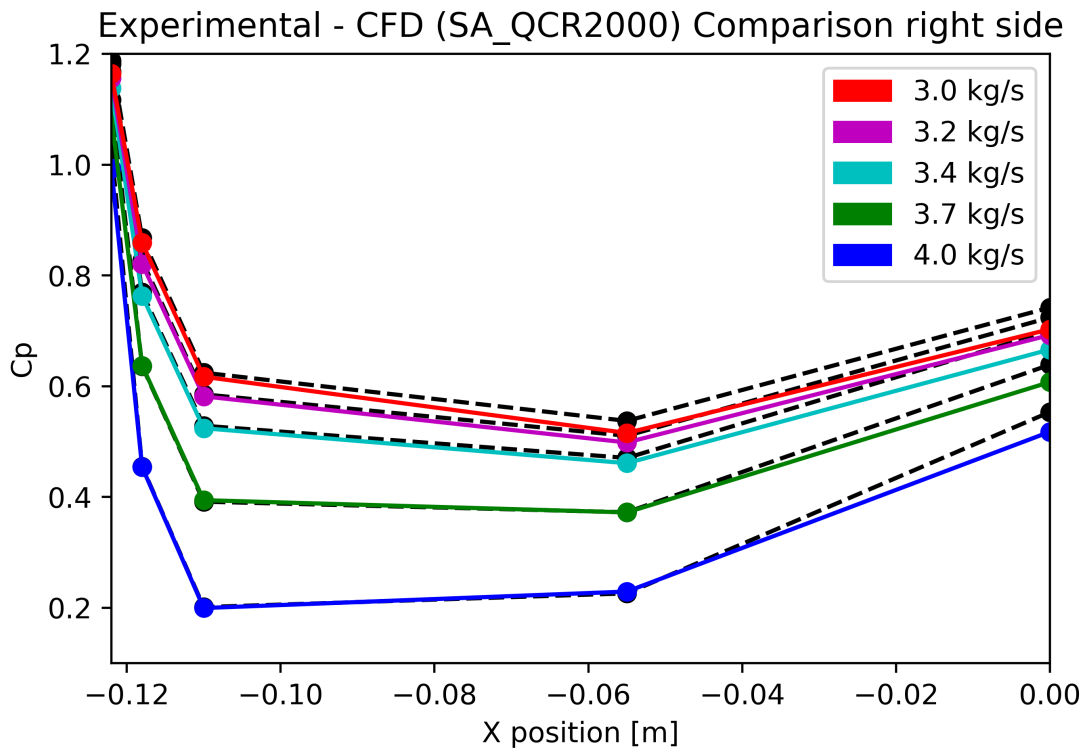


Figure 6.26: Comparison of wall pressure coefficients (C_p) over side-nacelle surfaces between experimental and numerical data obtained from Spalart-Allmaras model with quadratic constitutive relation (SA-QCR2000). Up: right-side. Down: left-side.

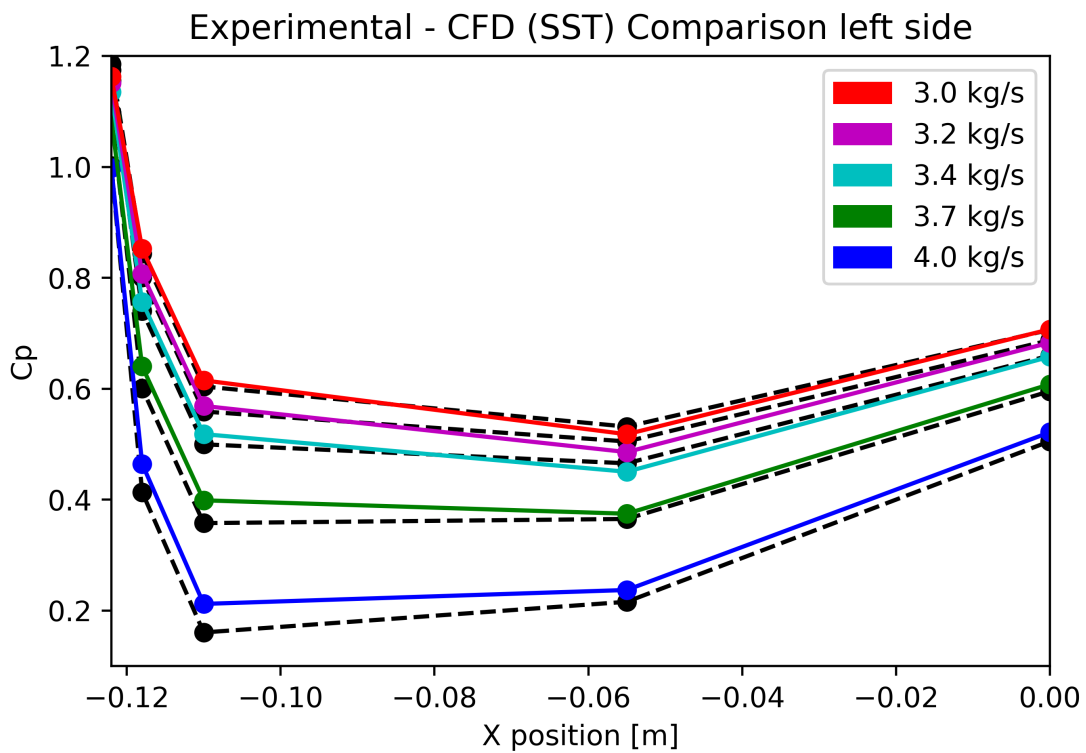
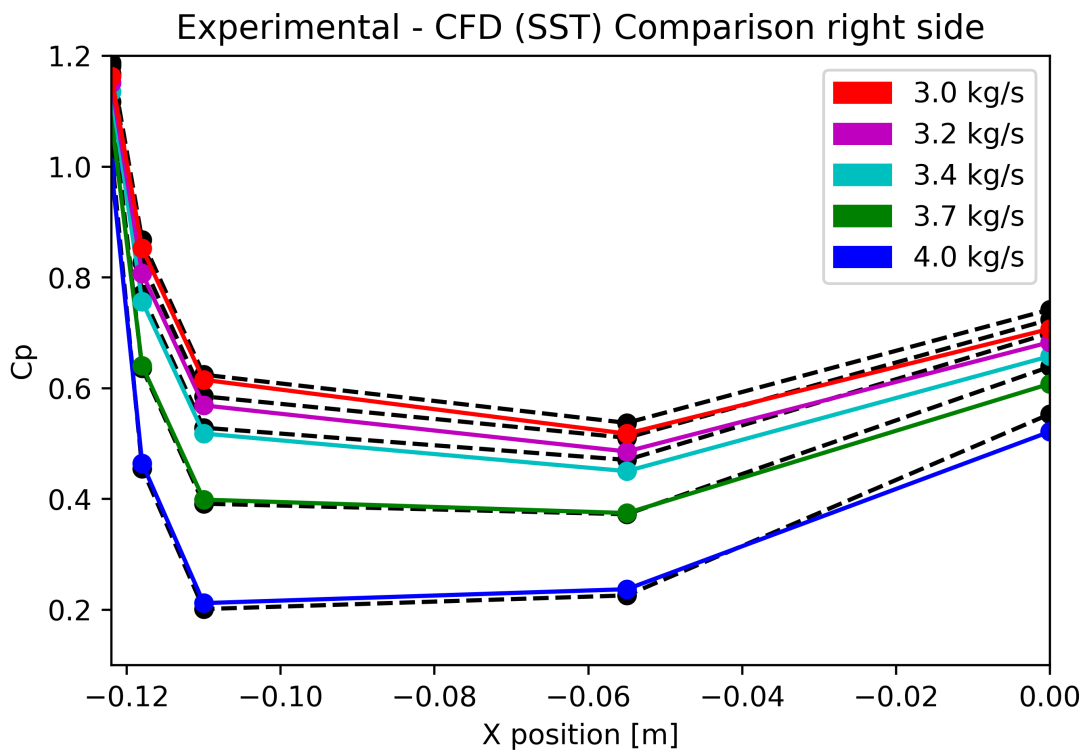


Figure 6.27: Comparison of wall pressure coefficients (C_p) over side-nacelle surfaces between experimental and numerical data obtained from $k-\omega$ SST model. Up: right-side. Down: left-side.

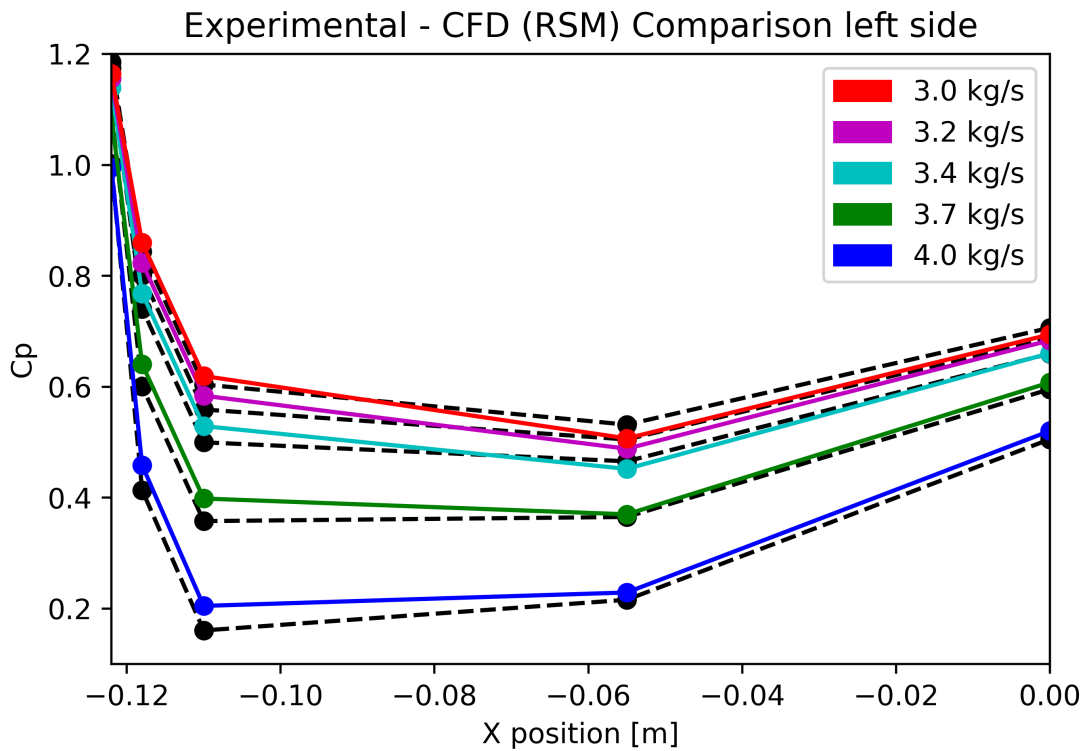
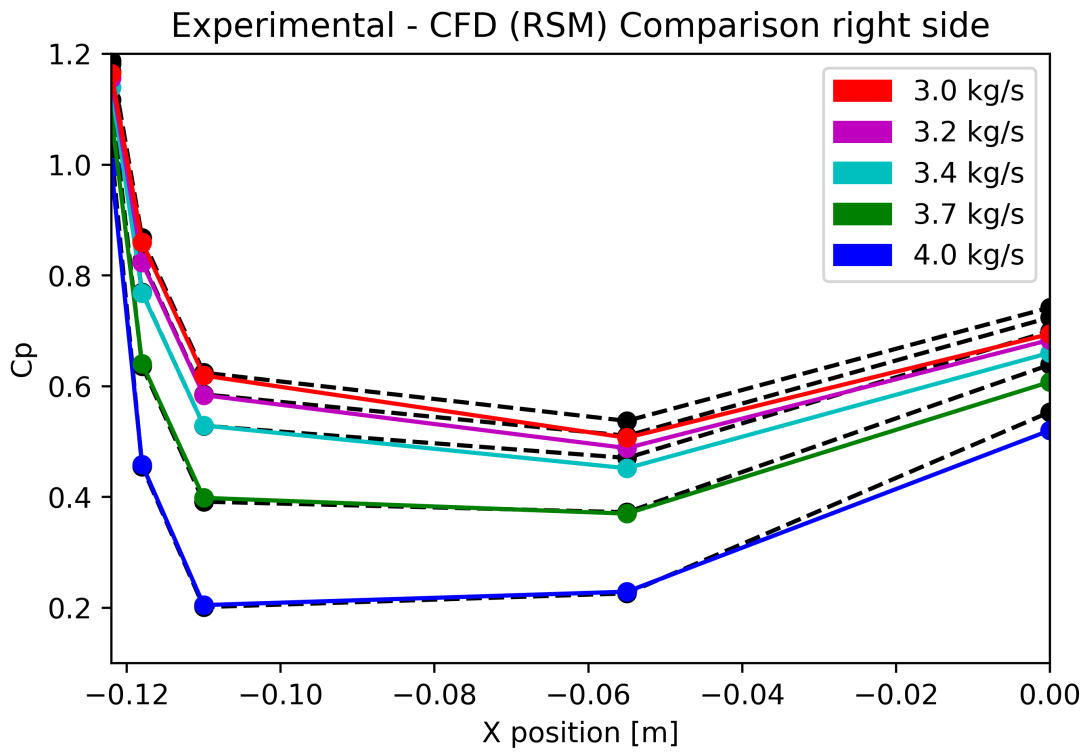


Figure 6.28: Comparison of wall pressure coefficients (C_p) over side-nacelle surfaces between experimental and numerical data obtained from Speziale–Sarkar–Gatski/Launder–Reece–Rodi differential Reynolds-stress model (RSM). Up: right-side. Down: left-side.

The observed discrepancies are concomitant with the manner in which various turbulence models reflect the intricate flow fields situated at the intake, particularly within the flow recirculation zone and in the downstream regions. It is anticipated that these variances will also manifest conspicuously in the distribution of total pressure loss at the AIP.

6.3.1 Flow condition parameters effects over C_p distribution

In the present section, it is proposed to analyze the effect of varying certain parameters, such as the boundary layer thickness and the number of Mach. Image 6.29 illustrates the pressure distribution on the entrance ramp. The left side of the image shows the pressure distribution for various boundary layer thicknesses, while the right side shows it for various Mach numbers. The corrected mass flow rate chosen is $3.4 \text{ kg}\cdot\text{s}^{-1}$ in both cases.

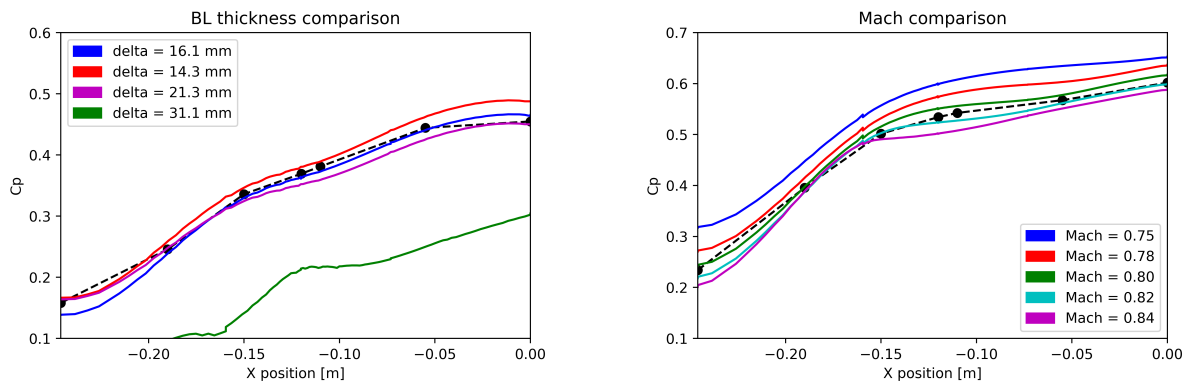


Figure 6.29: Comparison of wall pressure coefficients (C_p) over the intake ramp for different boundary layer thicknesses and Mach numbers. Left: Effect of the Boundary layer thickness. Right: Effect of the Mach number.

In terms of the variation of the boundary layer, it can be observed that the thickness has a direct effect on the pressure coefficient. Specifically, a larger boundary layer generates a more negative pressure coefficient. This difference is relative to the variation of the boundary layer thickness. Boundary layers with almost the same thickness maintain values and behaviors that are quite similar between them. The diminution of energy, accompanied by a corresponding decrease in pressure, is intrinsically linked to the frictional forces arising in the inner region of the boundary layer. A thick boundary layer has been generated using a longer development distance and same Reynolds number, which consequently allows the frictional forces to operate over an increased span, culminating in more energy dissipation.

The influence of the Mach number on the pressure coefficient distribution is evident: an increase in the Mach number leads to a diminution in the pressure coefficient over the ramp intake. The pattern of behavior is consistent, with variations appearing to induce solely a vertical shift in the C_p curve. This phenomenon can be attributed to the impact of frictional forces; as flow

velocity increases, the shear stress, and thus the skin friction drag, typically intensify, resulting in a reduction of energy over the surface.

6.4 Rake Analysis

6.4.1 Comparison of total pressures at the AIP

In this section, the impact of the boundary layer over the AIP is characterized, particularly the pressure loss generated at the AIP by comparing the numerical and experimental data. To measure this impact, the experimental rake, depicted in Figure 3.6, is employed.

The set of images presented in Figure 3.40 illustrate the experimentally measured P_i/P_{i0} at the AIP for different mass flow rate values. In all experimental cases, the upper half of the AIP remains unaffected by boundary layer thickening or possible flow separation. The ingestion of the boundary layer results in a loss of total pressure at the AIP, regardless of whether there is flow separation or not. The affected region is much larger for cases in which there is flow separation, even affecting the most internal radius. For cases in which the boundary layer is attached, the radius most affected by the loss of pressure is the most external. The total pressure loss zone is more evenly distributed for low mass flow values; conversely, for high mass flow values, the total pressure loss is highly concentrated in the lower part. This phenomenon occurs because when a flow separation appears, there is more energy exchange between the recirculation zone and the free stream. On the other hand, when the flow is attached, there is no large exchange of energy, and the loss of total pressure tends to concentrate on the boundary layer. In this latter case, the total pressure gradients are stronger.

Furthermore, another general behavior observed is that regardless of mass flow rate, the azimuthal region affected by total pressure loss remains constant. This region is located at the bottom between 200° and 340° . The images from Figures 6.30 to 6.36 show the total pressure field at the AIP normalized by the freestream total pressure obtained by the different RANS turbulence models and compared with the data obtained from the wind tunnel tests. Mass flow rates vary between $3.0 \text{ kg}\cdot\text{s}^{-1}$ and $4.0 \text{ kg}\cdot\text{s}^{-1}$. The results of different RANS turbulence models and the experimental data shows similar behaviors. It can also be noted that for high mass flow rates, turbulence models tend to predict a loss of maximum total pressure in the lower part of the boundary layer, as seen in the experimental data.

Images 6.30 and 6.32 also present a comparison of the AIP pressure loss between ZDES simulations and numerical data. In both cases, the affected azimuthal regions are quite similar. However, compared to the experimental results, the ZDES model tends to overestimate the loss of total pressure.

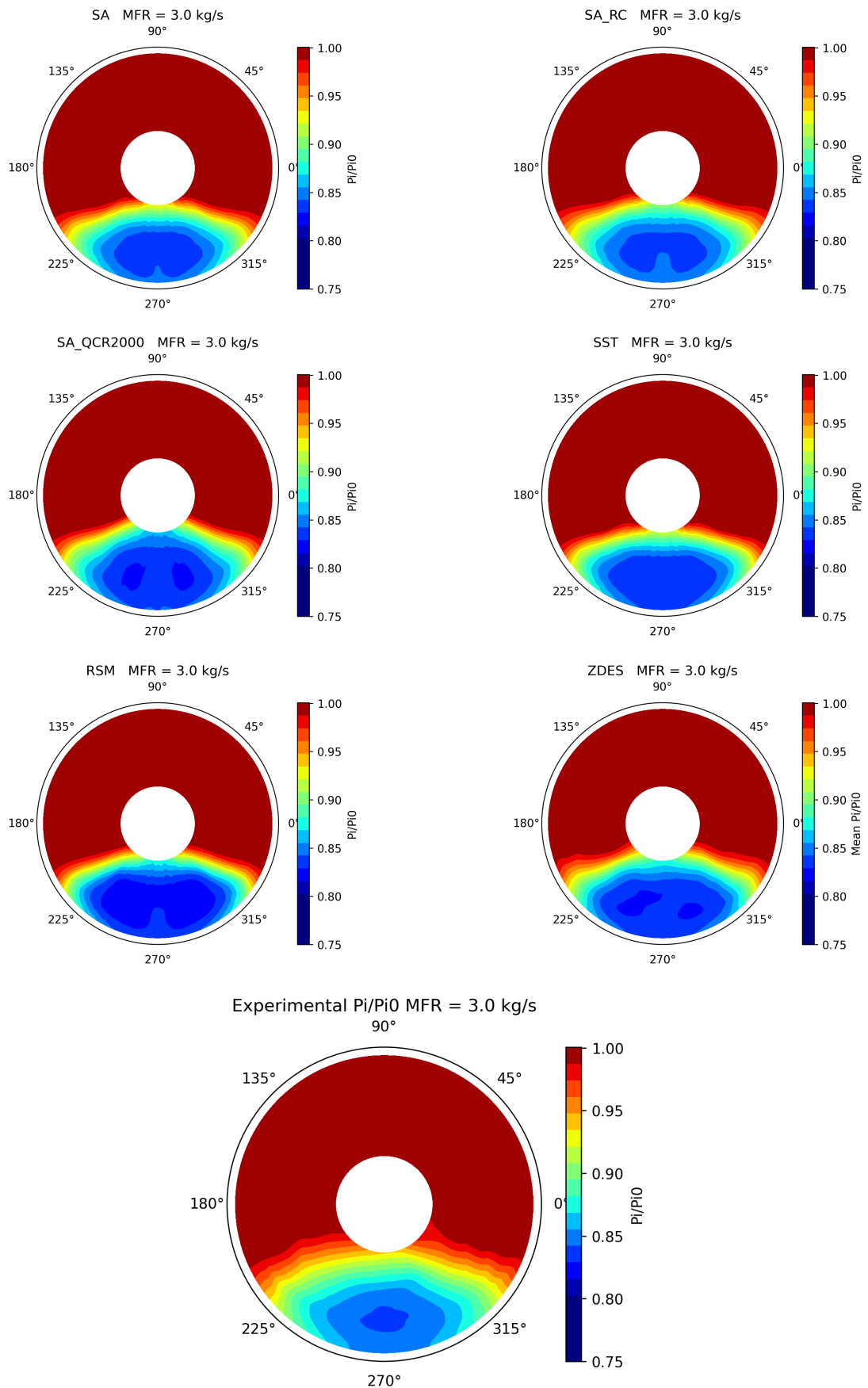


Figure 6.30: Comparison of pressure loss at the AIP between different turbulence models and experimental data for $3.0 \text{ kg}\cdot\text{s}^{-1}$. Up: Numerical simulations. Down: Experimental data.

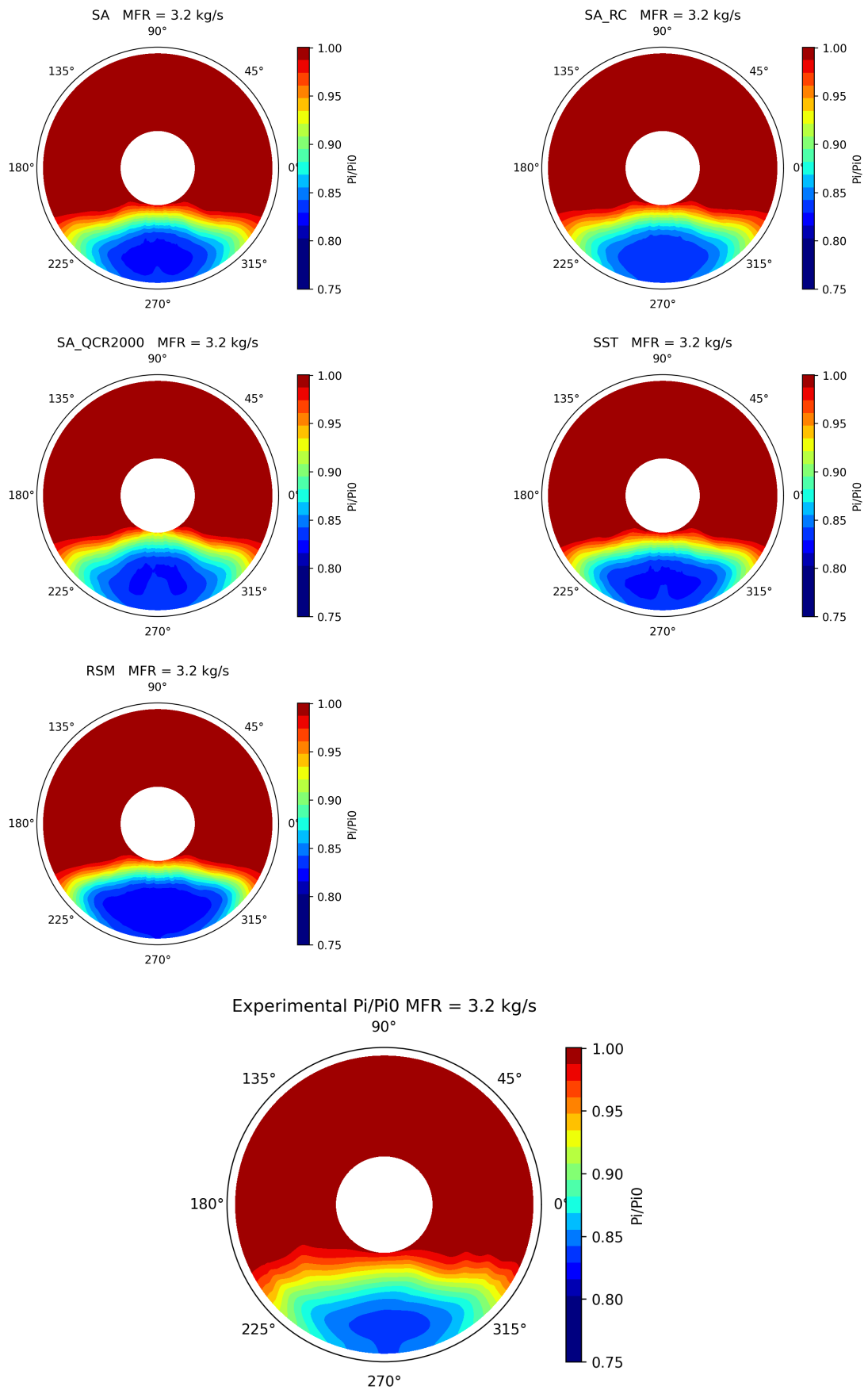


Figure 6.31: Comparison of pressure loss at the AIP between different RANS models and experimental data for $3.2 \text{ kg}\cdot\text{s}^{-1}$. Up: Numerical simulations. Down: Experimental data.

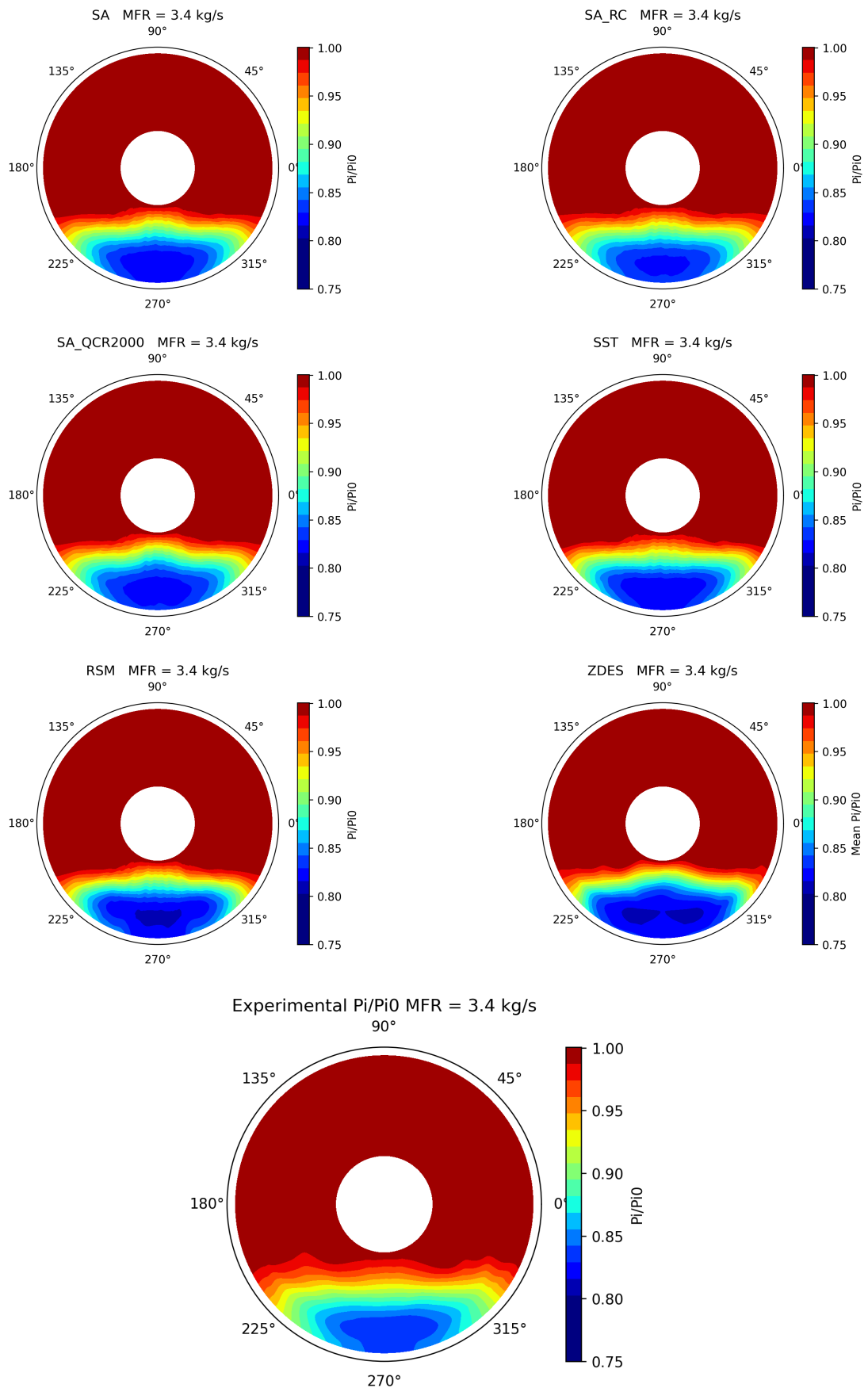


Figure 6.32: Comparison of pressure loss at the AIP between different turbulence models and experimental data for $3.4 \text{ kg}\cdot\text{s}^{-1}$. Up: Numerical simulations. Down: Experimental data.

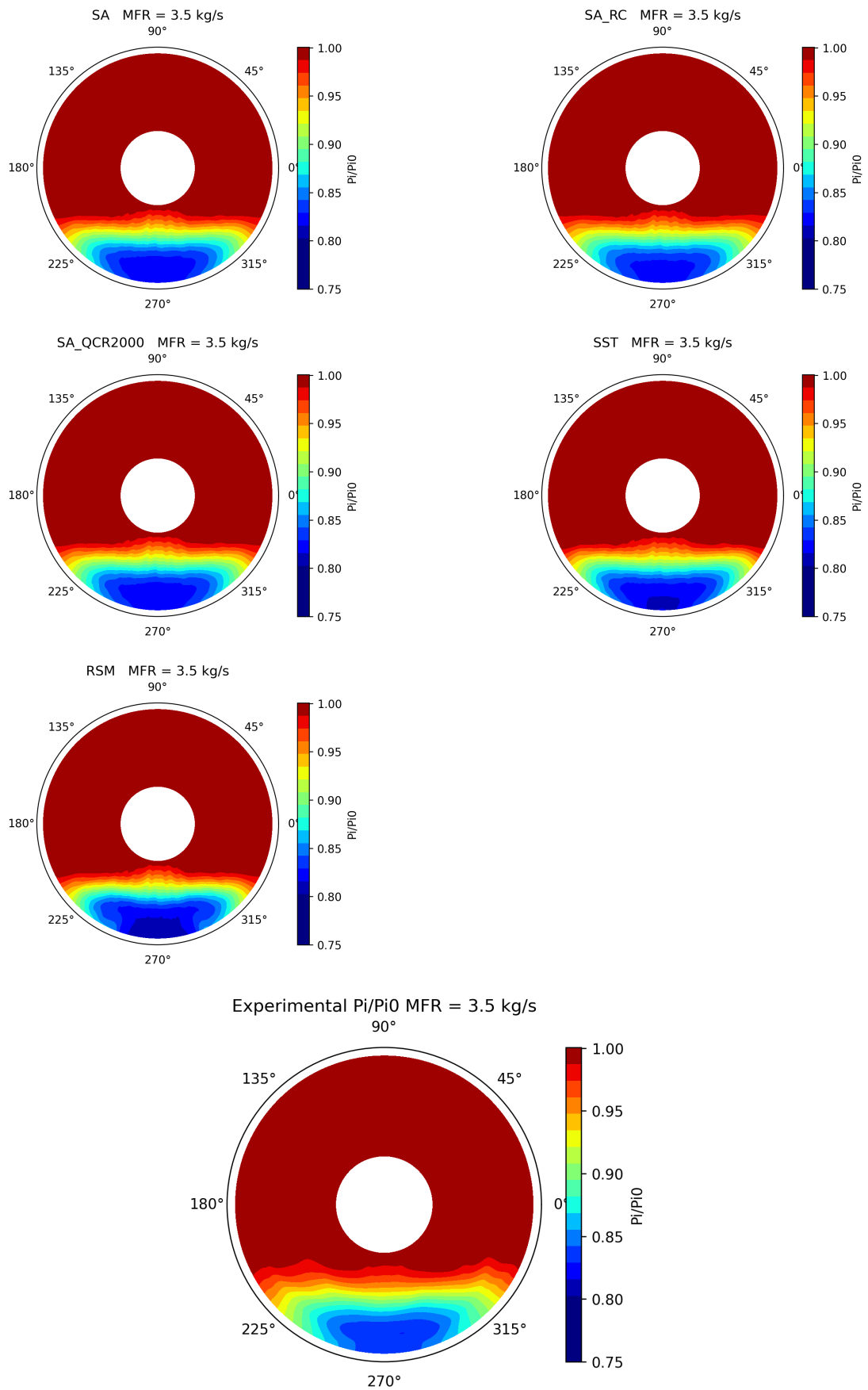


Figure 6.33: Comparison of pressure loss at the AIP between different RANS models and experimental data for $3.5 \text{ kg}\cdot\text{s}^{-1}$. Up: Numerical simulations. Down: Experimental data.

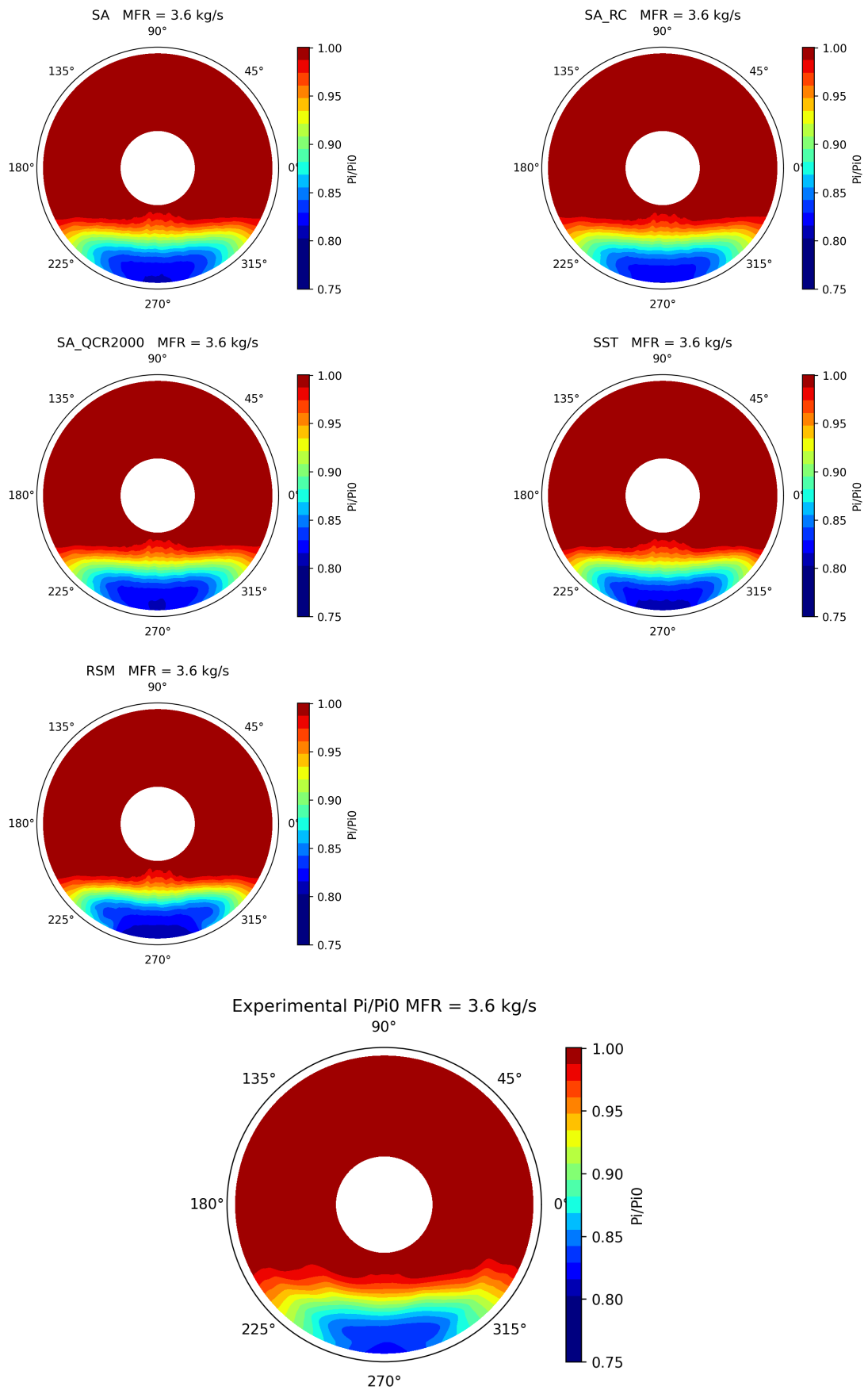


Figure 6.34: Comparison of pressure loss at the AIP between different RANS models and experimental data for $3.6 \text{ kg}\cdot\text{s}^{-1}$. Up: Numerical simulations. Down: Experimental data.

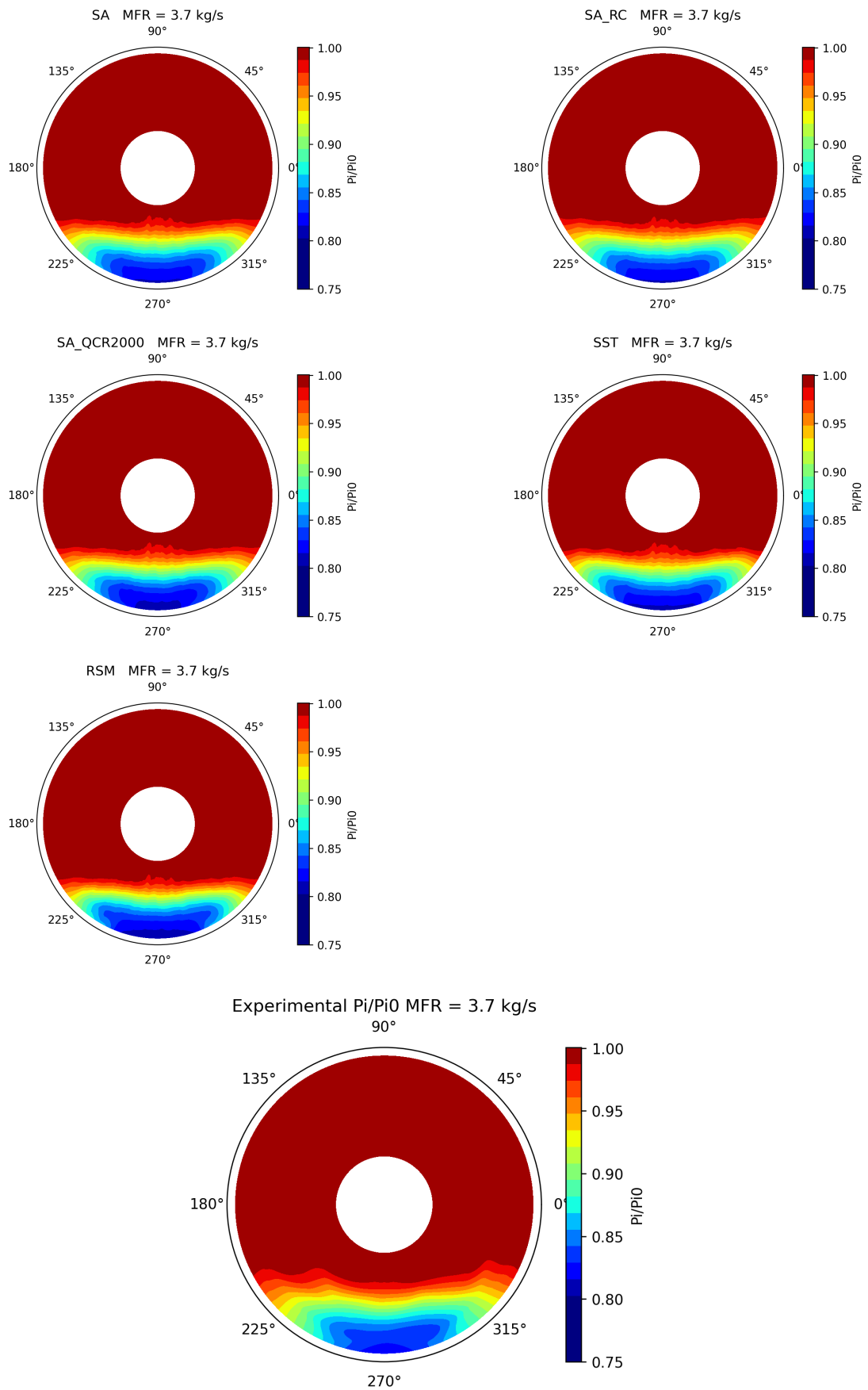


Figure 6.35: Comparison of pressure loss at the AIP between different RANS models and experimental data for $3.7 \text{ kg}\cdot\text{s}^{-1}$. Up: Numerical simulations. Down: Experimental data.

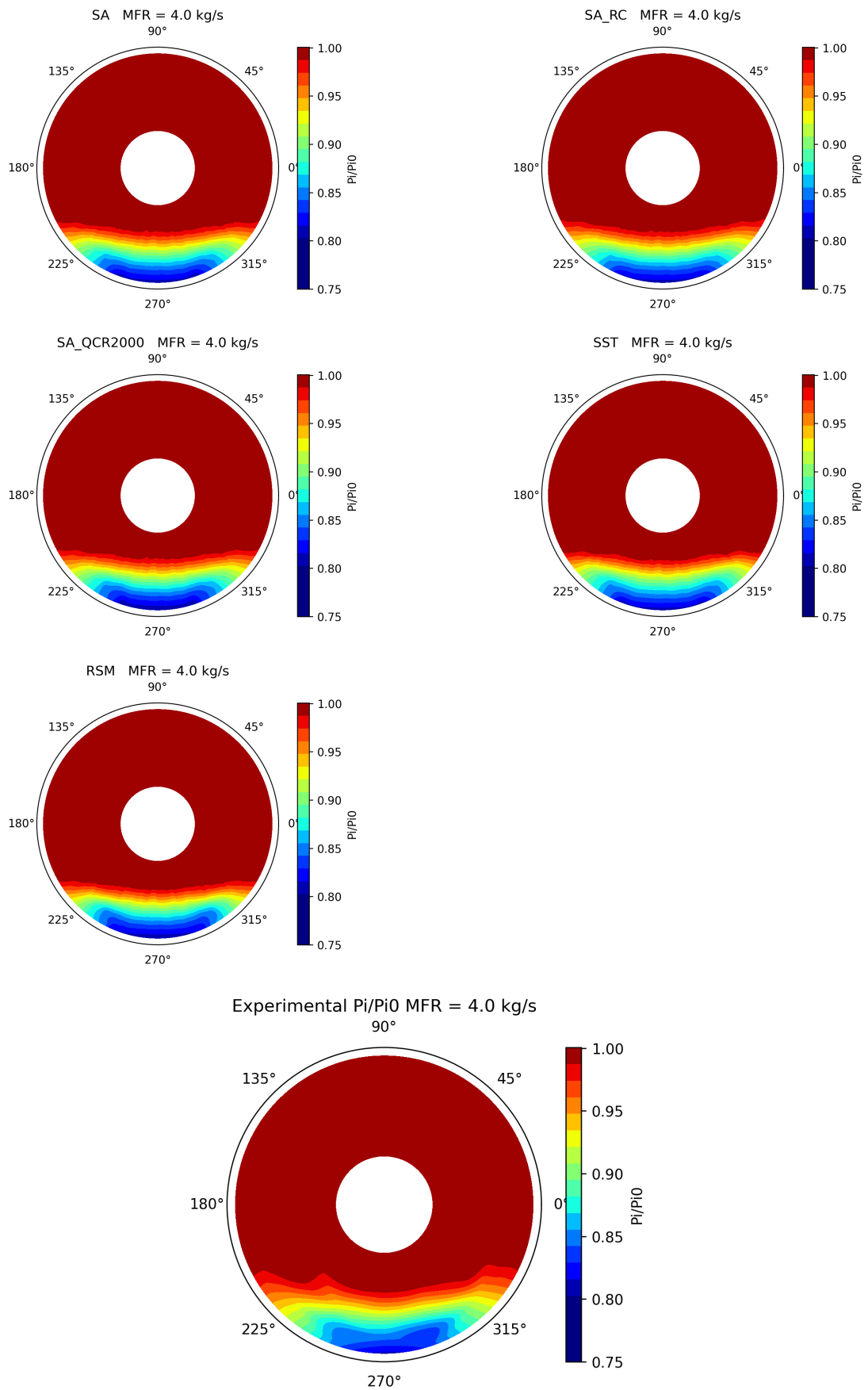


Figure 6.36: Comparison of pressure loss at the AIP between different RANS models and experimental data for $4.0 \text{ kg}\cdot\text{s}^{-1}$. Up: Numerical simulations. Down: Experimental data.

Additionally, the radial region affected by the loss of total pressure is also overestimated. The region with the highest total pressure loss seems to be located slightly higher than in the experimental results. It is possible that the recirculation region estimated by the mean value of the ZDES simulation is larger than observed in the experimental data. Furthermore, it appears that the shear layer is located closer to the center of the AIP.

The images above provide a visualization of the general behavior predicted by the turbulence models and compare them with the experimental data. In general, the behavior is similar to what was observed in the experimental data. However, there are some details that require further analysis to highlight other differences that may have been overlooked. Images 6.37 through 6.43 show the total pressure curves at the AIP, adimensioned with the total pressure in the freestream, of the different turbulence models and their comparison with the experimental results. Each color represents a different radius.

Figures 6.37 and 6.38 shows total pressure profiles corresponding to a massively separated case thus it exhibits significant discrepancies between the numerical results. The $k-\omega$ SST and Spalart-Allmaras without correction results exhibit the best agreement with the experimental data. The other turbulence models overestimate the total pressure loss at the AIP. This overestimation goes hand in hand with the prediction of a larger region affected by total pressure loss. This can be evidenced by looking at the profiles obtained in the most interior curves (R4-R5). In the case of ZDES the result obtained is quite similar to RSM. Figure 6.39 to 6.41 displays total pressure profiles for an MFR value with a small flow separation, revealing similar characteristics but with less noticeable differences amongst turbulence models. Particularly, for the $3.4 \text{ kg}\cdot\text{s}^{-1}$ case, the ZDES results overestimate total pressure losses in a larger way than the other turbulence models. In figures 6.42 and 6.43, all numerical results predict a flow without flow separation. These are the mass flow rate values for which the numerical simulations are in best agreement with the experimental data. The outer rings (R1-R2) exhibit very good agreement with the experimental data; nevertheless, in the regions impacted by the shear layer (R3-R4), the numerical simulations overestimate the loss of total pressure.

In general all turbulence models tend to over-estimate the loss of pressure without exception, this being still more evident in cases with large areas of recirculation and flow separation. This can also be seen in the cut-off layers or in regions where large amounts of turbulent kinetic energy accumulate, as shown in the case where there is no flow separation. It should also be noted that cases solved with the Spalart-Allmaras model with the quadratic constitutive relation (SA-QCR2000) tend to generate the greatest losses of total pressure, and even more the regions affected by it. A nonstationary analysis of the pressure measurements at the AIP, comparing the ZDES simulations and the experimental data, is performed in the following section.

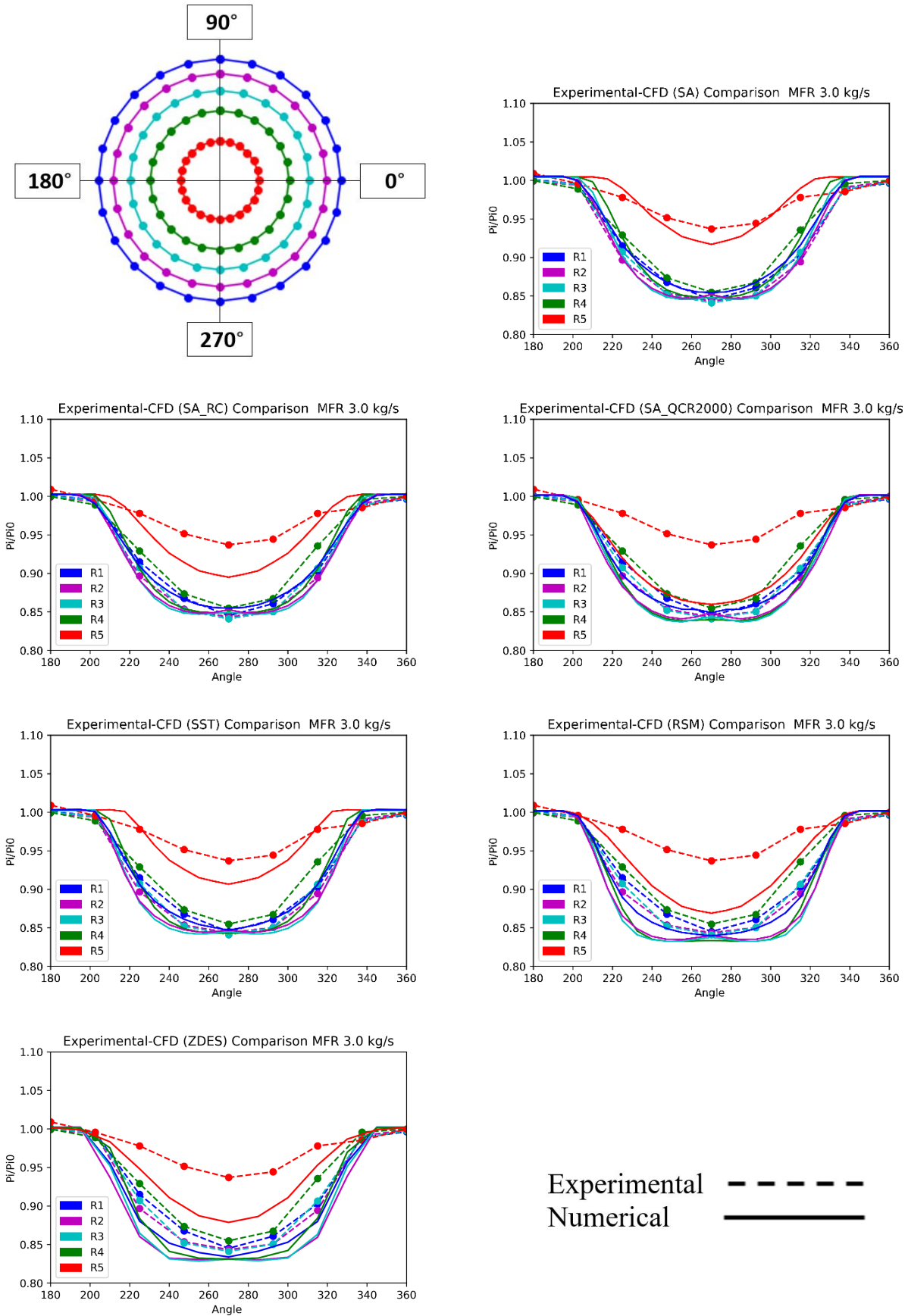
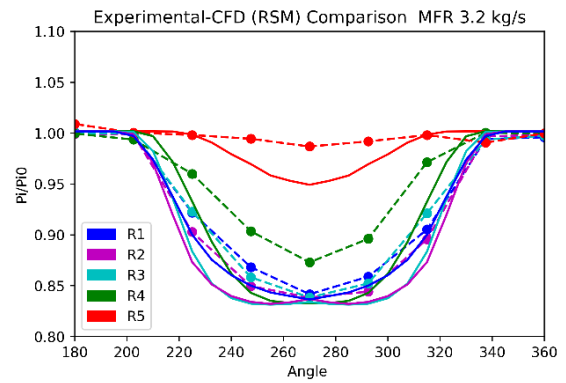
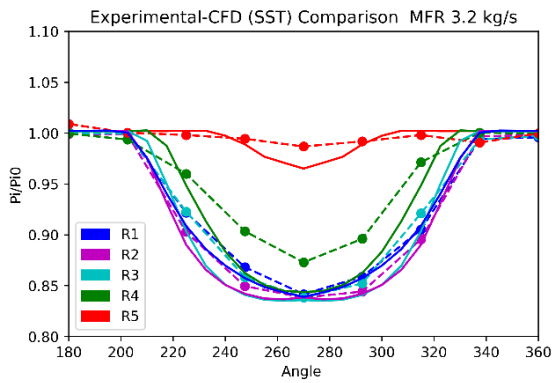
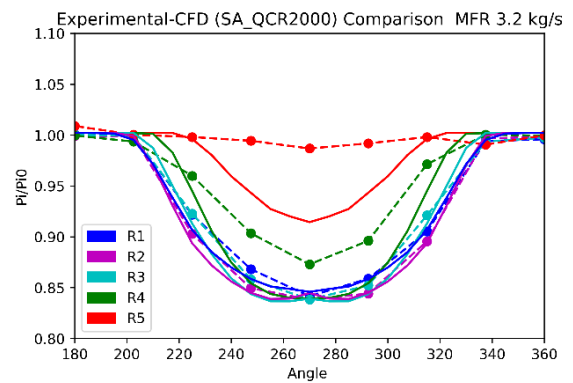
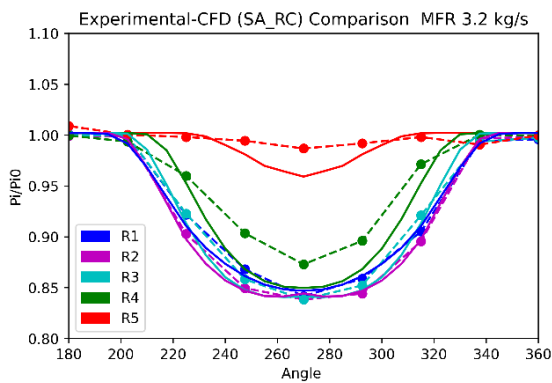
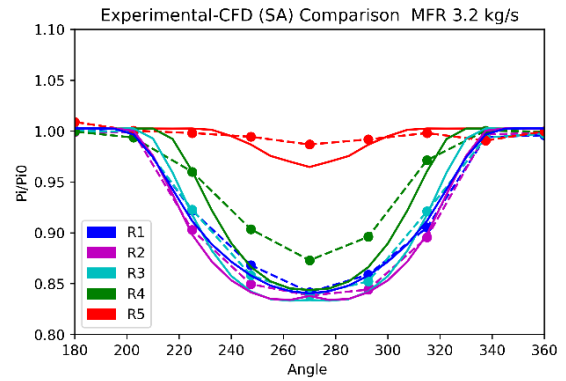
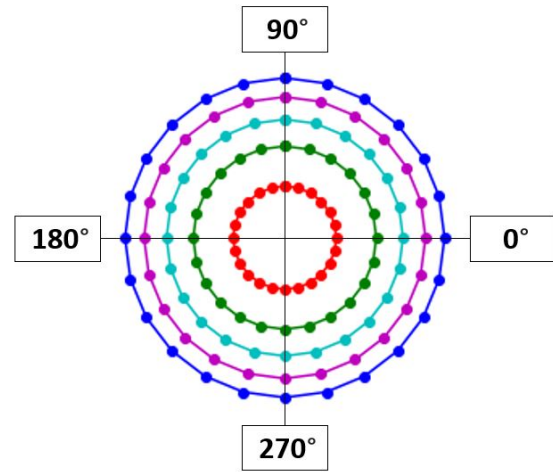


Figure 6.37: Comparison of the distribution of total pressure at the lower half of the fan face for various turbulence models at $3.0 \text{ kg}\cdot\text{s}^{-1}$.



Experimental - - - - -
 Numerical —————

Figure 6.38: Comparison of the distribution of total pressure at the lower half of the fan face for various turbulence models at $3.2 \text{ kg}\cdot\text{s}^{-1}$.

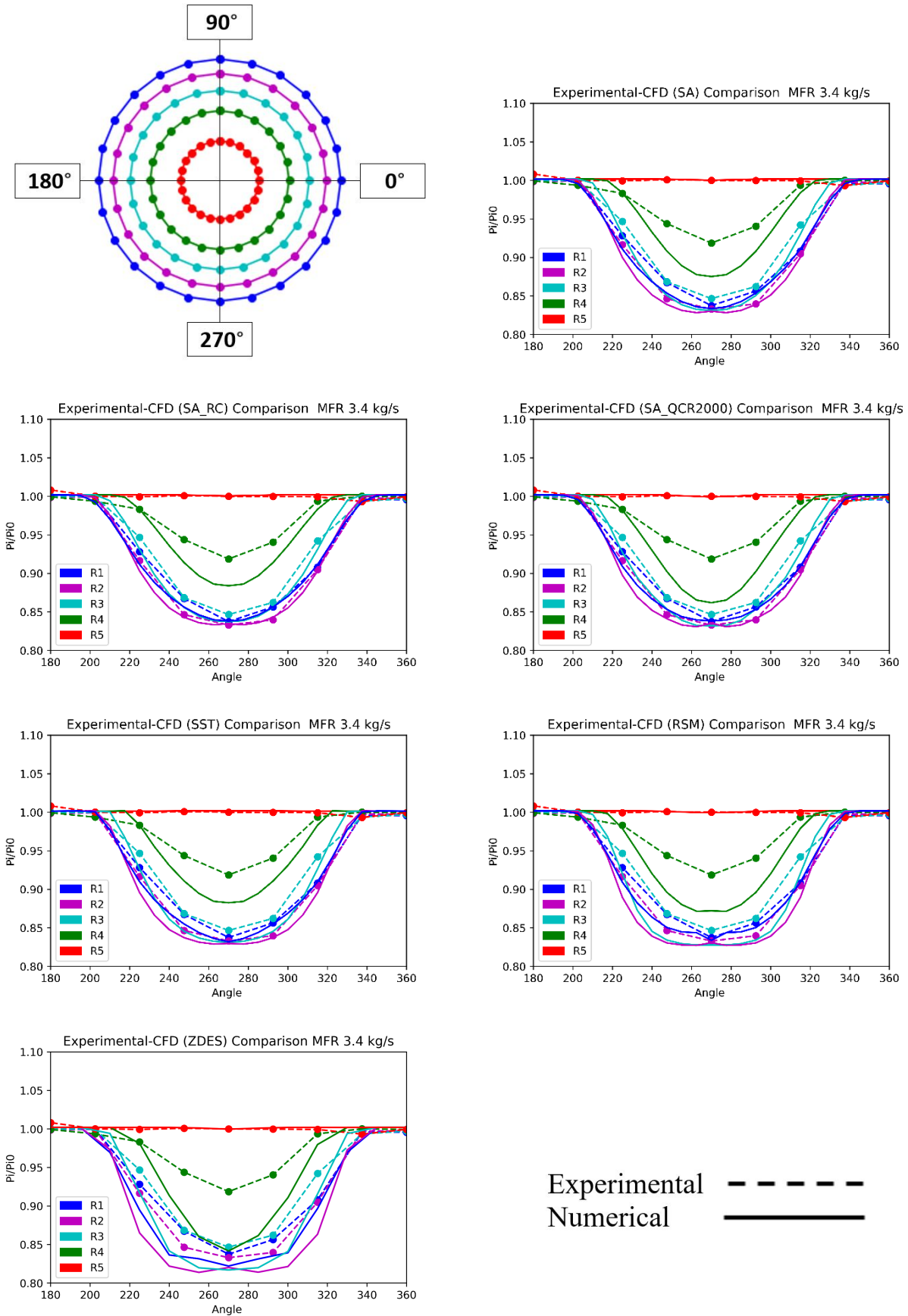
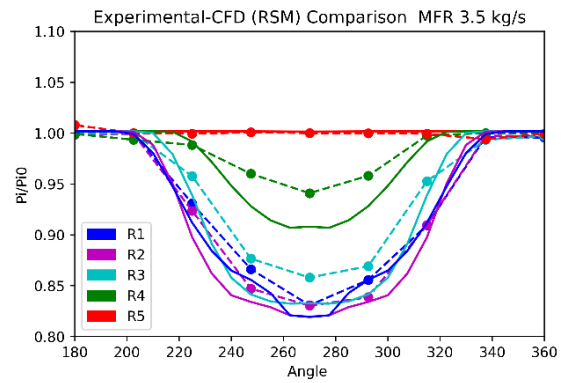
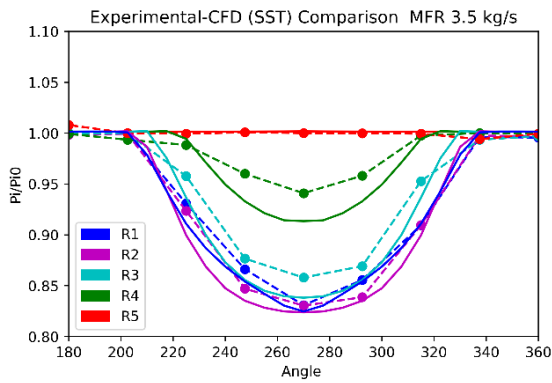
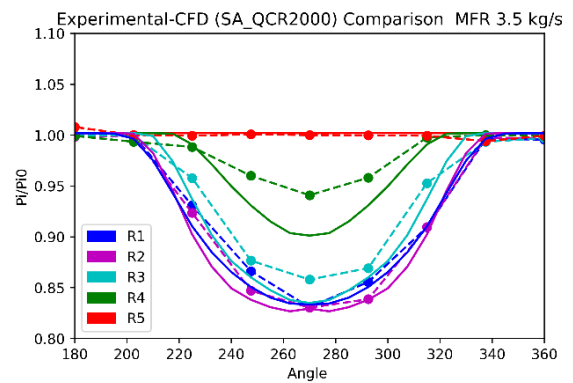
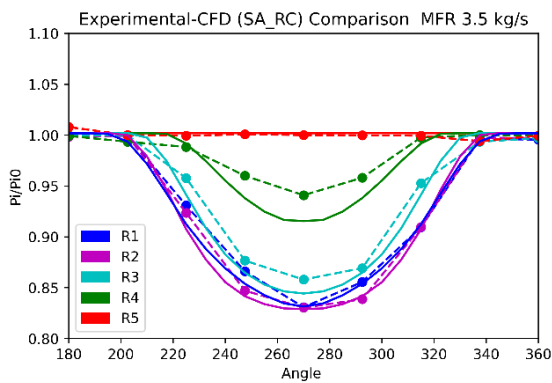
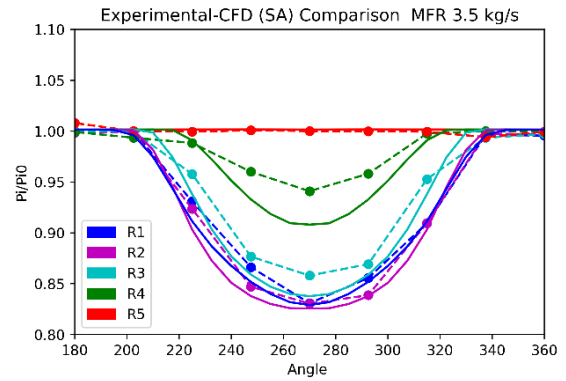
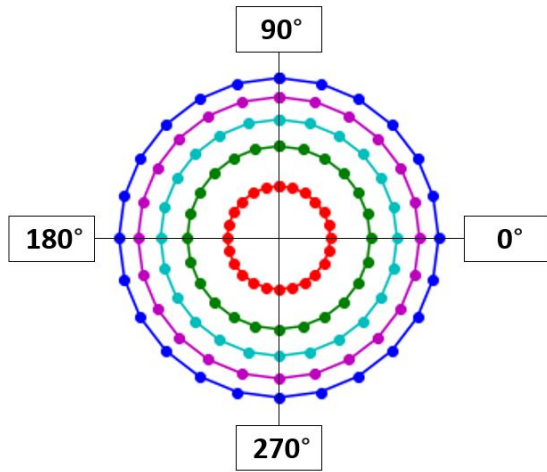


Figure 6.39: Comparison of the distribution of total pressure at the lower half of the fan face for various turbulence models at $3.4 \text{ kg}\cdot\text{s}^{-1}$.



Experimental - - - - -
 Numerical —————

Figure 6.40: Comparison of the distribution of total pressure at the lower half of the fan face for various turbulence models at $3.5 \text{ kg}\cdot\text{s}^{-1}$.

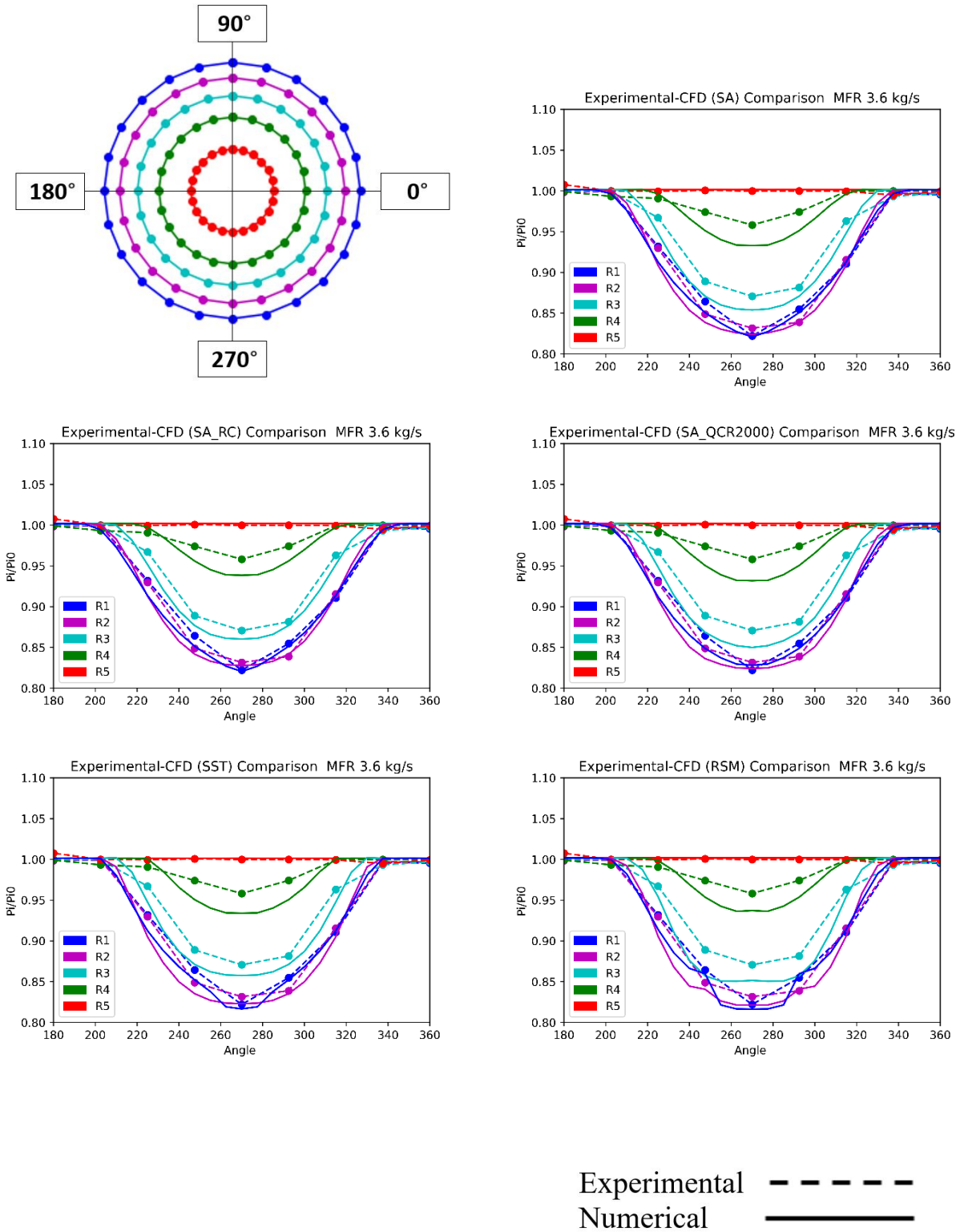
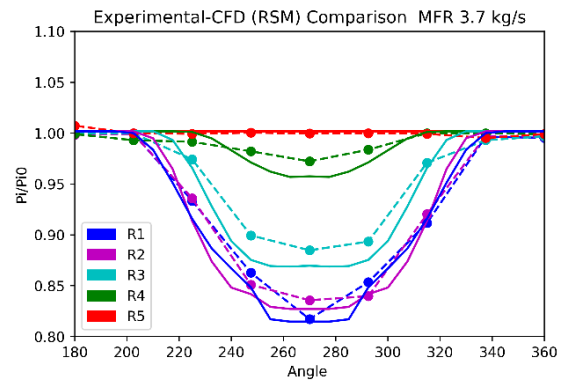
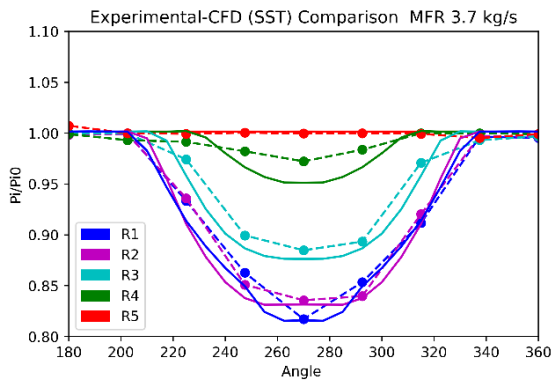
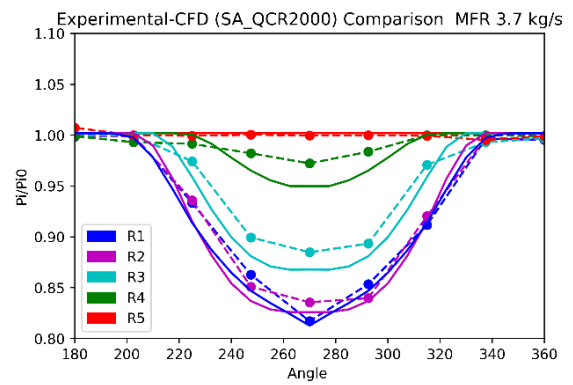
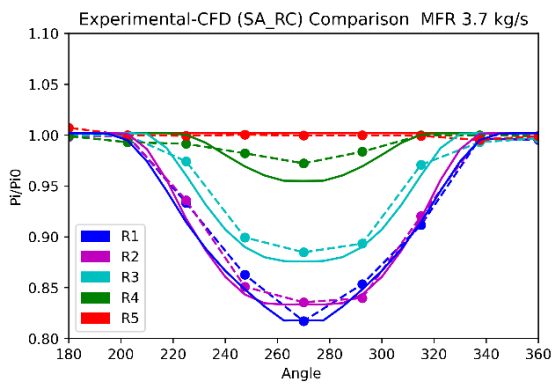
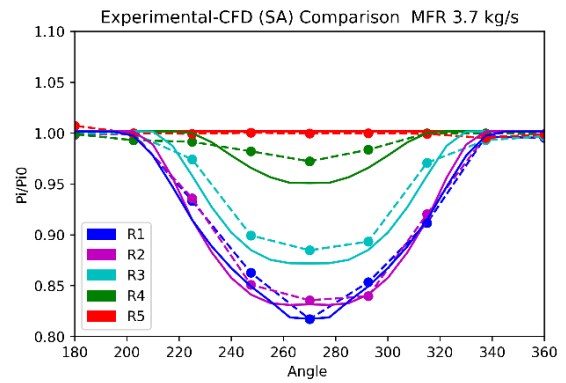
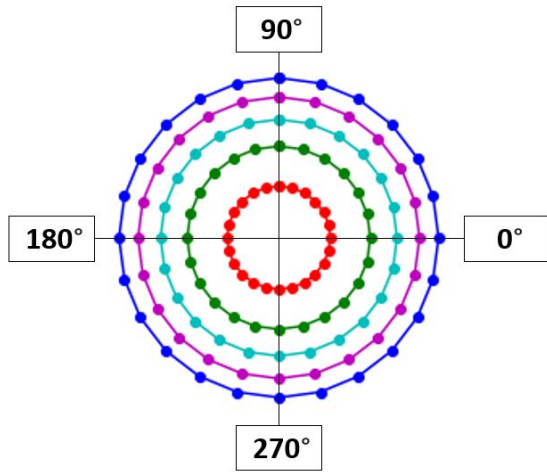
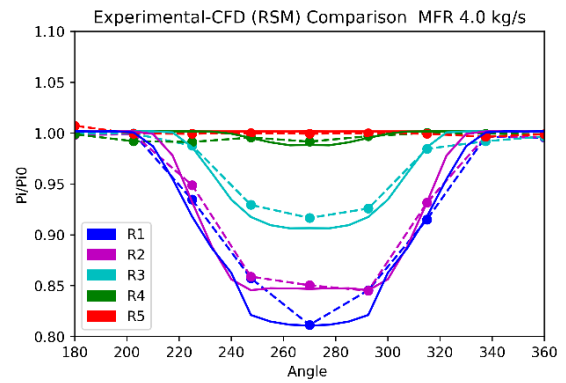
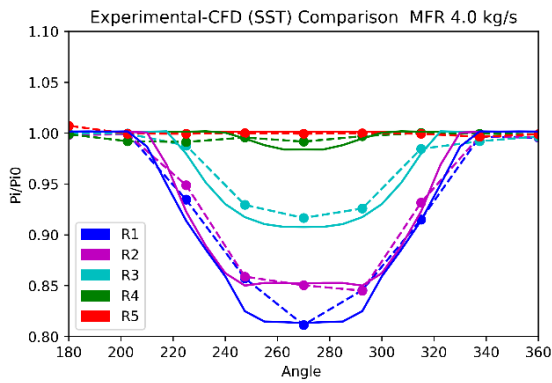
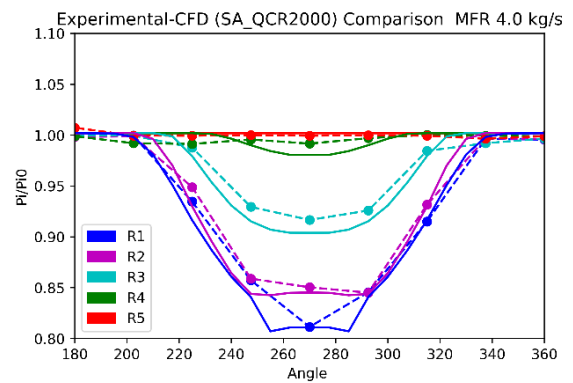
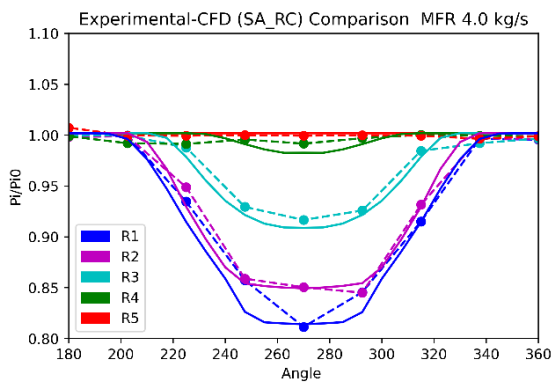
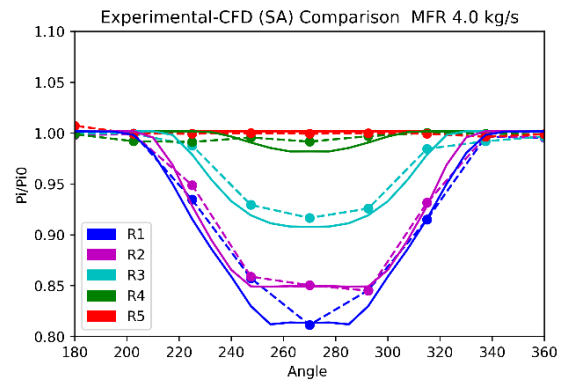
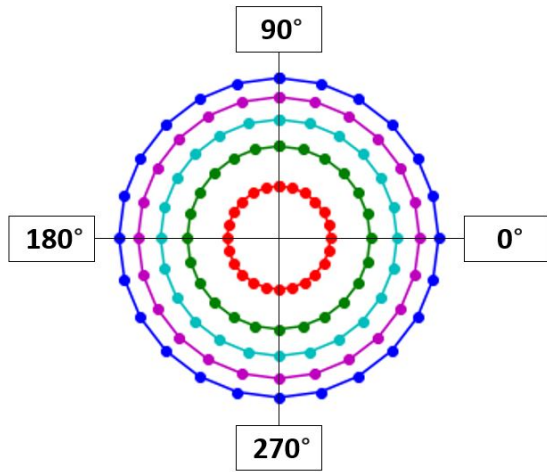


Figure 6.41: Comparison of the distribution of total pressure at the lower half of the fan face for various turbulence models at $3.6 \text{ kg}\cdot\text{s}^{-1}$.



Experimental - - - - -
 Numerical —————

Figure 6.42: Comparison of the distribution of total pressure at the lower half of the fan face for various turbulence models at $3.7 \text{ kg}\cdot\text{s}^{-1}$.



Experimental - - - - -
 Numerical —————

Figure 6.43: Comparison of the distribution of total pressure at the lower half of the fan face for various turbulence models at $4.0 \text{ kg}\cdot\text{s}^{-1}$.

6.5 Unsteady analysis over the AIP

This section presents a comparison between unsteady data obtained from wind tunnel experiments and numerical data from ZDES simulations. The primary aim is to compare turbulent kinetic energy levels and associated physical phenomena frequencies, as discussed in the previous chapter. The analysis is divided into two sections: one at the entrance ramp and another at the rake. Only Power Spectral Density (PSD) profiles of pressure measurements will be compared since available data from wind tunnel tests are limited to pressure measurements.

6.5.1 Intake ramp comparison

Figures 6.44 and 6.45 depict the frequency-dependent power spectral density (PSD) for both experimental and numerical data. The first set of images corresponds to cases with a mass flow rate of $3.0 \text{ kg}\cdot\text{s}^{-1}$, while the second set corresponds to cases with a mass flow rate of $3.4 \text{ kg}\cdot\text{s}^{-1}$. In both cases, the experimental data exhibits a double slope that is not present in the numerical data. This could be linked to the exchange of energy between the lowest layers within the boundary layer. A possible explanation for this behavior is provided in Chapter 3. Another general observation across all probes is that the amount of turbulent kinetic energy measured by the experimental data tends to be slightly higher for all probes compared to the numerical data. This difference in the amount of turbulent kinetic energy may be significant for some probes.

For cases with a mass flow rate of $3.0 \text{ kg}\cdot\text{s}^{-1}$, the PSD curves exhibit more aeroacoustic behavior at the start of the ramp. This trend is observed in both cases with different mass flows. The experimentally obtained curves seem to express a more characteristic profile of the turbulent energy cascade than those obtained numerically. For all cases except for the k101 probe, the amount of turbulent kinetic energy is quite similar between numerical and experimental data. However, no physical effect can be clearly identified at any common frequency. It can simply be highlighted, in the experimental plot, a very defined peak at 600 Hz which is linked to the operating frequency of the wind tunnel fan. Also, for some probes, a high level of coherency has been observed around 500-600 Hz. Small correlations are also noted at 1250 Hz, although they may be a harmonic associated with the previously mentioned 500-600 Hz mode.

The behavior of the case with a mass flow rate of $3.4 \text{ kg}\cdot\text{s}^{-1}$ is similar to that of other cases, except for probes k101 and k102. The correlation around 200-300 Hz spectrum is slightly higher for this case, particularly for probes k103 and k104. Additionally, there is a correlation around 1250 Hz, primarily for probes k105 and k106. The differences in the spectra between the probes could be explained by flow separation and generation of turbulent structures. However, due to the lack of other measurements in experimental tests, comparison and explanation of these differences are severely limited.

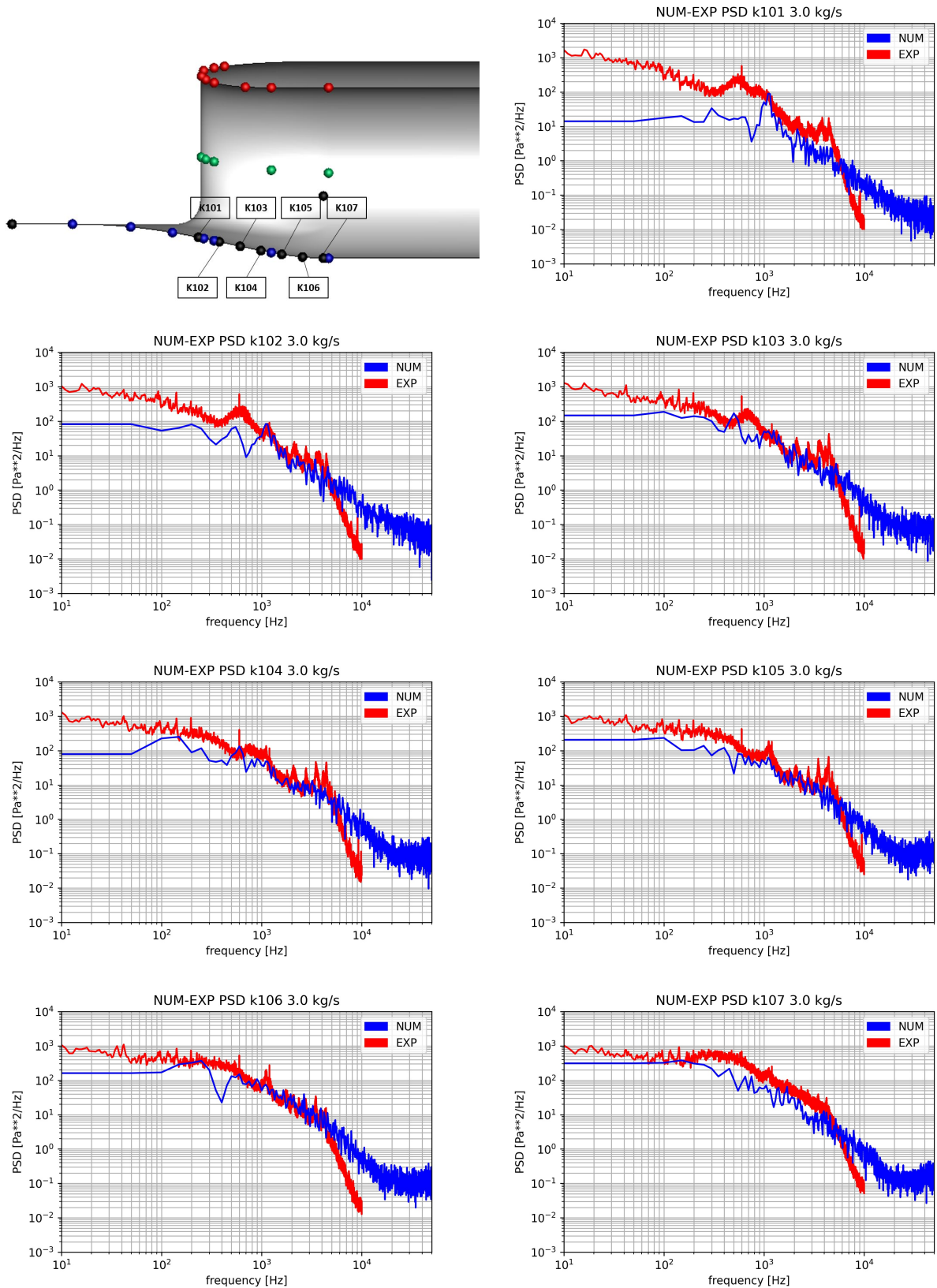


Figure 6.44: Power Spectral Density (PSD) comparison between experimental and numerical data, over the intake ramp probes, at $3.0 \text{ kg}\cdot\text{s}^{-1}$.

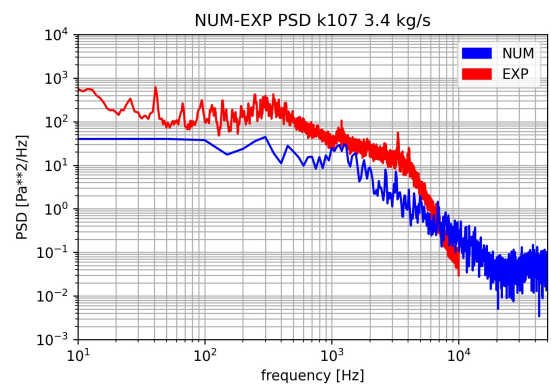
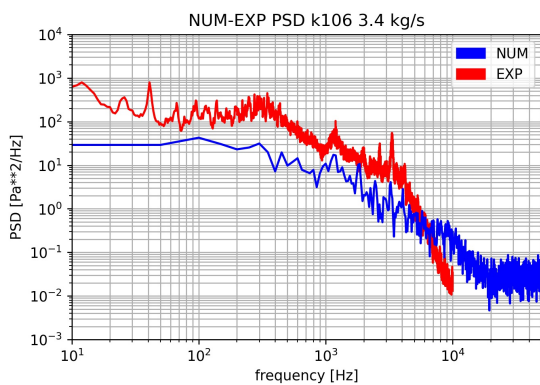
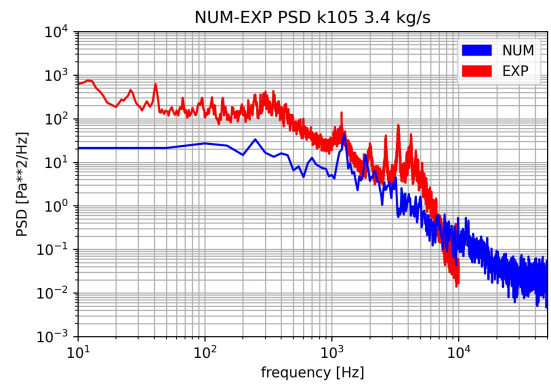
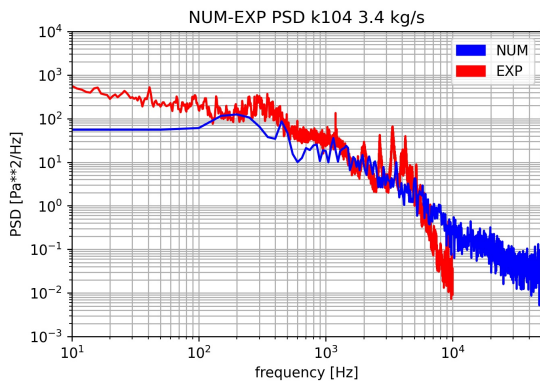
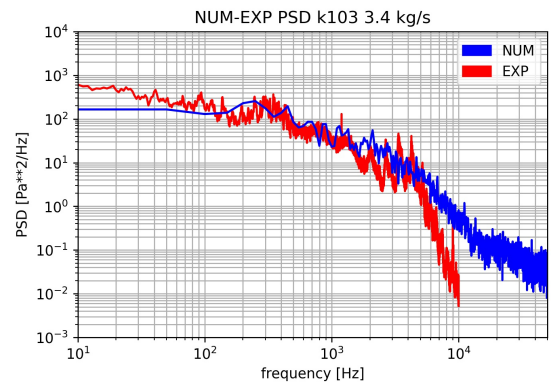
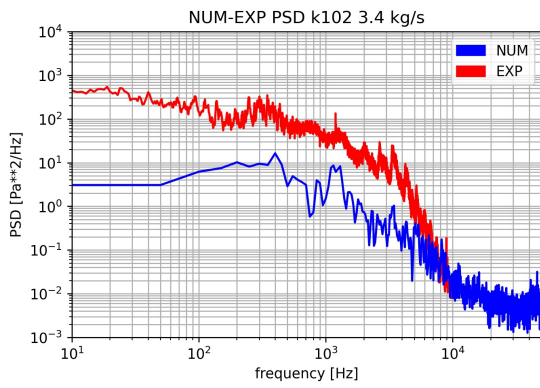
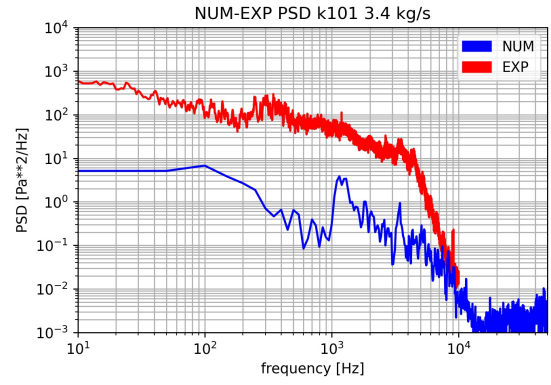
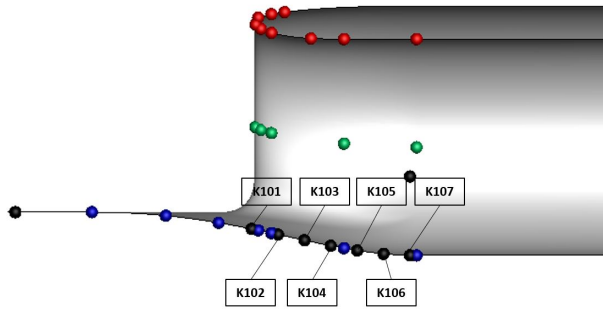


Figure 6.45: Power Spectral Density (PSD) comparison between experimental and numerical data, over the intake ramp probes, at $3.4 \text{ kg}\cdot\text{s}^{-1}$.

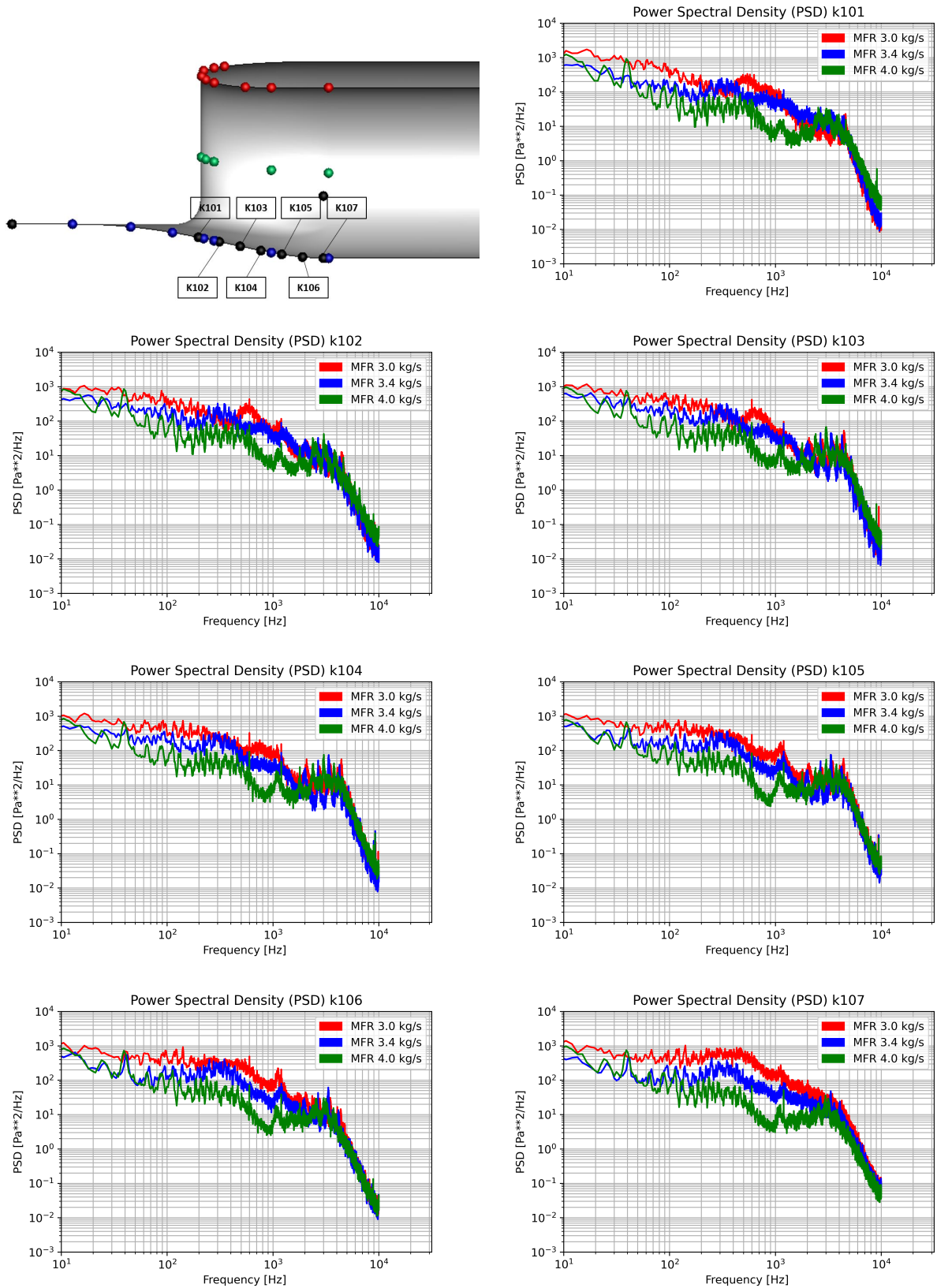


Figure 6.46: Comparison of experimental Power Spectral Density (PSD) results at different corrected mass flow rates.

Figure 6.46 compares the experimental power spectral density (PSD) plots for corrected mass flow rates of 3.0, 3.4, and 4.0 kg·s⁻¹. The results indicate that the most significant differences occur in frequency values less than 3 kHz, which are associated with the larger turbulent structures generated by the flow separation at the intake ramp. Some phenomena, such as bumps around 200-300 Hz or at 1250 Hz are always present, regardless of whether there is flow separation or not. However, phenomena between 500 Hz and 900 Hz appear to be related to flow separation, and it can be observed that the bump frequency increases with mass flow until they disappear without flow separation.

6.5.2 Rake comparison

Images 6.47 to 6.50 depict the analysis and comparison of the probes in the rake for cases of 3.0 kg·s⁻¹ and 3.4 kg·s⁻¹. The PSD curves exhibit quite similar behavior in all cases, presenting a characteristic turbulent cascade curve for the probes located in the region of recirculation and especially aerocoustic effects outside it. This region is not affected by energy exchange within the boundary layer as previous analysis, therefore there is no double slope. The slope between experimental and numerical data appears to coincide in most cases.

Image 6.47 displays the data of the probes located in arm 7 (figure 3.6) within the recirculation zone corresponding to the mass flow of 3.0 kg·s⁻¹. The behavior of these probes is mostly turbulent, in which oscillations of pressure measurements do not show significant physical phenomena. The amount of turbulent kinetic energy is quite similar between the numerical and experimental data, showing a significant increase near the shear layer. This increase in turbulent kinetic energy is shown in probes P73 and P74 for experimental data. The numerical data shows a maximum for the P75 probe. The location of the shear layer can also be seen in the RMS values of the pressure measurements on the AIP, which is shown at the top of Figure 6.47. The experimental case shows a shear layer that affects a larger region of the AIP. This increase in affected region is probably related to a greater flow separation, also demonstrated and discussed in the previous section. Image 6.48 presents the analysis for the same case in arm 3, which is located outside the recirculation zone. In this scenario, the majority of effects shown by PSD graphs are mostly aeroacoustic, both by numerical data and experimental ones. The amount of turbulent kinetic energy predicted by numerical models is quite close to that obtained by experimental data. Some correlations between PSD can be observed for frequencies of 500 and 600 Hz, as well as around the frequency of 1250 Hz.

Image 6.49 displays the results obtained for arm 7, located in the recirculation zone, in the case of 3.4 kg·s⁻¹. The comparison reveals that both cases have a lower location of the shear layer. For the experimental case, the PSD graph shows that the location of the shear layer is between the P72 and P73 sensors. However, there is also a turbulent kinetic energy increases in the P75 probe. Instead, numerical data estimate that the location of the shear layer is in the P74 probe.

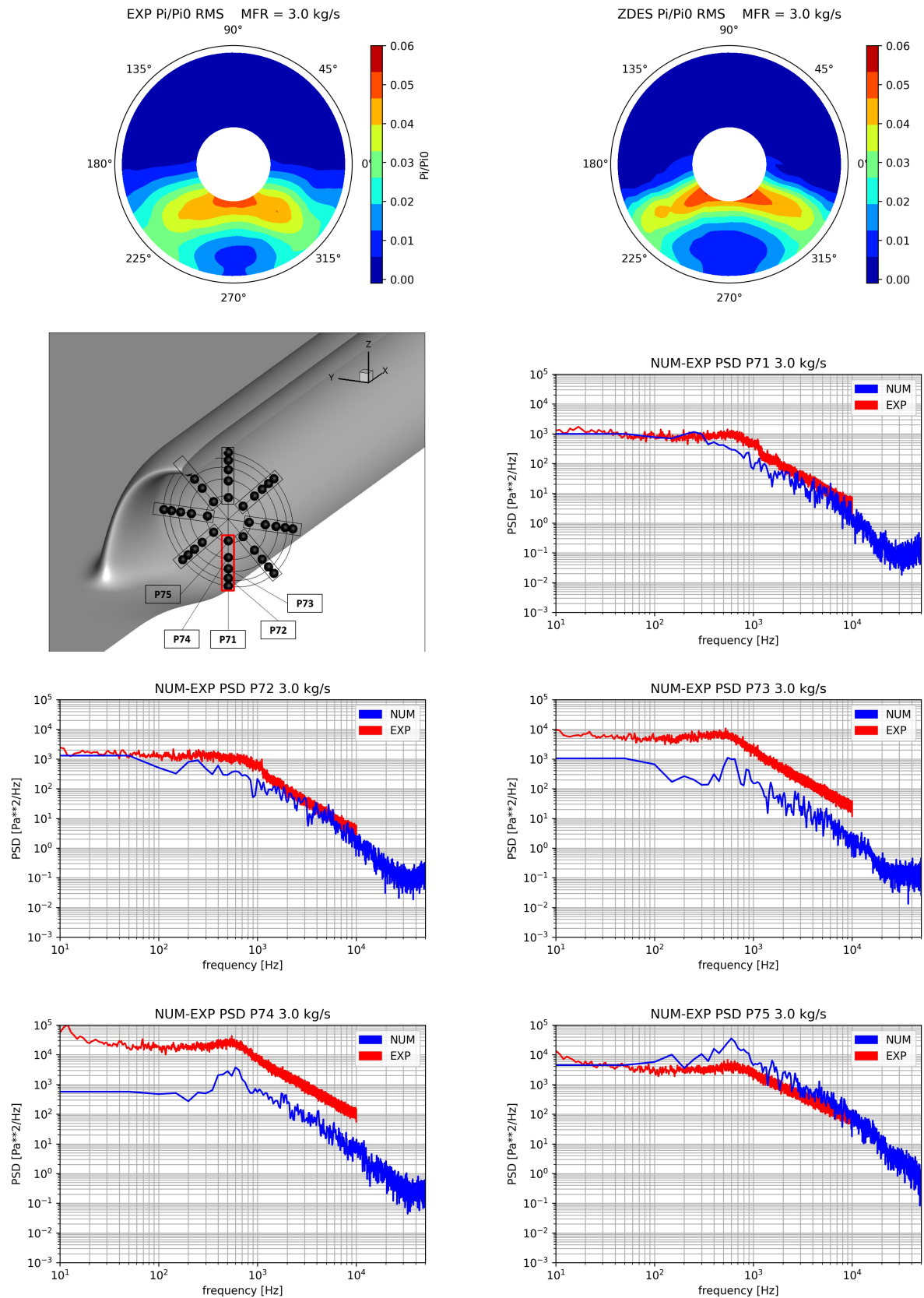


Figure 6.47: Power Spectral Density (PSD) comparison between experimental and numerical data, over the rake 7 at the AIP for $3.0 \text{ kg}\cdot\text{s}^{-1}$ case.

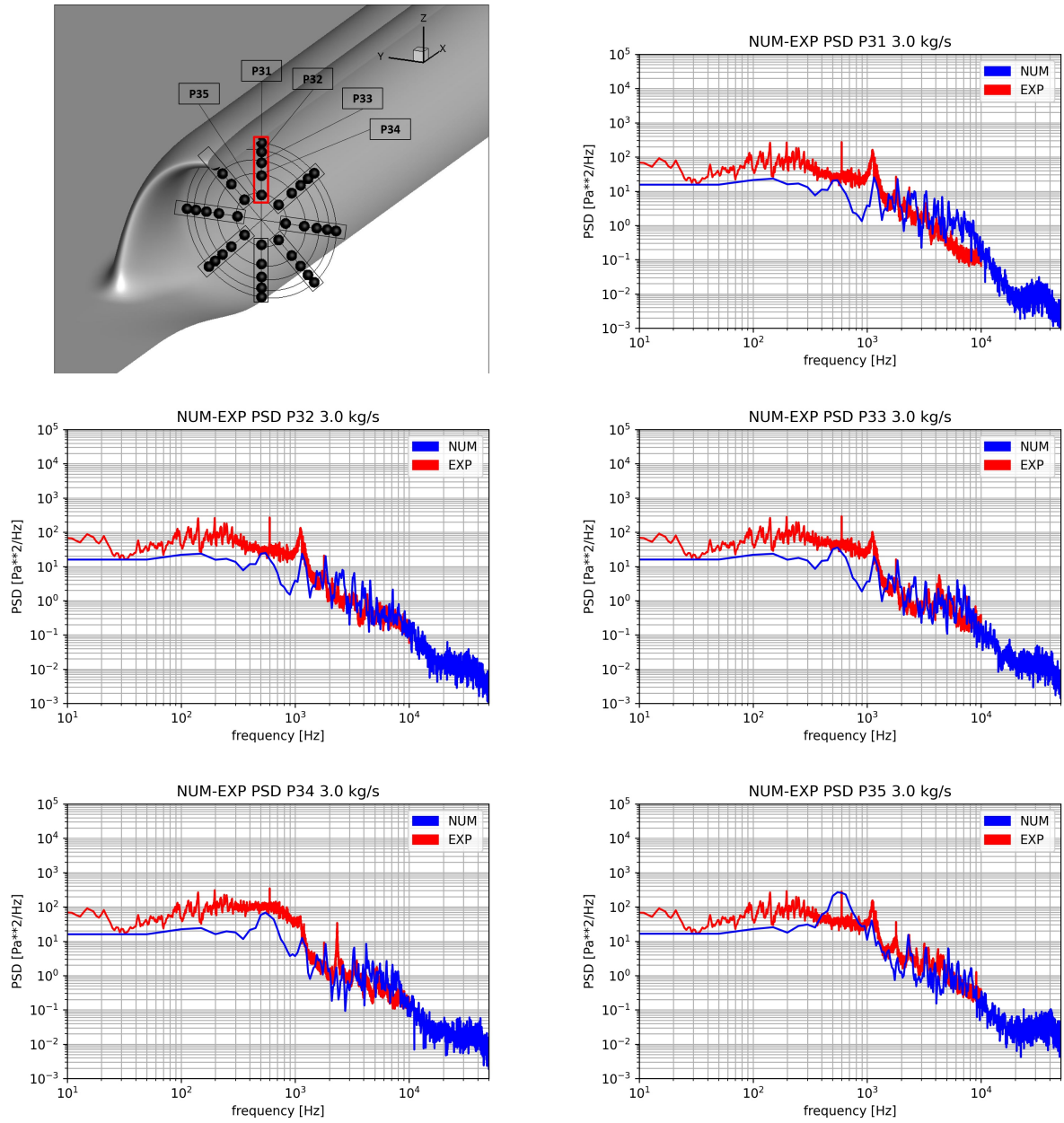


Figure 6.48: Power Spectral Density (PSD) comparison between experimental and numerical data, over the rake 3 at the AIP for $3.0 \text{ kg}\cdot\text{s}^{-1}$ case.

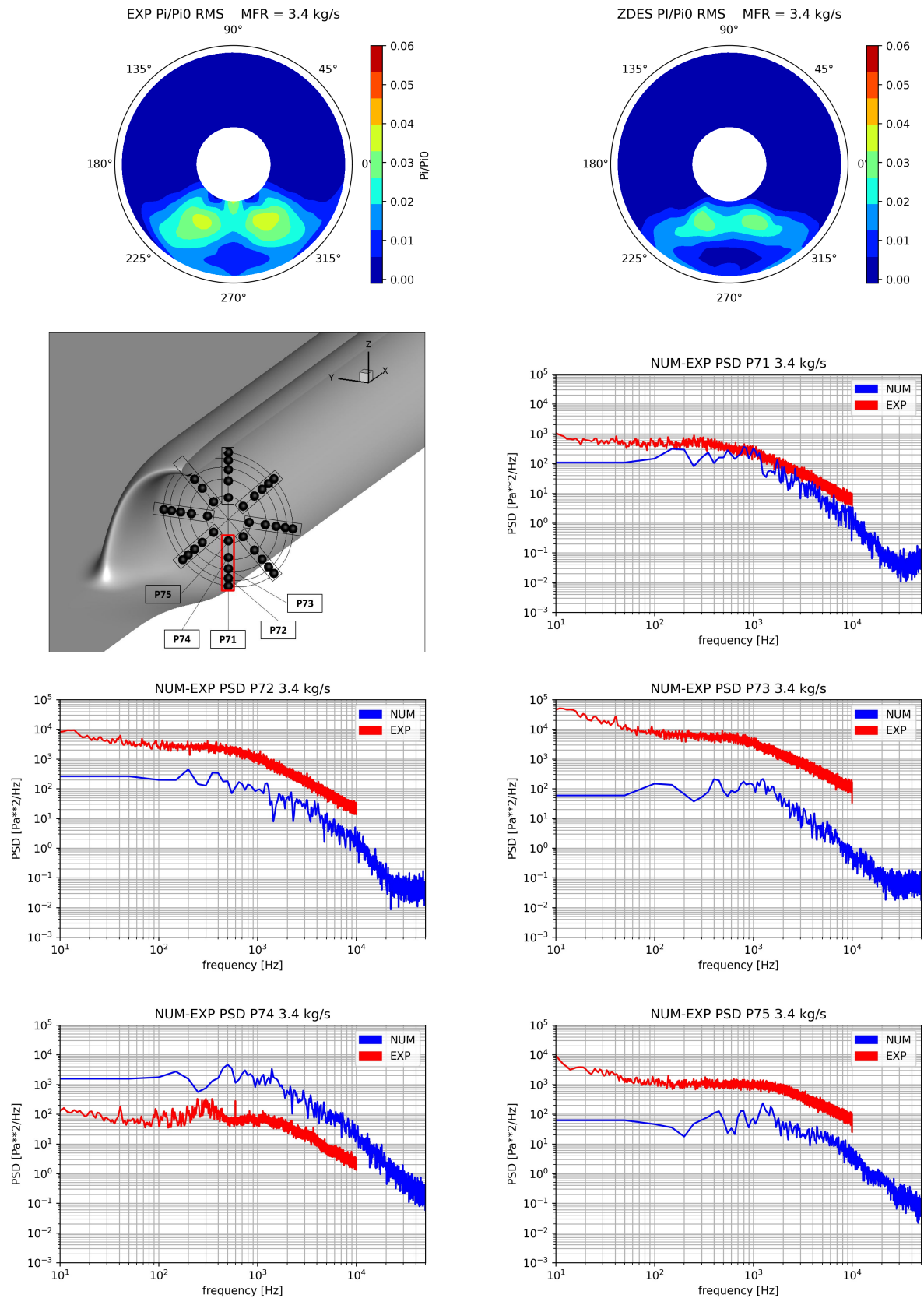


Figure 6.49: Power Spectral Density (PSD) comparison between experimental and numerical data, over the rake 7 at the AIP for 3.4 kg·s⁻¹ case.

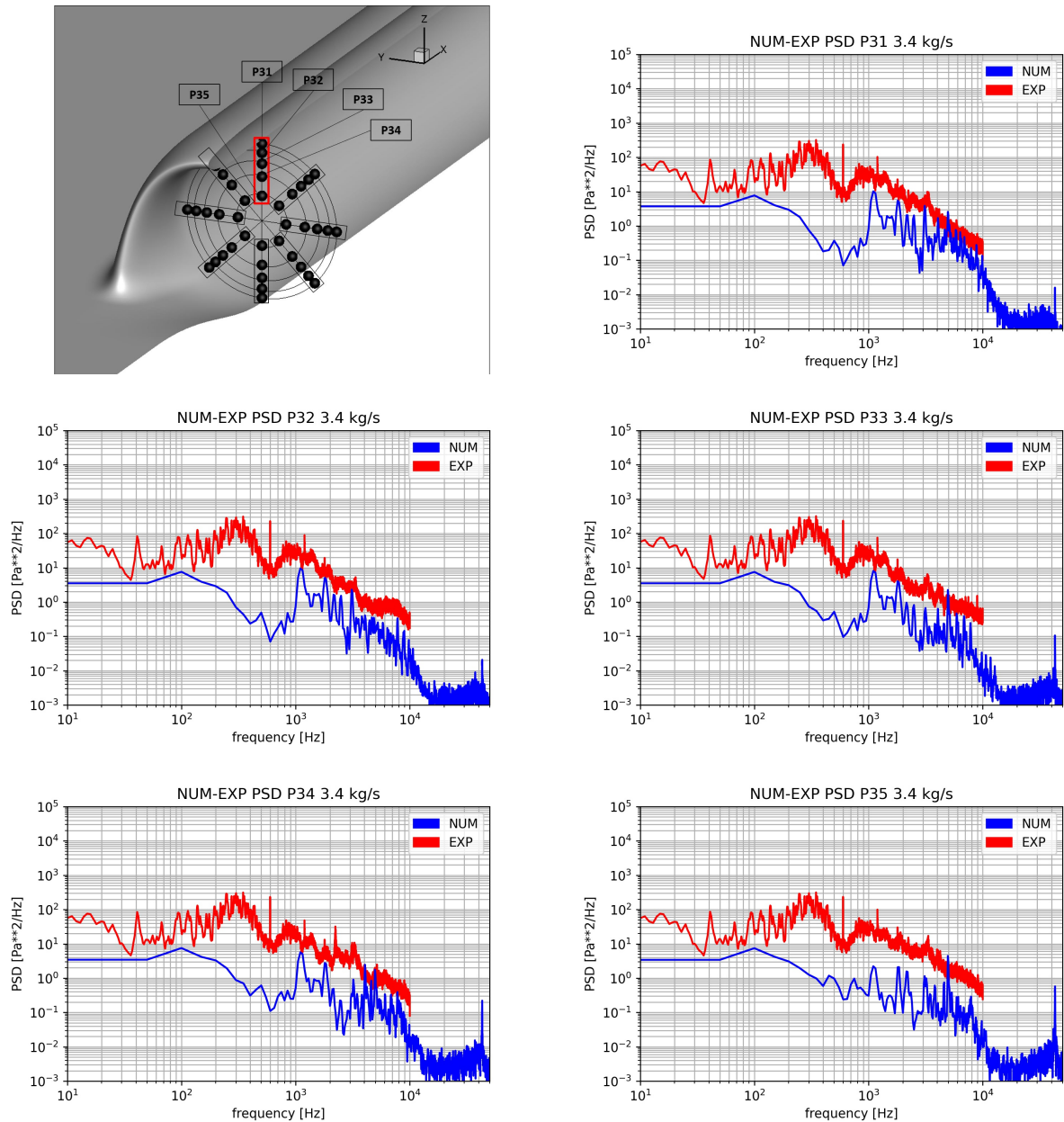


Figure 6.50: Power Spectral Density (PSD) comparison between experimental and numerical data, over the rake 3 at the AIP for $3.4 \text{ kg}\cdot\text{s}^{-1}$ case.

The location of the shear layer can be seen in the RMS plots at the AIP, shown at the top of the figure [6.49](#). In these images, this high RMS value can be observed in the P75 sensor for the experimental case. None of the probe comparisons can show any correlation between data obtained in AIP. Figure [6.50](#) shows PSD curves obtained from arm 3, which is located outside the recirculation zone. The effects shown by these graphs are mostly aeroacoustic; however, a greater amount of turbulent kinetic energy is noted in experimental data. No major correlations can be found between experimental and numerical graphs for these probes; only a small correlation near 1250 Hz.

6.6 Proper orthogonal decomposition at the AIP

This section aims to conduct a comprehensive analysis of all measurements taken at the AIP to identify behaviors that follow the corrected mass flow rate used. Both numerical and experimental data are analysed by proper orthogonal decomposition.

The Proper Orthogonal Decomposition (POD) is a mathematical technique that extracts a set of orthonormal bases from an original dataset. It was introduced by Lumley [48] and has been widely used in computational fluid dynamics, structural analysis and other dynamics systems. A detailed review of POD is provided by Berkooz et al. (1993) and Delville et al. (1999). The POD is applied on the unsteady total pressure flow field at the AIP of the BLI intake. The aim of the POD analysis is to identify the important modes α from the highly unsteady flow field. These modes correspond to a set of functions ϕ that maximise the projection of the total pressure onto ϕ on a mean square basis. The POD method decomposes the flow field into a set of modes, each with a temporal coefficient. The original flow field is then described as the linear summation of these identified modes and their respective temporal coefficients, as shown in equation 6.1 where a_j is the temporal coefficient and k the number of dimensions.

$$P(x, y, t)_k = \sum_{j=1}^k a_j(t) \vec{\phi}(x, y) \quad (6.1)$$

The contribution of each mode is assessed through the temporal coefficients, which are statically uncorrelated. This is determined by projecting the original total pressure flow field onto the POD basis. In fluid mechanics applications, POD is used to identify coherent flow structures that are typically obscured by the turbulent nature of the flow field.

The modes and power spectral density (PSD) obtained from matrix V, which contains the time coefficients of each mode, are presented in Figures 6.51 and 6.53. In the $3.0 \text{ kg}\cdot\text{s}^{-1}$ case, mode 1 characterizes a modulation along the vertical axis of the total pressure loss region initially located in the middle of the lower half of the AIP. This vertical perturbation of the pressure flow field can be mainly identified by the vertical oscillation movement of the total pressure loss region. This mode is similar to those reported by different authors in S-ducts studies [105] [106]. They claim that this mode is related to the instability of the shear layer associated with the flow separation region. The PSD obtained from the time coefficients associated with this mode is shown on the right side of Figure 6.51. mode 1 is associated with a high energy broadband frequency range from $St = 0.20$ to 0.70 with a spectral peak around $St = 0.76$.

The mode 2 for this same mass flow rate shows a lateral oscillation with an asymmetrical perturbations in time. This lateral motion is demonstrated in previous chapters by the individual analysis of signs at the AIP.

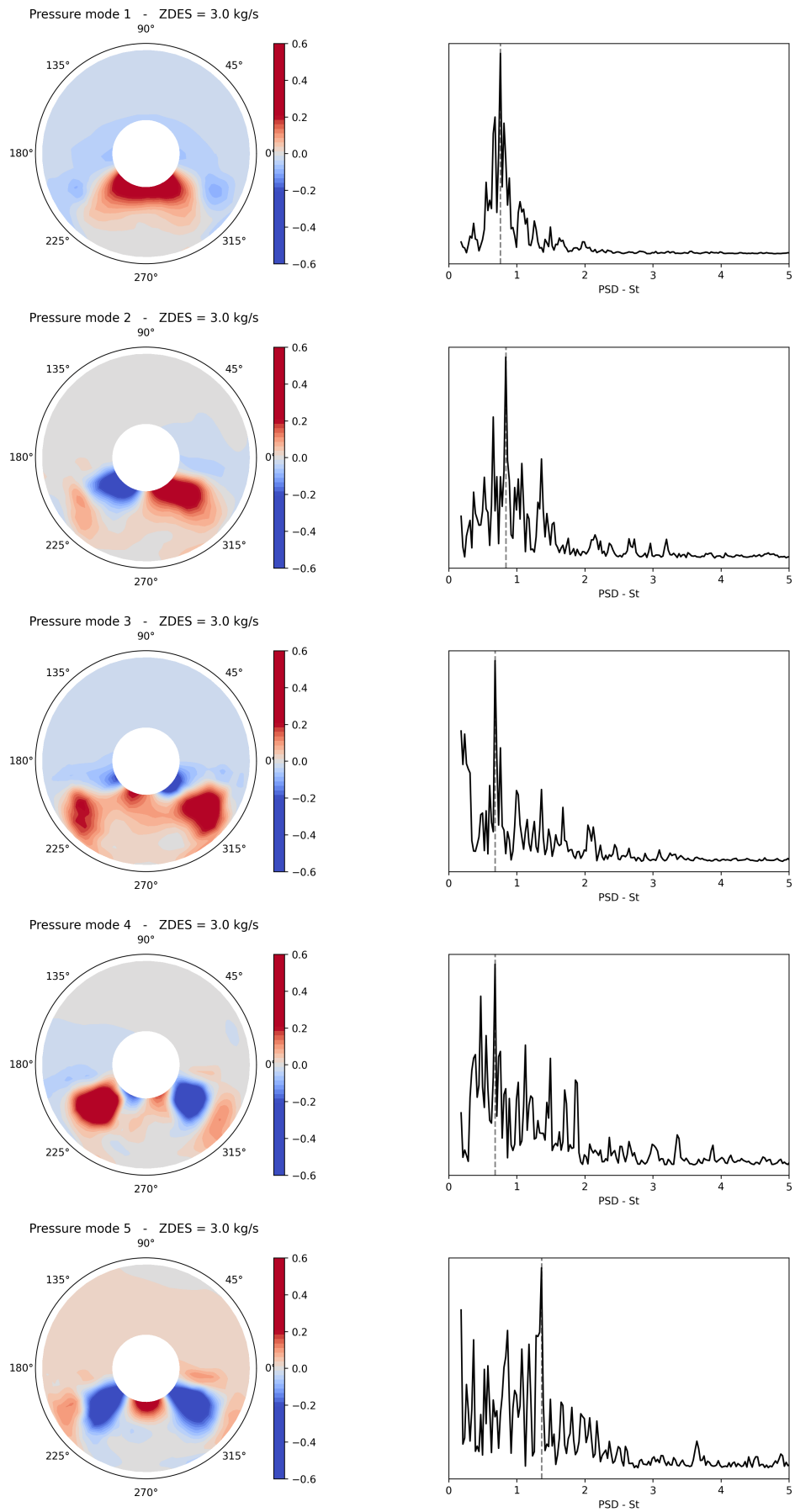


Figure 6.51: Distribution of the modal shape and PSD at the AIP for the ZDES simulation at $MFR = 3.0 \text{ kg}\cdot\text{s}^{-1}$.

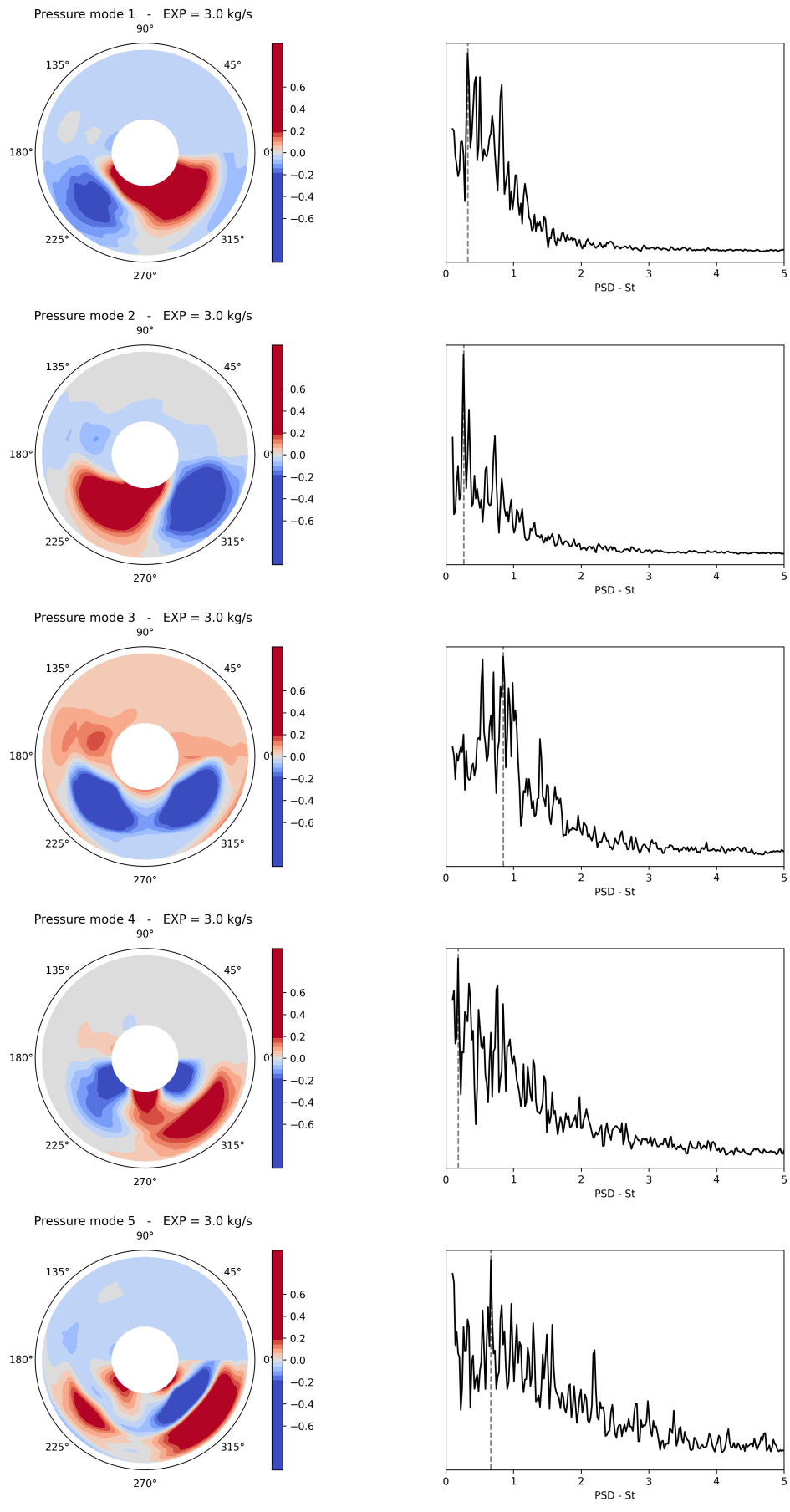


Figure 6.52: Distribution of the modal shape and PSD at the AIP for the experimental data at $MFR = 3.0 \text{ kg}\cdot\text{s}^{-1}$.

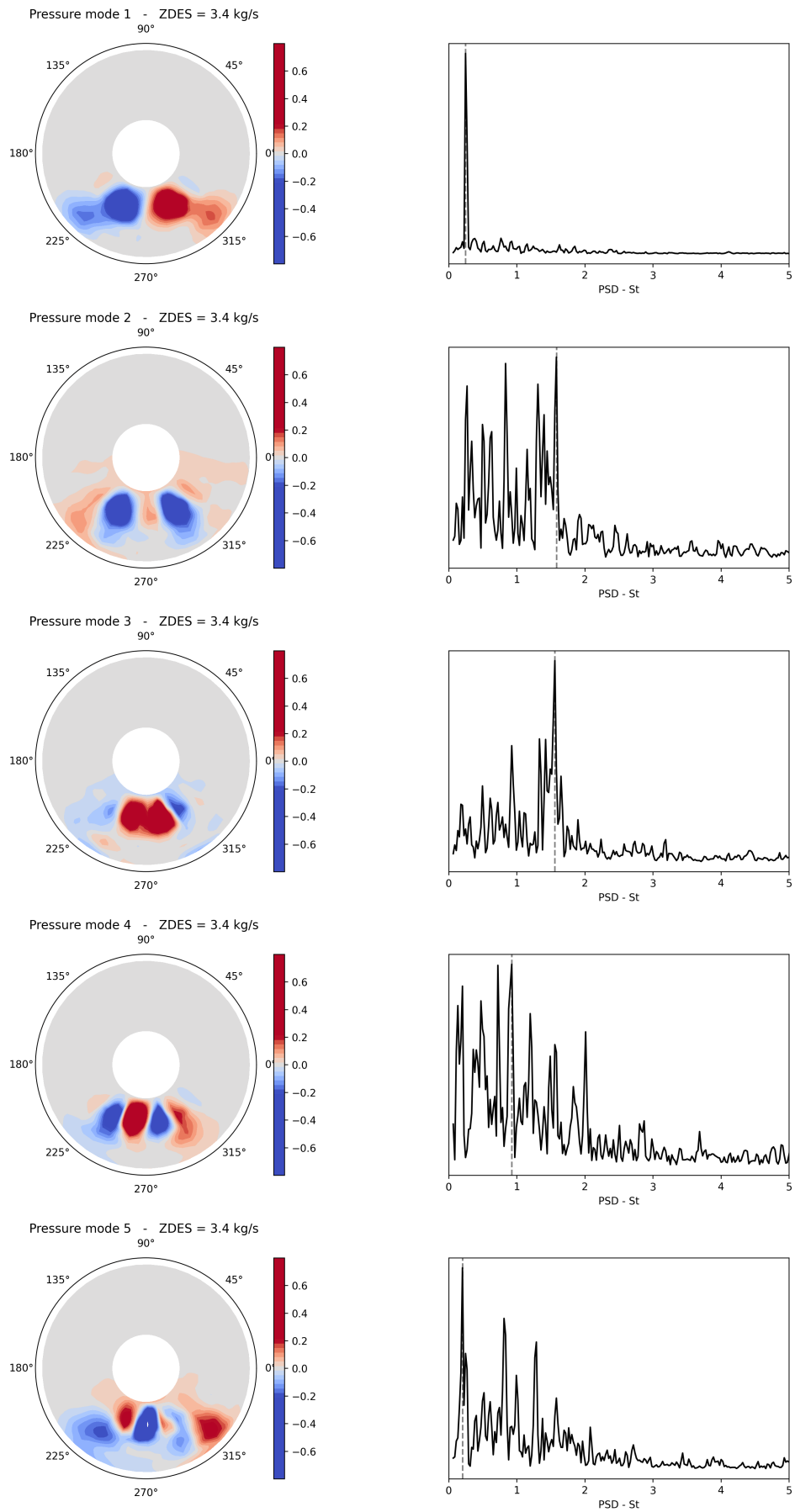


Figure 6.53: Distribution of the modal shape and PSD at the AIP for ZDES simulation at MFR = 3.4 kg·s⁻¹.

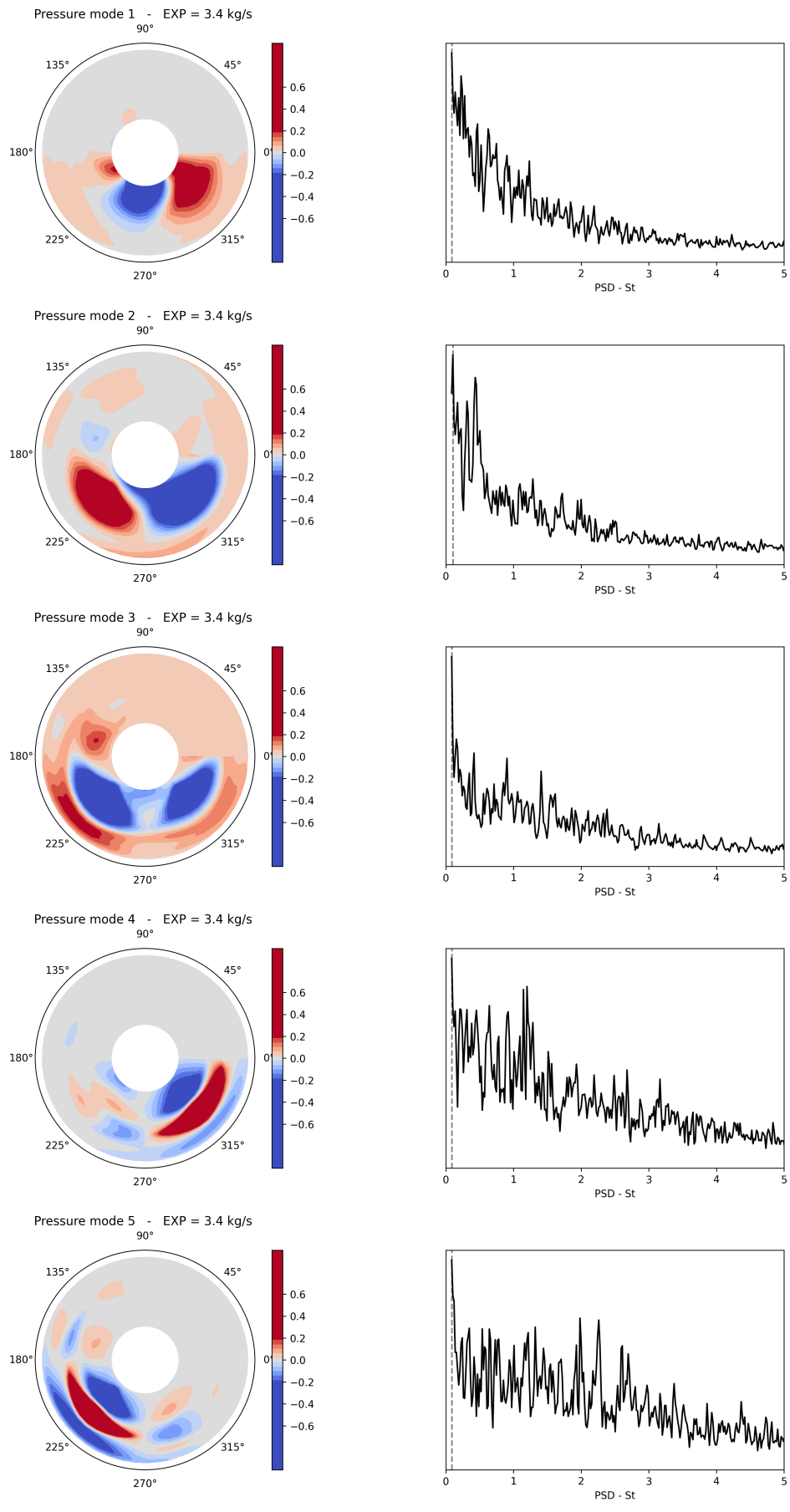


Figure 6.54: Distribution of the modal shape and PSD at the AIP for experimental results at $MFR = 3.4 \text{ kg}\cdot\text{s}^{-1}$.

Mode 2 is also similar to the switching mode identified on the velocity field in [106]. The maximum energy peak is also found for values near $St = 0.84$.

Modes 3 and 4 are observed to be linked to the second vertical and lateral modes, respectively, which are similar to the previous modes. Mode 3 exhibits a distinct peak at $St = 0.78$, along with a certain amount of energy at low frequencies and their corresponding harmonics. Mode 4 displays a greater dispersion of energy, with some concentration in the segment $St = 0.2 - 1$. The maximum peak is observed at $St = 0.78$. All modes have their peaks at the same Strouhal number values, which strongly suggests that these modes represent the influence of the same phenomena. Mode 5 is the least energetic, showing a symmetrical oscillation on the vertical axis. Its energy peak is at $St = 1.36$. Most likely a harmonic of the first mode.

For the case of $3.4 \text{ kg}\cdot\text{s}^{-1}$ this same analysis is also performed. Mode 1 shows antisymmetry lateral oscillations. These oscillations are clearly located in the spectrum, with a peak at $St = 0.25$. Modes 2 and 3 show symmetrical movements located in the lower part of the AIP related to vertical oscillations, similarly to that observed in modes 1, 3 and 5 for $3.0 \text{ kg}\cdot\text{s}^{-1}$. Both modes show a peak at $St = 1.58$, also they show a considerable amount of energy in the spectrum between $St = 0.2 - 2$. Mode 2 also shows a considerable amount of energy in $St = 0.17$. Modes 4 and 5 are antisymmetric and probably related to the phenomenon generated by mode 1. The maximum peak for the mode 4 is 0.92. In both modes there is an important peak at $St = 0.25$, however this high amount of energy also exists in values between $St = 0.2 - 2$.

The experimental data presented in figures 6.52 and 6.54 are not as evident as in the numerical cases. The possible causes of this lack of asymmetry and symmetry are discussed later. The analysis begins with the experimental case at $3.0 \text{ kg}\cdot\text{s}^{-1}$. Modes 1 and 2 appear to be associated with lateral oscillations in the lower part of the AIP, with maximum peaks at $St = 0.32$ and 0.26 , respectively. The amount of energy present is significant for Strouhal values less than 1 for both cases. Mode 3 appears to be the most symmetric, corresponding to movements on the vertical axis, which may be associated with shear layer oscillations. The peak is observed at $St = 0.78$, quite close to mode 1 observed in the ZDES case. In modes 4 and 5, the energy is quite dispersed in the spectrum, concentrating mainly in values less than 1.5 and 2 St , respectively. Mode 4 is probably another mode of vertical oscillation, while mode 5 corresponds to more lateral oscillations showing a maximum peak at $St = 0.66$. The case corresponding to $3.4 \text{ kg}\cdot\text{s}^{-1}$ shows modes quite similar to those observed in the case at $3.0 \text{ kg}\cdot\text{s}^{-1}$, with the exception of modes 4 and 5, which show diagonal oscillations. In general, the energy of these modes is quite dispersed in the spectrum, with peaks of all modes being placed at fairly low values of Strouhal numbers.

6.7 Chapter summary and conclusions

The prediction capability of the different turbulence models on a BLI configuration has been assessed by looking at different quantities: wall pressure distribution on the intake ramp, total pressure loss at the AIP and spectral analysis. All these quantities have been compared with experimental results obtained from a wind tunnel campaign.

Concerning the steady analysis, the turbulence models tend to exhibit minimal dispersion of results in the absence of flow separation. However, when flow separation occurs at the intake ramp, the understanding of the mechanisms that govern the flow behavior becomes more complicated due to the coupling between flow recirculation caused by separation and counter-rotating vortices due to secondary flow and horseshoe vortices. This mix of different physical phenomena tends to generate situations for which the turbulence models commonly used in industry were not designed.

All turbulence models predict the variation of the wall pressure distribution on the intake ramp well throughout the ramp, with very low dispersion between results. For cases with high MFR, the models give almost identical predictions and agree with the experimental data. Differences begin to appear for low MFR values, in which turbulence models have to predict a flow separation, couplings with other phenomena such as vortices, and subsequent reattachment of the boundary layer over the intake ramp. The predictive accuracy of each turbulence model was predominantly demonstrated under these latter conditions. Concerning the C_p prediction, the $k-\omega$ SST model stands out from the other models because it is the closest to the experimental data. The SA-QCR2000 and SSG-LRR RSM models results are also in quite good agreement with the experimental data. The SA, SA-RC, and ZDES (which also uses the SA equation) results are the farthest from the experimental curve. The $k-\omega$ SST and SSG-LRR RSM models exhibit enhanced predictive accuracy in the central segment of the ramp, specifically within the range of $x = -0.20$ to $x = -0.15$. This better accuracy is plausible, considering the proximity of the predicted separation points produced by both models. It is likely that these models are more adept at forecasting the precise location of flow separation. In the lower segment of the ramp, where $x > -0.10$, the $k-\omega$ SST and SA-QCR2000 models demonstrate superior predictive capabilities calculating the wall pressure coefficient.

The ZDES accuracy is lower than expected considering that part of turbulence is solved contrary to all the other RANS simulations. This can be explained by the fact that the separation size is small and mode 2 of the ZDES is not the most appropriate one for this type of flow where the ratio of the boundary layer height to the separation one is large. A ZDES mode 3, similar to WMLES, where the turbulence in the boundary layer is partly solved (above 0.1δ) and not modeled like in the mode 2 could give more accurate results on this configuration but would also be more computationally expensive since the mesh requirements would be higher to convect the

turbulence upstream of the separation point. Furthermore, it is noteworthy to mention that the employment of a chimera mesh induces alterations in the computational solution, as evidenced by Figure 6.14.

Furthermore, an analysis of the pressure coefficient (C_p) distribution on the intake ramp was conducted for a $3.4 \text{ kg}\cdot\text{s}^{-1}$ case. This analysis involved varying the boundary layer thickness and the Mach number in the free stream. The results obtained indicate that the boundary layer thickness has a direct impact on the value of C_p on the wall, generating more negative values of C_p with an increase in the boundary layer thickness. The Mach number also affects C_p , with an increase in Mach number resulting in more negative values of C_p . However, its effect is less intense compared to that of the thickness of the boundary layer. In both cases, there have been no changes in behavior along the intake ramp, and its variance is limited only to vertical displacements.

Concerning the total pressure at the AIP, all turbulence models tend to overestimate the pressure loss, which is especially noticeable in cases for which a flow separation appears on the intake ramp. When the mass flow rate is large, there is no difference between turbulence models as for the wall pressure distribution since the flow is attached. In this case, all models have minimal differences compared to experimental data. By contrast, when the flow is separated, large differences between turbulence models can be observed. All models overestimate the region affected by the recirculating zone compared to the experimental data. The SA model, followed by the $k-\omega$ SST one, are the two models that best estimate the impacted region at the AIP and the total pressure loss. Other models, especially ZDES and RSM, tend to overpredict the total pressure loss.

The results of the spectral analysis reveal that there are certain differences between the predictions generated from ZDES mode 2 simulations and experimental tests. These differences are more pronounced in the probes located on the intake ramp. The differences in the intake ramp could explain differences in flow recirculation and also affect the prediction of loss of total pressure at the AIP. In order to evaluate the behavior of the flow field across the signal spectrum, an analysis using the Proper Orthogonal Decomposition (POD) method at the AIP has been carried out in the last section. This analysis has been able to identify physical phenomena in both simulations and experimental results. Some agreement has been shown in the experimental-numerical comparison for the case of $3.0 \text{ kg}\cdot\text{s}^{-1}$, but not for the case of $3.4 \text{ kg}\cdot\text{s}^{-1}$, which exhibits quite different behaviors in the spectrum.

Chapter 7

Distortion characterisation for a BLI intake

As mentioned above, there are several parameters that can impact the efficiency of a BLI engine. One of the requirements is focused notably on the homogeneity of the flow at the engine intake. The heterogeneity of the flow, named distortion, may account for the appearance of aerodynamic instabilities of the fan blades. If the distortions are large enough, the fan might stall or the engine may surge. During the design phase, an index to measure the distortion is really useful to define the fan tolerance to perturbations on the ingesting flow. There are several indices used in the industry to characterize the distortion at engine intake. Most of these indices were designed to analyze the distortion in a standard engine configuration and are based on stagnation pressure losses. Several authors made their distortion analysis and performance prediction for a BLI engine by using these typical distortion indices [107] or using a pressure-based distortion criteria [13] [108]. Probably these distortion indices are not suitable for use in a BLI engine configuration, especially knowing that the physical phenomena of a BLI engine are different from an engine in a standard configuration.

This chapter aims to assess the common distortion indices used in the industry on a BLI engine. The most distorted flow appears when the aircraft is flying in off-design conditions. The most used distortion indices are the IDC and $DC(\theta)$, both based on stagnation pressure. In addition to these indices, an interesting methodology for assessing the inlet distortion swirl [38] is evaluated for a BLI engine application. An individual analysis of each distortion index is performed. These analysis allow to highlight their weaknesses and strengths by representing the physical phenomena on a BLI engine. Then, some new lines of research to improve a distortion index for a BLI engine are proposed. Finally, an unsteady distortion analysis is performed to understand the distortions in this kind of configurations.

7.1 Industrial distortion indices

The distortion criteria analyzed in the present study are the most common ones used to characterize the distortion in the industry. First, the well-known IDC and $DC(\theta)$ indices are described. Reference [37] proposes interesting distortion criteria by using the radial and circumferential distortion intensity. All distortion indices mentioned so far are based on pressure measurements, and were developed to be used in experimental tests.

The BLI engine intake solution exhibits also very important velocity gradients, both in axial and tangential directions. Therefore, distortion criteria based on velocity are included in this work. Reference [38] shows a methodology for assessing inlet swirl distortion. By using this methodology some stationary swirl distortion indices were proposed. The indices are designed, in general, to be used in experimental test, therefore the simulation measurements are taken by using the rake placed at the fan face shown in figure 3.6. This rake is composed of eight arms with 45° between them. Each arm has five measurement points.

According to the physical phenomena observed in the simulations, the distortion plots can be divided into 3 groups: cases with flow separation, cases without flow separation, and transition cases. The first case includes data obtained from corrected mass flow rates less than $3.5 \text{ kg}\cdot\text{s}^{-1}$. The second case includes data obtained from $4.0 \text{ kg}\cdot\text{s}^{-1}$ and the third group includes cases from $3.7 \text{ kg}\cdot\text{s}^{-1}$ up to $4.0 \text{ kg}\cdot\text{s}^{-1}$.

7.1.1 Pressure based distortion criteria

Averaged total pressure loss (P_{avg})

This distortion index simply shows the spatially-averaged value of the total pressure in the AIP divided by the total pressure in the free flow. As expected, both experimental results and numerical simulations predict a decrease in total pressure loss as mass flow increases through the BLI intake. No significant differences can be observed in the behavior of the curves according to their physical phenomena, being for numerical data quite similar to a reverse parabola. The values obtained from the ZDES simulation are quite close to the RANS models, showing slightly lower distortion values for the $3.4 \text{ kg}\cdot\text{s}^{-1}$ case.

The behavior of the curve obtained from the experimental data is somewhat different. It shows that the average total pressure loss is grouped around 3 values. 0.968 for corrected mass flow rates between $3.0 \text{ kg}\cdot\text{s}^{-1}$ and $3.2 \text{ kg}\cdot\text{s}^{-1}$, 0.976 for results between $3.4 \text{ kg}\cdot\text{s}^{-1}$ and $3.7 \text{ kg}\cdot\text{s}^{-1}$, and greater than 0.98 from $4.0 \text{ kg}\cdot\text{s}^{-1}$. In the first instance, this could lead to the conclusion that the experimental data were able to define the distortion values according to the physical phenomena present in such a case. However, as shown in Chapter 3, the amount of data available from the experiments does not make it possible to know exactly which phenomenon is involved.

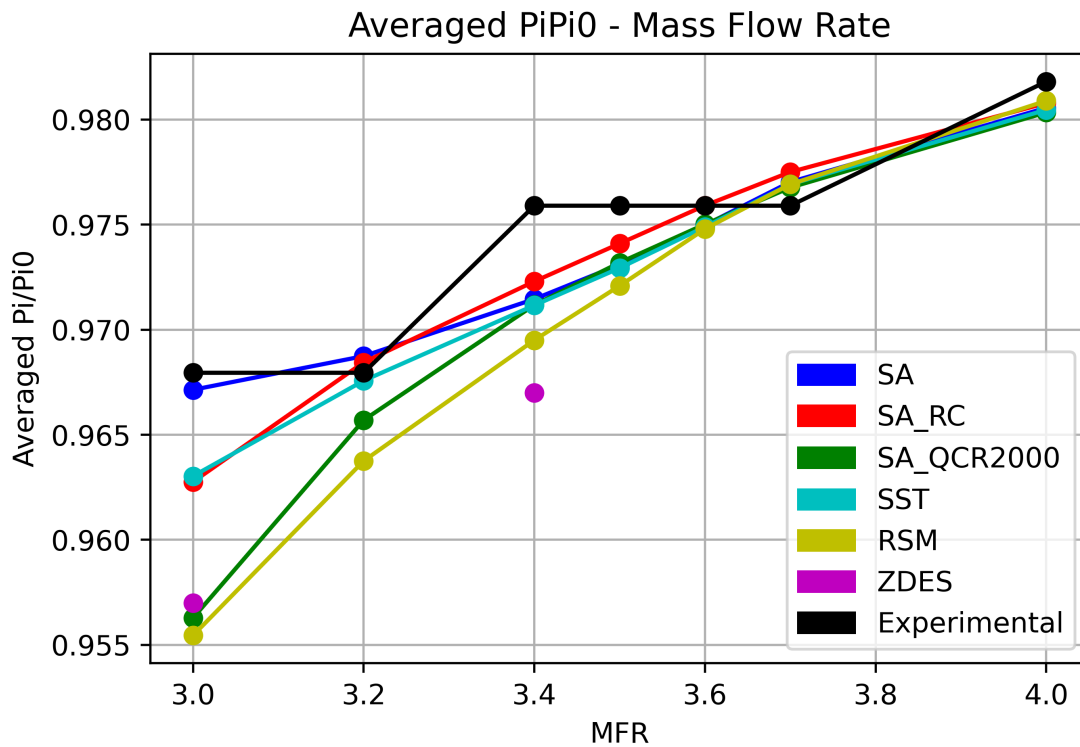


Figure 7.1: Comparison of numerical and experimental averaged total pressure loss for various corrected mass flow rate values.

Circumferential distortion ($(\Delta PC/P)_{ave}$)

This distortion index is defined as the ratio of the total pressure loss differences along each ring to the average total pressure throughout the AIP. The equation used to calculate this index is given by equation 2.9. Although there are significant discrepancies between numerical and experimental values, their behavior shows only minor differences. Numerical values are typically at least 10% higher than experimental values.

As a general trend, the distortion index values decrease almost linearly as the corrected mass flow rate increases. However, there are some exceptions to this trend. For instance, the distortion values obtained from ZDES simulations are practically identical for both $3.0 \text{ kg}\cdot\text{s}^{-1}$ and $3.4 \text{ kg}\cdot\text{s}^{-1}$. For the largest mass flow rates, between $3.4 \text{ kg}\cdot\text{s}^{-1}$ and $4.0 \text{ kg}\cdot\text{s}^{-1}$, the curves' behavior changes slightly, which is more evident in the experimental curve. However, it is not possible to clearly identify the presence or absence of any major physical phenomenon, such as flow separation or vortex intensity.

The turbulence model that most closely resembles the experimental data is SA-RC; however, there are notable differences between them. This data dispersion tends to decrease inversely with the corrected mass flow rate value.

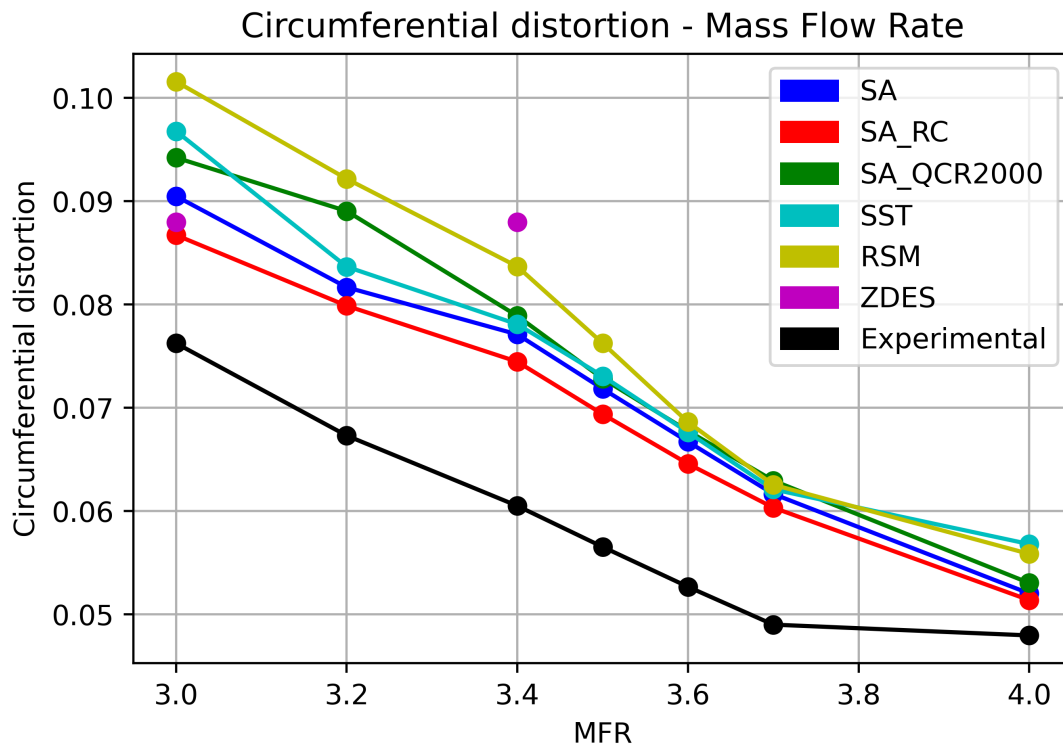


Figure 7.2: Comparison of numerical and experimental circumferential distortion index for various corrected mass flow rate values.

Circumferential distortion (DC(60))

DC(60) is another index of circumferential distortion. The most distorted region of 60° is used for this index. Their values have been calculated by using equation 2.7. Figure 7.4 shows the DC(60) values along the corrected mass flow rate from experimental and numerical data.

The plot shows that this index tends to decrease almost linearly with the mass flow rate value. At first it was expected that the DC(60) decrease would be linear until it reaches a mass flow rate value for which there is no more detached flow. However, there is no change in the behavior of this index. This linear evolution is due to the variation of the momentum at the fan face (q_f) which increases with the mass flow rate and to the difference between the mean stagnation pressure at the fan face and the mean stagnation pressure for a 60° sector ($P_f - P_\theta$) which have the same evolution. The DC(60) value will continue to decrease until the engine mass flow rate reaches sonic conditions.

The experimental data remains very close and between values obtained from numerical data, tending to give slightly higher values for high mass flow. In this case, the loss of total pressure in the 60° region is probably greater in comparison to numerical methods.

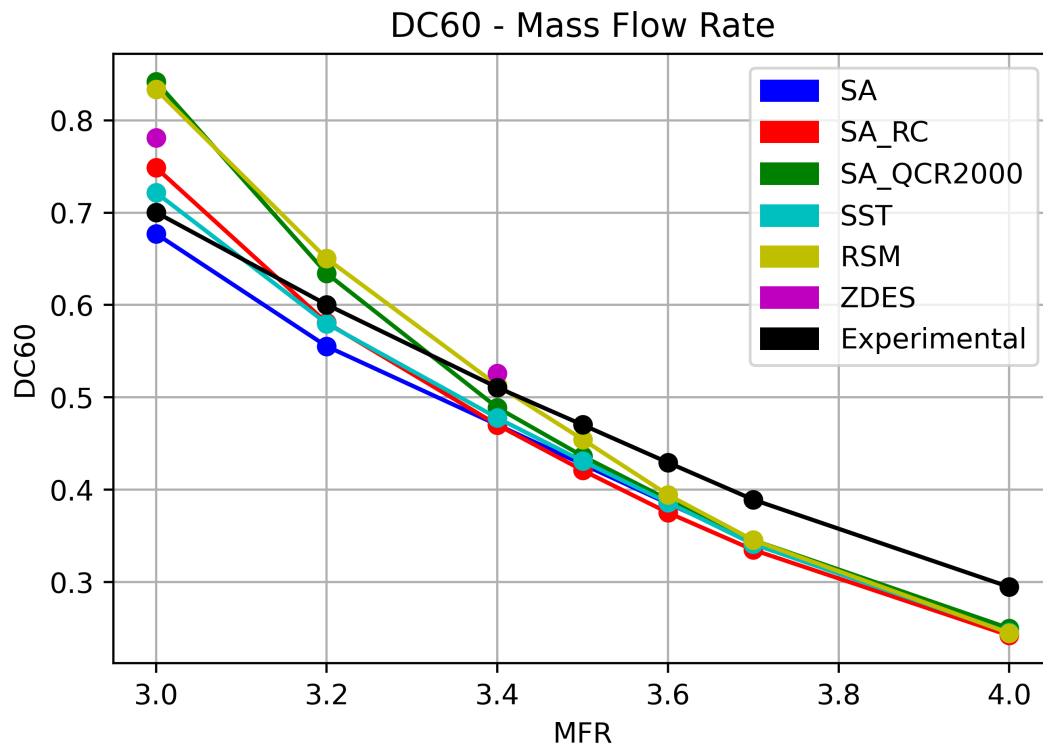


Figure 7.3: Comparison of numerical and experimental DC(60) index for various corrected mass flow rate values.

Circumferential distortion (IDC)

The IDC (Circumferential Distortion Index) is a measure of the heterogeneity of the flow, which takes into account the pressure distribution across the circumference. Its value is given by Equation 2.8. Both numerical and experimental data tend to predict similar indices of distortion. The maximum values are obtained between $3.6 \text{ kg}\cdot\text{s}^{-1}$ and $3.7 \text{ kg}\cdot\text{s}^{-1}$, according to the data used. Similarly to other circumferential distortion indices, the SA-RC model is the closer to the experimental results.

The IDC value shows an interesting correlation with flow separation, since its value is maximum for the mass flow value for which separation appears. If this hypothesis is correct, this implies that this index could be used to identify the mass flow rate for which separation appears. The IDC measures the difference of circumferential distortion between neighboring circumferences, and in the case where separation appears, this value is maximum because there is only a small area with low stagnation pressure. The highest IDC values are predicted by the RSM model, which along with ZDES, tends to predict a greater loss of total pressure located in the lower part of the AIP. Otherwise, the SA-RC model shows the lowest total pressure loss. Coinciding with the results obtained in the last chapter, experimental data show a lower loss of total pressure.

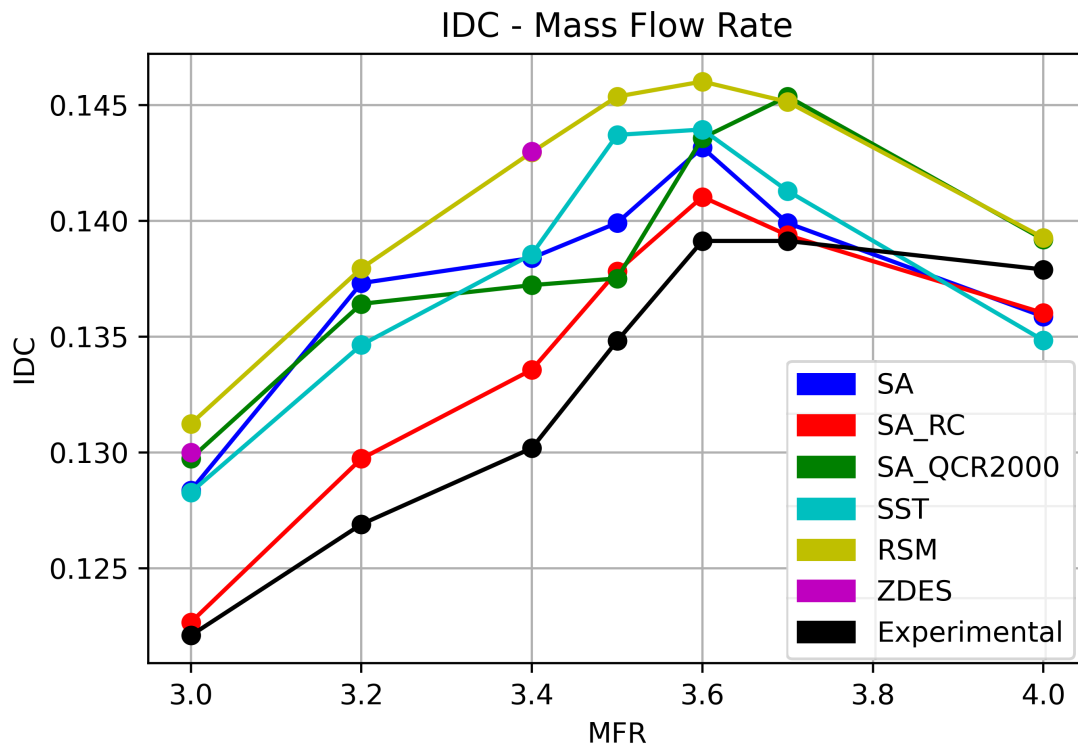


Figure 7.4: Comparison of numerical and experimental IDC index for various corrected mass flow rate values.

Radial distortion (RDI)

The distortion index is a measure of flow distortion between radial values at the AIP. The rate of distortion is calculated using Equation [2.10](#). The curves exhibit similar behavior, but it is noteworthy that the curve obtained from experimental data shows substantially lower distortion values than the numerical, particularly for corrected mass flow values greater than $3.4 \text{ kg}\cdot\text{s}^{-1}$.

The maximum values of the distortion index, both with numerical and experimental data, are between 3.2 and $3.4 \text{ kg}\cdot\text{s}^{-1}$. The values obtained from the ZDES are also close, with its maximum value for the corrected mass flow rate of $3.4 \text{ kg}\cdot\text{s}^{-1}$ being slightly higher than that of other turbulence models. Between the numerical models, there is high dispersion when the mass flow rate is low. The maximum value predicted changes according to the mass flow rate, with the $k-\omega$ SST model being the maximum for $3.0 \text{ kg}\cdot\text{s}^{-1}$, but from $3.2 \text{ kg}\cdot\text{s}^{-1}$, the maximum values are predicted by the RSM and ZDES models. These results are in accordance with the total pressure loss at the AIP predicted by each turbulent model.

For the cases without flow separation the numerical data exhibit minimal dispersion and the radial distortion index remains nearly constant for mass flow rates between $3.4 \text{ kg}\cdot\text{s}^{-1}$ and $4.0 \text{ kg}\cdot\text{s}^{-1}$.

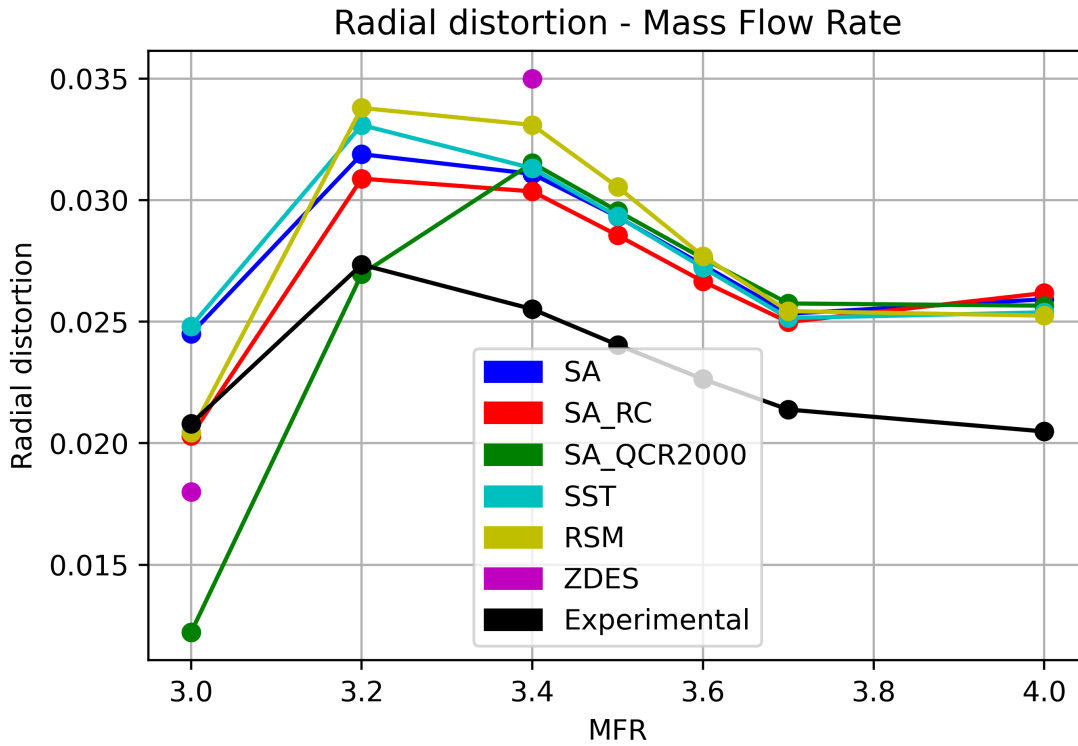


Figure 7.5: Comparison of numerical and experimental IDC index for various corrected mass flow rate values.

Table 7.1: Comparison of the distortion indices between numerical simulations and experimental data for $MFR = 4.0 \text{ kg}\cdot\text{s}^{-1}$.

$MFR = 4.0 \text{ [kg}\cdot\text{s}^{-1}]$	$DC(60)$	IDC	$(\Delta PC/P)_{ave}$	$(\Delta PR/P)_{max}$
Experiment	0.295	0.138	0.048	0.020
SA	0.244 (-17%)	0.136 (-2%)	0.052 (+9%)	0.026 (+27%)
SA-RC	0.242 (-18%)	0.136 (-1%)	0.051 (+7%)	0.026 (+28%)
SA-QCR2000	0.245 (-15%)	0.136 (-2%)	0.053 (+10%)	0.026 (+25%)
$k - \omega$ SST	0.245 (-17%)	0.135 (-2%)	0.057 (+18%)	0.025 (+24%)
RSM	0.244 (-17%)	0.139 (+1%)	0.056 (+16%)	0.025 (+24%)

Tables 7.1, 7.2 and 7.3 show a summary of the results obtained using these distortion indices, and their comparison with experimental data.

Table 7.2: Comparison of the distortion indices between numerical simulations and experimental data for $MFR = 3.4 \text{ kg}\cdot\text{s}^{-1}$.

MFR = 3.4 [$\text{kg}\cdot\text{s}^{-1}$]	DC(60)	IDC	$(\Delta PC/P)_{ave}$	$(\Delta PR/P)_{max}$
Experimental	0.511	0.130	0.060	0.025
SA	0.470 (-8%)	0.138 (+6%)	0.077 (+27%)	0.031 (+22%)
SA-RC	0.470 (-8%)	0.134 (+3%)	0.074 (+23%)	0.030 (+19%)
SA-QCR2000	0.489 (-4%)	0.138 (+6%)	0.079 (+30%)	0.031 (+24%)
$k - \omega SST$	0.478 (-6%)	0.139 (+7%)	0.078 (+29%)	0.031 (+23%)
RSM	0.513 (+1%)	0.143 (+10%)	0.084 (+38%)	0.033 (+29%)
ZDES	0.526 (+3%)	0.143 (+10%)	0.088 (+46%)	0.035 (+38%)

Table 7.3: Comparison of the distortion indices between numerical simulations and experimental data for $MFR = 3.0 \text{ kg}\cdot\text{s}^{-1}$.

MFR = 3.0 [$\text{kg}\cdot\text{s}^{-1}$]	DC(60)	IDC	$(\Delta PC/P)_{ave}$	$(\Delta PR/P)_{max}$
Experimental	0.700	0.122	0.076	0.021
SA	0.677 (-3%)	0.128 (+5%)	0.090 (+16%)	0.024 (+18%)
SA-RC	0.749 (+7%)	0.123 (+1%)	0.087 (+11%)	0.020 (-2%)
SA-QCR2000	0.842 (+20%)	0.130 (+6%)	0.094 (+20%)	0.012 (-41%)
$k - \omega SST$	0.722 (+3%)	0.128 (+5%)	0.097 (+34%)	0.029 (+19%)
RSM	0.833 (+19%)	0.131 (+8%)	0.101 (+30%)	0.020 (-2%)
ZDES	0.781 (+12%)	0.130 (+7%)	0.088 (+13%)	0.018 (+12%)

7.1.2 Velocity based distortion criteria

An important part of the physical phenomena under study are the counter-rotating vortices at the BLI intake. One way to measure these counter-rotating vortices is by using distortion indices that take into account the velocity field, especially the tangential velocities in the AIP. The swirl angle, computed by equation 2.11 gives a relation between the tangential velocity and axial velocity. In the presence of a flow separation, the velocity in the axial axis decreases, increasing the angle of swirl. In addition, the tangential velocity also increases this angle.

Figures 7.6, 7.7 and 7.8 show the swirl angle value along the azimuthal position for each turbulent model at 3.0, 3.4 and 4.0 $\text{kg}\cdot\text{s}^{-1}$ respectively. For the 3.0 $\text{kg}\cdot\text{s}^{-1}$ case, the largest angles are presented for SA-QCR2000, RSM and ZDES models. For this same case it can also be noted that the ZDES tends to predict the vortex core between r3 and r4, while for other models it is predicted between r2 and r3. For the 3.4 $\text{kg}\cdot\text{s}^{-1}$ case, all turbulence models show maximum values farther away from the center of the AIP, at radial position r1. For the 4.0 $\text{kg}\cdot\text{s}^{-1}$ case, all turbulence models show very similar values and behaviors. In this case, the values of the alpha

angle at r1 remain high due to the axial and tangential velocity ratio. For r1 the axial velocity decreases significantly due to the thickness of the boundary layer. This latter corresponds to a case without flow separation.

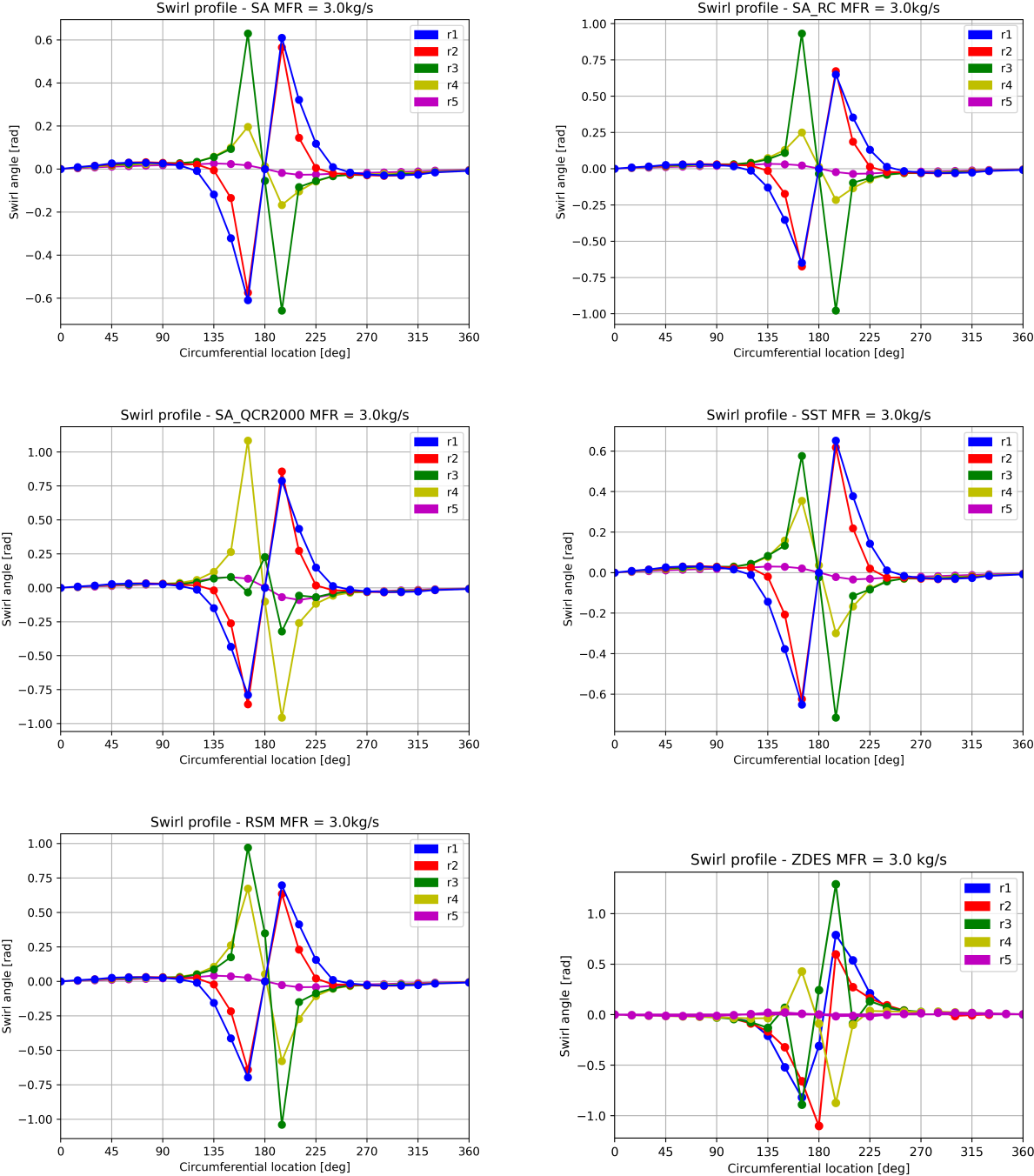


Figure 7.6: Swirl angle profile in function of azimuthal position according to different turbulence models for mass flow of $3.0 \text{ kg}\cdot\text{s}^{-1}$.

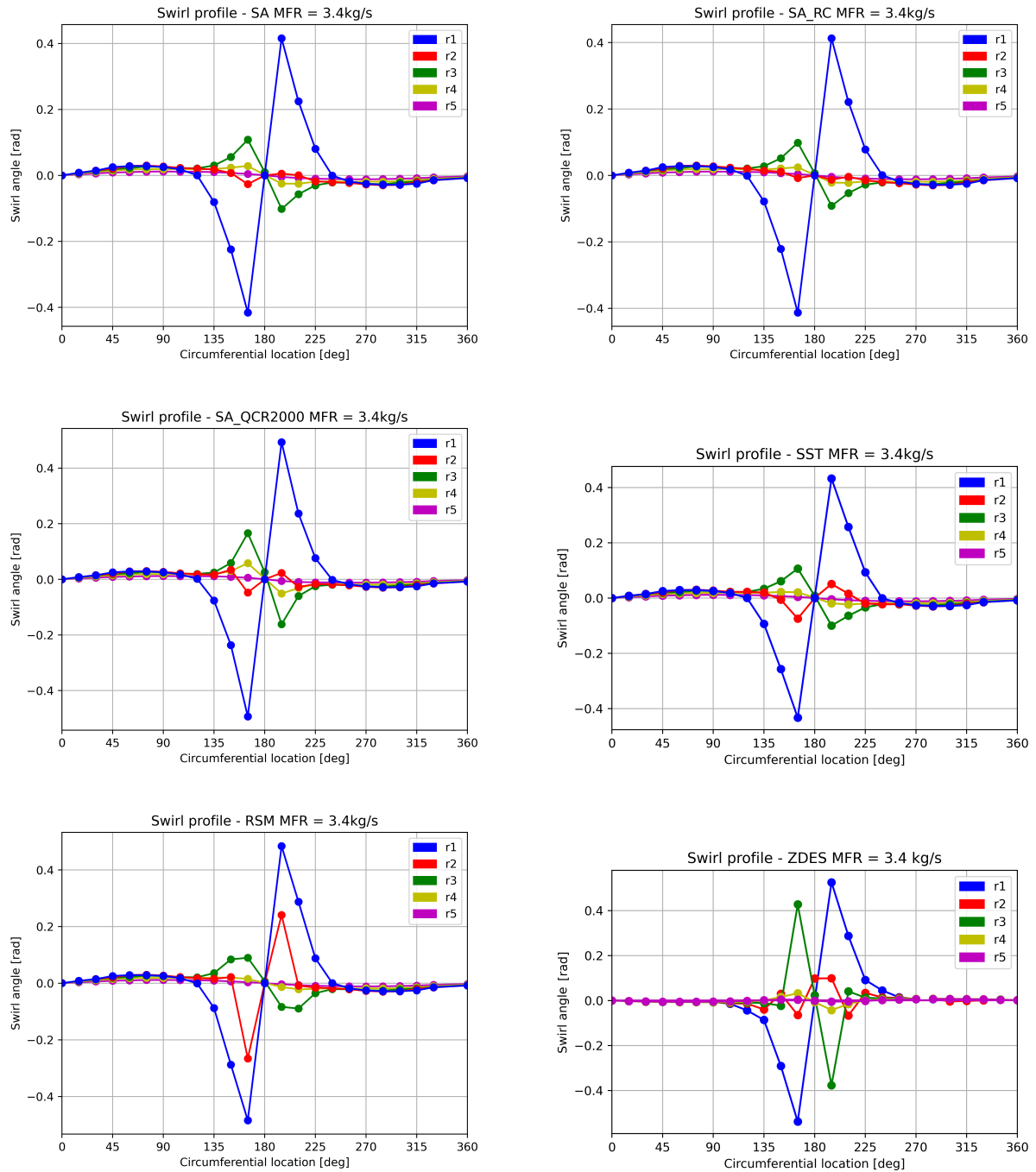


Figure 7.7: Swirl angle profile in function of azimuthal position according to different turbulence models for mass flow of $3.4 \text{ kg}\cdot\text{s}^{-1}$.

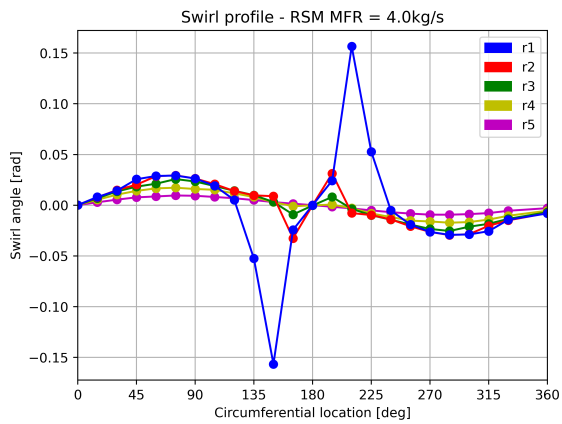
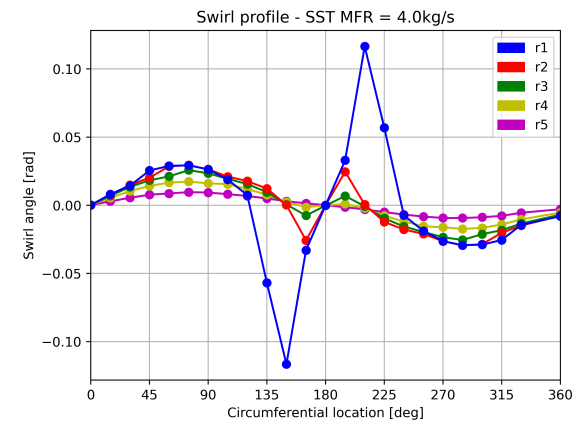
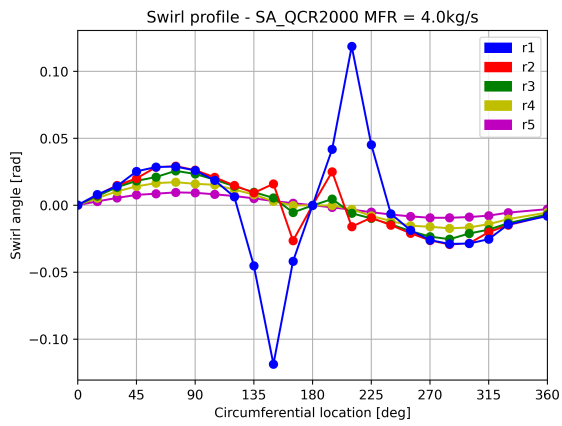
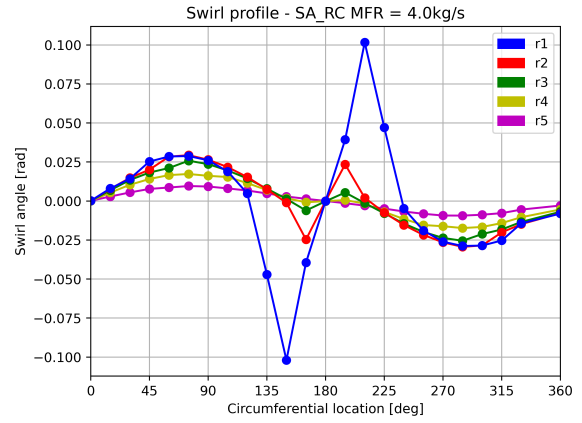
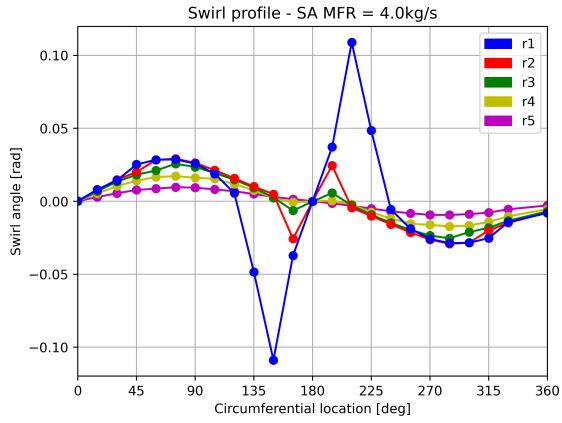


Figure 7.8: Swirl angle profile in function of azimuthal position according to different turbulence models for mass flow of $4.0 \text{ kg}\cdot\text{s}^{-1}$.

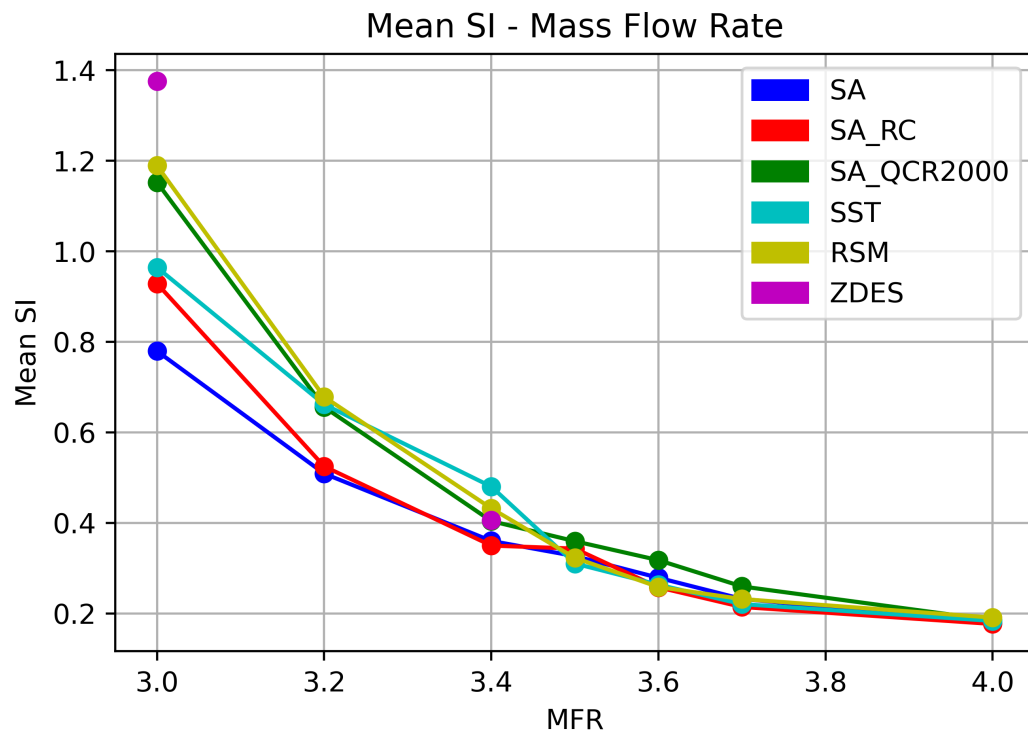


Figure 7.9: Comparison of numerical and experimental maximum swirl intensity for various corrected mass flow rate values.

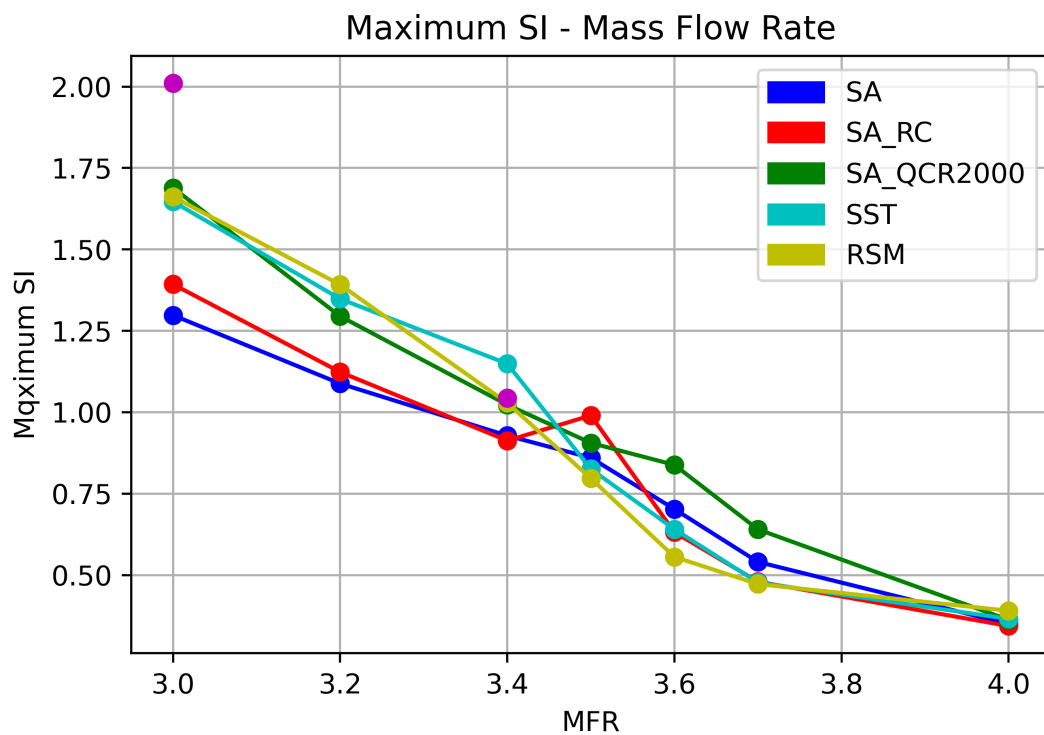


Figure 7.10: Comparison of numerical and experimental maximum swirl intensity for various corrected mass flow rate values.

The Swirl Intensity (SI) is an interesting parameter to characterize the distortion for this type of configurations. The SI index is defined as the “extent weighted” absolute swirl, and this value is calculated at each measurement ring on the rake. The SI is calculated according to equation 2.14. Based on this parameter, two distortion indices are proposed: the Mean SI and Maximum SI.

The mean SI takes the averaged of each ring value as distortion parameter. Figure 7.9 shows its value for each turbulence model as function of the mass flow rate. With this distortion index it is possible to define the three regions proposed at the beginning of this chapter. When there is no separation (between $MFR = 3.7$ and $4.0 \text{ kg}\cdot\text{s}^{-1}$) all turbulence models give very similar values. When the separation appears (for MFR between of 3.4 and $3.7 \text{ kg}\cdot\text{s}^{-1}$) the mean SI values predicted by the SA-QCR2000 model are larger, which could be linked to the early separation predicted by this model. For values less than $3.4 \text{ kg}\cdot\text{s}^{-1}$, there is a dispersion of the distortion values. The ZDES simulation gives a higher Mean SI value at $3.0 \text{ kg}\cdot\text{s}^{-1}$ compared to other numerical methods. The value at $3.4 \text{ kg}\cdot\text{s}^{-1}$ is similar to $k-\omega$ SST or SA-QCR2000 model.

Then the maximum SI is also analyzed. This criterion takes as distortion index the maximum value of SI of a ring. It is calculated by taking the maximum SI intensities from equation 2.14. Figure 7.9 presents the results obtained for each turbulence model. This distortion index, like the previous one, is reduced when the mass flow increases. However, it is not straightforward to differentiate aspects linked to physical phenomena by merely observing the plots obtained. The results show a larger data dispersion across different cases, showing a higher swirl intensity for the SA-QCR2000 model at mass flow rate values larger than $3.5 \text{ kg}\cdot\text{s}^{-1}$. For smaller values, the RSM, ZDES and $k-\omega$ models show larger index values.

7.2 Effects of flow conditions on distortion indices.

This section investigates the impact of flow conditions on distortion indices for our BLI intake. As demonstrated in Chapter 3, certain flow conditions in simulations lead to variations in the intensity and behavior of physical phenomena, which in turn generate a variation in distortion indices.

The first effect examined in this section is the variation of boundary layer thickness. Four different boundary layer thicknesses were investigated, while the other flow conditions remained constant, with mass flow rate varying from 3 to $4 \text{ kg}\cdot\text{s}^{-1}$. The same cases from the previous section were simulated. The second parameter considered is the Mach number in the freestream. Five different cases were studied, varying from $M = 0.75$ to 0.84 . Only one mass flow rate value was studied, corresponding $3.4 \text{ kg}\cdot\text{s}^{-1}$.

7.2.1 Boundary layer thickness effect

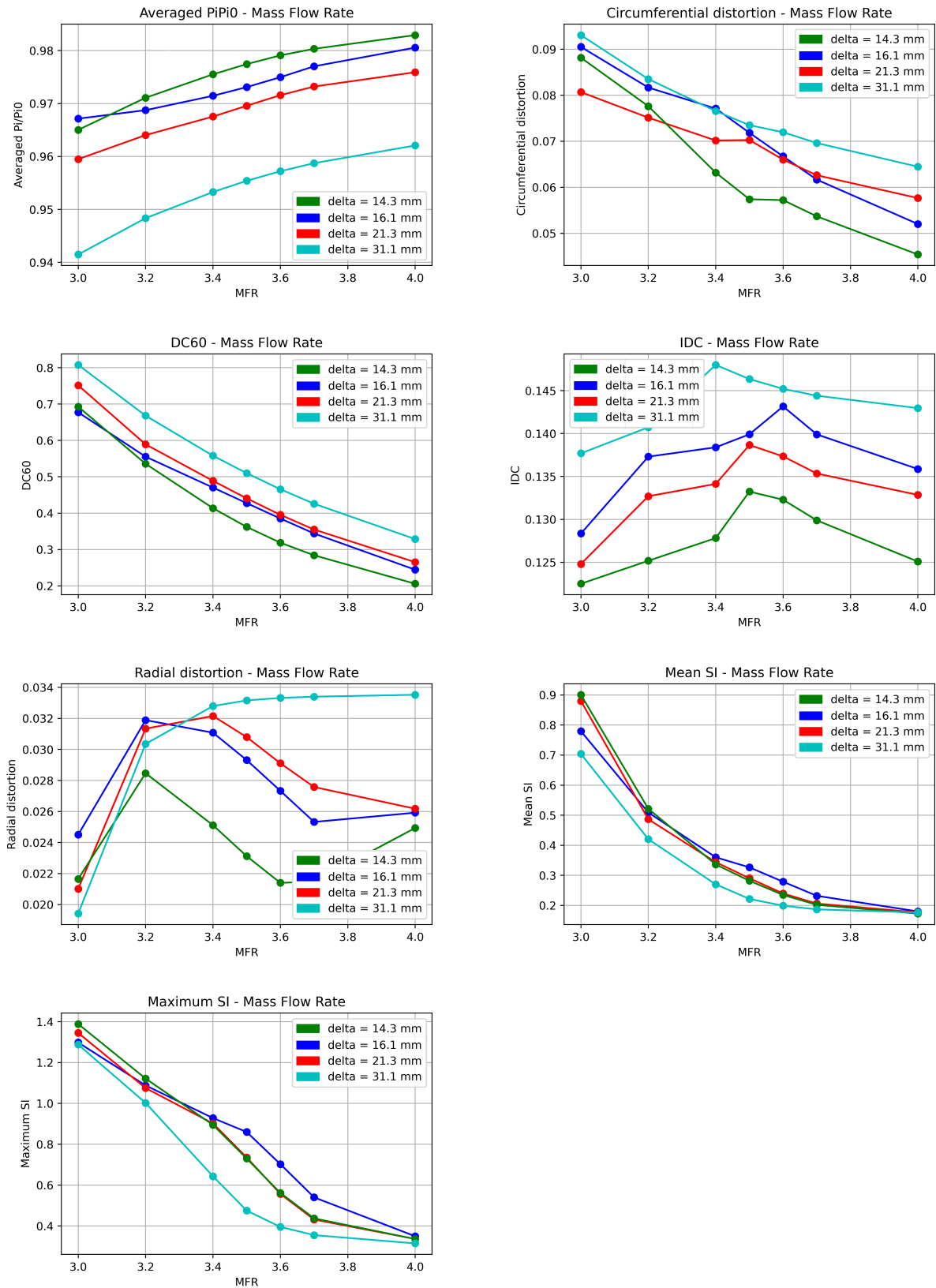


Figure 7.11: Effect of the boundary layer thickness on various distortion indices.

The effect of boundary layer thickness on the dispersion of data obtained for different distortion indices is shown in Figure 7.11. The plot at the top left shows the total pressure loss at the AIP. As expected, an increase in the thickness of the boundary layer leads to an increase in total pressure loss. This decrease in total pressure is quite constant through different mass flow rate values.

This overall increase in total pressure loss at the AIP leads to an increase in distortion described by pressure-based indices. DC(60) and IDC are two such indices that show an overall increase in distortion created by the thickness of the boundary layer. However, it should be mentioned that the distortion predicted by these indices is larger for a thickness of 16.1 mm than for 21.3 mm, which differs from the average loss of total pressure. It can also be noticed that IDC shows maximum values for different mass flows according to the thickness of the boundary layer. This is linked to the variation in physical phenomena generated by the boundary layer thickness variance.

Then, the effect of the boundary layer thickness on the circumferential and radial distortion indices is studied. Those indices generally increase with the thickness of the limit layer, but their evolution along mass flow is not similar between them. When the mass flow is equal to $4.0 \text{ kg}\cdot\text{s}^{-1}$, corresponding to a case without flow separation, distortion indices increase according to boundary layer thickness in both criteria. When flow separation begins to appear, this order disappears. In the case of radial distortion, behavior even changes with respect to boundary layer thickness. For thicker boundary layers, radial distortion is not reduced when mass flow is increased, even giving its maximum values for cases without flow separation.

In the context of distortion criteria based on tangential velocities at the AIP, it is observed that the behavior is inverse. Specifically, the distortion decreases inversely to the thickness of the boundary layer. This phenomenon can be attributed to a decrease in tangential velocities, which is primarily caused by counter-rotating vortices. It is worth noting that some of the energy in these vortices comes from secondary flow. As the boundary layer becomes thicker, the velocity gradient near the wall decreases, resulting in a lower secondary flow effect. All these distortion indices have been developed for use in experimental measurements. However, it should be kept in mind that the results of these measurements are quite sensitive to the position of the measurements and small changes in flow properties at the AIP.

7.2.2 Mach number effect

It is evident that the Mach number has a significant impact on the total pressure loss at the AIP. Specifically, as the Mach number increases, the total pressure loss in AIP also increases. This increase in total pressure loss leads to an increase in the values given by the distortion indices, as illustrated in Figure 7.12. It is worth noting that this increase in distortion generated at the AIP is expressed by both pressure-based and velocity-based distortion indices.

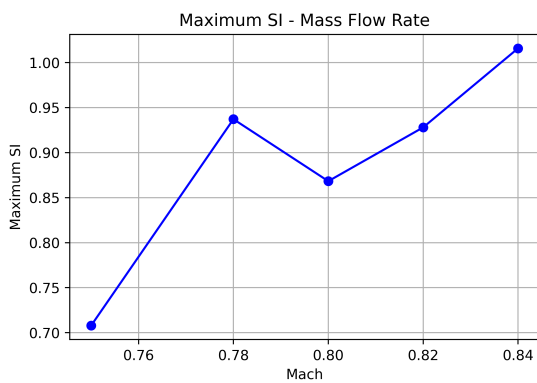
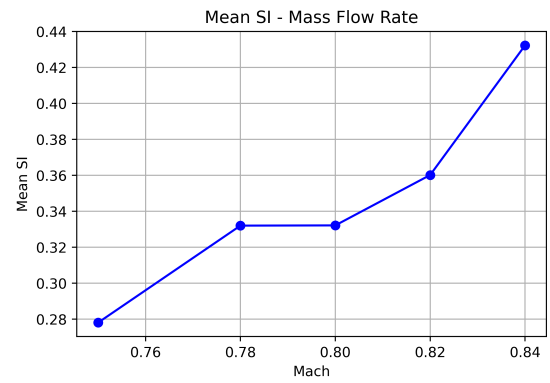
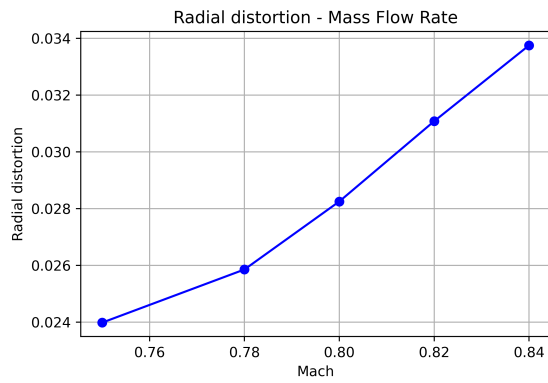
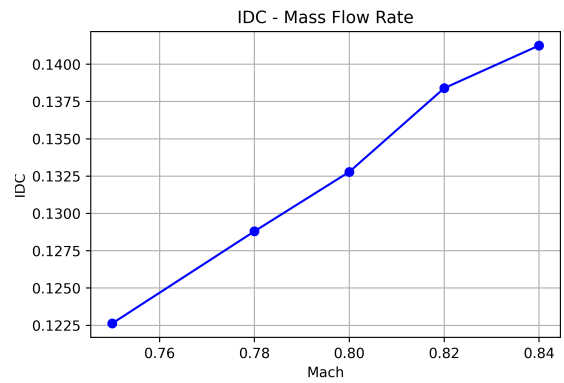
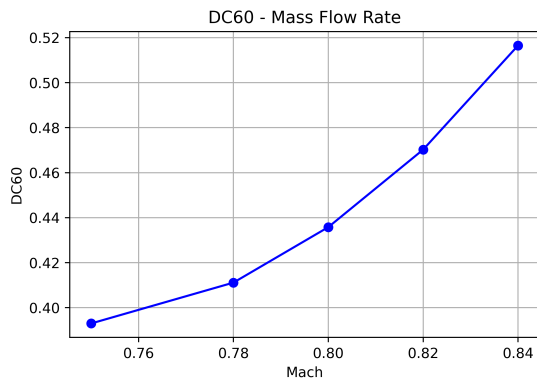
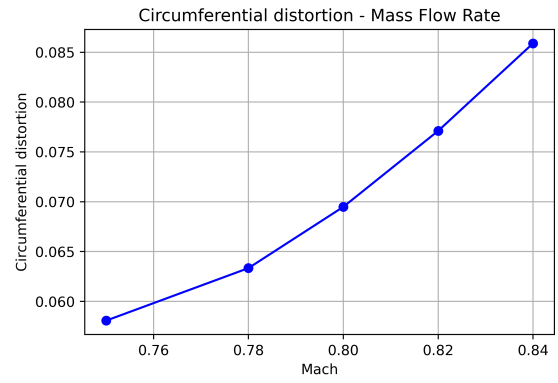
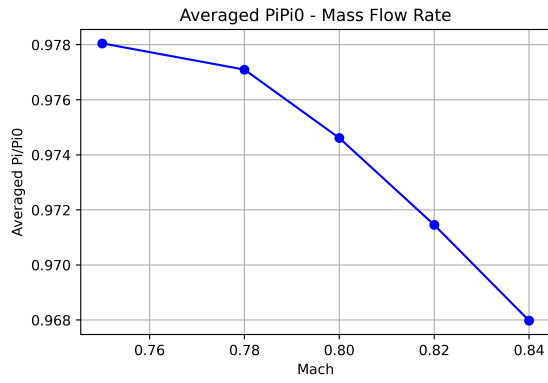


Figure 7.12: Effect of Mach number on various distortion indices.

7.3 Unsteady distortion analysis

As explained in previous sections, several indices have been developed in order to analyse the flow distortion at an AIP. These indices attempt to provide a characterisation of the non-uniform flow field at the AIP in terms of intensity and general shape. Several studies have shown that the use of distortion indices using the averaged time values fail to capture the totality of the physical phenomena [98] [105]. The unsteady distorted flow fields generated by a curved ramp intake can have a detrimental effect on the stability of the engine. The frequency signature in the distorted flow field is of key importance to the engine's response. The spectral analysis of the total pressure signals was conducted to identify the primary characteristic frequencies linked with the unsteady flow behavior. The conventional distortion indices were used to evaluate the unsteady distortion and highlight the distortion events that occurred at the AIP.

Both numerical and experimental results are analyzed and compared in this section. Each distortion index has been calculated for each timestep. In all cases Welch's method was used to estimate the PSD. The chosen segment window has 2000 measurements and the overlap between segments is equal to 500. The sampling frequency in the experiments is 20kHz, and the ZDES is 100kHz.

7.3.1 Pressure-based distortion criteria

The first distortion index assessed is the spatially-averaged total pressure loss at the AIP. Figure 7.13 illustrates the power spectral density (PSD) plots for both experimental and numerical data. For the $3.0 \text{ kg}\cdot\text{s}^{-1}$ case, the behavior between both plots is similar, with a peak observed at $St = 0.34$ and $St = 0.40$ for numerical and experimental cases, respectively. The spectral densities are mostly concentrated in the range $St = 0.1-0.5$, and the corresponding harmonics can be identified in the graph. However, the numerical case shows a peak at a value near $St = 2.05$.

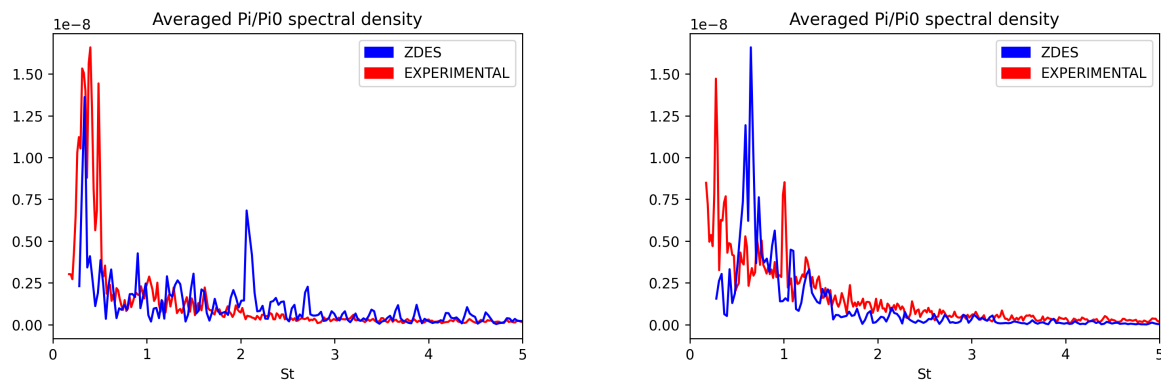


Figure 7.13: PSD of the spatially averaged total pressure at the AIP for the ZDES and the experiments. Left: $3.0 \text{ kg}\cdot\text{s}^{-1}$. Right: $3.4 \text{ kg}\cdot\text{s}^{-1}$

In the $3.4 \text{ kg}\cdot\text{s}^{-1}$ case, the behavior differs between the experimental and numerical cases, with a peak observed at $St = 0.27$ for the experimental case and $St = 0.65$ for the numerical case. For this scenario, both the numerical and experimental results indicate a greater dispersion of energy density in the spectrum. In the experimental case, a peak can even be identified at $St = 1$.

The spectral density obtained for the circumferential distortion is presented in figure 7.14. For a mass flow rate of $3.0 \text{ kg}\cdot\text{s}^{-1}$, the behavior between simulations and experimental results is quite similar. Most of the spectral density is concentrated in values less than $St = 1.5$, with a peak around $St = 0.65$. This peak is not so evident for the experimental data, which show a high density at those frequencies, however peaks are also observed at lower frequencies, corresponding to $St = 0.27$. Theoretically, the data obtained from the simulation will be able to show the phenomena that occur at low Strouhal numbers; however, the small amount of data at such low frequencies could be one of the reasons why this peak density is not captured. For a mass flow rate of $3.4 \text{ kg}\cdot\text{s}^{-1}$, the behavior is quite different. While the numeric result shows a clear peak around $St = 1.52$, the experimental results show no apparent concentrations at any specific frequency, giving a higher density at lower frequencies and tending to decrease almost exponentially as frequencies increase.

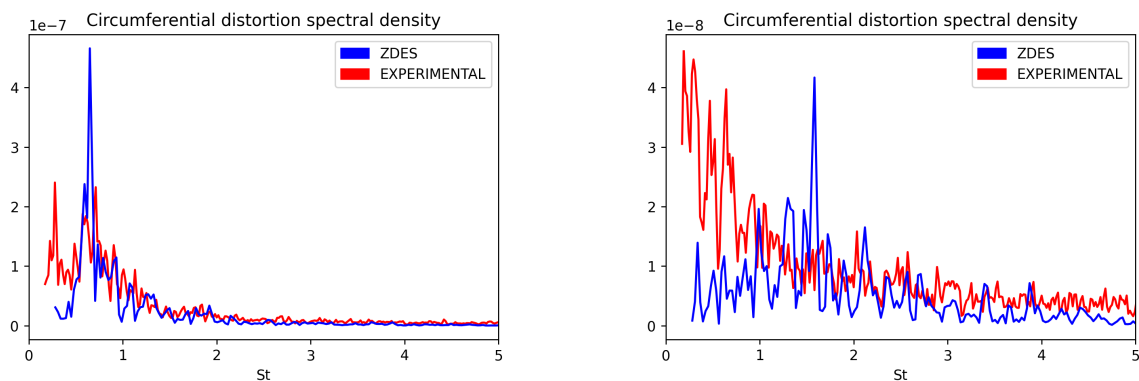


Figure 7.14: PSD of the circumferential distortion ($(\Delta PC/P)_{ave}$) for the ZDES and the experiments. Left: $3.0 \text{ kg}\cdot\text{s}^{-1}$. Right: $3.4 \text{ kg}\cdot\text{s}^{-1}$

The radial distortion index, as depicted in figure 7.15, exhibits a good agreement between the numerical and experimental results for the $3.0 \text{ kg}\cdot\text{s}^{-1}$ case. However, the behaviors are different for the $3.4 \text{ kg}\cdot\text{s}^{-1}$ case. For the lowest mass flow rate, the energy is concentrated in Strouhal number values less than 1. It is also noteworthy that the numerical results predict a peak at around $St = 0.65$, which is also present in the experimental data. No significant phenomena are observed in values greater than 1. For the second case, the behavior is similar to that observed in the circumferential pressure coefficients: the energy level is higher for the lowest Strouhal numbers, showing a maximum peak around $St = 0.27$. Some energy is also around $St = 1 - 1.5$.

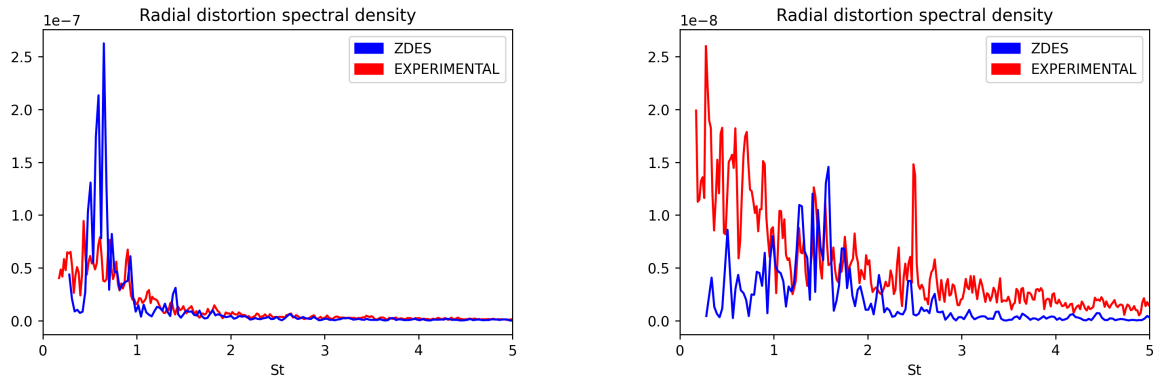


Figure 7.15: PSD of radial distortion for the ZDES and the experiments. Left: $3.0 \text{ kg}\cdot\text{s}^{-1}$. Right: $3.4 \text{ kg}\cdot\text{s}^{-1}$

The PSD obtained for the IDC is presented in Figure [7.16](#). The left plot case shows some agreement between the numerical and experimental results, although the peaks obtained in both cases are not identical. The experimental results exhibit a peak at $St = 0.33$, whereas the numerical case shows its maximum values around $St = 0.65$. Other secondary peaks are also predicted by simulations at around $St = 1.7$. The accuracy on the numerical results for low Strouhal values is lower due to the short duration of the signals in the ZDES. The behavior of the IDC for the $3.4 \text{ kg}\cdot\text{s}^{-1}$ case is completely similar to that of the other circumferential distortion index. In the experimental case, the maximum peak is observed at $St = 0.27$, while in the numerical case the maximum peak is at 1.55.

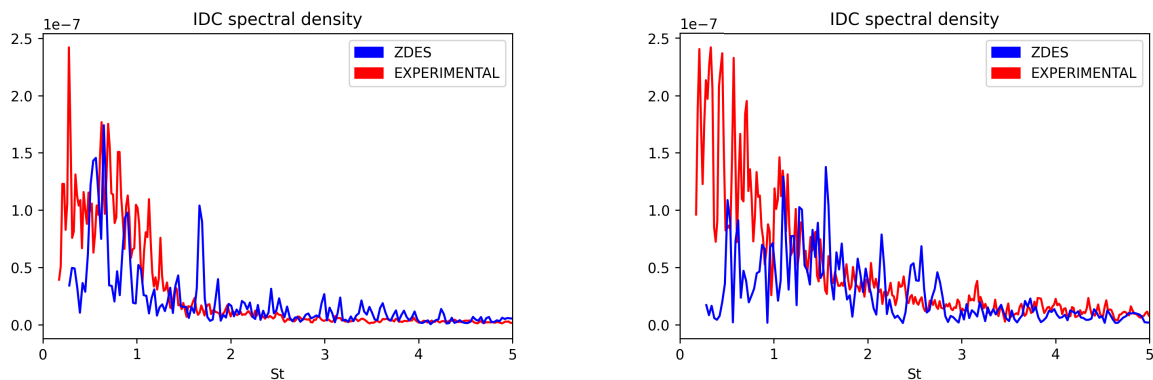


Figure 7.16: PSD of IDC value for the ZDES and the experiments. Left: $3.0 \text{ kg}\cdot\text{s}^{-1}$. Right: $3.4 \text{ kg}\cdot\text{s}^{-1}$

Finally, DC(60) is presented in Figure 5. For the case at $3.0 \text{ kg}\cdot\text{s}^{-1}$ the results obtained are quite similar, with a higher energy level for Strouhal values less than 1. For both the numerical simulation and experiments, the maximum peak is at $St = 0.65$. Experimental data also show another peak around $St = 0.33$. The results at mass flow of $3.4 \text{ kg}\cdot\text{s}^{-1}$ show no similarities

between the numerical and experimental data. The simulation shows a peak around $St = 1.3$, however the experimental results place the peaks at a lower Strouhal number, around $St = 0.20$.

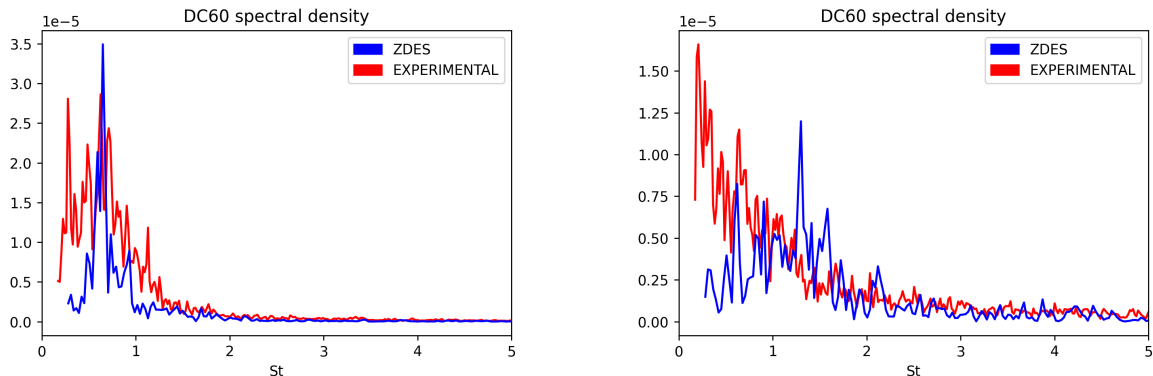


Figure 7.17: PSD of the DC(60) for the ZDES and the experiments. Left: $3.0 \text{ kg}\cdot\text{s}^{-1}$. Right: $3.4 \text{ kg}\cdot\text{s}^{-1}$

The spectral analysis of pressure-based distortion indices appears to be inconclusive with respect to the ability of the numerical simulations to take into account unsteady phenomena. For the first case there is some agreement between the numerical and experimental data, however for the second case, corresponding to $3.4 \text{ kg}\cdot\text{s}^{-1}$, the agreement is minimal.

7.3.2 Velocity-Based distortion criteria

The significance of velocity-based distortion indices for a BLI configuration was highlighted at the outset of this chapter. This subsection aims to analyse the PSDs of velocity-based distortion indices. Concerning the velocity fields, only the numerical one is available. Both distortion indices are based on swirl intensity.

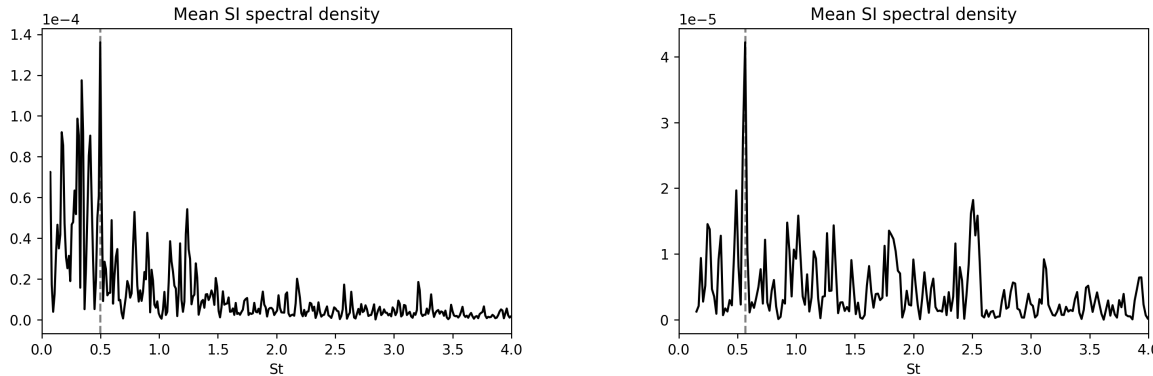


Figure 7.18: PSD of the mean swirl intensity value for the ZDES simulation. Left: $3.0 \text{ kg}\cdot\text{s}^{-1}$. Right: $3.4 \text{ kg}\cdot\text{s}^{-1}$

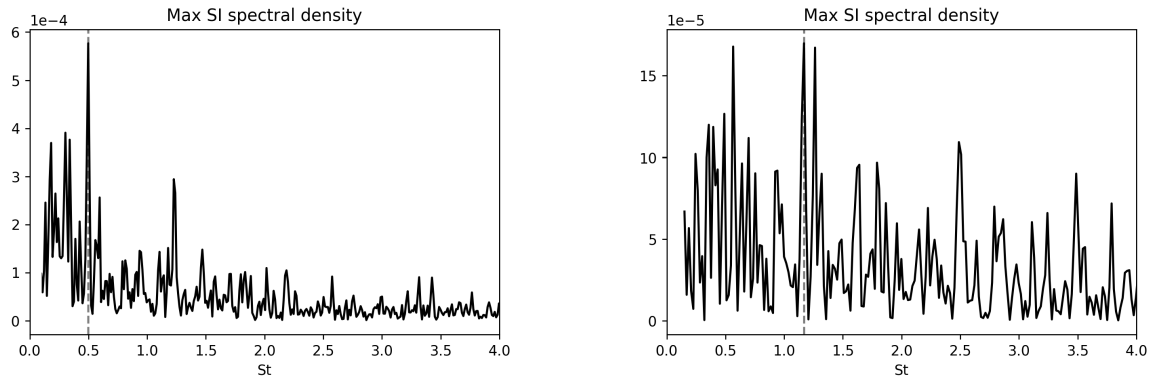


Figure 7.19: PSD of the maximum swirl intensity value for the ZDES simulation. Left: $3.0 \text{ kg}\cdot\text{s}^{-1}$. Right: $3.4 \text{ kg}\cdot\text{s}^{-1}$

Irrespective of the mass flow, it is evident that the energy of the swirl indices is widely distributed across the spectrum. Several peaks are observed for the mean swirl intensity at $3.0 \text{ kg}\cdot\text{s}^{-1}$, with the most prominent one located at $St = 0.49$. This peak is also present for the maximum SI. Other peaks can be observed around $St = 1.3$. In the case of $3.4 \text{ kg}\cdot\text{s}^{-1}$, the mean SI exhibits a peak at $St = 0.56$, while for the maximum SI, the peak is at $St = 1.16$. The energy density is widely distributed across the spectrum, similar to what was observed for the other distortion indices.

7.4 Chapter summary and conclusions

Distortion indices, which are commonly used in the industry, have been analyzed on a BLI intake configuration. The primary objective of computing distortion indices is to analyze the physical phenomena present in the flow and their impact on the distortion, so as to provide a driving parameter to design engine components. According to the parameters used to calculate the distortion index, they have been separated into two groups: velocity-based and pressure-based. Since only pressure results are available from the wind tunnel test, only this group has been directly compared.

In the pressure-based distortion index, the spatially-averaged total pressure loss obtained by numerical models tend to predict a larger loss of total pressure compared to experimental results. The remaining indices of distortion based on pressure exhibit mixed results. On one hand, the DC(60) or the index of circumferential distortion do not seem to be sensitive to any change in physical phenomena. On the other hand, indices such as IDC and radial distortion allow discrimination of certain changes in physical phenomena, such as flow separation. IDC is a promising index for a Boundary Layer Ingestion (BLI) intake, as it exhibits an interesting correlation between flow behavior and its value. The maximum value corresponds to the mass flow rate value for which a separated flow appears. Similar behavior is found with radial distortion,

which keeps the distortion index constant if there is no flow separation. In general, the SA-RC model is the one that gets closer to the experimental results by simply predicting a lower loss of total pressure in the AIP. However the dispersion on the distortion indices between the different turbulence models is not very large, reducing even more when there is no flow separation. The ZDES model does not show an improvement over the other turbulence models, generally giving results among the other models.

With regards to velocity-based distortion indices, consistent results are obtained. Through the slope of the plot, some clues can be obtained that allow for discrimination of the physical phenomena. For high mass flow, all turbulence models tend to give fairly similar values. However, these values tend to disperse as the mass flow decreases and more complex physical phenomena appear. The ZDES model tends to predict swirl velocities much higher than the rest of turbulence models for the $3.0 \text{ kg}\cdot\text{s}^{-1}$ case. However, this index becomes comparable to the rest when the mass flow goes up to $3.4 \text{ kg}\cdot\text{s}^{-1}$. The slope becomes almost zero when the flow separation disappears. Instead, it becomes more pronounced if the flow recirculation region increases.

In the same analysis of distortion indices obtained with steady data, certain parameters such as the Mach number or thickness of the boundary layer were analyzed to measure their impact. The thickness of the boundary layer has a significant effect on the distortion indices. The behavior of the distortion index is dependent on the type of index used. Pressure-based indices tend to show higher distortion values when the thickness of the boundary layer is decreased. In contrast, vortex velocity-based indices show a different behavior: the thinnest boundary layer shows the lowest distortion indices. The Mach number shows a clear trend: when the Mach number is increased, the distortion in the AIP is also increased.

Finally unsteady distortion analysis was performed with the same distortion indices used previously and calculated for each step of time. Some agreement has been shown between the ZDES and the experiments only for the case of $3.0 \text{ kg}\cdot\text{s}^{-1}$. The $3.4 \text{ kg}\cdot\text{s}^{-1}$ case differs considerably between the simulation and the experiments. For the case of $3.0 \text{ kg}\cdot\text{s}^{-1}$ the PSDs show that the energy in Strouhal numbers less than $St = 1.5$ with some peaks at $St = 0.66$, $St = 0.3$ and $St = 0.27$.

The numerical simulations are in quite good agreement with the experimental results. However, differences in both steady and unsteady analyses could be explained by several reasons. The first reason are the differences in the prediction obtained by the simulations due to the complexity of the flow. In addition, the change of discretization rake at the AIP in the experimental results, which could lead to the inability to legitimately represent the distortion. Other parameters that need to be taken into account include the small angle of side-slip in experimental cases or the effect of wind tunnel wall. Most distortion indices are quite sensitive to these small distribution fields in the AIP. In conclusion, it is necessary to propose new distortion indices that can account for both the loss of total pressure and the swirl velocities at the AIP.

Chapter 8

Work synthesis, conclusions and future work

The objective of the research was to identify the primary physical phenomena involved in a boundary layer intake, estimate the aerodynamic distortion generated by these physical phenomena, and analyze the predictive capacity of different turbulence models. The study was conducted using a BLI intake semi-buried on a flat plate, which did not take into account the effect of any compression stage. The geometry was studied both numerically and experimentally under transonic conditions. The main parameter varied in the study was the mass flow that passed through it. In addition, other important boundary layer ingestion parameters, such as the boundary layer thickness or freestream Mach number were analyzed. The wind tunnel tests were compared with the results of numerical simulations with different turbulence models. The most common turbulence models in the industry were used, such as $k\omega$ SST or Spalart-Allmaras including some of its corrections, in addition to a RSM model and a ZDES computation. The comparisons were made using the static pressure taps, kulite transducers, and a rake with 40 pressure sensors located at the AIP. The flow behavior and stationary phenomena were compared, in addition to the unsteady behavior by spectral analysis. Finally, the distortion levels generated in the tests were compared with those predicted by numerical methods.

8.1 Physical phenomena investigations

The physical phenomena that occur in a boundary layer intake are dependent on the geometry and configuration of the aircraft. For the specific configuration studied, the primary physical phenomena identified are as follows:

- The behavior of the boundary layer is the first parameter to consider for a boundary layer ingestion engine. Several parameters, such as thickness, momentum, or shape factor, can

affect its behavior. All these parameters depend on various external factors; however, their effect can greatly condition the viability and possible improvement of a boundary layer ingestion. The ingestion of a large amount of boundary layer at the engine intake results in a significant decrease in pressure recovery at the AIP.

- The loss of total pressure at the AIP is inherent in boundary layer ingestion. This loss of total pressure is mainly generated by boundary layer thickening; however, its impact is affected by different flow behaviors happening at the BLI intake, such as vortices or flow separations.
- The flow separation on the intake ramp is one of the phenomena that most affects the distortion at the AIP. This flow separation is due to the adverse pressure gradient found in the boundary layer. This pressure gradient depends on the geometry itself, as well as other flow conditions such as the mass flow through the engine, the thickness of the boundary layer or the velocity in the free flow.
- The presence of counter-rotating vortices is another physical phenomenon that conditions the behavior of the boundary layer ingestion (BLI) intake. The counter-rotating vortices are mainly created due the secondary flow, as well as the horseshoe vortex generated at the intersection of the nacelle with the flat plate. The vortices are always present, even if there is no flow separation, and their intensities can greatly affect the region affected by the loss of total pressure and distortion at the AIP.
- The behavior of these physical phenomena is not constant over time, varying greatly and affecting specific spectral values. The negative impact of these physical phenomena can lead to operability problems, such as material fatigue, aeroacoustic problems, or resonances.

8.2 Numerical prediction capabilities

The predictive capability was assessed by comparing the numerical results with the experiments. The time-averaged behavior was modeled using a RSM model, kw SST model, in addition to Spalart Allmaras, and their Quadratic Constitutive Relation, rotation and curvature corrections. The unsteady behavior was analyzed through ZDES simulations of mode 2. The corrected mass flow rate was varied between 3 and 4 kg·s⁻¹. The primary findings are:

- The steady flow behavior, both experimentally and numerically, is distinguished by the existence of counter-rotating vortices, in addition to the potential flow separation over the intake ramp. The Reynolds-averaged Navier-Stokes (RANS) simulations are able to characterize this flow behavior. The qualitative prediction provided by the different turbulence models is in close agreement, both among themselves and in comparison to

the experimental results. When complex events occur, such as flow separation, there is a tendency for some dispersion between different turbulent model predictions.

- Concerning the C_p prediction, the $k-\omega$ SST model stands out from the other models because it is the closest to the experimental data along the intake ramp. The results obtained from the SA-QCR2000 and SSG-LRR RSM models demonstrate also a commendable concordance with the experimental data. The first exhibits a higher degree of accuracy in the lower segment of the ramp, while the latter more closely aligns with the experimental observations in the vicinity of the flow separation point. The SA, SA-RC, and ZDES results are the farthest from the experimental curve. It can be concluded that RANS models using a one equation linear turbulence models have a worse performance relative to a two-equation linear turbulence or non-linear models, such as $k-\omega$ SST, quadratic constitutive relation and Reynolds-Stress models.
- All turbulence models tend to slightly overestimate the total pressure loss at the AIP, specially in cases for which there is a flow recirculation. This discrepancy can be attributed to the tendency of all models to overpredict the region of the recirculating zone compared to the experimental data. The SA model, followed by the $k-\omega$ SST one, are the two models that best estimate the impacted region at the AIP and the total pressure loss. Other models, especially ZDES and RSM, tend to over predict the total pressure loss. Turbulence models such as SA-QCR2000 or RSM tend to predict much stronger vortices, leading to greater energy dissipation.
- The results of the spectral analysis reveal certain differences between ZDES mode 2 prediction and experimental data. These differences are more pronounced for the probes located on the intake ramp. The differences could explain differences in flow recirculation and also affect the prediction of loss of total pressure at the AIP. The difference in flow recirculation zones is also substantiated by spectral comparisons conducted at the AIP, which indicate a shear layer position displacement corresponding to a larger region affected by total pressure loss in the ZDES than in the experiments.
- The experimental and numerical comparison of POD modal analysis for the flow rate of $3.0 \text{ kg}\cdot\text{s}^{-1}$ has shown some agreement, while the same cannot be said for the flow rate of $3.4 \text{ kg}\cdot\text{s}^{-1}$, which exhibits distinct behaviors in the spectrum. The third mode of the experimental analysis and the first mode of the numerical analysis have identified a vertical oscillatory movement for values close to $St = 0.77$ for the flow rate of $3.0 \text{ kg}\cdot\text{s}^{-1}$. This mode is associated with the instability of the shear layer in the flow separation region. The first and second experimental modes, which are associated with lateral movements, appear to be similar to those shown in numerical mode 2. However, several differences in behavior are shown in terms of spectral contain, one having a value of $St = 0.33$ and the other to $St = 0.84$ respectively.

8.3 Distortion description

The present study has analyzed industrial distortion indices on a boundary layer ingestion (BLI) configuration. The primary objective of computing distortion indices is to analyze the physical phenomena present in the flow and their impact on the distortion. This analysis provides a driving parameter to design engine components. The main conclusions derived from our analysis are as follows:

- The pressure-based distortion indices have been studied by using the time-averaged data. The results indicate that numerical models tend to predict a greater loss of total pressure compared to experimental results. These indices exhibit mixed results. While the DC(60) or the index of circumferential distortion do not seem to be sensitive to any change in physical phenomena, indices such as IDC and radial distortion allow discrimination of certain changes in physical phenomena, such as flow separation. IDC is a promising index for a BLI intake, as it exhibits an interesting correlation between flow behavior and its value. The maximum value corresponds to the mass flow rate value for which a separated flow appears. Similar behavior is found with radial distortion, which keeps the distortion index constant if there is no flow separation.
- The present study has also analyzed velocity-based distortion indices, which provide more consistent characterization of physical phenomena. The slope of the plot provides clues that allow for discrimination of the physical phenomena. For high mass flow, all turbulence models tend to give fairly similar values. However, these values tend to disperse as the mass flow decreases and more complex physical phenomena appear. The ZDES model predicts swirl velocities much higher than the rest of turbulence models for the $3.0 \text{ kg}\cdot\text{s}^{-1}$ case. However, this index becomes comparable to the rest when the mass flow goes up to $3.4 \text{ kg}\cdot\text{s}^{-1}$. The slope becomes almost zero when the flow separation disappears. Instead, it becomes more pronounced if the flow recirculation region increases.
- The thickness of the boundary layer has a significant impact on the distortion indices. The Pressure-based indices tend to exhibit higher distortion values when the thickness of the boundary layer is reduced. In contrast, vortex velocity-based indices exhibit a different behavior: the thinnest boundary layer shows the lowest distortion indices. The effect of the Mach number exhibits a clear trend: when the Mach number is increased, the distortion at the AIP also increases.
- The unsteady distortion analysis has revealed that the ZDES and the experiments exhibit some agreement only for the flow rate of $3.0 \text{ kg}\cdot\text{s}^{-1}$. However, the numerical and experimental behavior of the flow rate of $3.4 \text{ kg}\cdot\text{s}^{-1}$ differs considerably. For the flow rate of $3.0 \text{ kg}\cdot\text{s}^{-1}$, the peak distortion is observed in ranges less than $St = 1.5$, with values of $St = 0.66$, $St = 0.3$, and $St = 0.27$ being highlighted.

8.4 Recommendations for future work

Corresponding to experimental measurements

- The present results are limited by the type of data obtained. To overcome this limitation, it is necessary to complement the experimental analyses with a Particle Image Velocimetry (PIV) analysis at the AIP. This will allow for direct observation of the different physical phenomena and enable analysis of velocity-based distortion indices.
- Furthermore, measurement of PIV along the symmetry plane should provide valuable information for the validation of CFD models. This could identify certain areas of recirculation over the intake ramp and provide unsteady data linked to the shear layer.

Corresponding to numerical methods

- It would be interesting to investigate in more detail the effect that the diffusivity terms of the RANS models generate on the results obtained in order to better simulate the curved flows and the presence of secondary flows. This can also be applied to adjust total pressure loss and vortex intensity.
- The accuracy of the ZDES model is lower than expected, despite the fact that part of the turbulence is solved, contrary to all other Reynolds-Averaged Navier-Stokes (RANS) simulations. It is possible that ZDES mode 2 is not the most appropriate for this type of flow. A ZDES mode 3, similar to Wall-Modeled Large Eddy Simulation (WMLES), where the turbulence in the boundary layer is partly solved (above 0.1δ) and not modeled like in mode 2, could provide more accurate results on this configuration. However, it would also be more computationally expensive since the mesh requirements would be higher. Another possible improvement to the prediction provided by the ZDES model could be the use of synthetic turbulence injection in the free stream.
- The prediction of complex flows can be affected by various sources of error. One such source is the phenomenon of model stress depletion. The blending functions used in turbulence models are typically designed for simple physical phenomena. However, in the presence of flow separation, vorticity, and intense vortices, the behavior and shape of the boundary layer can be affected, which in turn conditions the flow downstream. Therefore, it is important to carry out more studies to estimate the effect of model stress depletion and define possible improvements to apply it to this type of case.

Corresponding to physical phenomena comprehension and industrial applications

- Novel distortion indices should be developed to more accurately describe the physical phenomena in a BLI intake and their adverse effects. These new distortion criteria could

incorporate parameters related to both velocity and pressure at the aerodynamic interface plane (AIP). Alternatively, an energetic approach could be employed to characterize the flow distortion. It is also necessary to quantify the impact that this distortion would have on different stages of an aero-engine.

- The impact of varying conditions, such as the angle of sideslip, subsonic conditions, or interactions with other aircraft components, on certain conditions should be investigated. In addition, the inclusion of a compression stage could greatly affect the flow behavior on the intake.
- The effect of incorporating flow control devices should be studied in order to reduce distortion at the AIP and improve overall engine performance.

Bibliography

- [1] Leroy H. Smith. Wake ingestion propulsion benefit. *Journal of Propulsion and Power* Vol. 9(1) (1993) 74–82. DOI: [10.2514/3.11487](https://doi.org/10.2514/3.11487).
- [2] A Arntz. “Civil Aircraft Aero-thermo-propulsive Performance Assessment by an Exergy Analysis of High-fidelity CFD-RANS Flow Solutions”. PhD thesis. PhD Thesis from Université de Lille 1, 2014.
- [3] Mark Drela. “Development of the D8 Transport Configuration”. In: *29th AIAA Applied Aerodynamics Conference. AIAA Paper 2011-3970*. DOI: [10.2514/6.2011-3970](https://doi.org/10.2514/6.2011-3970).
- [4] Nils Budziszewski, Jens Friedrichs. Modelling of A Boundary Layer Ingesting Propulsor. *Energies* Vol. 11 (2018) 708. DOI: [10.3390/en11040708](https://doi.org/10.3390/en11040708).
- [5] Anne-Laure Delot, Eric Garnier, Didier Pagan. Flow Control in a High-Offset Subsonic Air Intake. *47th AIAA/ASME/SAE/ASEE Joint Propulsion Conference and Exhibit 2011. Paper No. 2011-5569* (2011). DOI: [10.2514/6.2011-5569](https://doi.org/10.2514/6.2011-5569).
- [6] Hector Solorzano, Ana Scarabino. Innovación en Sistemas de Propulsión: Métodos, Propuestas y Desafíos. *Revista Ciencias Espaciales* 13 (2020) 108–123. DOI: [10.5377/ce.v13i1.11257](https://doi.org/10.5377/ce.v13i1.11257).
- [7] Martin Rein, Stefan Koch. Experimental Study of Boundary-Layer Ingestion into a Diverterless S-Duct Intake. *AIAA Journal* Vol. 53 (2015) 1–5. DOI: [10.2514/1.J053902](https://doi.org/10.2514/1.J053902).
- [8] Tom Hickling, G. Ingram. Reynolds-Averaged Navier–Stokes Modelling in Transonic S-ducts with Passive Flow Control. *Proceedings of the Institution of Mechanical Engineers, Part A: Journal of Power and Energy* Vol. 234 (2019). DOI: [10.1177/0957650919845765](https://doi.org/10.1177/0957650919845765).
- [9] Andrew Cary et al. CFD Vision 2030 Road Map: Progress and Perspectives. *AIAA AVIATION 2021 FORUM. AIAA Paper 2021-2726* (2021). DOI: [10.2514/6.2021-2726](https://doi.org/10.2514/6.2021-2726).
- [10] D. Rutherford, M. Zeinali. *Efficiency trends for new commercial jet aircraft. Technical report, International Council on Clean Transportation*. 2009.
- [11] R. OWENS, K. HASEL, D. MAPES. “Ultra high bypass turbofan technologies for the twenty-first century”. In: *26th Joint Propulsion Conference. AIAA Paper 1990-2397*. DOI: [10.2514/6.1990-2397](https://doi.org/10.2514/6.1990-2397).

- [12] Brian M. Yutko et al. “Conceptual Design of a D8 Commercial Aircraft”. In: *17th AIAA Aviation Technology, Integration, and Operations Conference. AIAA Paper 2017-3590*. DOI: [10.2514/6.2017-3590](https://doi.org/10.2514/6.2017-3590).
- [13] Justin Gray et al. Coupled Aeropropulsive Optimization of a Three-Dimensional Boundary-Layer Ingestion Propulsor Considering Inlet Distortion. *Journal of Aircraft* Vol. 57 (2020) 1–12. DOI: [10.2514/1.C035845](https://doi.org/10.2514/1.C035845).
- [14] Ludovic Wuart et al. “Development of NOVA Aircraft Configurations for Large Engine Integration Studies”. In: *33rd AIAA Applied Aerodynamics Conference. AIAA Paper 2015-2254*. DOI: [10.2514/6.2015-2254](https://doi.org/10.2514/6.2015-2254).
- [15] Mark Drela. Power Balance in Aerodynamic Flows. *AIAA Journal* Vol. 47 (7) (2009) 1761–1771. DOI: [10.2514/1.42409](https://doi.org/10.2514/1.42409).
- [16] W Froude. “Supplementary note by Mr. Froude to his remarks on Professor Rankine’s paper on the mechanical principles of the action of propellers”. In: *Transactions of the Institution of Naval Architects*, VI:35–39.
- [17] A Betz. Interference between propeller and vehicle; the ducted propeller. In *Introduction to the Theory of Flow Machines* (1966) 215–220. DOI: [10.1016/b978-0-08-011433-0.50063-19](https://doi.org/10.1016/b978-0-08-011433-0.50063-19).
- [18] Alejandra Uranga et al. Analysis of the Aerodynamic Benefit from Boundary Layer Ingestion for Transport Aircraft. *AIAA Journal* Vol. 56 (11) (2018) 4271–4281. DOI: [10.2514/1.J056781](https://doi.org/10.2514/1.J056781).
- [19] Cesare A. Hall, Emily Schwartz, James I. Hileman. Assessment of Technologies for the Silent Aircraft Initiative. *Journal of Propulsion and Power* Vol. 25 (6) (2009) 1153–1162. DOI: [10.2514/1.43079](https://doi.org/10.2514/1.43079).
- [20] Cheryl L. Bowman, Ty V. Marien, James L. Felder. Turbo- and Hybrid-Electrified Aircraft Propulsion for Commercial Transport. *2018 AIAA/IEEE Electric Aircraft Technologies Symposium. AIAA Paper 2018-4984* (2018). DOI: [10.2514/6.2018-4984](https://doi.org/10.2514/6.2018-4984).
- [21] Askin Isikveren et al. Distributed Propulsion and Ultra-high By-Pass Rotor Study at Aircraft Level. *Aeronautical Journal -New Series-* Vol. 119 (2015) 1327–1376. DOI: [10.1017/S0001924000011295](https://doi.org/10.1017/S0001924000011295).
- [22] Arne Seitz et al. Proof of Concept Study for Fuselage Boundary Layer Ingesting Propulsion. *Aerospace* Vol. 8 (Jan. 2021) 16. DOI: [10.3390/aerospace8010016](https://doi.org/10.3390/aerospace8010016).
- [23] Panagiotis Giannakakis et al. Fuel Burn Evaluation of a Turbo-electric Propulsive Fuselage Aircraft. *AIAA Propulsion and Energy 2019 Forum. AIAA Paper 2019-4181* (2019). DOI: [10.2514/6.2019-4181](https://doi.org/10.2514/6.2019-4181).
- [24] David Hall et al. Assessment of a Boundary Layer Ingesting Turboelectric Aircraft Configuration using Signomial Programming. *2018 Aviation Technology, Integration, and Operations Conference. AIAA Paper 2018-3973* (2018). DOI: [10.2514/6.2018-3973](https://doi.org/10.2514/6.2018-3973).

- [25] A Plas et al. Performance of a Boundary Layer Ingesting (BLI) Propulsion System. *45th AIAA Aerospace Sciences Meeting and Exhibit. AIAA Paper 2007-450* (). DOI: [10.2514/6.2007-450](https://doi.org/10.2514/6.2007-450).
- [26] Hector Solorzano, Ana Scarabino. Innovación en Sistemas de Propulsión: Métodos, Propuestas y Desafíos. *Revista Ciencias Espaciales* Vol. 13 (2020) 108–123. DOI: [10.5377/ce.v13i1.11257](https://doi.org/10.5377/ce.v13i1.11257).
- [27] Christopher Chiang, David Koo, David Zingg. Aerodynamic Shape Optimization of an S-Duct Intake for a Boundary Layer Ingesting Engine. *Journal of aircraft* Vol. 59 (2021) 1–17. DOI: [10.2514/6.2021-2468](https://doi.org/10.2514/6.2021-2468).
- [28] A. Rabe et al. A facility for active flow control research in serpentine inlets. *40th AIAA Aerospace Sciences Meeting Exhibit. AIAA Paper 2002-510* (2002). DOI: [10.2514/6.2002-510](https://doi.org/10.2514/6.2002-510).
- [29] Jai Ahuja, Dimitri Mavris. Sensitivity of Boundary Layer Ingestion Effects to Tube and Wing Airframe Design Features. *AIAA Scitech 2020 Forum, AIAA Paper 2020-1523* (2020). DOI: [10.2514/6.2020-1523](https://doi.org/10.2514/6.2020-1523).
- [30] Brian Allan, Lewis Owens, Bobby Berrier. Numerical Modeling of Active Flow Control in a Boundary Layer Ingesting Offset Inlet. *2nd AIAA Flow Control Conference, AIAA Paper 2004-2318* (2004). DOI: [10.2514/6.2004-2318](https://doi.org/10.2514/6.2004-2318).
- [31] Bobby Berrier, Brian Allan. Experimental and Computational Evaluation of Flush-Mounted, S-Duct Inlets (Invited). *42nd AIAA Aerospace Science Meeting and Exhibit, AIAA Paper 2004-764* (2004). DOI: [10.2514/6.2004-764](https://doi.org/10.2514/6.2004-764).
- [32] Sheldon Green. *Fluid Vortices*. Vol. 30. Jan. 1995. ISBN: 978-94-010-4111-9. DOI: [10.1007/978-94-011-0249-0](https://doi.org/10.1007/978-94-011-0249-0).
- [33] Kazuomi Yamamoto, Kentaro Tanaka, Mitsuhiro Murayama. Effect of a Nonlinear Constitutive Relation for Turbulence Modeling on Predicting Flow Separation at Wing-Body Juncture of Transonic Commercial Aircraft. *30th AIAA Applied Aerodynamics Conference 2012. AIAA Paper 2012-2895* (2012). DOI: [10.2514/6.2012-2895](https://doi.org/10.2514/6.2012-2895).
- [34] Byung Lee, Meng Liou, Chongam Kim. Optimizing a Boundary-Layer-Ingestion Offset Inlet by Discrete Adjoint Approach. *AIAA Journal* Vol. 48 (2010) 2008–2016. DOI: [10.2514/1.J050222](https://doi.org/10.2514/1.J050222).
- [35] Chengyuan Liu et al. Thermal Cycle Analysis of Turboelectric Distributed Propulsion System with Boundary Layer Ingestion. *Aerospace Science and Technology* Vol. 27 (2013) 163–170. DOI: [10.1016/j.ast.2012.08.003](https://doi.org/10.1016/j.ast.2012.08.003).
- [36] Gaetan Kenway, Cetin Kiris. Aerodynamic Shape Optimization of the STARC-ABL Concept for Minimal Inlet Distortion. *2018 AIAA/ASCE/AHS/ASC Structures, Structural Dynamics, and Materials Conference. AIAA Paper 2018-1912* (Jan. 2018). DOI: [10.2514/6.2018-1912](https://doi.org/10.2514/6.2018-1912).
- [37] SAE Aerospace Information. *Inlet Total-Pressure-Distortion Considerations for Gas-Turbine Engines - Report -1419*. 1999.

- [38] SAE Aerospace Information. *A Methodology for Assessing Inlet Swirl Distortion*. 2010.
- [39] Yann Colin et al. Numerical Simulation and Analysis of Crosswind Inlet Flows at Low Mach Numbers. *Proceedings of the 8th International Symposium on Experimental and Computational Aerothermodynamics of Internal Flows, Paper reference ISAI8-0058*. hal-03224309 (Aug. 2007).
- [40] Gérald Carrier et al. Numerical and Experimental Aerodynamic Investigations of Boundary Layer Ingestion for Improving Propulsion Efficiency of Future Air Transport. *31st AIAA Applied Aerodynamics Conference. AIAA Paper 2013-2406* (2013). DOI: [10.2514/6.2013-2406](https://doi.org/10.2514/6.2013-2406).
- [41] James Giuliani et al. Numerical Simulation of Boundary Layer Ingesting (BLI) Inlet/Fan Interaction. *50th AIAA/ASME/SAE/ASEE Joint Propulsion Conference. AIAA Paper 2014-3731* (2014). DOI: [10.2514/6.2014-3731](https://doi.org/10.2514/6.2014-3731).
- [42] Chad M. Winkler, Zach Davis. Summary of the 3rd Propulsion Aerodynamics Workshop: S-duct Results. *53rd AIAA/SAE/ASEE Joint Propulsion Conference. AIAA Paper 2017-4912* (). DOI: [10.2514/6.2017-4912](https://doi.org/10.2514/6.2017-4912).
- [43] Deric A. Babcock, Luiz Tobaldini Neto, Zachary S. Davis. Summary of the 4th Propulsion Aerodynamics Workshop: S-duct Results. *AIAA Propulsion and Energy 2019 Forum. AIAA Paper 2019-3845* (). DOI: [10.2514/6.2019-3845](https://doi.org/10.2514/6.2019-3845).
- [44] Romain Laraufie, Sébastien Deck. Zonal Detached Eddy Simulation (ZDES) study of a 3D curved duct. *THMT-12. Proceedings of the Seventh International Symposium On Turbulence, Heat and Mass Transfer* (2012) 4. DOI: [10.1615/ICHMT.2012.ProcSevIntSympTurbHeatTransfPal.400](https://doi.org/10.1615/ICHMT.2012.ProcSevIntSympTurbHeatTransfPal.400).
- [45] David Hall, E. Greitzer, Choon Tan. Analysis of Fan Stage Conceptual Design Attributes for Boundary Layer Ingestion. *Journal of Turbomachinery* Vol. 139 (2017). DOI: [10.1115/1.4035631](https://doi.org/10.1115/1.4035631).
- [46] E. Gunn, Cesare Hall. Aerodynamics of Boundary Layer Ingesting Fans. *ASME Turbo Expo 2014: Turbine Technical Conference and Exposition* (2014). DOI: [10.1115/GT2014-26142](https://doi.org/10.1115/GT2014-26142).
- [47] V. Fidalgo, Cesare Hall, Yann Colin. “A Study of Fan-Distortion Interaction Within the NASA Rotor 67 Transonic Stage”. Vol. Vol. 134. Oct. 2010. DOI: [10.1115/GT2010-22914](https://doi.org/10.1115/GT2010-22914).
- [48] H. Tennekes, John Lumley. A First Course in Turbulence. *SERBIULA (sistema Librum 2.0)* (Nov. 2014).
- [49] Hermann Schlichting, Klaus Gersten. *Boundary-Layer Theory*. Jan. 2017. ISBN: 978-3-662-52917-1. DOI: [10.1007/978-3-662-52919-5](https://doi.org/10.1007/978-3-662-52919-5).
- [50] Wolf-Christian Müller, Mark Thiele. Scaling and energy transfer in rotating turbulence. *EPL (Europhysics Letters)* Vol. 77 (2007) 34003. DOI: [10.1209/0295-5075/77/34003](https://doi.org/10.1209/0295-5075/77/34003).

- [51] Stefano Musacchio, Guido Boffetta. Split energy cascade in turbulent thin fluid layers. *Physics of Fluids* Vol. 29 (Nov. 2017) 111106. DOI: [10.1063/1.4986001](https://doi.org/10.1063/1.4986001).
- [52] Luca Biferale, Stefano Musacchio, Federico Toschi. Inverse Energy Cascade in Three-Dimensional Isotropic Turbulence. *Physical review letters* Vol. 108 (2012) 164501. DOI: [10.1103/PhysRevLett.108.164501](https://doi.org/10.1103/PhysRevLett.108.164501).
- [53] Steven Wellborn, Bruce Reichert, Theodore Okiishi. An experimental investigation of the flow in a diffusing S-duct. *Lewis Research Centre. NASA Technical Memorandum 106411* (1993).
- [54] Kewei Xu, Gecheng Zha. Mitigation of Serpentine Duct Flow Distortion Using CoFlow Jet Active Flow Control. *AIAA AVIATION 2020 FORUM, AIAA Paper No 2020-2954* (2020). DOI: [10.2514/6.2020-2954](https://doi.org/10.2514/6.2020-2954).
- [55] Yahya Shanan. Active flow control of a diffusing S-duct. *International Journal of Engineering, Science and Technology* Vol. 12 (2020) 1–10. DOI: [10.4314/ijest.v12i2.1](https://doi.org/10.4314/ijest.v12i2.1).
- [56] Antoine Debien et al. Salient and smooth edge ramps inducing turbulent boundary layer separation: Flow characterization for control perspective. *Comptes Rendus Mécanique* Vol. 342 (2014). DOI: [10.1016/j.crme.2014.05.003](https://doi.org/10.1016/j.crme.2014.05.003).
- [57] Fadla Fawzi et al. Investigation of the dynamics in separated turbulent flow. *European Journal of Mechanics - B/Fluids* Vol. 76 (2019) 190–204. DOI: [10.1016/j.euromechflu.2019.01.006](https://doi.org/10.1016/j.euromechflu.2019.01.006).
- [58] Robert Bush et al. Recommendations for Future Efforts in RANS Modeling and Simulation. *AIAA Scitech 2019 Forum. AIAA Paper 2019-0317* (2019). DOI: [10.2514/6.2019-0317](https://doi.org/10.2514/6.2019-0317).
- [59] David Wilcox. Reassessment of the Scale-determining Equation for Advanced Turbulence Models. *AIAA Journal* Vol. 26 (1988) 1299–1310. DOI: [10.2514/3.10041](https://doi.org/10.2514/3.10041).
- [60] Philippe Spalart, Steven Allmaras. A One-Equation Turbulence Model for Aerodynamic Flows. *AIAA Journal* Vol. 439 (1992). DOI: [10.2514/6.1992-439](https://doi.org/10.2514/6.1992-439).
- [61] Philippe Spalart, Steven Allmaras. A One-Equation Turbulence Model for Aerodynamic Flows. *La Recherche Aérospatiale* Vol. 1 (1994) 1(1): 5–21. DOI: [10.2514/6.1992-439](https://doi.org/10.2514/6.1992-439).
- [62] Michael Shur et al. Turbulence Modeling in Rotating and Curved Channels: Assessing the Spalart-Shur Correction. *Aiaa Journal - AIAA J* Vol. 38 (2000) 784–792. DOI: [10.2514/2.1058](https://doi.org/10.2514/2.1058).
- [63] Philippe Spalart. Strategies for Turbulence Modelling and Simulations. *International Journal of Heat and Fluid Flow* Vol. 21 (2000) 252–263. DOI: [10.1016/S0142-727X\(00\)00007-2](https://doi.org/10.1016/S0142-727X(00)00007-2).
- [64] F. Menter. Two-Equation Eddy-Viscosity Turbulence Models for Engineering Applications. *AIAA Journal* Vol. 32 (1994) 1598–1605.

- [65] Werner Haase et al. FLOMANIA — A European Initiative on Flow Physics Modelling, Results of the European-Union funded project, 2002 – 2004. *Notes on Numerical Fluid Mechanics and Multidisciplinary Design* Vol. 94 (2006). DOI: [10.1007/978-3-540-39507-2](https://doi.org/10.1007/978-3-540-39507-2).
- [66] Brian Launder, B. Sharma. Application of Energy Dissipation Model of Turbulence to the Calculation of Flow Near Spinning Disc. *Letters Heat Mass Transfer* Vol. 1 (1974) 131–137. DOI: [10.1016/0735-1933\(74\)90024-4](https://doi.org/10.1016/0735-1933(74)90024-4).
- [67] Charles Speziale, Sutanu Sarkar, T. Gatski. Modelling the Pressure-Strain Correlation of Turbulence - An Invariant Dynamical Systems Approach. *Journal of Fluid Mechanics* Vol. 227 (1991). DOI: [10.1017/S0022112091000101](https://doi.org/10.1017/S0022112091000101).
- [68] C. Shir. A Preliminary Study of Atmospheric Turbulent Flow in the Idealized Planetary Boundary Layer. *Journal of Atmospheric Sciences* Vol. 30 (Sept. 1973) 1327–1339. DOI: [10.1175/1520-0469\(1973\)030<1327:APNSOA>2.0.CO;2](https://doi.org/10.1175/1520-0469(1973)030<1327:APNSOA>2.0.CO;2).
- [69] Bart Daly, Francis Harlow. Transport Equations in Turbulence. *Physics of Fluids - PHYS FLUIDS* Vol. 13 (1970) 2634–2649. DOI: [10.1063/1.1692845](https://doi.org/10.1063/1.1692845).
- [70] Brian Launder, G. Reece, W. Rodi. Progress in the Development of a Reynolds Stress Turbulence Closure. *Journal of Fluid Mechanics* Vol. 68 (1975) 537–566. DOI: [10.1017/S0022112075001814](https://doi.org/10.1017/S0022112075001814).
- [71] Bernhard Eisfeld, Christopher Rumsey. Second-Moment RANS Model Verification and Validation using the Turbulence Modeling Resource Website (Invited). *22nd AIAA Computational Fluid Dynamics Conference. AIAA Paper 2014-2924* (2015). DOI: [10.2514/6.2015-2924](https://doi.org/10.2514/6.2015-2924).
- [72] P. Kumar, J. Dey. Shape Factor of the Turbulent Boundary Layer on a Flat Plate and the Reynolds Shear Stress in the Outer Region. *Physical Review Fluids* Vol. 4 (2019). DOI: [10.1103/PhysRevFluids.4.024605](https://doi.org/10.1103/PhysRevFluids.4.024605).
- [73] Ricardo Vinuesa et al. Turbulent Boundary Layers around Wing Sections up to $Re_c = 1,000,000$. *International Journal of Heat and Fluid Flow* Vol. 72 (2018) 86–99. DOI: [10.1016/j.ijheatfluidflow.2018.04.017](https://doi.org/10.1016/j.ijheatfluidflow.2018.04.017).
- [74] Paul Durbin, Bjørn Reif. *Statistical Theory and Modeling for Turbulent Flows*, Second Edition, Second Edition (2011). DOI: [10.1002/9780470972076](https://doi.org/10.1002/9780470972076).
- [75] David Wilcox. *Turbulence Modeling for CFD (Third Edition)*. 2006.
- [76] Parviz Moin, Krishnan Mahesh. Direct Numerical Simulation: A Tool in Turbulence Research. *Annu. Rev. Fluid Mech.* Vol. 30 (1998) 539–578. DOI: [10.1146/annurev.fluid.30.1.539](https://doi.org/10.1146/annurev.fluid.30.1.539).
- [77] Pierre Sagaut. Large Eddy Simulation for Incompressible Flows. An Introduction (2001) 1745–1746. DOI: [10.1088/0957-0233/12/10/707](https://doi.org/10.1088/0957-0233/12/10/707).
- [78] Jung-Il Choi, Jack Edwards, Robert Baurle. Compressible Boundary Layer Predictions at High Reynolds Number using Hybrid LES/RANS Methods. *AIAA Journal* Vol. 47 (2009) 2179–2193. DOI: [10.2514/1.41598](https://doi.org/10.2514/1.41598).

- [79] Daniel Gieseke et al. Compressible-Flow Simulations Using a New Large-Eddy Simulation/Reynolds-Averaged Navier-Stokes Model. *AIAA Journal* Vol. 49 (2011) 2194–2209. DOI: [10.2514/1.J051001](https://doi.org/10.2514/1.J051001).
- [80] Michael Shur et al. A hybrid RANS-LES Approach with Delayed-DES and Wall-modelled LES Capabilities. *International Journal of Heat and Fluid Flow* Vol. 29 (2008) 1638–1649. DOI: [10.1016/j.ijheatfluidflow.2008.07.001](https://doi.org/10.1016/j.ijheatfluidflow.2008.07.001).
- [81] Cédric Uribe. “Développement d’une approche ZDES à deux équations de transport et application turbomachines”. PhD thesis. Sept. 2018.
- [82] Philippe Spalart et al. Comments on the Feasibility of LES for Wings, and on a Hybrid RANS/LES Approach. *Conference: Advances in DNS/LES* (1997).
- [83] Sébastien Deck. Zonal-Detached-Eddy Simulation of the Flow Around a High-Lift Configuration. *Aiaa Journal - AIAA J* Vol. 43 (Nov. 2005) 2372–2384. DOI: [10.2514/1.16810](https://doi.org/10.2514/1.16810).
- [84] Sébastien Deck. Recent improvements in the Zonal Detached Eddy Simulation (ZDES) formulation. *Theoretical and Computational Fluid Dynamics* Vol. 26 (Dec. 2011) 1–28. DOI: [10.1007/s00162-011-0240-z](https://doi.org/10.1007/s00162-011-0240-z).
- [85] Philippe Spalart et al. A New Version of Detached-eddy Simulation, Resistant to Ambiguous Grid Densities. *Theoretical and Computational Fluid Dynamics* Vol. 20 (2006) 181–195. DOI: [10.1007/s00162-006-0015-0](https://doi.org/10.1007/s00162-006-0015-0).
- [86] Nicolas Renard, Sébastien Deck. Improvements in Zonal Detached Eddy Simulation for Wall Modeled Large Eddy Simulation. *AIAA Journal* Vol. 52 (2015) 1–5. DOI: [10.2514/1.J054143](https://doi.org/10.2514/1.J054143).
- [87] Sébastien Deck, Nicolas Renard. Towards an Enhanced Protection of Attached Boundary Layers in Hybrid RANS/LES Methods. *Journal of Computational Physics* Vol. 400 (2019). DOI: [10.1016/j.jcp.2019.108970](https://doi.org/10.1016/j.jcp.2019.108970).
- [88] Sébastien Deck, Romain Laraufie. Numerical Investigation of the Flow Dynamics Past a Three-element Aerofoil. *Journal of Fluid Mechanics* Vol. 732 (2013). DOI: [10.1017/jfm.2013.363](https://doi.org/10.1017/jfm.2013.363).
- [89] Sébastien Deck et al. Large-scale Contribution to Mean Wall Shear Stress in High-Reynolds-number Flat-plate Boundary Layers up to $Re=13650$. *Journal of Fluid Mechanics* Vol. 743 (2014). DOI: [10.1017/jfm.2013.629](https://doi.org/10.1017/jfm.2013.629).
- [90] Sébastien Deck et al. Zonal Detached Eddy Simulation (ZDES) of a Spatially Developing Flat Plate Turbulent Boundary Layer over the Reynolds number Range 3150–14000. *Physics of Fluids* Vol. 26 (2014). DOI: [10.1063/1.4866180](https://doi.org/10.1063/1.4866180).
- [91] Pierre-Élie Weiss, Sébastien Deck, Nicolas Renard. A Rapid and Low Noise Switch from RANS to WMLES on Curvilinear Grids with Compressible Flow Solvers. *Journal of Computational Physics* Vol. 363 (2018). DOI: [10.1016/j.jcp.2018.02.028](https://doi.org/10.1016/j.jcp.2018.02.028).
- [92] Benjamin Francois, Raphael Barrier, C Polacsek. Zonal Detached Eddy Simulation of the Fan-OGV Stage of a Modern Turbofan Engine. *ASME Turbo Expo 2020: Turbo-*

- machinery Technical Conference and Exposition. Paper No. 2020-14239* (2020). DOI: [10.1115/GT2020-14239](https://doi.org/10.1115/GT2020-14239).
- [93] Jolan Reynaud et al. A Comprehensive Framework for High Fidelity Computations of Two-species Compressible Turbulent Flows. *Journal of Computational Physics* Vol. 462 (2022). DOI: [10.1016/j.jcp.2022.111222](https://doi.org/10.1016/j.jcp.2022.111222).
- [94] Julien Marty, Cédric Uribe. Impact of Underlying RANS Turbulence Models in Zonal Detached Eddy Simulation: Application to a Compressor Rotor. *International Journal of Turbomachinery, Propulsion and Power* Vol. 5 (2020) 22. DOI: [10.3390/ijtpp5030022](https://doi.org/10.3390/ijtpp5030022).
- [95] Adrien Chatelier. “Modeling questions for numerical simulations of aeronautical combustors”. PhD thesis. June 2019.
- [96] Jaime Vaquero, Nicolas Renard, Sébastien Deck. Advanced Simulations of Turbulent Boundary Layers under Pressure-gradient Conditions. *Physics of Fluids* Vol. 31 (2019). DOI: [10.1063/1.5126932](https://doi.org/10.1063/1.5126932).
- [97] Jaime Vaquero, Nicolas Renard, Sébastien Deck. Outer Layer Turbulence Dynamics in a High-Reynolds-number Boundary Layer up to Recovering from Mild Separation. *Journal of Fluid Mechanics* Vol. 942 (2022). DOI: [10.1017/jfm.2022.389](https://doi.org/10.1017/jfm.2022.389).
- [98] Geoffrey Tanguy, David MacManus, Eric Garnier. Numerical Investigation of the Unsteady Distortion for an S-duct Intake with Mechanical Vortex Generators. *International Journal of Heat and Fluid Flow* Vol. 95 (2022). DOI: [10.1016/j.ijheatfluidflow.2022.108975](https://doi.org/10.1016/j.ijheatfluidflow.2022.108975).
- [99] Fabien Gand. Investigation of Turbulence Development in Incompressible Jets with Zonal Detached Eddy Simulation (ZDES) and Synthetic Turbulent Inflow. *International Journal of Heat and Fluid Flow* Vol. 61 (2016). DOI: [10.1016/j.ijheatfluidflow.2016.06.003](https://doi.org/10.1016/j.ijheatfluidflow.2016.06.003).
- [100] Nicolas Chauvet, Sébastien Deck, Laurent Jacquin. Zonal Detached Eddy Simulation of a Controlled Propulsive Jet. *AIAA Journal* Vol. 45 (2007) 2458–2473. DOI: [10.2514/4.1.28562](https://doi.org/10.2514/4.1.28562).
- [101] Daniel Gil-Prieto et al. Unsteady Characteristics of S-duct Intake Flow Distortion. *Aerospace Science and Technology* Vol. 84 (2018). DOI: [10.1016/j.ast.2018.10.020](https://doi.org/10.1016/j.ast.2018.10.020).
- [102] Eric Garnier. Flow Control by Pulsed Jet in a Curved S-Duct: A Spectral Analysis. *AIAA Journal* Vol. 53 (2015) 1–15. DOI: [10.2514/1.J053422](https://doi.org/10.2514/1.J053422).
- [103] Daniel Gil-Prieto et al. Delayed Detached-Eddy Simulation and Particle Image Velocimetry Investigation of S-Duct Flow Distortion. *AIAA Journal* Vol. 55 (2017) 1–16. DOI: [10.2514/1.J055468](https://doi.org/10.2514/1.J055468).
- [104] Anne-Laure Delot, Richard Scharnhorst. A Comparison of Several CFD Codes with Experimental Data in a Diffusing S-Duct. *49th AIAA/ASME/SAE/ASEE Joint Propulsion Conference. AIAA Paper 2013-3796* (2013). DOI: [10.2514/6.2013-3796](https://doi.org/10.2514/6.2013-3796).

- [105] Geoffrey Tanguy. “Experimental and Computational Aerodynamics Study of Convolved Intakes Duct”. PhD thesis. Cranfield University, 2018.
- [106] Daniel Gil-Prieto et al. Convolved Intake Distortion Measurements Using Stereo Particle Image Velocimetry. *AIAA Journal* Vol. 55 (2017) 1–15. DOI: [10.2514/1.J055467](https://doi.org/10.2514/1.J055467).
- [107] James Lucas, Walter O’Brien, Anthony Ferrar. Effect of BLI-Type Inlet Distortion on Turbofan Engine Performance. *ASME Turbo Expo 2014: Turbine Technical Conference and Exposition. Paper No. 2014-26666* (2014). DOI: [10.1115/GT2014-26666](https://doi.org/10.1115/GT2014-26666).
- [108] Gregory Heinlein, M. Bakhle, Jen-Ping Chen. Aeromechanic Response of a Coupled Inlet-Fan Boundary Layer Ingesting Distortion-Tolerant Fan. *ASME Turbo Expo 2019: Turbomachinery Technical Conference and Exposition. Paper No. 2019-91866* (2019). DOI: [10.1115/GT2019-91866](https://doi.org/10.1115/GT2019-91866).
- [109] Wasdell D Miller D. Off-design Prediction of Compressor Blade Losses. *MECHE C279/87* Vol. 1 (1987) 249–260.
- [110] Esteban Valencia Torres et al. Discretized Miller Approach to Assess Effects on Boundary Layer Ingestion Induced Distortion. *Chinese Journal of Aeronautics* Vol. 30 (2016). DOI: [10.1016/j.cja.2016.12.005](https://doi.org/10.1016/j.cja.2016.12.005).

Appendix A

Study of the effect of the boundary layer thickness and freestream Mach number

A.1 Boundary layer thickness effect

Several simulations were performed to study the effect that the thickness of the boundary layer would have on the BLI intake physical phenomena. Simulations were performed using the Spalart-Allmaras model with several mass flow rate values. Figures [A.1](#), [A.2](#) and [A.3](#) shows the total pressure and velocity behavior at the AIP for 3.0, 3.4 and 4.0 kg·s⁻¹ respectively.

In general, the total pressure at the AIP decreases with the increase in the thickness of the boundary layer, this was reflected with the increase in pressure-based distortion indices made in chapter 7. There was also an increase in the velocity-based distortion indices in that same chapter.

There are two mechanisms that explain this: First, the axial velocity distribution depends on the region affected by the boundary layer. If the boundary layer is thinner, the region with low velocity will also be small, and as a result, the region with high velocity will need to have a lower average velocity in order to allow the same MFR going through. Second, as the velocity gradient is greater in the boundary layer (the velocity changes in a smaller thickness), the vortices generated by the secondary fluxes are somewhat stronger. The position of the center of the vortices generated by the secondary flow also changes. If the boundary layer is thinner, the velocity gradient is located closer to the wall, so the vortices are generated closer too. The position of the swirls also affects the morphology and timing of the flow separation. It seems that there is a stronger coupling between the vortices and the separation regions with a thinner boundary layer. A thinner boundary layer can also generate a flow separation even at higher mass flow rate values.

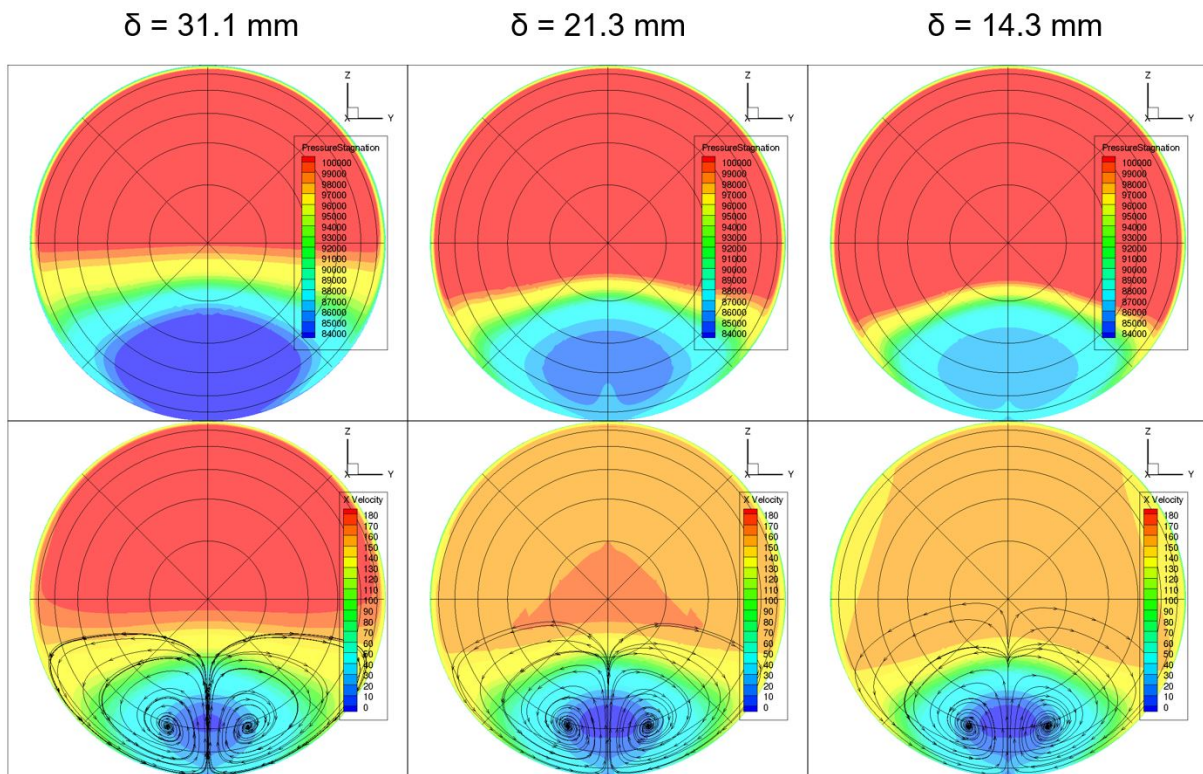


Figure A.1: Boundary layer thickness effects at AIP for $3.0 \text{ kg}\cdot\text{s}^{-1}$. Up: Total pressure field. Down: Axial velocity and streamlines.

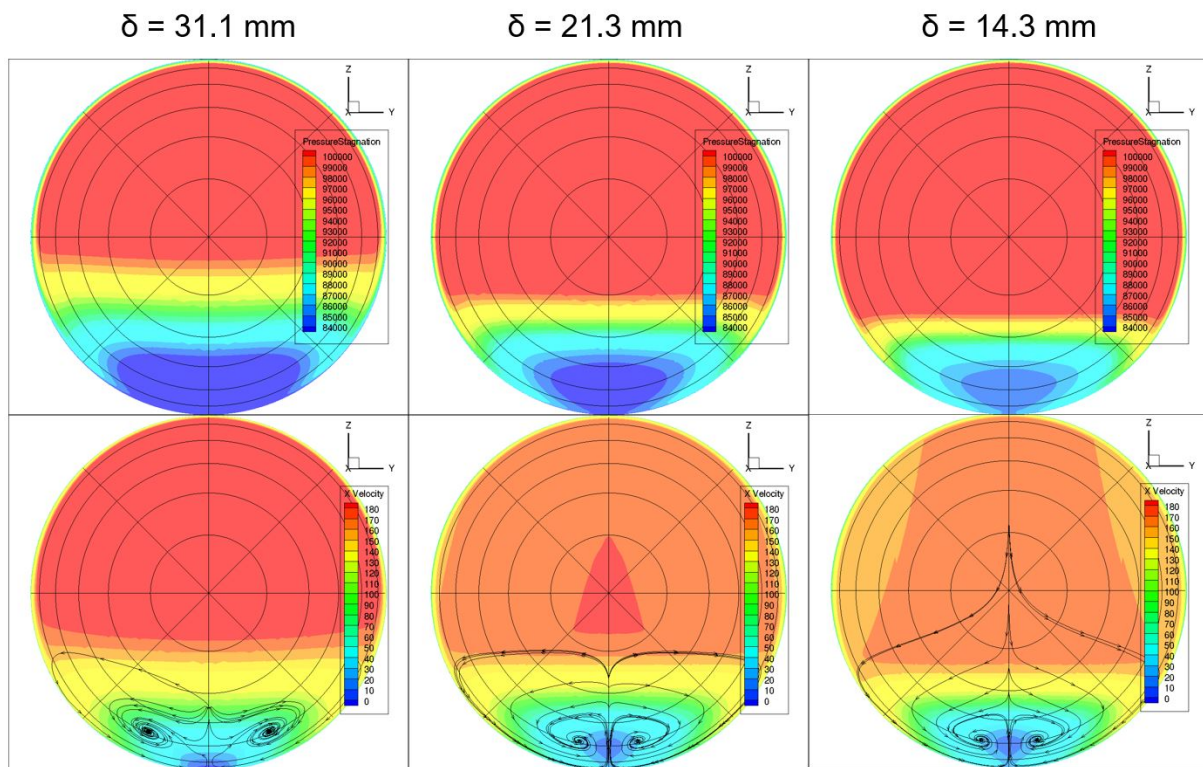


Figure A.2: Boundary layer thickness effects at AIP for $3.4 \text{ kg}\cdot\text{s}^{-1}$. Up: Total pressure field. Down: Axial velocity and streamlines.

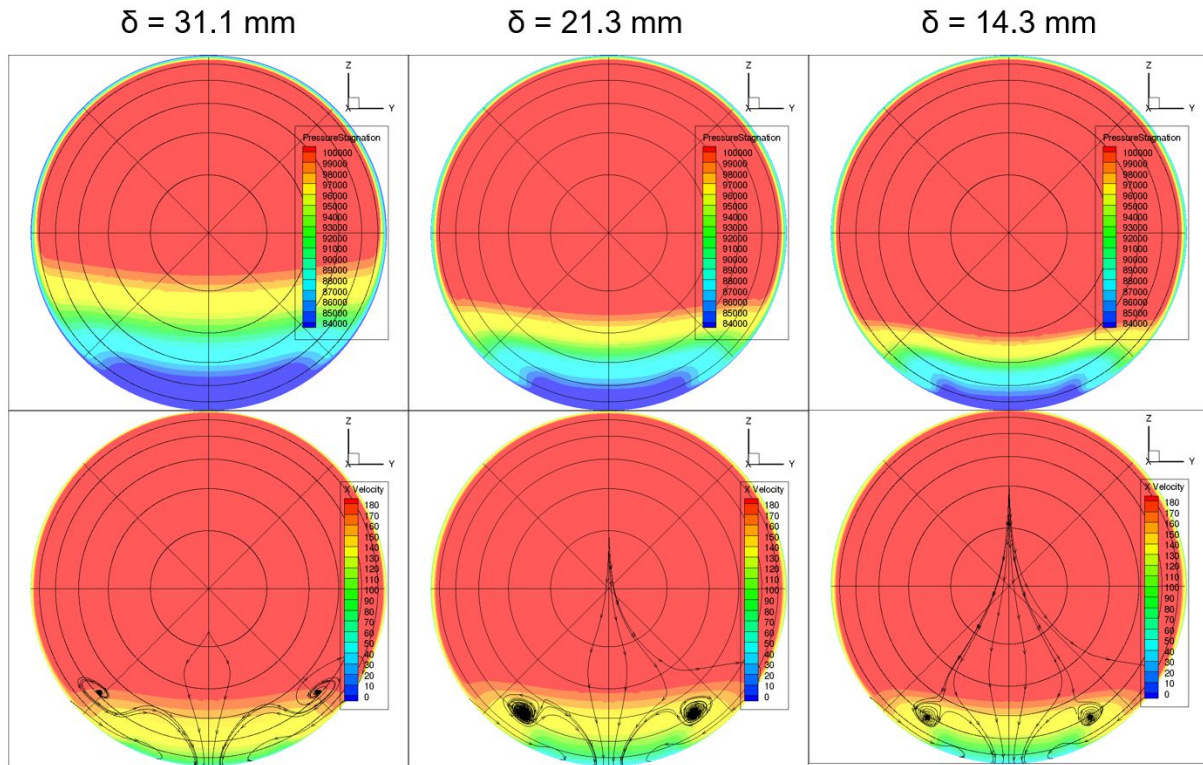


Figure A.3: Boundary layer thickness effects at AIP for $4.0 \text{ kg}\cdot\text{s}^{-1}$. Up: Total pressure field. Down: Axial velocity and streamlines.

A.2 Mach number effect

An investigation into the effects of the Mach number on the freestream was conducted using the Spalart-Allmaras model. The Mach number was varied between 0.75 and 0.84, while the mass flow rate was kept constant at $3.4 \text{ kg}\cdot\text{s}^{-1}$. The results indicate that the effect of the Mach number on flow behavior is linear. Specifically, an increase in Mach number leads to a corresponding increase in total pressure loss at the AIP, as discussed in Chapter 7. Figure [A.4](#) illustrates the behavior from three different perspectives. It is observed that the recirculation volume increases with Mach number, and the separation point on the intake ramp moves upstream. Chapter 4 also demonstrated that an increase in Mach number results in a proportional increase in vorticity magnitude at the AIP.

The alterations in the morphology of the recirculation region and their impact on flow distribution at the AIP are generated by two primary mechanisms. The first mechanism is the increase in the adverse pressure gradient at the intake ramp, which is generated by both geometry and flow conditions. This gradient slows down the flow even more when the Mach number is high. The second mechanism is the impact of the Mach number on the development of the boundary layer, which generates a slightly thinner boundary layer when the Mach number is increased.

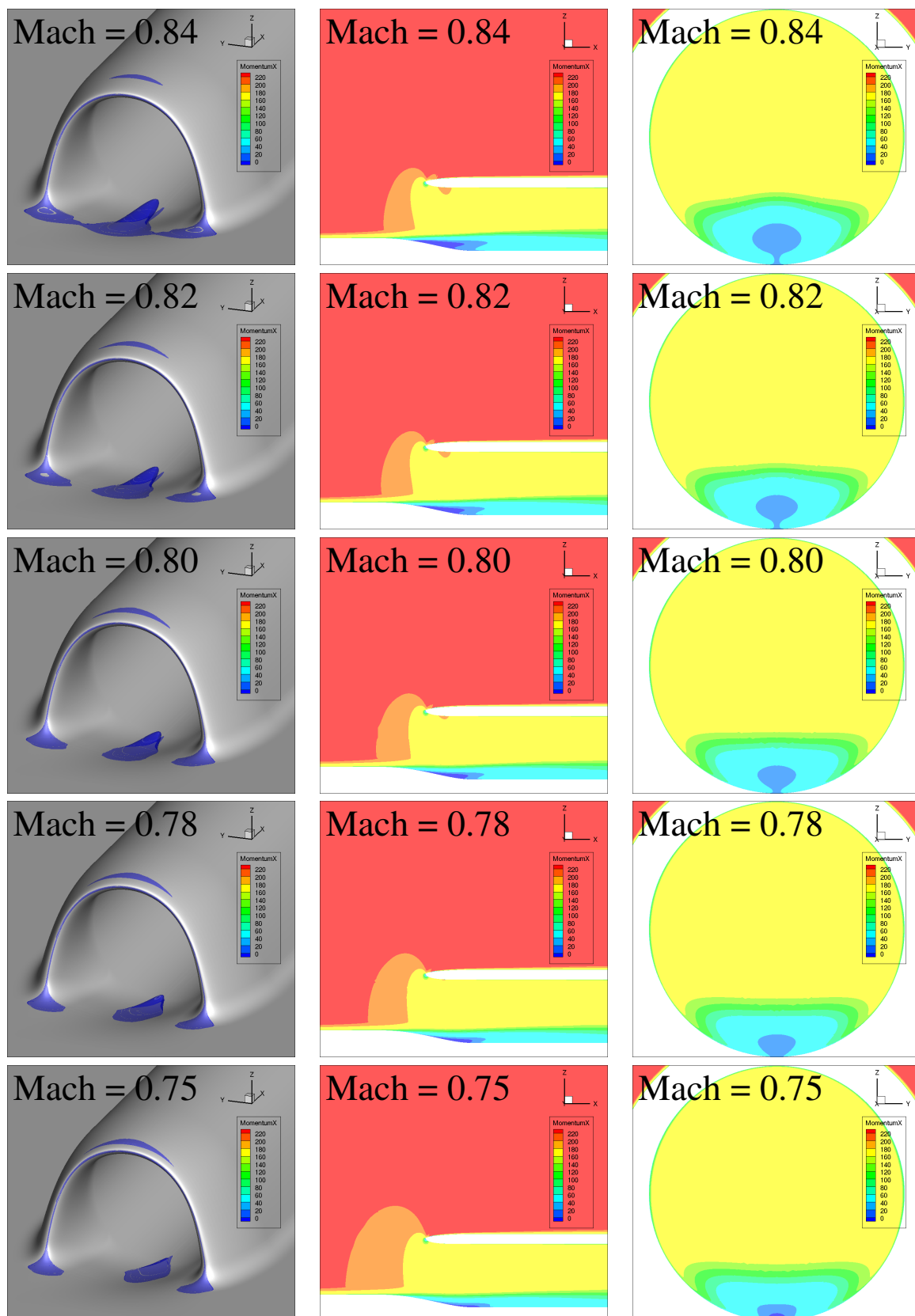


Figure A.4: Effect of the freestream Mach number. Left: recirculation region over the intake ramp shown in blue. Center: Momentum in the axial direction over the symmetry plane. Right: Momentum in the axial direction over the AIP.

Appendix B

Distortion indices propositions for a boundary layer intake

B.1 Velocity and Pressure Distortion Index (VPDI)

The aerodynamic distortion on a BLI engine is clearly affected by both pressure losses and swirl velocity. It is very likely that a distortion criterion suitable for BLI configurations needs to take into account both parameters. Therefore, as a first attempt to provide a more adapted distortion index based on a mixture of both parameters is proposed. This index is called VPDI (Velocity and Pressure Distortion Index). Its value is computed following Equation [B.1](#).

$$VPDI = \max \left(\int_0^{2*\pi} \left[(|\alpha_{i,j}| + 1 - \frac{Pt_{i,j}}{Pt}) \right] d\theta \right) \quad (\text{B.1})$$

α is an angle which takes into account the ratio between the axial velocity and the tangential velocity. Its value is calculated in equation [2.11](#). Pt is the total pressure. The subscripts j indicate where this angle/pressure is calculated. In the first instance, those parameters can be calculated along a measured ring. In this case the ring is discretized in i positions. The distortion criteria value is the maximum value between the j rings.

VPDI takes the integral of a variable that depends on a velocity term and a pressure term. When there are pressure losses the term on the right tends to decrease. When the ratio of tangential and axial velocity increases, the velocity term increases too. At lower MFR values, the VPDI value tends to predict a higher distortion. This higher value is linked to the pressure losses and tangential velocities. Radial and tangential velocities tend to be weaker with higher MFR values, contrary to the total pressure, which is always affected even at high MFR. Figure [B.1](#) shows this term calculated in some simulation cases.

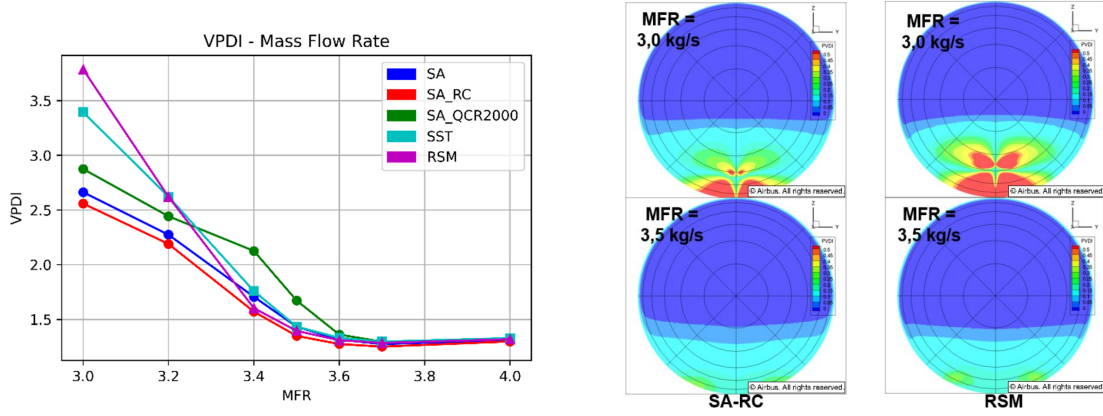


Figure B.1: Velocity and Pressure Distortion Index for different turbulence models at various mass flow rates.

This distortion index tends to predict a similar behavior as the one obtained with distortion criteria only based on swirl parameters. The only advantage shown by the IDC, to locate when the detachment occurs, is less evident in the proposed criterion.

B.2 β -IDC

Another research direction would be to take advantage of velocity-based distortion criteria to assess the homogeneity of the angle of attack perceived by the fan blades. A first approach has been done using the velocity triangle, as shown on the right of figure B.2, to calculate this angle for a generic fan. A generic V_{rot} is used as the rotation velocity of the fan. V_{real} is the velocity perceived by the intake affected by the boundary layer. Finally, the angle β is the angle created between the rotation velocity vector and relative velocity vector. The mathematical approach for this index is based on the IDC formulation, shown in Equation B.2. This formulation highlights the angle of attack changes along the rotation of the blade.

$$\beta_{IDC} = \max_{1 \leq i \leq 5} 0.5 \left(\frac{\overline{\beta}_i - \beta_i^{min} - \overline{\beta}_{i+1} - \beta_{i+1}^{min}}{\overline{\beta}_f} \right) \quad (B.2)$$

The left side of figure B.2 shows the evolution of this distortion index as function of the MFR value. It can be observed that the distortion predicted by this index increases when the MFR value decreases. This result shows some relation with the negative effects of the BLI configuration, however, it is not possible to clearly identify for which MFR values separation appears. Several authors have made similar approximations to characterize the distortion [109] [110]. However these approximations are more oriented to evaluate the impact on the operation of the engine and not on the characterization of the flow behaviour.

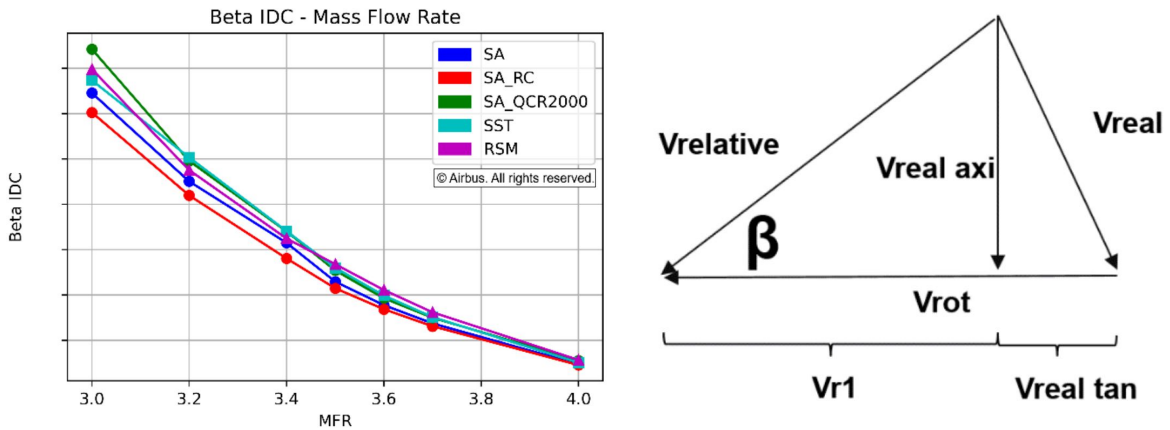


Figure B.2: Left: β -IDC Index for different turbulence models at various mass flow rates. Right: Velocity triangle

New distortion indices have been proposed to assess the distortion for BLI configurations. First, mixture of both pressure and velocity parameters is interesting, since they are the main physical phenomena that affect distortion in this type of configuration. The VPDI is only a first approach, more work needs to be done on this type of distortion criterion in order to achieve a some progress with respect to conventional distortion indices. β -IDC proposes an interesting way to couple distortion at the engine intake and the relative angle of attack perceived by the fan. Although this index shows disadvantages with respect to other more traditional ones, it leads to think about another way to link the flow behaviour at the intake, and also to predict the impact on the engine response. An energetic analysis, taking the work done by the fan to re-homogenize the flow might be an interesting analysis to complement this research direction.

Titre : Etude et prédiction des écoulements aérodynamiques sur une entrée d'air de moteur à ingestion de couche limite pour un avion commercial

Mots clés : Ecoulement transonique, Ingestion de couche limite, décollement, écoulement instationnaire

Résumé : Le concept BLI (Boundary Layer Ingestion ou ingestion de couche limite) propose d'ingérer et de profiter de la faible quantité de mouvement dans la couche limite pour générer une poussée de manière plus efficace. Cette amélioration potentielle présente plusieurs inconvénients qui rendent difficile le respect de certaines contraintes du moteur. L'une de ces contraintes concerne particulièrement la distorsion d'écoulement à l'entrée du moteur, affectée par une perte de pression totale et des vitesses tangentielles au plan d'interface aérodynamique (AIP). L'objectif de la thèse était d'identifier les principaux phénomènes physiques impliqués dans une prise d'air ingérant une couche limite, d'estimer la distorsion aérodynamique générée par ces phénomènes physiques et d'analyser la capacité prédictive de différents modèles de turbulence. L'étude a été menée en utilisant une prise d'air BLI semi-enfouie sur une plaque plane, non munie d'un étage de compression. La géométrie a été étudiée à la fois numériquement et expérimentalement dans des conditions transso-

niques. Le principal paramètre variant dans l'étude était le débit massique qui la traversait. En outre, d'autres paramètres importants d'ingestion de couche limite, tels que l'épaisseur de la couche limite ou le nombre de Mach de l'écoulement libre, ont été analysés.

Les essais en soufflerie ont été comparés aux résultats des simulations numériques avec différents modèles de turbulence. Les modèles de turbulence les plus courants dans l'industrie ont été utilisés, tels que k-SST ou Spalart-Allmaras, y compris certaines de ses corrections, en plus d'un modèle RSM et d'un calcul ZDES. Les comparaisons ont été effectuées à l'aide de prises de pression statique, de transducteurs kulite et d'un peigne de 40 capteurs de pression instationnaires situés à l'AIP. Le comportement de l'écoulement et les phénomènes stationnaires ont été comparés, ainsi que le comportement instationnaire par analyse spectrale. Enfin, les niveaux de distorsion générés lors des essais ont été comparés à ceux prédits par les méthodes numériques.

Title : Understanding and prediction of flow physics on a boundary layer ingestion air intake for a commercial aircraft

Keywords : Transonic flow, Boundary layer ingestion, Flow separation, Unsteady flow

Abstract : The BLI (Boundary Layer Ingestion) concept proposes to ingest and take advantage of the low momentum in the boundary layer to generate thrust in a more efficient way. This potential improvement has several drawbacks that make it difficult to fulfil some engine requirements. One of these requirements particularly concerns the flow distortion at the engine intake affected by a loss of total pressure and tangential velocities at the Aerodynamic Interface Plane (AIP). The objective of the research was to identify the primary physical phenomena involved in a boundary layer ingestion intake, estimate the aerodynamic distortion generated by these physical phenomena, and analyse the predictive capacity of different turbulence models.

The study was conducted using a BLI intake semi-buried on a flat plate, which did not take into account the effect of any compression stage. The geometry was studied both numerically and experimentally un-

der transonic conditions. The main parameter varied in the study was the mass flow that passed through it. In addition, other important boundary layer ingestion parameters, such as the boundary layer thickness or freestream Mach number were analysed.

The wind tunnel tests were compared with the results of numerical simulations with different turbulence models. The most common turbulence models in the industry were used, such as k-SST or Spalart-Allmaras including some of its corrections, in addition to a RSM model and a ZDES computation. The comparisons were made using the static pressure taps, kulite transducers, and a rake with 40 pressure sensors located at the AIP. The flow behaviour and stationary phenomena were compared, in addition to the unsteady behaviour by spectral analysis. Finally, the distortion levels generated in the tests were compared with those predicted by numerical methods.